A CONTRIBUTION TO THE STUDY OF THE MOLECULAR MOBILITY IN POLYMERIC MATERIALS BY THERMAL AND DIELECTRIC ANALYSIS

THESIS SUBMITTED BY

BELÉN REDONDO FOJ

TO OBTAIN THE DEGREE OF DOCTOR OF PHILOSOPHY AT THE

UNIVERSITAT POLITÈCNICA DE VALÈNCIA

VALENCIA, DECEMBER 2015

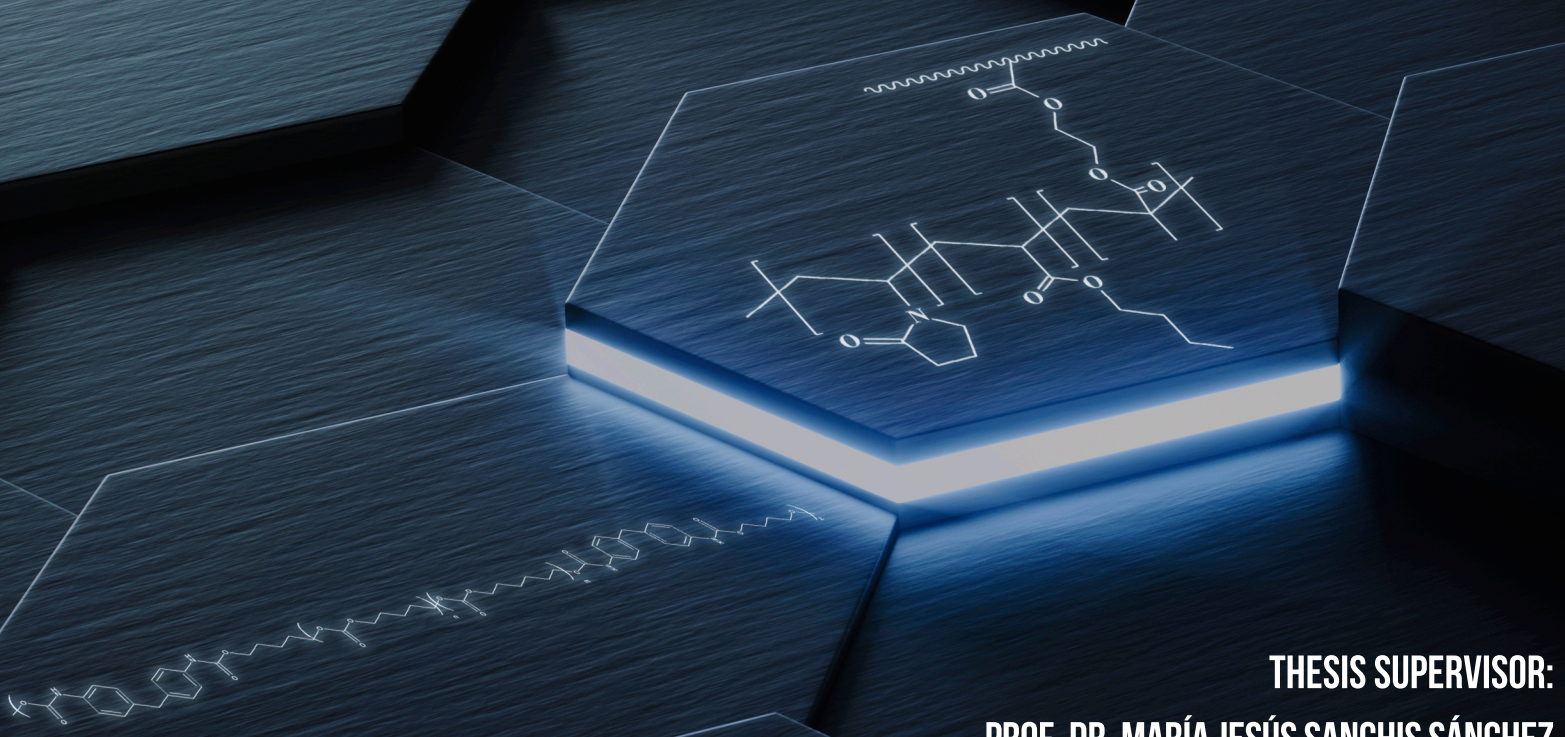

THESIS SUPERVISOR:

PROF. DR. MARÍA JESÚS SANCHIS SÁNCHEZ

UNIVERSITAT POLITÈCNICA DE VALÈNCIA

ITE INSTITUTO DE TECNOLOGÍA ELÉCTRICA

UNIVERSITAT POLITÈCNICA DE VALÈNCIA

ITE
INSTITUTO DE TECNOLOGÍA ELÉCTRICA

A CONTRIBUTION TO THE STUDY OF THE MOLECULAR MOBILITY IN POLYMERIC MATERIALS BY THERMAL AND DIELECTRIC ANALYSIS

Thesis submitted by

Belén Redondo Foj

to obtain the degree of Doctor of Philosophy at the

Universitat Politècnica de València

Valencia, December 2015

Thesis Supervisor:

Prof. Dr. María Jesús Sanchis Sánchez

The work presented in this thesis was carried out at the Universitat Politècnica de València and was financially supported by the Spanish Ministry of Economy and Competitiveness (Projects Nos. **MAT2008-06725-C03-03** and **MAT2012-33483)**.

"Cuando quieres algo, todo el Universo conspira para que realices tu deseo"

El Alquimista, Paulo Coelho

*A mis **padres**, Eloy y María –*

por su amor y apoyo incondicional.

*A **Samuel** –*

porque gracias a él, esta tesis es una realidad.

TABLE OF CONTENTS

ACKNOWLEDGEMENTS

Tras estos años de trabajo, llega el momento de mostrar mi agradecimiento a todas las personas que me han acompañado y apoyado durante el desarrollo de mi tesis doctoral.

En primer lugar, me gustaría expresar mi gratitud a mi directora de tesis María J. Sanchis por su inestimable ayuda durante todos estos años. Muchas gracias por confiar en mí, por darme esta oportunidad y por las incalculables horas invertidas tanto para el desarrollo de esta tesis como al mío propio.

También me gustaría agradecer a mis estimadas compañeras Marta Carsí y Pilar Ortiz su ayuda y amistad en este largo recorrido que suponer realizar una tesis doctoral. He aprendido mucho de vosotras tanto científica como personalmente. En este punto, no puedo olvidarme de mi querida Aurora Alonso, que pese a no formar parte de nuestro grupo de investigación, me ha apoyado, aconsejado y dado su amistad durante todos estos años.

Quiero mostrar mi agradecimiento a los profesores José M. García y Félix C. García del Grupo de Polímeros de la Universidad de Burgos y a los profesores Andrés Cantarero y Clara M. Gómez del Instituto de Ciencia de los Materiales de la Universidad de Valencia por el suministro de las muestras que han sido objeto de análisis en esta tesis doctoral.

I would like to thank Dr. Michael Nugent and Dr. Declan Devine from the Athlone Institute of Technology, for their support and advice during my research stay. I would also like to thank my office colleagues Ian Major, Joshua Yoon, John Killion, Michael J. Hopkins and Diwakar Kanwar for their support and friendship during those months in Ireland.

También quiero recordar a Lucía, María y Silvia, que sin su amistad, mi paso por Athlone no hubiese sido el mismo. Fue una gratísima sorpresa y una inesperada suerte encontraros en mi camino.

Tengo que agradecer a mis amigos segorbinos la alegría y apoyo que me han mostrado durante estos años, especialmente a mis queridas Irene, Asun y Ana. Y como no, a mis amigos valencianos, con los que he compartido tantas horas contándoles mis aventuras con la tesis. Especial mención a mis amigos almerienses Juan y Nazaret, por la bonita amistad que nos han brindado desde que entraron en nuestras vidas. No me olvido de mis compañeras de Máster Elena y Sara, que me acompañaron con su amistad en la primera etapa de la tesis y mis amigas Ana Isabel y Marta, que lo hicieron en la carrera.

También quiero expresar mi agradecimiento a mi nueva familia Ximo y Rosa Mari, por su apoyo y por cuidarme tanto durante todos estos años, así como a Miguel, Tere, Miguel hijo y Delfi.

Finalmente, agradezco enormemente a mi estimada familia todo el apoyo y amor que siempre me han mostrado. A mis primos Amparo y Luis, por su afecto y cariño. Muy especialmente a mis hermanos Maribel, Reme y Eloy por su amor, su respaldo y por estar siempre a mi lado. A mis cuñados Jose y Emi, que desde el primer día me han mostrado su aprecio y consejo. Y, por supuesto, a mis padres Eloy y María, gracias por vuestra dedicación, sacrificio y amor, os debo todo lo que soy. No me puedo olvidar de mis niños “los Bliblos” Pablo, Miguel, Alicia y Alejandra, que siempre me arrancan una sonrisa con su cariño y alegría. Y, por último, muchísimas gracias a Samuel, por su apoyo, consejo, positivismo y amor.

ABSTRACT

The development of new and more complex polymeric materials involves challenging problems to basic sciences. The relationship between structure and molecular dynamics assumes great importance for the future development of novel technologies based on such polymers. Thus, the understanding of how small changes in the chemical structure affect the properties of the material is essential to progress in the technological and scientific area. An in-depth analysis of the molecular mobility leads to establish the structure-properties relationships. On this basis, the main aim of the present work is to study the molecular mobility of two different families of polymeric materials. For this purpose, the experimental techniques mainly used were Differential Scanning Calorimetry (DSC) and Dielectric Relaxation Spectroscopy (DRS) (Chapter 3).

The first family of polymers characterized was a series of chemically cross-linked copolymers composed by Vinylpyrrolidone (VP) and Butyl Acrylate (BA) monomers. The study was divided in two parts, which are collected in Chapter 4 and 5.

In the first place, Chapter 4 contains the influence of the monomer molar ratio (*X*VP/*Y*BA) on the copolymer properties. Thus, a Fourier Transform Infrared Spectroscopy (FTIR) analysis verified dipole-dipole interactions between amide groups. The influence of these interactions on several parameters related to the molecular mobility was evidenced by the DSC, DRS and Dynamic Mechanical Analysis (DMA) techniques. The glass transition temperature (T_g) was found to increase with the VP content due to a reduction of the molecular mobility. The dielectric and mechanical spectra showed γ, β and α relaxations in increasing order of temperature, followed by conductive contributions in the dielectric spectrum. The γ process was related to the local motions of the butyl units, and the β process was a Johari–Goldstein (JG) secondary relaxation related to the local motions of the pyrrolidone group together with the motion of polymer backbone segments. Finally, the *dc* conductivity (σ_{dc}) was observed to increase with VP content. The conductivity was found to decouple from segmental dynamics at temperatures near glass transition.

Secondly, Chapter 5 presents the analysis of the effect of the cross-link density on the molecular dynamics of *60*VP/*40*BA copolymers using DSC and DRS. One single glass transition was detected by DSC measurements. The dielectric spectra exhibited, for all the samples, conductive processes and three dipolar relaxations labeled as α, β and γ in decreasing order of temperatures. An increase of the cross-linking produced a typical effect on the α process dynamics. However, the β process, which possessed typical features of pure JG relaxation, unexpectedly lost the intermolecular character for the highest cross-linker content. The fastest γ process was relatively unaffected.

The second family of polymeric materials studied was a series of segmented polycarbonatediol polyurethane (PUPH) modified with different amounts of expanded graphite (EG) conductive filler. The results are presented and discussed in Chapter 6. Scanning Electron Microscopy (SEM), X-ray diffraction measurements and FTIR analysis demonstrated a homogeneous dispersion of the EG filler in the matrix. DRS was used to study the dielectric properties of the PUPH/EG composites. The dielectric permittivity of the composites showed an insulator to conductor percolation transition with the increase of

the EG content. Significant changes in the dielectric permittivity took place when the weight fraction of EG is in the range of 20–30 wt%. The addition of expanded graphite to the matrix caused a dramatic increase in the electrical conductivity of ten orders of magnitude, which is an indication of percolative behavior.

Finally, the general conclusions are summarized in Chapter 7.

RESUMEN

El desarrollo de nuevos materiales poliméricos de mayor complejidad produce un desafío cada vez mayor en el área de las ciencias básicas. La relación entre la estructura y la dinámica molecular resulta de gran importancia para el desarrollo de nuevas tecnologías basadas en estos materiales poliméricos. Así, una mayor comprensión de cómo pequeños cambios en la estructura química afectan a las propiedades de los materiales resulta esencial para el progreso científico y tecnológico. Un análisis en profundidad de la movilidad molecular permite establecer las relaciones estructura-propiedades. Partiendo de esta base, el principal objetivo del presente trabajo es el estudio de la movilidad molecular de dos familias diferentes de materiales poliméricos. Para ello, las técnicas experimentales utilizadas fueron principalmente la Calorimetría Diferencial de Barrido (DSC) y la Espectroscopia de Relajación Dieléctrica (DRS).

La primera familia de polímeros caracterizada fue una serie de copolímeros entrecruzados químicamente compuestos por los monómeros Vinilpirrolidona (VP) y Acrilato de Butilo (BA). El estudio de dicha familia se dividió en dos partes, recogidas en los Capítulos 4 y 5.

En primer lugar, el Capítulo 4 contiene el estudio de la influencia de la proporción molar de monómero (*X*VP/*Y*BA) en las propiedades del copolímero. A través de un análisis por Espectroscopia de Infrarrojo por Transformada de Fourier (FTIR), se verificó la existencia de interacciones dipolo-dipolo entre los grupos amida. Mediante el análisis por DSC, DRS y Análisis Dinamomecánico (DMA), se evidenció la influencia de estas interacciones en diferentes parámetros relacionados con la movilidad molecular. Se observó una única temperatura de transición vítrea (T_g) cuyo valor incrementaba con el contenido en VP, debido a la reducción en la movilidad molecular. Los espectros mecánicos y dieléctricos mostraron tres relajaciones γ, β y α en orden creciente de temperatura, seguidos por una contribución conductiva, observada únicamente en el espectro dieléctrico. El proceso de relajación γ se relacionó con el movimiento local de las unidades butilo y el proceso β resultó ser una relajación secundaria Johari-Goldstein (JG), que está relacionada con movimientos locales del grupo pirrolidona junto con el movimiento de segmentos de la cadena principal. Se observó que la conductividad *dc* (σ_{dc}) aumentó con el contenido en VP. Por último, se encontró que la conductividad se desacoplaba de la dinámica segmental a temperaturas cerca de la transición vítrea.

En segundo lugar, el Capítulo 5 recoge el análisis del efecto de la densidad de entrecruzamiento en la dinámica molecular de los copolímeros *60*VP/*40*BA usando DSC y DRS. A través de las medidas de DSC se observó una única transición vítrea para todos los entrecruzamientos. El espectro dieléctrico mostró, para todas las muestras, procesos conductivos y tres relajaciones dipolares α, β y γ en orden decreciente de temperatura. El incremento en entrecruzante produjo el típico efecto en la dinámica del proceso α. Sin embargo, el proceso β, que tenía las características típicas de una relajación JG, perdió de forma inesperada su carácter intermolecular para el mayor contenido en entrecruzante. El proceso γ no se vio afectado.

La segunda familia de materiales poliméricos estudiada fue una serie de poliuretanos segmentados (PUPH) modificados con diferentes cantidades de grafito expandido (EG), utilizado como relleno conductivo (desde 0 a 50% en peso). La presentación y discusión de los resultados se recoge en el Capítulo 6. El análisis de los resultados obtenidos mediante Microscopía Electrónica de Barrido (SEM), Difracción de Rayos X y FTIR demostró la homogénea dispersión del relleno de EG en la matriz de PUPH. La técnica DRS se usó para estudiar las propiedades dieléctricas de los materiales compuestos PUPH/EG. La permitividad dieléctrica de los materiales mostró una transición de percolación desde aislante a conductor al incrementarse el contenido en EG. Se observaron cambios significativos en la permitividad dieléctrica cuando la fracción en peso de EG estaba en el rango de 20-30% en peso. La adición de grafito expandido a la matriz de PUPH causó un incremento significativo en la conductividad dieléctrica de diez órdenes de magnitud, lo que indica el comportamiento de percolación.

Finalmente, las conclusiones generales se resumen en el Capítulo 7.

RESUM

El desenvolupament de nous materials polimèrics de major complexitat produeix un desafiament cada vegada major en l'àrea de les ciències bàsiques. La relació entre l'estructura i la dinàmica molecular resulta de gran importància per al desenrotllament de noves tecnologies basades en aquests materials polimèrics. Així, una major comprensió de com petits canvis en l'estructura química afecten a les propietats dels materials, resulta essencial per al progrés científic i tecnològic. Un anàlisis en profunditat de la mobilitat molecular permet establir les relacions estructura-propietats. Partint d'aquesta base, el principal objectiu del present treball és l'estudi de la mobilitat molecular de dues famílies diferents de materials polimèrics. Per a això, les tècniques experimentals utilitzades van ser principalment la Calorimetria Diferencial de Rastreig (DSC) i l'Espectroscòpia de Relaxació Dielèctrica (DRS)

La primera família de polímers caracteritzada va ser una sèrie de copolímers entrecreuats químicament compostos pels monòmers Vinilpirrolidona (VP) i Acrilat de Butilo (BA) . L'estudi d'aquesta família es va dividir en dues parts, que s'arrepleguen en els Capítols 4 i 5.

En primer lloc, el Capítol 4 conté el estudi de la influència de la proporció molar de monòmer (XVP/YBA) en les propietats del copolímer. A través d'una anàlisi per Espectroscòpia d'Infraroig per Transformada de Fourier (FTIR), es va verificar l'existència d'interaccions dipol-dipol entre els grups amida. Mitjançant l'anàlisi per DSC, DRS i Anàlisi Dinamomecánico (DMA), es va evidenciar la influència d'aquestes interaccions en diferents paràmetres relacionats amb la mobilitat molecular. Es va observar una única temperatura de transició vítria (T_g), el valor de la qual incrementava amb el contingut en VP per la reducció en la mobilitat molecular. Els espectres mecànics i dielèctrics van mostrar tres relaxacions γ, β i α en orde creixent de temperatura, seguits per una contribució conductiva, observada únicament en l'espectre dielèctric. El procés de relaxació γ està relacionat amb el moviment local de les unitats butil i el procés β va resultar ser una relaxació secundària Johari-Goldstein (JG), que està relacionada amb moviments locals del grup pirrolidona junt amb el moviment de segments de la cadena principal. Es va observar que la conductivitat *dc* (σ_{dc}) va augmentar amb el contingut en VP. Finalment, es va trobar que la conductivitat es desacoblava de la dinàmica segmental a temperatures prop de la transició vítria

En segon lloc, el Capítol 5 arreplega l'anàlisi de l'efecte de la densitat d'entrecreuament en la dinàmica molecular dels copolímers *60*VP/*40*BA mitjançant DSC i DRS. A través de les mesures de DSC es va observar una única transició vítria per a tots els continguts d'agent entrecreuant . L'espectre dielèctric va mostrar, per a totes les mostres, processos conductius i tres relaxacions dipolars α, β i γ en orde decreixent de temperatura. L'increment en agent entrecreuant va produir l'efecte esperat en la dinàmica del procés α. En canvi, el procés β, que tenia les característiques típiques d'una relaxació JG, va perdre de forma inesperada el seu caràcter intermolecular per al major contingut en agent entrecreuant. El procés més ràpid γ no es va veure afectat.

La segona família de materials polimèrics estudiada va ser una sèrie de poliuretans segmentats (PUPH) modificats amb diferents quantitats de grafit expandit (EG) , utilitzat com a farcit conductiu (des de 0 a 50% en pes). La presentació i discussió dels resultats s'arreplega en el Capítol 6. L'anàlisi dels resultats obtinguts per mitjà de Microscòpia Electrònica de Rastreig (SEM), Difracció de Rajos X i FTIR va mostrar la dispersió homogènia del EG en la matriu de PUPH. La tècnica DRS es va utilitzar per a estudiar les propietats dielèctriques dels materials compostos PUPH/EG. La permitivitat dielèctrica dels materials va mostrar una transició de percolació des d'aïllant a conductor amb l'increment de contingut en EG. Es van observar canvis significatius en la permitivitat dielèctrica quan la fracció en pes d'EG estava en el interval de 20-30% en pes. L'addició d'EG a la matriu de PUPH va causar un increment significatiu en la conductivitat dielèctrica, de deu ordes de magnitud.

Finalment, les conclusions generals es resumeixen en el Capítol 7.

LIST OF ABBREVIATIONS

ARR	Arrhenius
BA	Butyl Acrylate
C	Cross-linker
CC	Cole/Cole
CD	Cole/Davidson
CM	Coupling Model
CRT	Cathode Ray Tube
DMA	Dynamic Mechanical Analysis
DMAc	Dimethyl Acetamide
DRS	Dielectric Relaxation Spectroscopy
DSC	Differential Scanning Calorimetry
EG	Expanded Graphite
EGDMMA	Ethylene Glycol Dimethacrylate
EP	Electrode Polarization
Expt	Experimental
FK	Fuoss/Kirkwood
FTIR	Fourier Transform Infrared Spectroscopy
HN	Havriliak/Negami
IR	Infrared
JG	Johari-Goldstein
KWW	Kohlrauch/Williams/Watts
MDI	4,4'–diphenylmethane diisocyanate
MWS	Maxwell-Wagner-Sillars
PBA	Poly(Butyl Acrylate)
PH	Polyhexamethylene–Pentamethylene Carbonate Diol
PUPH	Segmented Polycarbonatediol Polyurethane
PVP	Polyvinylpirrolidone
SEM	Scanning Electron Microscopy

TGA	Thermogravimetry Analysis
UV	Ultraviolet
VFTH	Vogel Fulcher Tamman Hesse
VP	Vinylpyrrolidone
WSP	Water-Swelling Percentage
XRD	X-ray Diffraction
*X*VP/*Y*BA-*Z*C	Cross-linking Vinylpyrrolidone/ Butyl Acrylate Copolymers
X	VP content
Y	BA content
Z	Cross-linker content

LIST OF SYMBOLS

A	Factor of the *ac* conductivity model
A_s	Area of the sample
α_f	Expansion coefficient of the free volume
α_p	Molecular polarizability
α process	Main or segmental relaxation process
ac	Alternating current
a_{CC}	Shape parameter of the Cole/Cole model
a_{HN}, b_{HN}	Symmetric and asymmetric broadening of the relaxation function for the Havriliak/Negami model
$\beta, \gamma, \delta \ldots$processes	Secondary relaxation processes
b_{CD}	Asymmetric broadening of the relaxation function for the Cole/Davidson model
β_{KWW}	Parameter that describes the non-exponential behavior of the decay function of Kohlrauch/Williams/Watts model
C_p	Heat capacity
d	The Bragg's spacing of the repeating domain unit
$D(t)$	Dielectric displacement
D_0	Strength parameter
dc	Direct current
ΔC_p	Heat capacity jump at the glass transition
ΔC_{pnor}	Normalized heat capacity jump at the glass transition
$\Delta\varepsilon = \varepsilon_s - \varepsilon_\infty$	Dielectric strength, dielectric intensity
ΔH_c	Enthalpy of fusion
$\Delta H_{100\%}$	Enthalpy of fusion of the hard segment of PUPH
ΔT	The broadening of the glass transition
ΔT_g	Difference between the T_g values calculated in the first (T_{g1}) and second (T_{g2}) heating ramps.
$\vec{E}$	Electric field

ε	Relative Permittivity of the Material $\left(\varepsilon = \varepsilon_a / \varepsilon_0\right)$
$\varepsilon^*(\omega); \varepsilon'(\omega), \varepsilon''(\omega)$	Complex dielectric function; Real and Imaginary part of the complex dielectric function
$\varepsilon^*_{dip}(\omega)$	Complex dielectric function of the dipolar contribution
$\varepsilon^*_{cond}(\omega)$	Complex dielectric function of the conductivity contribution
ε_0	Dielectric permittivity of the vacuum (ε_0=8.854·10^{-12} A·s·V^{-1}·m^{-1})
E_a	Activation energy
ε_a	Permittivity of the material
$E^*(\omega); E'(\omega), E''(\omega)$	Complex mechanical modulus; storage modulus, loss modulus
$\vec{E}_{loc}$	Local electric field
$\varepsilon''_{\max}$	Imaginary part of the complex dielectric function at the maximum of the peak.
ε_s	Static permittivity $\left(\varepsilon_s = \lim_{\omega \to 0} \varepsilon'(\omega)\right)$
ε_∞	Permittivity of the induced polarization $\left(\varepsilon_\infty = \lim_{\omega \to \infty} \varepsilon'(\omega)\right)$
$\Phi(t)$	Dielectric function
$\phi(t)$	Decaying function
f	Frequency of the external electric field
$F_{Onsager}$	Parameter of Onsanger-Fröhlich theory
Φ_g/B	Relative free volume
f_{max}; T_{max}	Frequency and Temperature of the $\varepsilon''_{\max}$
$g = 1 + \left\langle \cos\theta_{ij} \right\rangle$	Correlation Factor; where θ_{ij} is the angle formed by the dipolar moment *i* with his neighbor *j*
η	Viscosity
k_B	Boltzmann constant
λ	Wavelength of the incident wave in the XRD technique

$L(\tau)$	Relaxation time distribution
$L_{\alpha}(\tau)$	Relaxation time distribution for α Relaxation
$M^{*}(\omega)$; $M'(\omega)$, $M''(\omega)$	Complex modulus function; Real and Imaginary part of the complex modulus function
M_{∞}	$M_{\infty} = 1/\varepsilon_{\infty}$
m	Dynamic fragility index
m^{*}	Dynamic fragility index obtained from the Quin and Mckenna model
m_{FK}	Shape parameter related to the width of the relaxation process for the Fuoss/Kirkwood model
$\vec{\mu}_{ind}$	Induced dipole moment
μ	Dipolar moment
N	Number of molecular dipoles that participates in the relaxation
$n = (1-\beta_{KWW})$	Coupling parameter
P	Pressure
p	Weight fraction of filler
p_c	Weight fraction of filler of the percolation treshold
$\vec{P}$	Polarization vector
q	Scattering wave vector in the XRD technique
R	Ideal gas constant
R_p	Polarization resistance
R_{τ}	Decoupling index
ρ	Density
s	Frequency exponent ($0 \leq s \leq 1$) of the *ac* conductivity model
$\sigma^{*}(\omega)$	Complex conductivity function
$\sigma'(\omega)$	Real Part of the complex conductivity function
$\sigma''(\omega)$	Real Part of the complex conductivity function
$\sigma_{dc} \equiv \sigma_0$	*dc* Conductivity

2θ	Scattering angle in the XRD technique
$\tan\delta(\omega)$	$\tan\delta(\omega) = \varepsilon''(\omega)/\varepsilon'(\omega)$
t	Critical exponent related to the dimensionality of the system
τ	Characteristic or Relaxation time
τ_α	Characteristic time of α relaxation
τ_{KWW}	Characteristic time of α Relaxation obtained from Kohlrauch/Williams/Watts model
τ_β	Characteristic time of β Relaxation
τ_γ	Characteristic time of γ Relaxation
τ_σ	Characteristic time of Conductivity (σ) Relaxation
τ_0	Characteristic time of molecular vibrations
τ_0^{CM}	Primitive (non-cooperative) relaxation time of the Coupling Model
τ_{CC}	Characteristic relaxation time of the Cole/Cole Model
τ_{CD}	Characteristic relaxation time of the Cole/Davison Model
τ_{FK}	Characteristic relaxation time of the Fuoss/Kirkwood Model
τ_{HN}	Characteristic relaxation time of the Havriliak/Negami Model
$\tau_{HN,\alpha}$	Characteristic relaxation time of the Havriliak/Negami Model for the α Relaxation
τ_{JG}	Characteristic relaxation time of Johari-Goldstein Model
τ_{KWW}	Characteristic relaxation time of Kohlrauch/Williams/Watts Model
τ_∞	Pre-exponential Factors of the Arrhenius Equation
t_c	Temperature-Insensitive Crossover Time of the Coupling Model
T	Temperature
T_{on}, T_{end}	Onset and Endset Temperature of the Glass Transition (DSC) and Decomposition Process (TGA)
T_g	Glass transition temperature

T_g^{MDSC} ; T_g^{DRS}	Glass transition temperature obtained by MDSC and DRS
T_{g1}; T_{g2}	T_g values calculated in the first (T_{g1}) and second (T_{g2}) heating ramps
T_m	Melting temperature
T_p	Temperature of the maximum rate of weight loss
T_v	Vogel temperature
ν	Wavenumber of a FTIR absorption band
ω	Angular frequency
ω_c	Critical angular frequency
w_d	Weight of the dry sample
ω_{VP} , ω_{BA}	Weight fractions of VP and BA
ω_{max}	Angular Frequency at the maximum of the loss peak
w_s	Weight of the swollen sample
$wt\%$	Weight Percentage
ξ	Viscosity (η) or Relaxation time (τ) of the α relaxation
χ_c	Degree of crystallinity
$Z'(\omega)$	Real part of the complex impedance function
$Z''(\omega)$	Imaginary Part of the complex impedance function

LIST OF TABLES

LIST OF FIGURES

Chapter 1:

Introduction

1. INTRODUCTION

Polymers are chemically defined as long-chain molecules of very high molecular weight, often measured in the hundreds of thousands. Thus, a polymer is a macromolecule that contains many groups of atoms, called monomeric units, which are covalently bonded. Polymer chains are typically linear, branched, or cross-linked, *i.e.* interconnected forming a three-dimensional network (see **Figure 1.1**) (Sperling, 2006; Nicholson, 1994). In cross-linked polymers, covalent bonds connect different chains, and quite literally their molecular weight approaches infinity.

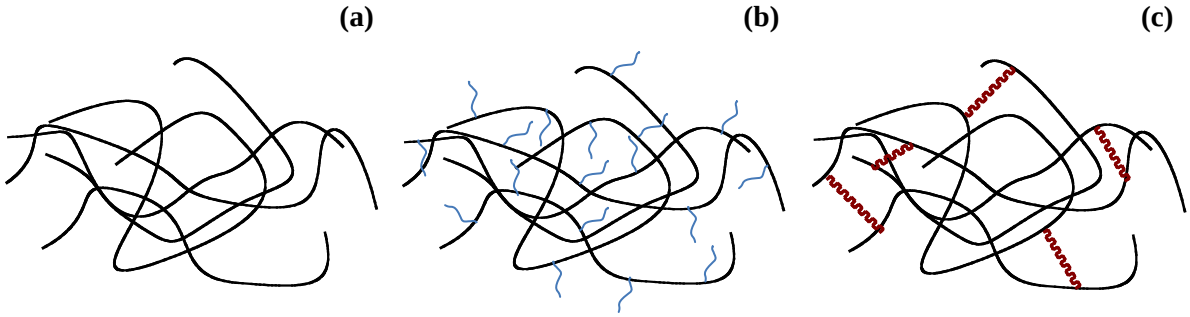

Figure 1.1. Scheme of the types of polymers: (a) linear, (b) branched and (c) cross-linked.

The term homopolymer is used to describe the polymers whose chemical structure can be represented by the multiple repetition of a single type of repeating unit, which can contain one or more kinds of monomeric units. The chemical structure of a polymer is usually represented by placing the repeating unit between square brackets (Riande, et al., 2004).

The term copolymer is used to describe the polymers whose molecules contain two or more different types of repeating units. Depending on how the repeating units are organized along the polymer chain, there are different copolymers: (i) random copolymers, in which

the distribution of the repeating units is random, (ii) alternating copolymers, which consist in two types of repeating units arranged alternately along the polymer chain, (iii) block copolymers, which are linear copolymers in which the repeating units appear in groups or blocks of the same type, and (iv) graft copolymers, which are branched copolymers in which the chemical structure of the branches differs from that of the main chain.

The majority of polymers are organic in nature, that is, they are based on covalent compounds of carbon. Although silicones are based on silicon-oxygen backbones, they usually contain significant proportions of hydrocarbon groups. The other elements that are able to form covalent bonds, albeit of some polarity, with carbon are hydrogen, oxygen, chlorine, fluorine, phosphorous and sulfur. In addition to primary valence forces, polymer molecules are also subject to various secondary intermolecular forces. These forces are the dipole forces between oppositely charged ends of polar bonds, and the dispersion forces, which arise due to perturbations of the electron clouds about individual atoms within the polymer molecule. Hydrogen bonding is important in certain polymers and it arises from the particularly intense dipoles associated with hydrogen atoms attached to electronegative elements such as oxygen or nitrogen (Nicholson, 1994).

Solid polymers can be in the amorphous or crystalline state. Polymers in the amorphous state are characterized by a disordered arrangement of the macromolecular chains, which adopt conformations corresponding to statistical coils. However, polymers in the crystalline state are characterized by a long-range three-dimensional order, which is extended to distances of hundreds or thousands of times the molecular size of the repeating unit. The macromolecular chains in this state adopt fixed conformations and are aligned

parallel to each other, forming a compact packing. **Figure 1.2** shows the differences in the arrangement of polymer chains in the crystalline and amorphous state (Riande, et al., 2000).

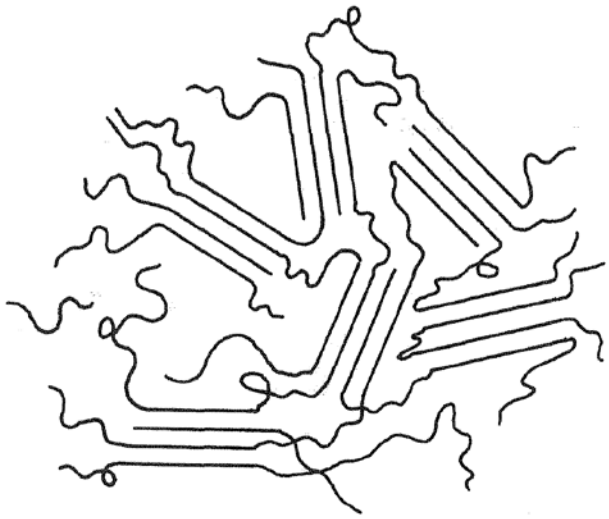

Figure 1.2. Polymer chains conformations in the amorphous and crystalline states. Taken from (Riande, et al., 2004).

The amorphous polymers have different properties depending on structure and temperature. When they are in the glassy state at low temperatures, they are hard and brittle. A glass can be explained as a solid that has been frozen in a liquid-like disorder. When the temperature is increased, it is produced the glass transition and the glasses go over to the liquid viscoelastic state. Glassy polymers are usually prepared by rapid cooling of molten polymers. The amorphous polymers have some irregularity in their structure.

The polymers that have the capability to crystallize are usually called semicrystalline polymers. The term *semycristalline* is used instead of the term *crystalline* because regions, in which the chains or part of them have an ordered and regular spatial arrangement, coexist with disordered regions typical of the amorphous state. The capability to crystallize

basically depends on the structure and regularity of the chains and on the interactions between them.

The properties of a polymer are intimately related to its chemical structure. The polymer science describes the interrelationships among polymer structure, morphology, and physical/chemical behavior. The study of these interrelationships has been widely reported in the literature during the last decades.

Thus, the main aim of this thesis is to study the influence of the structure on the properties of different polymeric materials. This work is mainly based on the study of the liquid and glass state of polymers, especially by the analysis of their thermal and dielectric properties.

As stated before, the glass transition process implies a change of state from the metastable liquid to a glassy non-equilibrium state. This change is described by the glass transition temperature (T_g), which is still an unsolved problem in the condensed matter physics. Therefore, it remains important to continue with the study of the glass transition in order to achieve a better understanding of this process.

The most important techniques to study the glass transition process are those that study the molecular motions in the transition region. The response of a liquid in equilibrium or moderately undercooled to an external field is a prominent absorption. As temperature decreases and approaches to T_g, this absorption is usually split into two relaxation processes: a slow one (primary) called α, and a faster one (secondary) called β. The temperature dependence of the α process obeys the Vogel-Fulcher-Tamman-Hesse (VFTH) equation (Vogel, 1921; Fulcher, 1925; Tamman, et al., 1926). However, the temperature dependence of the β relaxation follows the Arrhenius equation. The α process freezes at T_g,

while the β process remains active in the glassy state. An in-depth study of the microscopic origin of these process allows to understand the glass transition and, in general, the glass state. For this reason, it is important to analyze the molecular dynamics of the supercooled liquids and the correlation with their chemical structure.

The origin of the macroscopic response of a material can be different types of microscopic motions. Thus, the simplest motions in a polymer can be related with local motions, which include rotations (i) around the covalent bonds between the side groups and the main chain, (ii) within the side chains, or (iii) in the main chain (intramolecular motions). On the other hand, the segmental dynamics of the polymeric chain is a cooperative motion, *i.e.* segments from different polymeric chains participate in the motion (intermolecular motions).

Among all the methods used to study the polymer dynamics, the dielectric relaxation spectroscopy (DRS) is one of the most powerful techniques. DRS studies dielectric relaxation processes in a broad range of characteristic times, from 10^{4} to 10^{-12} s. Thus, this technique provides information about the structural and dynamic properties of the materials and allows determining the temperature dependence of the relaxation time.

However, a relaxation process cannot be directly related to a specific motion using DRS. This information is usually obtained by other techniques such as nuclear magnetic resonance (RMN), molecular mechanics simulations, etc.

1.1. The Glass Transition

1.1.1. General Aspects

The evolution from supercooled liquid to a glassy solid is known as the glass transition. This transition is considered to be more similar to a kinetic process than to a thermodynamic process, because the material cannot reach the equilibrium state when the temperature decreases. Thus, glassy state is an out-of equilibrium state in which the material lacks of any molecular order, that is, the material continues being a liquid but the conformational mobility is mostly frozen. As a consequence, the material presents a mechanical behavior similar to that of the solids, but a disorder typical of a liquid (Dyre, 1998).

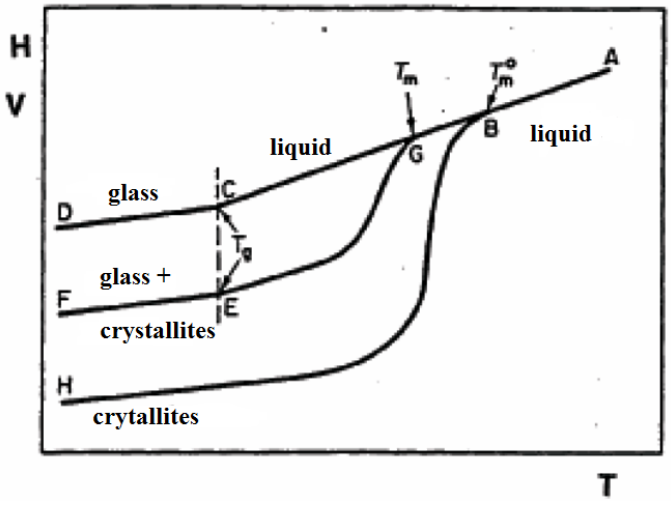

Figure 1.3. Scheme of the specific volume-enthalpy as a function of temperature for an amorphous polymer (DCA), semicrystalline (FGA) and crystalline (HBA).

The transition from the liquid phase and the glass state takes place in a range of temperatures and not in a specific temperature (see **Figure 1.3**). However, the term *glass*

transition temperature (T_g) is commonly used and its value can be determined by different experimental methods. Due to the non-thermodynamic character of this transition, the T_g value can vary between the different techniques used.

The glass transition temperature is extremely important from a practical perspective. Thus, for many polymers it can determine the highest temperature of use, while at the same time it defines the lowest processing temperature (Menczel, et al., 2009).

The polymers are rigid and hard solids at low temperatures. If the temperature is increased, the polymer obtains the thermal energy to allow the free motion of its chains. Thus, the polymer behaves as a viscous liquid. The polymer can follow two different paths from the solid phase to the liquid phase, which depend on the polymer chains arrangement.

The volume or enthalpy changes in the **amorphous polymers** follow the path DCA in the **Figure 1.3**. The polymer is a glass in the region DC. However, if the polymer is heated, there is a slope change characterized by the glass transition temperature (point C). At temperatures above T_g, the polymer is softened and has a rubber-like texture. If the temperature continues increasing, the polymer follows the path CBA and becomes a viscous liquid.

All the chains in a **crystalline polymer** would be ordered in crystallites. The glass transition is not observed because the polymeric chains are not disordered. If a crystalline polymer is heated, it follows the path HBA in the **Figure 1.3**. At the melting temperature (T_m), the polymer becomes a viscous liquid (point B, T_m^0). However, the polymers cannot have a total crystalline structure, but they have ordered and disordered regions.

The **semicrystalline polymers** show both characteristic temperatures, T_g and T_m. These polymers follow the FEGA path in the **Figure 1.3**. The T_m value is lower than that corresponding to a crystalline polymer.

The glass transition is also observed as a change in the thermal expansion coefficient (α) or the heat capacity (C_p) as a function of the temperature (see **Figure 1.4**). When the polymer is heated, it is observed a discontinuity in the temperature dependence of α or C_p in the glass transition region.

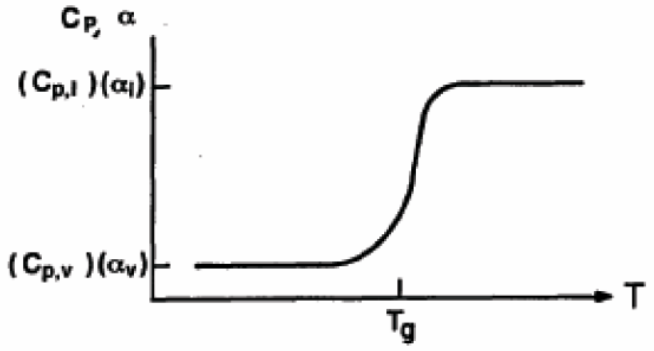

Figure 1.4. Schematic representation of the temperature dependence of the expansion coefficient (α) and the heat capacity ($C_{p,l}$ and $C_{p,v}$ are the liquid and glass heat capacities respectively).

Theoretically, the polymers can be amorphous solids if they are cooled fast enough. The reason is because the molecular rearrangements that give rise to crystallization are slower than the cooling rate, so the crystallization cannot be produced. In general, a material is considered as *glass former* when the crystallization is avoided at cooling rates lower than 1 $K \cdot s^{-1}$. This behavior reaffirms the kinetic nature of the glass transition process. Moreover, the **Figure 1.5** shows how different glass states can be obtained in the same material, using different cooling rates.

The time scale for the molecular motions increases dramatically as the supercooled liquid cooled towards T_g, due to the viscosity variation. Close to the T_g, the viscosity (η) is very sensible to the temperature changes, from low viscosity values in the liquid state (10^{-1}-10^{-2} P) to high viscosity values (10^{13} P). Thus, the glass transition from liquid to glass can be explained as an increase of the viscosity instead of as a phase transition. (Ediger, et al., 1996)

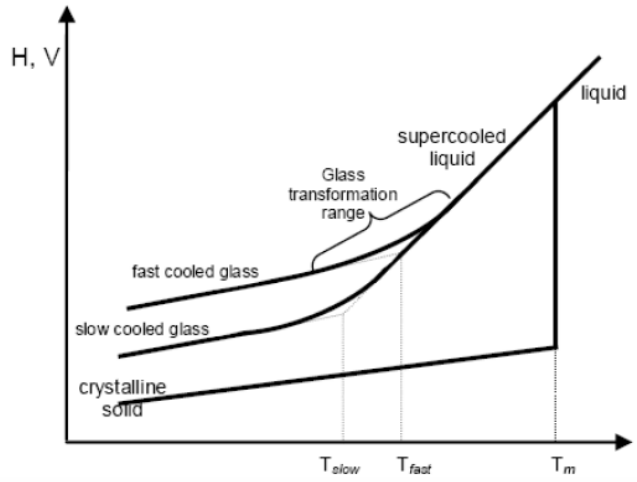

Figure 1.5. Schematic representation of the temperature dependence of the specific volume-enthalpy of a polymer. It can crystallize (T_m) or vitrify following different paths, which depend on the cooling rate.

Due to the kinetic nature of the glass transition, it is necessary to establish a criterion to define its characteristic temperature. Thus, the T_g is defined as (i) the temperature at which the viscosity is 10^{12} Pa·s, (ii) the temperature at which the relaxation time is 100 s or (iii) the onset temperature of the heat capacity change.

In the glassy state, the material is in a non-equilibrium state and has a certain molecular mobility. It is needed long time to reach the equilibrium due to the limited mobility of the molecular chains. If the material is kept at a specific temperature for a long

time, the molecular rearrangements will take place in order to reach the equilibrium. This process is known as structural relaxation or physic ageing. Thus, *the structural relaxation is the process by which an amorphous material tends to reach the equilibrium in the glassy state.*

1.1.1.1. Factors affecting the glass transition

In general, the factors that can influence the T_g values can be classified in two types: (i) molecular factors, *i.e.*, those related to the chemical structure of the polymer chain, and (ii) external or controllable factors (Sperling, 2006; Riande, et al., 2000; Bower, 2002):

(i) Factors related to the chemical structure.

- *Main chain:* The chemical structure has a determining influence on the flexibility of the chain, which measures the ease of rotation around its chain bonds. As a consequence, a polymer with a flexible chain shows a low T_g. The incorporation into the main chain of units that hinder rotation and increase the rigidity of the chain causes an increase in T_g.
- *Side groups:* Large, inflexible and bulky side groups cause an increase in rigidity, which causes an increase in T_g. However, flexible side groups have not marked effect on the T_g.
- *Polarity of the chain:* The T_g value is increased with the polarity of the polymer chain. An increase in intermolecular forces can produce a decrease in the mobility of the chain.

(ii) External or controllable factors.

- *Effect of Pressure:* When a polymer is subjected to a compression and it is at a temperature above its T_g, the free volume decrease. Consequently, the T_g value increases and the polymer will be closer to its T_g. For small pressure changes, the effects are clearly negligible.

- *Effect of Molecular Weight:* The T_g value depends on the polymeric chain length. For high molecular weights, T_g remains practically constant, but when molecular weight decreases, T_g also decreases following the Fox-Flory equation (Fox, et al., 1950).
- *Effect of Cross-linking:* Polymers with strong intermolecular interactions present high T_gs, because great energy is required to separate their chains. Thus, cross-linkings are the strongest intermolecular interactions because they are real chemical bonds. Therefore, as the cross-linking increases, the free volume decreases, and the T_g increases because the molecular mobility is more hindered.
- *Homogeneous Copolymer systems and miscible mixtures:* the copolymerization influences the T_g value. In general, a random copolymer of two monomers with different T_g values has a glass transition temperature intermediate between those of the homopolymers, showing a single T_g. Such is the case also for miscible mixtures of polymers or polymer blends.
- *Plasticizers:* The glass transition temperature of polymers decreases when plasticizers are mixed with them. Plasticizers, which are generally low molecular weight organic compounds, weaken the intermolecular interactions due to a solvating action.
- *Cristallinity:* The glass transition temperature of the amorphous phase in a polymer depends on the degree of crystallinity. However, the T_g value can increase or decrease with the degree of crystallinity. It has been suggested that it could depend on the relative densities of the amorphous and crystalline phases (Plazek, et al., 1996).

1.1.1.2. Structural Relaxation

As stated before, the glass transition can be considered to have a kinetic nature. In order to understand this nature, we can consider a glass former in equilibrium at a

temperature slightly higher than the T_g value. Then, the temperature is drastically decreased and the system is not able to reach the thermodynamic equilibrium. As a result the material can be considered as a frozen liquid, which has volume, enthalpy and entropy values higher than those associated to an equilibrium state. Thus, the *structural relaxation* can be defined as the evolution of this system to a new thermodynamic equilibrium with the new external conditions. As a consequence, the thermodynamic properties associated to the material (specific enthalpy, volume, entropy…) change over time. Therefore, although the glass transition is basically a kinetic process, a thermodynamic change is produced, which is associated to the glass-liquid transition.

At the molecular scale, the glass transition is produced when the experimental time is equal to the time required for the polymeric chains to reach their equilibrium configurations. That time is defined as the *relaxation time* (Roberts, et al., 1973).

1.1.1.3. Properties of the Structural Relaxation

The main properties of the structural relaxation are the NON-LINEARITY and the NON-EXPONENTIALLITY.

The non-linearity is observed when the glass transition is characterized analyzing the volume or the enthalpy as a function of the temperature using, for instance, dilatometric or calorimetric measurements, respectively. Thus, the temperature dependence of the volume and enthalpy is different depending on whether the material is subjected to a heating or a cooling program. This behavior is known as *hysteresis*. This effect depends on the relation between the cooling rate (q_1) and the heating rate (q_2) (see **Figure 1.6**).

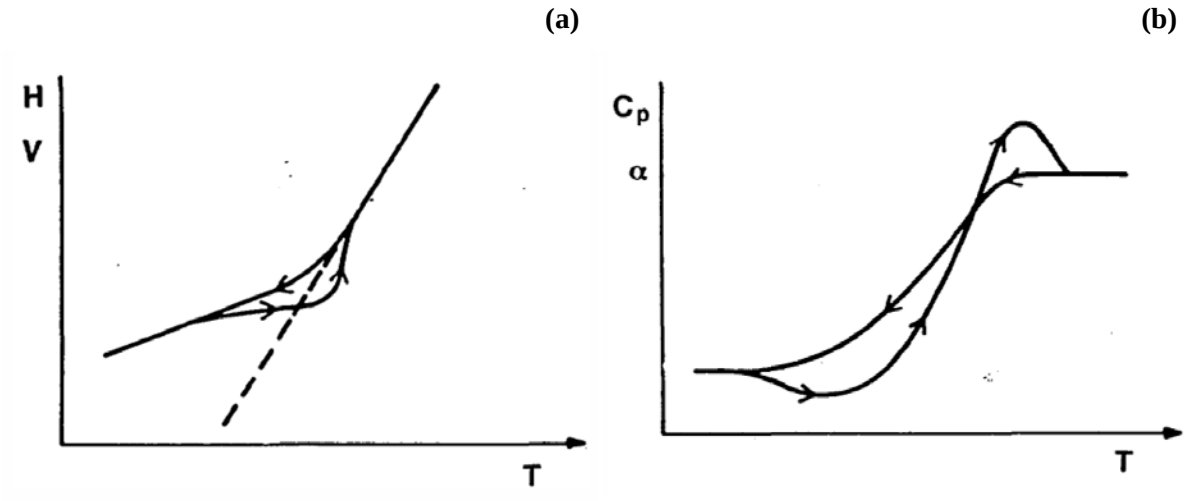

Figure 1.6. (a) Temperature dependence of the enthalpy and volume for a process at the same heating and cooling rate. (b) Temperature dependence of the heat capacity and coefficient of thermal expansion for a process at the same heating and cooling rate.

On the other hand, the non-exponentially is a consequence of the distribution of relaxation times. The evidence of this distribution was demonstrated by A.J. Kovacs (Kovacs, 1963; Kovacs, et al., 1979).

1.1.2. Experimental determination of the Glass transition. Molecular Mobility.

The characterization of the glass transition can be carried out using different parameters: enthalpy or volume, mechanical modulus, dielectric permittivity, or the index of refraction. However, the glass transition values obtained with these parameters differs between them.

The Differential Scanning Calorimetry (DSC) is widely used to obtain the glass transition temperature. The T_g is obtained from the heating curves at a constant heating rate. Thus, the T_g can be calculated as (ii) the temperature at the half-height of the heat capacity

increased, or (ii) the inflection point, which is slightly different and corresponds to the peak in the derivative of the heat flow or heat capacity versus temperature. There is no heat of transition at the glass transition, since only first-order transitions have a heat of transition. In addition to the transition temperature, the glass transition is characterized by the heat capacity jump or heat capacity increase (ΔC_p).

On the other hand, the glass transition can be also characterized when the material analyzed is subjected to an external force or an electric field. This external stimulus produces a change in the state of the material, which is analyzed by the temperature dependence of some macroscopic properties, such as elastic modulus or dielectric permittivity. The change is due to molecular motions, which allow the rearrangements of the molecules or chain segments to reach a new equilibrium state. This process is known as vicoelastic or dielectric relaxation. The viscoelastic relaxations are determined by the Dynamic Mechanical Analysis (DMA) and the dielectric relaxations are analyzed by the Dielectric Relaxation Spectroscopy (DRS). Both techniques allow analyzing the molecular motions associated to different relaxation processes.

The conformational mobility, *i.e.* the molecular rearrangements that change the space disposition of the molecules, determines the behavior of a liquid. When this liquid is cooled, its viscosity increases and the molecular mobility decreases continuously up to reach the glass transition region. In this region, the time scale of the intermolecular rearrangements is comparable to that of the experiment.

In the glass state, the slow dynamics process associated to the structural recovery is not completely *frozen* (Alegría, et al., 1995). In addition to this process, there are other

processes associated to local motions at temperatures below T_g. These local motions are the origin of the secondary relaxation processes.

In the literature, the relaxation processes analyzed are usually classified in decreasing order of temperature. Therefore, the first process detected, which corresponds to the glass transition, is called α process. The secondary processes are called β, γ, δ…relaxations, which correspond to decreasing relaxation times and increasing molecular mobility. The following sections describe in more detail each region.

1.1.2.1. Glass transition. α Relaxation

The α relaxation process takes place in amorphous polymers and in glass formers with low molecular weight, at temperatures above T_g.

When an external electric field is applied, the material is reorganized by cooperative conformational motions. Thus, the molecular motions associated to the α relaxation are the same as those that cause the structural relaxation. At temperatures slightly above T_g, the relaxation times of these cooperative motions are just a few seconds and they rapidly decrease as the temperature increases. For this reason, the structural relaxation cannot be detected at temperatures above T_g using calorimetric or dilatometric techniques, whose response times are much longer. However, the dielectric relaxation spectroscopy can detect motions with relaxation times as small as 10^{-6} s, which allow characterizing the α relaxation at temperatures much higher than the T_g. Hence, the α relaxation and the glass transition are related between them due to their molecular origin (Riande, et al., 2004).

Some authors designate the α dielectric relaxation as the structural relaxation (McCrum, et al., 1991). However, in order to avoid confusion, the dielectric process detected at temperatures above T_g is defined as α or main relaxation. While the process dependent on the time is defined as structural relaxation and it is detected when the thermodynamic variables are approached to the equilibrium in the glass state.

The molecular motions involved in the α relaxation are cooperative, *i.e.* a specific part of the system is moved together with other parts of the system. In polymers, the α relaxation is associated to micro-brownian motions of the main chain segments, where the some monomers are rearranged cooperatively (Schönhals, 1997). Therefore, the α relaxation is associated to both intramolecular and intermolecular interactions.

Due to the strong slowdown of the α relaxation when the process approaches to the glass state, the temperature dependence of the α relaxation times is not Arrhenius (ARR). Thus, for the α process, the activation energy is dependent on the temperature:

$$E_a(T) = R\frac{d\ln T}{d(1/T)} \tag{1.1}$$

where R is the ideal gas constant. As observed in **Figure 1.7**, the activation energy increases dramatically as temperature approaches to T_g.

The deviation of the α relaxation from the Arrhenius behavior may be quantified by the Vogel-Fulcher-Tamman-Hesse (VFTH) equation (Vogel, 1921; Fulcher, 1925; Tamman, et al., 1926) given by

$$\tau = \tau_0 \cdot \exp\left(\frac{D_0 \cdot T_v}{T - T_v}\right),\ T_v < T_g \tag{1.2}$$

where τ_0 is a prefactor corresponding to a characteristic time of molecular vibrations and has a typical value of about $\cong 10^{-13}$ (Atkins, 1990; Kremer, et al., 2003); D_0 is the strength parameter, which defines the boundary between the fragile glasses (D_0<10) from the strong glasses (D_0>10); and T_v is the Vogel Temperature with a value around 30 K-50 K lower than T_g. For the α relaxation, the temperature dependence of the relaxation process is governed by the volume.

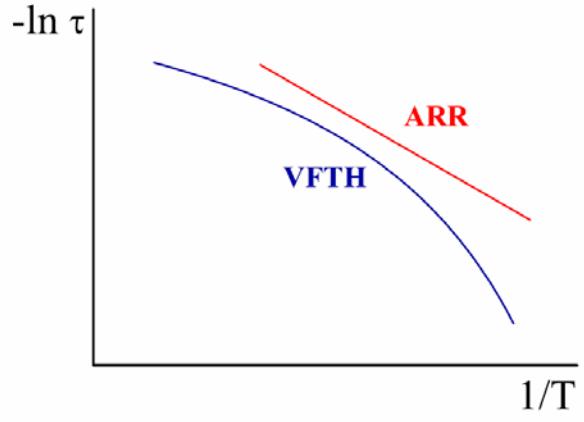

Figure 1.7. Temperature dependence of the relaxation time for a VFTH and ARR behavior.

The Doolittle equation can be defined as:

$$\tau_\alpha = \tau_0 \cdot \exp\left(\frac{B}{\Phi}\right) \tag{1.3}$$

where Φ is the relative free volume and B is a parameter near 1, which relates the necessary volume to the relaxation process takes place with the volume of segments participating in the relaxation. If the VFTH equation (1.2) is compared with the Doolittle equation (1.3), it is obtained the following expression:

$$\frac{\Phi}{B} = \frac{T - T_v}{D_0 \cdot T_v} \tag{1.4}$$

which relates the free volume of the Doolittle equation with the D_0 and T_v parameters of the equation (1.2).

Angell (Angell, 1991) proposed a classification of the materials as *strong* or *fragile*. Thus, Angell observed that the curvature in the plot ln η vs. *1/T* (deviation from the Arrhenius behavior) is not the same for all the materials. This plot is known as the *Angell Plot*, which is shown in the **Figure 1.8** for different kind of materials. Other properties, like the diffusion constant or the α relaxation time, also follows this temperature dependence of η. There are some materials (top curves), like the SiO2, which their η (*T*) follows approximately the Arrhenius behavior. On the contrary, there are other materials (bottom curves), which the curvatures of the η (T) are high, approximately at T_g/T ~0.7. Thus, Angell differentiated between the strong and fragile materials using the results obtained in this graphic (Angell, 1988).

Thus, in order to characterize quantitatively the fragility, the *dynamic fragility index*, *m*, is evaluated as (Bohmer, et al., 1993; Bohmer, et al., 1992; Bohmer, et al., 1993):

$$m = \lim_{T \to T_g} \left[\frac{d \log \xi}{d\left(T_g / T\right)} \right]$$
$$m = \left| \frac{d \log_{10}\left(\xi\right)}{d\left(T_g / T\right)} \right|_{T=T_g} \tag{1.5}$$

where ξ is usually the viscosity η or the relaxation time τ of the α absorption. Fragile glass formers (high values of *m*) have a high slope because ξ intensely changes through the reference temperature, consequently a dramatic departure from the Arrhenius behavior is observed. On the other hand, strong glass formers (low values of *m*) show a slight deviation

from the Arrhenius behavior, maintaining their properties in the transition region. In general, the structure of strong glass formers is compact, while the structure of fragile glass formers is relatively open.

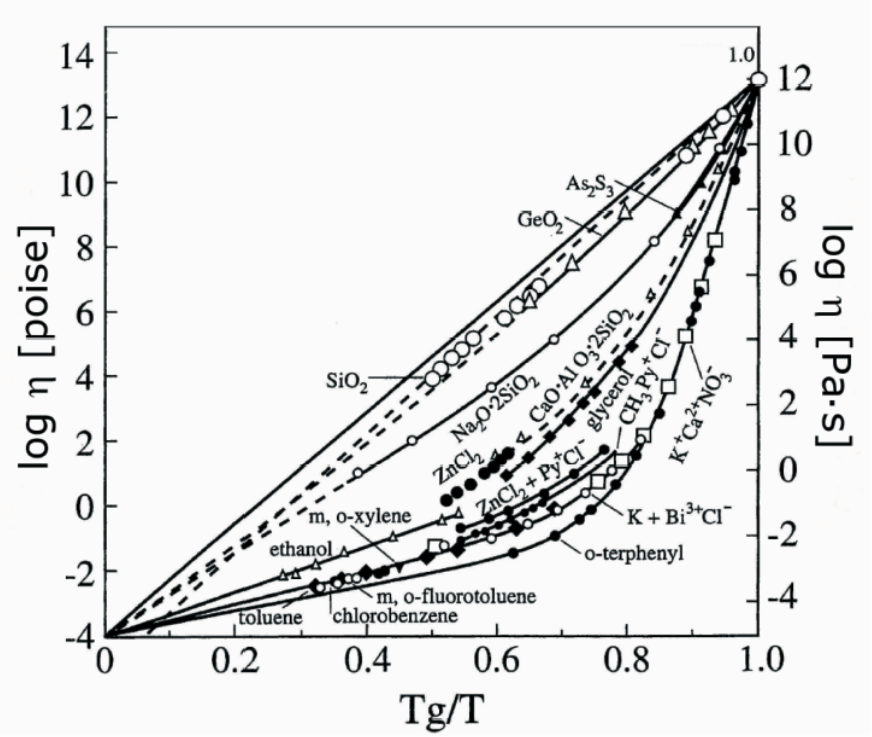

Figure 1.8. log η of the some liquid glass formers as a function of the reduced reciprocal temperature T_g/T, where T_g is defined as $\eta(T_g)=10^{13}$ poises. (Angell, 1988)

The fragility is a parameter that shows the thermal stability of the structure in the supercooled regime. The structure of a typical strong liquid is a tridimensional network made up of covalent bonds, while the molecules of the fragile liquids tend to form weak directional, or even non-directional, non-covalent bonds.

1.1.2.2. Local motions. Secondary Relaxations.

The secondary relaxations, called β, γ, δ, … relaxations, are generally less intense than the α relaxation. They are processes thermally activated, so the temperature dependence of their relaxation times follows the Arrhenius model:

$$\tau(T) = \tau_{\infty} \cdot \exp\left(\frac{E_a}{R \cdot T}\right) \tag{1.6}$$

where τ_{∞} is the relaxation time in the high temperature limit (Kremer, et al., 2003), and E_a is the activation energy. The inter/intramolecular motions associated to the energetic barriers are simpler and more localized than those corresponding to the α relaxation.

In particular for polymeric materials, the secondary processes are associated to motions limited to the chain or rotations of the side chains, which can be produced independently of the main chain motions.

However, the molecular origin of the β relaxation is not known completely. It is found that some molecular processes are thermally activated (Arrhenius), but they are partly cooperative. These processes are known as Johari-Goldstein relaxations and they are associated to motions of the whole molecule (Johari, et al., 1970; Johari, et al., 1971; Johari, et al., 1972; Johari, et al., 1986).

1.2. Polarization and Dielectric Spectroscopy

The capacitance of a capacitor increases when an insulator material is introduced between its plates. The ratio of the capacitance of a capacitor using a specific material as a

dielectric, to the capacitance of a capacitor using a vacuum as a dielectric was called *specific inductive capacity* by Faraday. Nowadays, this concept is called relative dielectric permittivity of a specific material. This behavior is due to the fact that the insulator produces a decrease of the electric field between the plates of the capacitor. When an electric field is applied to a material, the electric field is partially trapped inside the material due to the polarization phenomena.

Debye (Debye, 1929) related the dielectric relaxation to the orientation motions of the molecular dipoles. From then on, the Dielectric Relaxation Spectroscopy has increasingly used as a characterization technique.

Thus, the interaction between an electric field and a specific material can be measured by DRS in broad range of frequencies (10^{-6}-10^{11} Hz). The frequency and temperature dependence of the dielectric constant allows analyzing the motions of dipolar reorientation and electric conduction. Consequently, it is possible to relate the molecular structure to the dynamics of molecular reorientation.

1.2.1. Polarization

The difference between the dielectric constant of a material and that of free space is due to the restricted movements of charges within the material. When an external electric field is applied, it alters the equilibrium state. Thus, the positive charges move with the electric field and the negative charges move against it, resulting in an induced dipole moment. The field within the material is produced by a larger field outside it. This general process is called *Polarization* (Ku, et al., 1987).

If the material is a conductor, the interaction electric field-material produces a charges motion, which generates conduction phenomena. If the material is dielectric, the electric field induces a deformation in the charges distribution. The charges displacement is the origin of the polarization in the dielectric material, which is defined by the polarization vector $\vec{P}$. $\vec{P}$ gives the dipolar moment per unit volume present in the dielectric.

The relation between the electric field applied, $\vec{E}$, and the induced dipole moment generated, $\vec{\mu}_{ind}$, can be complicated. However, for low electric fields applied, the $\vec{\mu}_{ind}$ and the local electric field, $\vec{E}_{loc}$, are parallel in all directions, fulfilling the following relation:

$$\vec{\mu}_{ind} = \alpha_p \cdot \vec{E}_{loc} \tag{1.7}$$

where α_p is the molecular polarizability. If N is the number of molecular dipoles in the system per unit volume, it is obtained the following microscopic relation:

$$\vec{P} = N \cdot \vec{\mu}_{ind} = N \cdot \alpha_p \cdot \vec{E}_{loc} \tag{1.8}$$

The macroscopic relation between the polarization and the external electric field:

$$\vec{P} = (\varepsilon_a - \varepsilon_0) \cdot \vec{E} = (\varepsilon - 1) \cdot \varepsilon_0 \cdot \vec{E} \tag{1.9}$$

where ε_0 is the dielectric permittivity of the vacuum (ε_0=8.854·10^{-12} A·s·V^{-1}·m^{-1}); ε_a is the permittivity of the material; and ε is the relative permittivity of the material $(\varepsilon = \varepsilon_a / \varepsilon_0)$.

1.2.1.1. Polarization mechanisms

The permittivity of the medium depends on the polarizability of its molecules. When an electric field is applied to a dielectric material, three different mechanisms of polarization can be produced at microscopic level (Ku, et al., 1987; Blythe, et al., 2005):

– **Electronic Polarization**.

The electric field causes a slight displacement of the electron cloud of any atom in the polymer molecule relative to its positive nucleus. The applied electric field (~10^8 V) is very weak compared with the intra-atomic field at an electron (~10^{11} V), which is caused by the nucleus. This difference induces a weak polarization. Electronic polarization, which is observed at very high frequencies, occurs in all materials and is responsible for the refraction of light. This polarization is produced at times around 10^{-15} s.

– **Atomic Polarization**.

The electric field also causes a change in the relative position of the atomic nuclei in the molecule or atomic network. The motion of the nuclei is slower than that of the electrons, so the atomic polarization cannot occur at as high frequencies as electronic polarization. This polarization is produced at times around 10^{-13} s. In polymers, the force constants for bending or twisting of molecules, involving changes in angles between bonds, are generally much lower than those for bond stretching. This means that the major contribution to atomic polarization comes from bending and twisting motions of the molecular bonds.

– **Orientation Polarization**.

This polarization only occurs in materials that already have a permanent dipole moment, which will tend to be aligned by the applied field to give a net polarization in that direction. This polarization is produced at times around 10^{-9} s. The dipoles can be imagined pointing in all directions and continually jumping from one orientation to another as a result of thermal agitation. The polarization that develops when the field is applied is a relatively small average of orientation favoring the direction of the applied field. The tendency to revert to random orientation opposes the tendency of the field to align the dipoles and thus allows for polarization to vary in proportion to the applied field.

Figure 1.9 shows the frequency dependence of the polarization under the application of a electric field (Blythe, et al., 2005). This figure shows: (i) the frequency band in which the different polarization mechanisms are located; (ii) the different intensity of the processes; and (iii) the breadth of the different bands, which is wider for the orientational polarization than for the other two polarization mechanisms. This is due to the resistance of the medium to the dipole motion, while for the atomic and electronic polarization, the response is practically instanteneous.

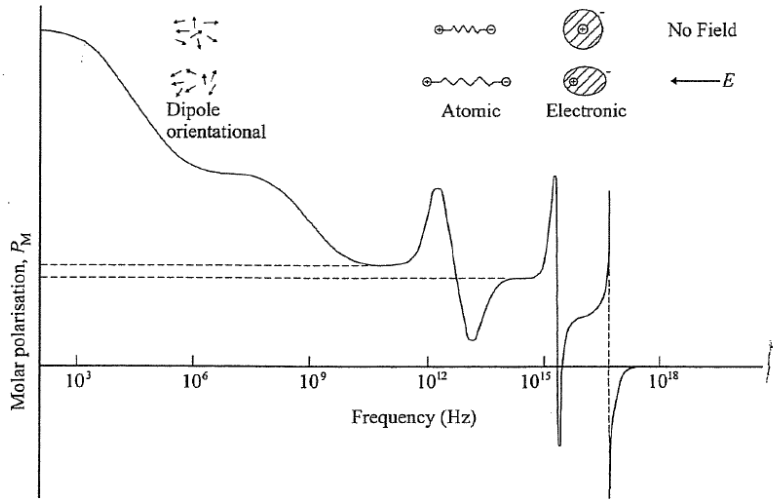

Figure 1.9. Scheme of the molar polarization in a dielectric material as function of frequency. Taken from (Blythe, et al., 2005).

When the electric field is removed, both the electronic and atomic polarizations immediately disappear. However, the orientational polarization falls down slowly in comparison with the other two polarization mechanisms. This delay is due to the internal friction of the material, which depends on the viscosity. In order to describe the polarization loss when the electric field is removed, a characteristic time is used, which is known as *relaxation time*. This parameter corresponds to the necessary time to decrease the polarization by a factor of *1/e* from its initial value.

The dielectric relaxation spectroscopy is based on the measurement of the polarizability loss, *i.e.* the dielectric relaxation, after removing a sinusoidal electric field at a specific temperature. The relaxation of these dipoles is related to the molecular mobility of the system.

1.2.2. Phenomenological description of the dielectric measurements

In the dielectric relaxation spectroscopy, the stimulus is an electric field *E(t)*, and the response is the dielectric displacement *D(t)*. When the electric field is static, the resultant dielectric displacement at the instant *t*=0 is:

$$D(t) = \varepsilon_0 \cdot \left[\varepsilon_\infty + \left(\varepsilon_s - \varepsilon_\infty\right) \cdot \Phi\left(t\right)\right] \cdot E = \varepsilon_0 \cdot \varepsilon_\infty \cdot E + \varepsilon_0 \cdot \left(\varepsilon_s - \varepsilon_\infty\right) \cdot \Phi\left(t\right) \cdot E \qquad (1.10)$$

where ε_0 is the dielectric permittivity of the vacuum; ε_∞ is the permittivity of the induced polarization $\left(\varepsilon_\infty = \lim_{\omega \to \infty} \varepsilon'(\omega)\right)$; ε_s is the static permittivity $\left(\varepsilon_s = \lim_{\omega \to 0} \varepsilon'(\omega)\right)$; and $\Phi(t)$ is the dielectric function, which describes the response after removing the electric field (in the equilibrium, the orientational polarization will decay to cero at long times, so $\Phi\left(t \to \infty\right) = 0$). The first term of equation (1.10), $\left[\varepsilon_0 \cdot \varepsilon_\infty \cdot E\right]$, represents the instantaneous response of the dielectric material to an electric field, and the second term, $\left[\varepsilon_0 \cdot \left(\varepsilon_s - \varepsilon_\infty\right) \cdot \Phi\left(t\right) \cdot E\right]$, is related to the dipolar polarization. After removing the electric field, the polarization decrease can be expressed by the decaying function $\phi(t)$, which is related to $\Phi(t)$ by: $\phi\left(t\right) = 1 - \Phi\left(t\right)$.

If the applied electric field is not static, the *D(t)* variation produced by the increment *dE* in the instant *t*=*u* is:

$$dD\left(t\right) = \varepsilon_0 \cdot \varepsilon_\infty \cdot dE + \varepsilon_0 \cdot \left(\varepsilon_s - \varepsilon_\infty\right) \cdot \Phi\left(t - u\right) \cdot dE \qquad (1.11)$$

which, using the Boltzmann's principle, can be expressed as:

$$dD\left(t\right) = \varepsilon_0 \cdot \varepsilon_\infty \cdot E\left(t\right) + \varepsilon_0 \cdot \left(\varepsilon_s - \varepsilon_\infty\right) \cdot \int_{-\infty}^{t} \Phi\left(t - u\right) \cdot \frac{dE}{du} du \qquad (1.12)$$

If t' is substituted by $t-u$, and the equation (1.12) is integrated, it is obtained the following expression:

$$D(t)=\varepsilon_0\cdot\varepsilon_\infty\cdot E(t)+\varepsilon_0\cdot(\varepsilon_s-\varepsilon_\infty)\cdot\int_0^\infty E(t-t')\cdot\left[-\frac{d\phi(t')}{dt'}\right]dt' \tag{1.13}$$

In a typical dielectric experiment, the stimulus is an harmonic electric field $E(t)=E_0\cdot\exp(i\omega t)$. If this function is inserted in the equation (1.13), it is obtained:

$$\frac{D(t)}{\varepsilon_0\cdot E(t)}=\varepsilon_\infty+(\varepsilon_s-\varepsilon_\infty)\cdot\int_0^\infty\exp(-i\omega t')\cdot\left[-\frac{d\phi(t')}{dt'}\right]dt' \tag{1.14}$$

where $\frac{D(t)}{\varepsilon_0\cdot E(t)}$ represents the dielectric permittivity, $\varepsilon^*(\omega)$. From the equation (1.14), it is obtained the following relation:

$$\frac{\varepsilon^*(\omega)-\varepsilon_\infty}{\varepsilon_s-\varepsilon_\infty}=\int_0^\infty\exp(-i\omega t)\cdot\left[-\frac{d\phi(t)}{dt}\right]dt \tag{1.15}$$

where $\varepsilon^*(\omega)=\varepsilon'(\omega)-i\varepsilon''(\omega)$.

When a relaxation is produced, it can be detected as a peak in the imaginary part of the permittivity, $\varepsilon''(\omega)$, or as inflection point in the real part of the permittivity, $\varepsilon'(\omega)$. Therefore, the real and imaginary parts of the permittivity are dependent between them, they are related by the Kramers-Kroning relationships (Lovel, 1974; Wübbenhorst, et al., 2002).

1.2.2.1. The Debye Model

Debye published a study about the dielectric properties of polar liquids (Debye, 1945). In this work, for a non-equilibrium system, he proposed that the relaxation is produced at a rate that increases linearly with the distance to the equilibrium. This condition can be described by a first order differential equation:

$$\frac{dP(t)}{dt} = -\frac{P(t)}{\tau_D} \tag{1.16}$$

where τ_D is the characteristic relaxation time.

The model proposed by Debye, takes account different initial hypothesis: (i) there is no interaction between dipoles, (ii) only one process leads to the equilibrium, and (iii) all the dipoles can be considered equivalent, *i.e.* all the dipoles are relaxed in average in one single characteristic time.

The solution to equation (1.16) leads to an exponential decay of the correlation function $\Phi(t)$:

$$\Phi(t) = \exp\left[-\frac{t}{\tau_D}\right] = -\frac{d\phi(t')}{dt'} \cdot P(t) = P_0 \cdot \exp\left(-\frac{t}{\tau_D}\right) \tag{1.17}$$

If the equation (1.17) is substituted in the equation (1.15), the relation for the complex permittivity is obtained:

$$\varepsilon^* = \varepsilon'(\omega) - i\varepsilon''(\omega) = \varepsilon_\infty + \frac{\varepsilon_s - \varepsilon_\infty}{1 + i\omega\tau} \tag{1.18}$$

$$\varepsilon^* = \varepsilon'(\omega) - i\varepsilon''(\omega) = \left[\varepsilon_\infty + \frac{\varepsilon_s - \varepsilon_\infty}{1 + (\omega\tau)^2}\right] - i\left[\varepsilon_\infty + \frac{(\varepsilon_s - \varepsilon_\infty)\omega\tau}{1 + (\omega\tau)^2}\right] \tag{1.19}$$

where $\varepsilon_s - \varepsilon_\infty$ represents the strength of the dielectric relaxation, $\Delta\varepsilon$. This model is known as *Debye Model* (see **Figure 1.10**). The representation of $\varepsilon'(\omega)$ and $\varepsilon''(\omega)$ as a function of $f = \omega/2\pi$ (f is the frequency of external electric field) shows that (i) $\varepsilon'(\omega)$ falls from ε_s to ε_∞ as frequencies increase and (ii) $\varepsilon''(\omega)$ is a symmetric peak and its maximum is produced at $\omega_{\max} \cdot \tau = 1$, with an amplitude of $\varepsilon''_{\max} = (\varepsilon_s - \varepsilon_\infty)/2$. The width of the peak at half height is a constant value of 1.1444 decades of frequency. The mean relaxation time of the process, $\langle\tau\rangle$, is defined as the inverse of $\omega_{\max}\left[\langle\tau\rangle = (2\pi f_{\max})^{-1}\right]$.

The Debye behavior is not usually observed for complex systems, such as polymers, except for a few exceptions (Floudas, et al., 1995).

In order to characterize the relaxation processes, the representation of the $\varepsilon''(\omega)$ *vs.* $\varepsilon'(\omega)$ is also useful, which is known as *Cole-Cole* diagram. As observed in **Figure 1.10**, the Cole-Cole diagram for the Debye model is a semicircle which intersects $\varepsilon'(\omega)$ in ε_∞ and $\varepsilon_\infty + \Delta\varepsilon$.

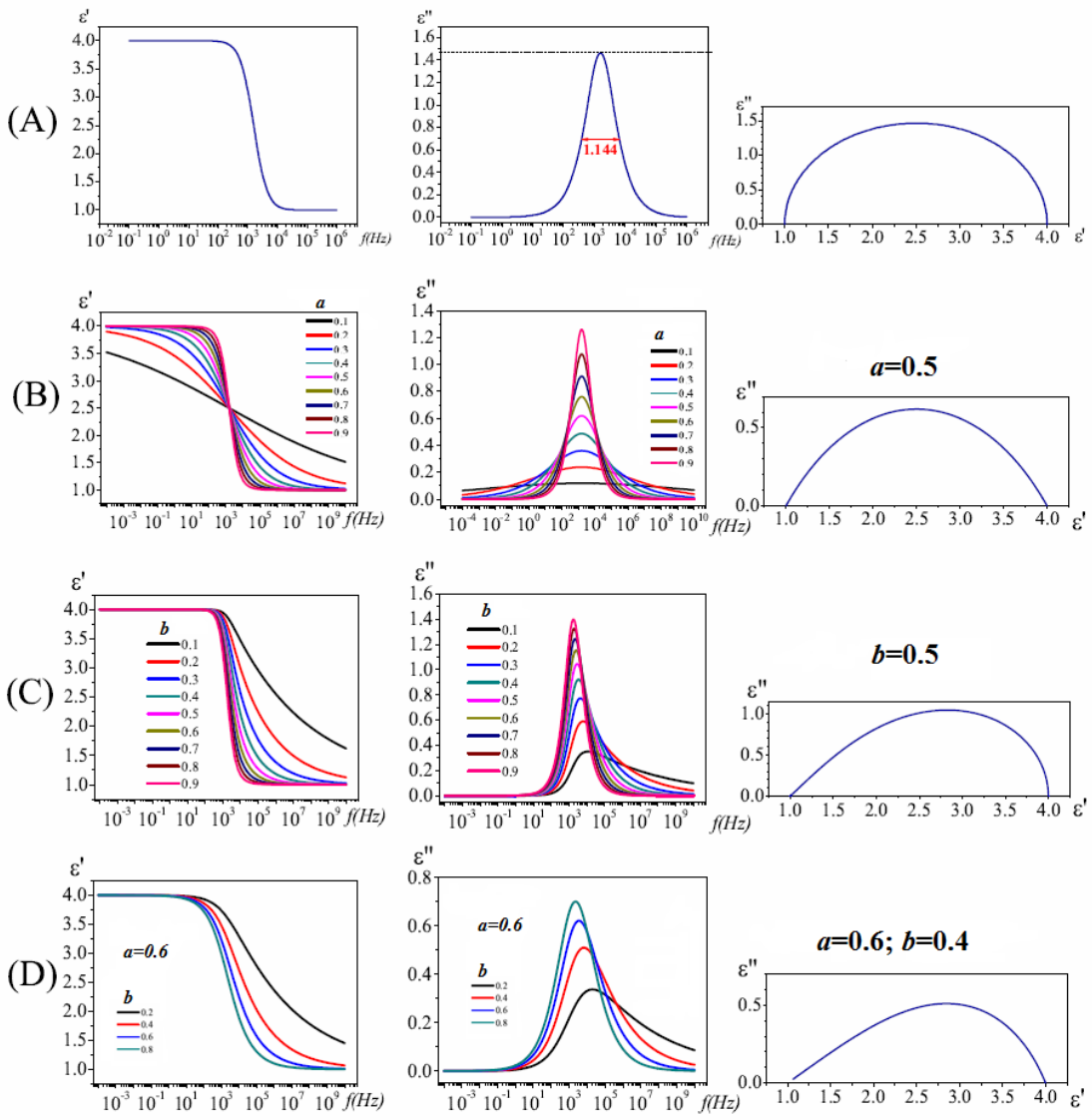

Figure 1.10. Representation of ε' and ε''as a function of frequency and ε' *vs.* ε'', for the following models: (A) Debye, (B) Cole-Cole, (C) Cole-Davidson and (D) Havriliak-Negami with $\Delta\varepsilon = 3$ and $\varepsilon_\infty = 1$.

1.2.2.2. Complex Systems. Distribution of the relaxation times.

In the real systems, the decay functions are generally non-exponentials. The polarization loss is not only described by one characteristic time, so the width of $\varepsilon''(\omega)$ *vs.* $\log f$ is wider than the corresponding to a Debye process.

In generally, the non-Debye behavior is interpreted as the existence of different relaxing units which relax at different relaxing times and follow an exponential decay. Thus, the material is interpreted as a set of heterogeneous regions and the global decay function is defined by the superposition of all the individual relaxation processes (Ediger, et al., 1996).

K. S. Cole and R. H. Cole (Cole, et al., 1941) proposed the first modification to the Debye theory. The broadening of the dielectric function was described by the COLE/COLE (CC) function. They introduced a shape parameter, a_{CC}, in order to considerate the increase in the amplitude of the symmetric relaxation $(\omega_{\max} \cdot \tau_{CC}) = 1$ (see **Figure 1.10**):

$$\varepsilon^*(\omega) = \varepsilon_\infty + \frac{(\varepsilon_s - \varepsilon_\infty)}{1 + (i\omega\tau_{CC})^{a_{CC}}} \tag{1.20}$$

where $0 < a_{CC} \leq 1$ leads to a symmetrical broadening for the relaxation function. For $a_{CC} = 1$ the Debye function is obtained. The Cole/Cole relaxation time τ_{CC} gives the position of maximal loss by $\omega_p = 2 \cdot \pi \cdot f = 1/\tau_{CC}$.

Afterwards, D.W. Davidson and R.H. Cole (Davidson, et al., 1950) proposed another modification to the Debye model. The COLE/DAVIDSON (CD) model described the complex dielectric function when it has an asymmetric broadening (see **Figure 1.10**).

$$\varepsilon^*(\omega) = \varepsilon_\infty + \frac{(\varepsilon_s - \varepsilon_\infty)}{1 + (i\omega\tau_{CD})^{b_{CD}}} \tag{1.21}$$

where b_{CD} ($0 < b_{CD} \leq 1$) describes an asymmetric broadening of the relaxation function for frequencies $\omega > 1/\tau_{CD}$ and τ_{CD} is the Cole/Davidson relaxation time. The τ_{CD} of the model function does not coincide with the relaxation time, which is related to the position of maximal loss (ω_p):

$$\omega_p = \frac{1}{\tau_{CD}} \tan\left[\frac{\pi}{2\gamma + 2}\right] \tag{1.22}$$

A more general model function was introduced by S. Havriliak and S. Negami (Havriliak, et al., 1966). Thus, the HAVRILIAK/NEGAMI (HN) model is a combination of the Cole/Cole and the Cole/Davidson function (see **Figure 1.10**).

$$\varepsilon^*(\omega) = \varepsilon_\infty + \frac{(\varepsilon_s - \varepsilon_\infty)}{\left[1 + (i\omega\tau_{HN})^{a_{HN}}\right]^{b_{HN}}} \tag{1.23}$$

For the shape parameters a_{HN} and b_{HN}, which describe the symmetric and asymmetric broadening of the complex dielectric function, $0 < a_{HN}$, $a_{HN} \cdot b_{HN} \leq 1$ holds. The parameters a_{HN} and $a_{HN} \cdot b_{HN}$ are the slopes of $\log\varepsilon''$ *vs.* $\log\omega$ at low and high frequencies, respectively, with regard to the position of maximal loss (Kremer, et al., 2003). The position of the maximal loss (ω_p) depends on the parameters a_{HN} and b_{HN} according to:

$$\omega_p = \frac{1}{\tau_{HN}} \cdot \left[\sin\frac{a_{HN} \cdot \pi}{2 + 2 \cdot b_{HN}}\right]^{1/a_{HN}} \cdot \left[\sin\frac{a_{HN} \cdot b_{HN} \cdot \pi}{2 + 2 \cdot b_{HN}}\right]^{-1/a_{HN}} \tag{1.24}$$

An empirical model was proposed by R.M. Fuoss and J.G. Kirkwood (Fuoss, et al., 1941). The FUOSS/KIRKWOOD (FK) model has been widely used to characterize secondary relaxation processes.

$$\varepsilon''(\omega) = \varepsilon''_{\max} \cdot \sec h\left[m_{FK} \cdot x\right] \tag{1.25}$$

$$x = \ln\left(\frac{f_{\max}}{f}\right) = \frac{m_{FK} \cdot E_a}{R}\left(\frac{1}{T} - \frac{1}{T_{\max}}\right) \tag{1.26}$$

where E_a is the energy barrier associated to a specific molecular motion; f_{max} and T_{max} represent the frequency and temperature of the $\varepsilon''_{\max}$; and m_{FK} is a shape parameter related to the width of the relaxation process, which is equal to 1 for a process with only one relaxation time (Debye process). The relaxation strength can be evaluated as $\Delta\varepsilon = 2 \cdot \varepsilon''_{\max} / m_{FK}$.

Accordingly to the previous models, the peak of $\varepsilon^*(\omega)$ function is characterized by (i) the frequency of the maximum, f_{max}, with which the characteristic relaxation time can be calculated as $\tau = 1/2\pi f_{\max}$; (ii) its shape properties as breadth and symmetry, and (iii) the strength of the relaxation, which is given by:

$$\Delta\varepsilon = \varepsilon_s - \varepsilon_\infty = \int_{peak} \varepsilon''(\omega)\, d\ln\omega \tag{1.27}$$

The relaxation strength, $\Delta\varepsilon$, is related to the effective dipolar moment and can be evaluated with the Debye theory of the dielectric relaxation (Fröhlich, 1958). This theory was improved by Onsanger-Fröhlich and Kirkwood and they proposed the following relation:

$$\Delta\varepsilon = \varepsilon_s - \varepsilon_\infty = F_{Onsanger} \cdot g \cdot \frac{N \cdot \mu^2}{3 \cdot k_B \cdot T} \tag{1.28}$$

with $F_{Onsager} = \frac{1}{3}\frac{\varepsilon_s\left(\varepsilon_\infty + 2\right)^2}{2\varepsilon_s + \varepsilon_\infty}$; μ is the dipolar moment; N is the number of dipoles that participates in the relaxation; k_B is the Boltzmann constant; and g is the correlation factor, an empirical parameter introduced by Kirkwood as $g = 1 + \left\langle \cos\theta_{ij} \right\rangle$, where θ_{ij} is the angle formed by the dipolar moment i with his neighbor j. This factor g can be obtained using, for example, statistical mechanics.

Tabla 1.1. Empirical models of $\varepsilon^*(\omega)$ function.

MODEL	$\boldsymbol{\varepsilon^*(\omega)}$
DEBYE	$\varepsilon^* = \varepsilon_\infty + \frac{\varepsilon_s - \varepsilon_\infty}{1 + i\omega\tau}$
COLE/COLE	$\varepsilon^*(\omega) = \varepsilon_\infty + \frac{\left(\varepsilon_s - \varepsilon_\infty\right)}{1 + \left(i\omega\tau_{CC}\right)^{a_{CC}}}$
COLE/DAVIDSON	$\varepsilon^*(\omega) = \varepsilon_\infty + \frac{\left(\varepsilon_s - \varepsilon_\infty\right)}{\left[1 + \left(i\omega\tau_{CD}\right)\right]^{b_{CD}}}$
HAVRILIAK/NEGAMI	$\varepsilon^*(\omega) = \varepsilon_\infty + \frac{\left(\varepsilon_s - \varepsilon_\infty\right)}{\left[1 + \left(i\omega\tau_{HN}\right)^{a_{HN}}\right]^{b_{HN}}}$
FUOSS-KIRKWOOD	$\varepsilon''(\omega) = \varepsilon''_{\max} \cdot \sec h\left[m_{FK} \cdot x\right]$ $x = \ln\left(\frac{f_{\max}}{f}\right) = \frac{m_{FK} \cdot E_a}{R}\left(\frac{1}{T} - \frac{1}{T_{\max}}\right)$

Therefore, the relaxation strength, which is obtained by the fitting of the experimental data to one of the empirical models previously described, allows obtaining information about the correlation of the dipolar moments. As a consequence, $\Delta\varepsilon$ also allows obtaining information about the correlation between molecules.

The HN equation is the most used model to characterize the relaxation processes. The deconvolution of the relaxation processes is carried out by the fitting of the experimental data $\left(\varepsilon''(\omega)\right)$ to a sum of as many HN functions as existing relaxation processes (additive rule) (Schröter, et al., 1998; Kahle, et al., 1997; Bergman, et al., 1998; Alvarez, et al., 2005). However, sometimes the characterization of the relaxation processes is complicated because the processes are strongly overlapped. In this case, the relaxation processes are better defined in the time domain than in the frequency domain.

In the time domain, the dielectric behavior is expressed using the time dependent dielectric function, $\varepsilon(t)$ (Kremer, et al., 2003):

$$\frac{d\varepsilon(t)}{dt} = \frac{1}{2\pi}\int_0^{\infty}\left[\varepsilon^*(\omega) - \varepsilon_{\infty}\right]\cdot\exp(i\omega t)d\omega \tag{1.29}$$

The function of the relaxation time distribution $\left[L(\tau)\right]$ can be evaluated from the experimental data. The relaxation processes can be described as the superposition of several Debye functions with different relaxation times:

$$\varepsilon^*(\omega) = \varepsilon_{\infty} + \int_{-\infty}^{+\infty}\frac{\Delta\varepsilon}{1+i\omega\tau}L(\tau)d\ln\tau \tag{1.30}$$

where the relaxation time distribution, $L(\tau)$, fulfils the normalization condition $\int L(\tau)d\ln\tau = 1$.

In a previous work (Dominguez-Espinosa, et al., 2008), a procedure to carry out the transformation from the frequency domain to the time domain was published. Thus, the retardation loss spectra, $L(\tau)$, can be evaluated from the experimental data of the dielectric permittivity function, $\varepsilon^*(\omega)$. Once $L(\tau)$ is obtained, the overlapped processes can be separated because they are better defined in this time domain. Moreover, the normalized α relaxation in the time domain can be calculated from the retardation loss spectra: $\phi(t) = \int_{-\infty}^{\infty} L_\alpha(\ln\tau) e^{-t/\tau} d\ln\tau \Big/ \int_{-\infty}^{\infty} L_\alpha(\ln\tau) d\ln\tau$

It is very interesting the empirical distribution proposed by Kohlrauch (Kohlrausch, 1854), which was applied to the dielectric relaxation by Williams and Watts (Williams, et al., 1970; Williams, 1979). Thus, the decay function was described by these authors (KWW) as:

$$\phi(t) = \exp\left[-\left(\frac{t}{\tau_{KWW}}\right)^{\beta_{KWW}}\right] \tag{1.31}$$

where τ_{KWW} is the characteristic relaxation time and β_{KWW} $(0 < \beta_{KWW} \leq 1)$ is a parameter that describes the non-exponential behavior of the decay function. If the value of β_{KWW} is low, the distribution of relaxation times is wide and the process is asymmetric. β_{KWW} parameter is related to the interaction degree between dipolar moments.

Both KWW and HN equation can be simultaneously used to analyze the dielectric data. A significant effort has been made to relate the parameters obtained using these two equations. Thus, Patterson and Lindsay (Lindsay, et al., 1980) derived a relationship between the Cole/Davidson function and KWW formula which both have one shape

parameter only. This work was extended by Colmenero et al. (Colmenero, et al., 1991). They related the HN and KWW equations leading to the following approximations (Kremer, et al., 2003):

$$\log\frac{\tau_{HN}}{\tau_{KWW}} \approx 2.6\left(1-\beta_{KWW}\right)^{0.5}\exp\left(-3\beta_{KWW}\right) \tag{1.32}$$

$$a_{HN}\cdot b_{HN} = \beta_{KWW}^{1.23} \tag{1.33}$$

The HN function has two shape parameters while the KWW equation has only one. Therefore, during the transformation from the frequency to the time domain information is lost.

1.2.2.3. The Coupling Model

In the recent years, a lot of works have studied the glass transition and the glassy state in order to understand the underlying dynamics, which range from the microscopic regime on the order of picoseconds to the macroscopic regime on the order of days or longer. The structural α relaxation rate is dependent on specific volume and entropy and, therefore, the glass transition is partly caused by the densification as well as reduction in entropy. However, the motions of the molecules in the glass formers are not independent of each other and these complex motions, described as many-body relaxation, may have an effect on the structural relaxation rate not accountable by volume and entropy (Capaccioli, et al., 2012). Thus, the dynamics of the glass transition can be influenced not only by factors like the specific volume, configurational entropy but also by intermolecular coupling. The last one includes effects such as caging, cooperativity, non-exponentiality and dynamic heterogeneity. Moreover, these factors are influenced by temperature and pressure

(Casalini, et al., 2003).

As explained in the subsection 1.1.2.2, the secondary relaxations are associated to inter/intramolecular motions more localized than those corresponding to the α relaxation. Although these processes are thermally activated (Arrhenius), it was found that some of them are partly cooperative. Thus, the secondary relaxations can have (i) an intramolecular origin, which involves the independent motion of an isolated group or (ii) an intermolecular origin, which involves the motion of essentially the entire molecule (repeat unit in the case of a polymer). The latter are known as *Johari-Goldstein* (JG) relaxations (Johari, et al., 1970; Johari, et al., 1972) and are connected with the structural α relaxation, since they are defined as the initiator of the structural α relaxation (Ngai, 2011; Capaccioli, et al., 2012). However, only from the dielectric relaxation data, it is difficult to know whether the secondary relaxations have an intra- or intermolecular origin. To overcome this difficulty, Ngai et al. proposed the comparison of the JG secondary relaxation time, τ_{JG}, and the relaxation time of the primitive (non-cooperative) relaxation, τ_0^{CM}, of the Coupling Model (CM) (Paluch, et al., 2005; Ngai, 1998; Ngai, et al., 2004; Ngai, et al., 2007; Casalini, et al., 2003; Ngai, 2003). The JG secondary relaxation is related to the primitive relaxation of the CM because both are precursor of the α relaxation and have the same attribute, *i.e.* they are local processes (Capaccioli, et al., 2012; Ngai, et al., 2012).

The Coupling Model tries to account mainly the effects of intermolecular coupling, such as the many-body cooperative dynamics and dynamic heterogeneity (Casalini, et al., 2003). The basis of the CM is the existence of a temperature-insensitive crossover time, t_c, which is about 2 ps for small molecules and polymeric glass formers (Ngai, 1979; Ngai, et al., 1999). At times shorter than t_c, the basic molecular units relax independently of each

other. The relaxation function of these primary species can be described by a simple exponential decay:

$$\phi(t) = \exp\left[-\left(t/\tau_0^{CM}\right)\right],\ t < t_c \tag{1.34}$$

However, at times longer than t_c, the intermolecular interactions (i.e. cooperativity, which is associated with the dynamic heterogeneity) slow the relaxation, there is a coupling between the motion of the different primary species. Therefore, the normalized correlation function assumes the KWW form (Eq. 1.31):

$$\phi(t) = \exp\left[-\left(t/\tau_{KWW}\right)^{\beta_{KWW}}\right],\ t > t_c \tag{1.35}$$

where τ_{KWW} is the α relaxation time, *i.e.* $\tau_{KWW} = \tau_\alpha$. When t=t_c, $\phi(t)$ has a continuity, which leads to the relation between the two relaxation times:

$$\tau_\alpha = \left[t_c^{\beta_{KWW}-1} \cdot \tau_0^{CM}\right]^{1/\beta_{KWW}},\ t = t_c \tag{1.36}$$

Thus, due to the similarity of the JG relaxation to the primitive relaxation, a secondary process is considered a JG relaxation when its relaxation time, τ_β, obeys the following criterion (Ngai, et al., 2004):

$$\tau_\beta = \tau_{JG} \approx \tau_0^{CM} \tag{1.37}$$

This relation has been fulfilled for genuine JG relaxations in many glass formers (Ngai, et al., 2004; Casalini, et al., 2003). At any temperature, the primitive relaxation time can be calculated by the CM using the Eq. (1.36). The coupling parameter *n*, which characterizes the strength of the intermolecular constraints on segmental relaxation, can be evaluated as $n = (1-\beta_{KWW})$. As a consequence, τ_0 can be calculated using the Eq. (1.36), as

follows:

$$\tau_0^{CM} = t_c^n \cdot \left(\tau_\alpha\right)^{1-n} \tag{1.38}$$

The parameter n, related to the width of the α dispersion, governs many general properties of the structural α relaxation and JG processes. Capaccioli et al. (Capaccioli, et al., 2012) have reported that there is a general property of coinvariance of τ_α, n and τ_{JG}, oblivious to changing thermodynamics conditions (temperature and pressure) accompanied by large variations of specific volume and entropy. This remarkable property is additional strong evidence that the JG β relaxation is fundamentally important, with inseparable relation to the α relaxation.

Chapter 2:

Objectives

2. OBJECTIVES

2.1. General and specific objectives

The general objective of the present thesis is to study and characterize the physico-chemical properties of different polymeric materials. The work is based on the analysis of the effect of the macromolecular structure on the properties of the materials. Thus, an in-depth analysis of the liquid and glass state of the polymers has been carried out. To this purpose, mainly the materials are thermally, mechanically and/or electrically perturbed and the corresponding response generated is analyzed as a function of the external perturbation.

The properties of the materials are intimately related to their molecular mobility, which in turn depends on the macromolecular structure. Therefore, the analysis of the structure-properties relationship requires the study of the molecular mobility of the materials.

The characterization of the materials enables us to relate their properties to their chemical structure. Thus, this information can be used to optimize the design of new materials according to specific technological requirements.

In the present thesis, two families of polymers have been analyzed in order to determine their properties as function of their chemical structure. The selection of the materials is deeply discussed in the introduction part of Chapters 4, 5 and 6.

The first polymers characterized were chemically cross-linked copolymers composed of Vinylpyrrolidone (VP) and Butyl Acrylate (BA) monomers. The dynamics of cross-linked polymers should be influenced by the network composition and the polymer chain

architecture Thus, it was studied (i) the effect of the copolymer composition on the properties of VP/BA copolymers with a fixed cross-linker molar ratio of 1% and (ii) the effect of the cross-linking on the characteristics of *X*VP/*Y*BA copolymers with a fixed copolymer composition of 60/40.

The specific objectives for *X*VP/*Y*BA copolymers family with a fixed cross-linker molar ratio were:

- To verify the chemical structure and to determine the possible existence of interactions between chemical groups by chemical characterization.
- To determinate the thermal stability and main thermal transitions, as well as their dependence with the copolymer composition by thermal analysis.
- To analyze the molecular mobility of the copolymers by dielectric characterization (DRS). To study the effect of copolymer composition on the dielectric properties and conductivity.
- To study the effect of the copolymer composition on their static and dynamic mechanical properties.
- To establish the relationships between the results obtained from chemical characterization with those obtained from thermal analysis, dynamic mechanical analysis and dielectric relaxation spectroscopy.

To accomplish the study of the effect of the cross-linking on the *60*VP/*40*BA copolymers, the following specific goals were set out:

- To study the effect of the cross-linking on the thermal transitions, mainly in the glass transition.
- To analyze the effect of the cross-linking on the molecular mobility of the copolymers. The study will be focused on both cooperative and non-cooperative processes. For this purpose, the intra/intermolecular character of the secondary relaxations will be analyzed.

The second polymeric materials studied were composites composed of Polycarbonatediol Polyurethane (PUPH) and Expanded Graphite (EG). It was characterized the behavior of a PUPH matrix modified by different amounts of EG conductive filler (from 0 to 50%).

The following specific objectives were set out for the PUPH/EG composites:

- To evaluate the dispersion of the EG in the polymer matrix.
- To characterize the effect of the EG content on the thermal, mechanical and dielectric properties of PUPH/EG composites.
- To study the influence of the hard/soft domains on the molecular dynamics of polycarbonatediol polyurethane.
- To analyze the conductivity behavior of PUPH/EG composites as a function of the EG content, temperature and frequency.

Chapter 3:

Materials and Methods

The experimental methods described in this Chapter were published in: B. Redondo-Foj, M. Carsí, P. Ortiz-Serna, M. J. Sanchis, F. García and J. M. García, *J. Phys. D: Appl. Phys.,* vol. 46, pp. 295304-295315, **2013**.; B. Redondo-Foj, M. Carsí, P. Ortiz-Serna, M. Sanchis, S. Vallejos, F. García and J. García, *Macromolecules,* vol. 47(15), p. 5334–5346, **2014**.; B. Redondo-Foj, M. J. Sanchis, P. Ortiz-Serna, M. Carsí, J. M. García and F. García, *Soft Matter*, vol. 11, p. 7171–7180, **2015**.; C.M. Gómez, M. Culebras, A. Cantarero, B. Redondo-Foj, P. Ortiz-Serna, M. Carsí and M. Sanchis, *Appl. Surf. Sci,* vol. 275, pp. 295-302, **2013**.; B. Redondo-Foj, P. Ortiz-Serna, M. Carsí, M. Sanchis, M. Culebras, C.M. Gómez and A. Cantarero, *Polym. Int.,* vol. 64, pp. 284-292, **2015**.; P. Ortiz-Serna, M. Carsí, B. Redondo-Foj, M. Sanchis, M. Culebras, C.M. Gómez and A. Cantero, *J. Appl. Polym. Sci.,* DOI:10.1002/APP.42007, **2015**.

3. Materials and Methods

The aim of this chapter is to describe the experimental methods and techniques commonly carried out in all the sections of this thesis. A more detailed description will be specified in each subsection for each familiy of polymers studied.

3.1. Materials

As stated in Chapter 2, two families of polymers have been analyzed in this thesis in order to determine their properties as function of their chemical structure. The introduction parts of Chapter 4, 5 and 6 explain in more detail the justification for selecting these polymeric materials.

The first family of polymers characterized was chemically cross-linked copolymers composed of VP and BA monomers. The copolymerization of VP with BA, as well as the cross-linking process, is used to modify, to improve and to adapt the properties of the homopolymers separately.

Thus, the effect of the copolymer composition on the properties of VP/BA copolymers with a fixed cross-linker molar ratio of 1% was studied. Moreover, the influence of the cross-linking on the characteristics of VP/BA copolymers with a fixed copolymer composition of 60/40 was also examined.

The second family of polymers studied was composites composed of PUPH and EG. EG was dispersed in the PUPH especially in order to increase the polyurethane conductivity. Thus, the behavior of a PUPH matrix modified by different amounts of EG conductive filler (from 0 to 50%) was characterized using different techniques.

3.1.1. Synthesis of VP/BA Copolymers

All the chemically cross-linked VP/BA Copolymers used for this thesis work have been synthesized by the Polymer Group led by Prof. José Miguel García Pérez, University of Burgos (Spain).

All chemicals were commercially obtained and used as received: 1-Vinyl-2-pyrrolidone (Aldrich, 99%), butyl acrylate (Fluka, 99.5%), ethylene glycol dimethacrylate (EGDMMA) (Aldrich, 98%), and 2,2-dimethoxy-2-phenylacetophenone (Aldrich, 99%). Samples of poly(vinylpyrrolidone-co-butyl acrylate) were prepared by radical polymerization of VP and butyl acrylate BA mixture varying the molar ratio. EGDMMA was used as the cross-linker (C). The molar ratio of cross-linker to the other comonomers, VP and BA, was also varied from 0.2% to 2%. 2-Dimethoxy-2-phenylacetophenone (1.56 wt%) was used as a radical photoinitiator. The homogenous solution comprised of VP, BA and EGDMMA, and the photoinitiator were transferred to an ampoule, degassed by nitrogen bubbling for 15 min, and injected into an oxygen-free atmosphere. The photoinitiated bulk polymerization was performed in a 100 μm thick silanised glass hermetic mould upon irradiation with a Ultraviolet (UV) mercury lamp (250w, Philips HPL-N, emission band in the UV region at 304, 314, 335 and 366 nm, with maximum emission at 366 nm), at 293 K, for 1 h. The sample containing only BA and EGDMMA was prepared using a 300 μm thick silanised glass hermetic mould, in order to obtain a tractable material, due to its softness. Then, the samples were conditioned by means of a thoroughly wash with acetone (two washing cycles each of 3h) followed by a drying process at room temperature and a dip into pure water overnight. Finally, they were dried in a vacuum oven at 293 K.

The chemical structures of the monomers (VP and BA), cross-linker and the copolymer samples (*X*VP/*Y*BA-*Z*C) are shown in **Figure 3.1**. Moreover, the molar ratios of VP and BA, and the molar ratios of EGDMMA to the other comonomers, are collected in **Table 3.1** and **Table 3.2**.

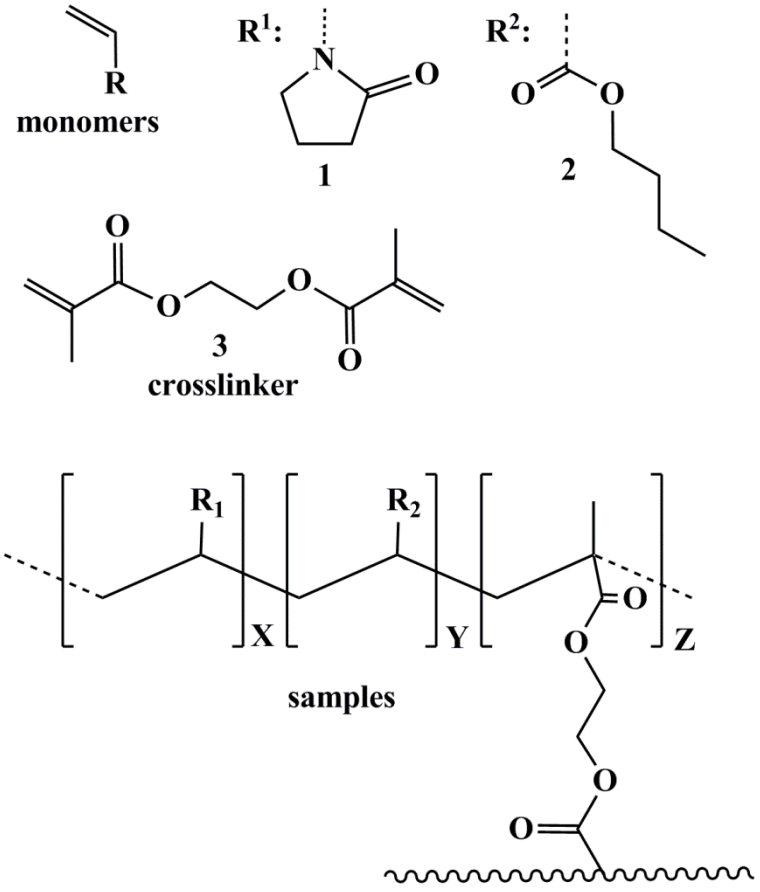

Figure 3.1. Scheme of the chemical structure of *X*VP/*Y*BA-*Z*C samples (R^1=VP, R^2=BA).

Table 3.1 Chemical Composition of the copolymer samples with different proportions of monomers and a fixed cross-linker molar ratio (*X*VP/*Y*BA-*1*C)

	monomer molar ratio		
Sample code	***X***	***Y***	***Z***
*100*VP/*0*BA	100	0	1
*70*VP/*30*BA	70	30	1
*60*VP/*40*BA	60	40	1
*50*VP/*50*BA	50	50	1
*0*VP/*100*BA	0	100	1

Table 3.2. Chemical composition of the copolymer samples with a fixed monomer content and different cross-linker molar ratios (*60*VP/*40*BA-*Z*C).

	monomer molar ratio		
Sample code	***X***	***Y***	***Z***
*60*VP/*40*BA-*0.2*C	60	40	0.2
*60*VP/*40*BA-*1*C	60	40	1
*60*VP/*40*BA-*2*C	60	40	2

3.1.2. Synthesis of EG-PUPH Composites

The segmented thermoplastic polyurethanes modified with different amounts of expanded graphite have been synthesized by the Group of Prof. Andrés Cantarero Sáez and Prof. Clara M. Gómez Clari, Materials Science Institute, University of Valencia (Spain).

Segmented thermoplastic polyurethanes are copolymers formed by hard and soft segments. In the present thesis, 4,4'–diphenylmethane diisocyanate (MDI) (see **Figure 3.2**), and 1,4–butanediol (see **Figure 3.3**) supplied by Aldrich (Barcelona, Spain) constituted the polyurethane hard segment and polyhexamethylene–pentamethylene carbonate diol (PH) (see **Figure 3.4**) of average molar mass 1000 supplied by UBE Chem Eur (Castellon, Spain) the soft one. Natural graphite powder lower than 20 μm size, dimethyl acetamide (DMAc) as solvent, nitric acid and sulfuric acid were purchased from Aldrich (Barcelona, Spain).

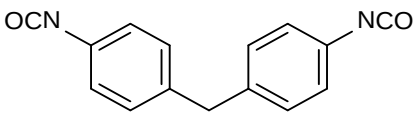

Figure 3.2. Chemical structure of 4,4'–diphenylmethane diisocyanate

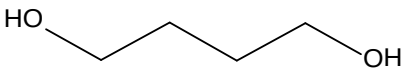

Figure 3.3. Chemical structure of 1,4–butanediol

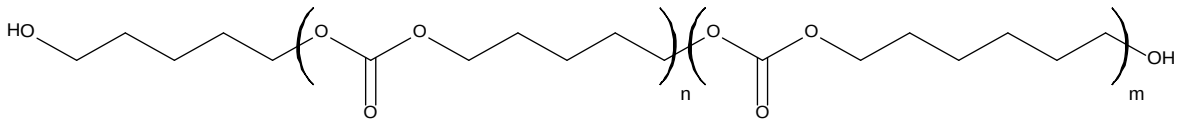

Figure 3.4. Chemical structure of polyhexamethylene–pentamethylene carbonate diol (PH)

Expanded graphite was obtained by the method of chemical oxidation (Dhakate, et al., 2008). The natural graphite was dried at 348 K in a vacuum oven for 10 h. Then, it was blended for 12 h with a 3:1 sulfuric and nitric mixture in order to form the graphite inserted compound. The nitric acid was used as an oxidizer and the sulfuric acid as an intercalating agent. The mixture was stirred from time to time to get a uniform intercalation of the sulfuric acid into the graphite flakes. After that, the mixture was washed to obtain a neutral pH, then it was filtered and the resulting material was dried at 333 K in vacuum for 5h. Afterwards, it was subjected to a thermal shock at 800ºC for 20s in order to form the expanded graphite.

Polyurethane solutions were obtained by a standard polymerization method based on the two–step process in DMAc (Costa, et al., 2012). In the first step one equivalent of polycarbonatediol PH was inserted in the reactor, previously dried for 24 h at 373 K, with three equivalents of MDI. The reaction was carried out at 343 K for 2 h under argon atmosphere. The second step corresponds to the addition of the chain extender, butanediol. Two equivalents of butanediol were added to obtain a viscous amber polyurethane solution with approximately 25 wt% in solid content. The solution was stored for 24 h in order to remove the bubbles produced in the synthesis process. The scheme of the chemical structure of the segmented polyurethane is shown **Figure 3.5.** Scheme of the chemical structure of the segmented polyurethane in soft and hard segments.

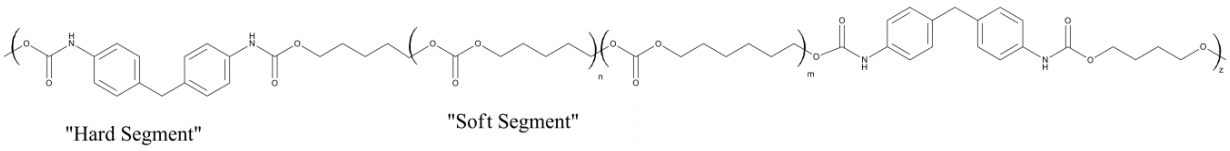

Figure 3.5. Scheme of the chemical structure of the segmented polyurethane in soft and hard segments.

In order to prepare the composites, different weight fractions of EG between 0 and 50 wt% were introduced in the PUPH solution. The blend was sonicated in an ultrasonic bath for 1 h, in order to disaggregate the flakes and also was vigorously stirred for 5 h to obtain a stable dispersion. The suspensions were cast on glass slides, which were previously washed in an ultrasonic bath with distilled water and later with acetone in order to eliminate the water. The polyurethane/expanded graphite composites (PUPH/EG) coated glasses were kept at 343 K during 12h. Films were prepared with dimensions of (4 ×2.7) cm^2 and with a thickness that ranged between 200 and 250 μm. The nomenclature used for labeling the samples and the filler content in weight and volume percentage are summarized in **Table 3.3**.

Table 3.3. Sample name and the filler content for all the composites analyzed.

Sample name	Filler content by weight (%)	Filler content by volume (%)
PUPH	0	0
PUPH/5EG	5	2.5
PUPH/15EG	15	8.1
PUPH/20EG	20	11.1
PUPH/30EG	30	17.6
PUPH/40EG	40	25.0
PUPH/50EG	50	33.3

3.2. Experimental Techniques

As stated before, the main idea of this thesis is to study the relationship between structure and properties of two families of polymers. The study has mainly been done using a combination of techniques such as Dielectric Relaxation Spectroscopy (DRS) and Differential Scanning Calorimetry (DSC), since DSC is sensitive to the thermal properties whereas DRS is also selective to dipole moment fluctuations. Moreover, other complementary physical and chemical characterization techniques were also performed to support the interpretation of DSC and DRS results.

The *X*VP/*Y*BA-*Z*C samples were characterized using other techniques by the Polymer Group led by Prof. José Miguel García Pérez, University of Burgos (Spain). The physical characterization was carried out by hydrophilicity measurements, Thermogravimetry Analysis (TGA) and mechanical analysis. Moreover, a chemical characterization was also performed by Fourier Transform Infrared (FTIR) Measurements.

The PUPH/EG composites were also analyzed using other additional physical and chemical characterization techniques by the Group of Prof. Andrés Cantarero Sáez and Prof. Clara M. Gómez Clari, Materials Science Institute, University of Valencia (Spain). The techniques used were TGA, X-ray Diffraction (XRD), FTIR, Dynamic Mechanical Analysis (DMA) and Scanning Electron Microscopy (SEM).

All these experimental methods used in this thesis are deeply described in the following subsections.

3.2.1. Sample hydrophilicity characterization

The *X*VP/*Y*BA-*Z*C samples were immersed in pure water at 293 K until reaching the swelling equilibrium (constant weight). Then, they were weighted (w_s), dried in an air-circulating oven at 333 K for 2h, and weighted again (w_d). Next, the water-swelling percentage (WSP) was calculated, where WSP is defined as the weight percentage of water uptake when the sample is soaked until equilibrium in pure water. It is obtained as follows: $100 \cdot [(w_s - w_d)/w_d]$ (Devine, et al., 2005; Hu, et al., 2005).

3.2.2. Fourier Transform Infrared Measurements

Infrared spectroscopy technique is useful for the identification of both organic and inorganic compounds. Aggregates of atoms (or functional groups) such as C=O, $-NO_2$, C-N, O-H, etc are associated with characteristic infrared absorptions. Thus, IR is ideal for the identification of functional groups present within a sample (Schlessinger, 1995).

IR absorption arises from a direct resonance between the frequency of the IR radiation and the vibrational frequency of a particular normal mode of vibration. The change in the dipole moment of the molecule with respect to its vibrational motion is the property of the molecule involved in the resonant interaction. IR absorption is a one-photon event. The IR photon encounters the molecule, the photon disappears, and the molecule is elevated in vibrational energy by the energy of the photon at the frequency of vibrational resonance (Lewis, et al., 2001).

Infrared spectra of the *X*VP/*Y*BA-*Z*C samples were recorded with a JASCO FT/IR-4100 fitted with a PIKE TECH "Miracle" ATR accessory (see **Figure 3.6**).

Figure 3.6. Picture of the JASCO FT/IR-4100 spectrometer.

The FTIR measurements of the PUPH/EG composites were performed in a Nicolet Nexus FTIR spectrometer (see **Figure 3.7**) over the range 450-4000 cm^{-1} with the

attenuated total reflectance accessory by co-addition of 60 scans with a spectral resolution of 2 cm^{-1}.

Figure 3.7. Pictures of Nicolet Nexus FTIR spectrometer.

3.2.3. Thermogravimetric Analysis

TGA is a technique where the mass of a polymer is measured as a function of temperature or time when the sample is subjected to a controlled temperature program and atmosphere. The temperature range usually used is from ambient temperature to 1273 K or more. A controlled atmosphere is created using a purge gas. This atmosphere can be inert (nitrogen, argon or helium), oxidizing (air or oxygen) or reducing (forming gas). The moisture content of the purge gas can vary from dry to saturated (Menczel, et al., 2009).

The TGA data of the *X*VP/*Y*BA-*Z*C samples were obtained for dried samples of 5 mg under nitrogen flow, using a TA Instruments Q50 TGA analyzer (see **Figure 3.8**) at a scan rate of 10 $K \cdot min^{-1}$.

Figure 3.8. Picture of the TA Instruments Q50 TGA analyzer.

The TGA of the PUPH/EG composites was carried out on a Setaram Setsys 16/18TGA-ATD analyzer (see **Figure 3.9**). The samples were analyzed in platinium pans at a heating-cooling rate of 10 $K \cdot min^{-1}$ from 303 to 1273 K under oxygen atmosphere. Samples masses ranged from 7 to 10 mg.

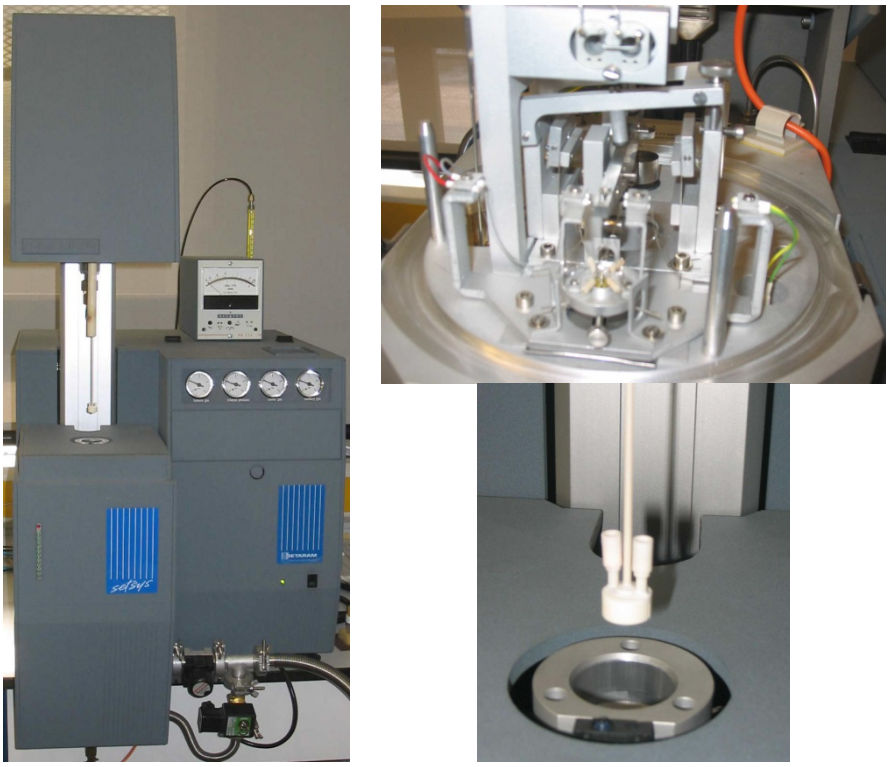

Figure 3.9. Pictures of the Setaram Setsys 16/18TGA-ATD analyzer.

3.2.4. Morphological analysis

SEM is a method for high-resolution imaging of surfaces. The electron microscope produces images of a sample by scanning it with a focused beam of electrons. The atoms in the sample interact with the beam of electrons producing different signals that contain information about the sample's surface topology and composition. SEM is used in polymer science to elucidate the microscopic structure or to differentiate several phases from each other (Michler, 2008).

The two main components of an SEM are the electron column and the control console (see **Figure 3.10**). The electron column is composed by an electron gun and two or more electron lenses, which influence the paths of electrons traveling down an evacuated tube, an electron detection system, and a set of deflectors. The base of the column is usually taken

up with vacuum pumps. The control console is a cathode ray tube (CRT) viewing screen and the knobs and computer keyboard that control the electron beam (Goldstein, et al., 2003; Khursheed, 2011).

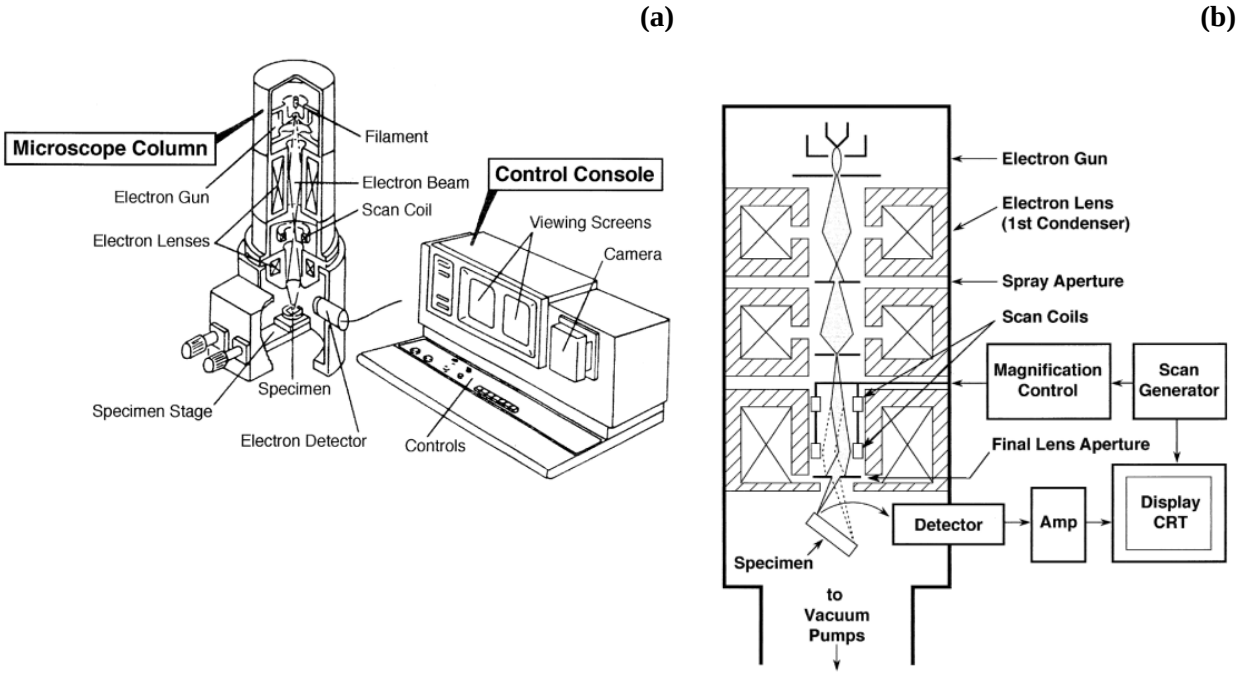

Figure 3.10. (a) The two main parts of the SEM: the electron column and the electronics console and (b) Schematic drawing of a SEM (Goldstein, et al., 2003).

The interaction of the beam with the specimen or sample produces various kinds of signals that are collected by the electron detectors (see **Figure 3.11**). When the primary beam interacts with the surface of the sample, it scatters electrons from a range of different depths, some of which escape from the surface. The electrons that escape from close to the sample surface are known as secondary electrons and are created by inelastic collisions. The electrons that escape from deeper levels are known as backscattered electrons and are

generated by multiple elastic collisions. Thus, secondary and backscattered electrons are the two most common signals used to form SEM image (Khursheed, 2011).

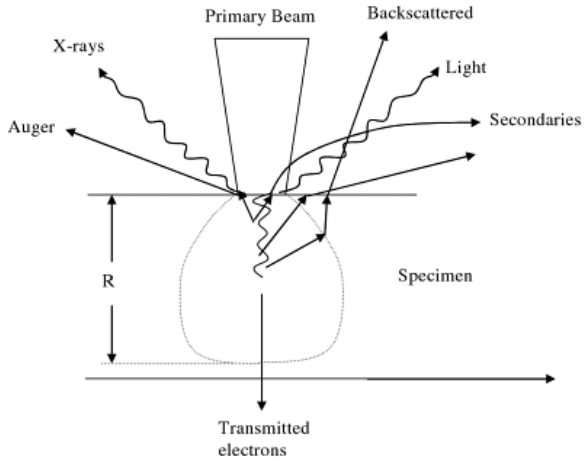

Figure 3.11. Interaction between the beam and the specimen (sample) (Khursheed, 2011).

SEM of the PUPH/EG composites was performed to determine the morphology on a Hitachi S-4800 microscope at an accelerating voltage of 20 kV and a working distance of 14 mm. Small pieces of sample were placed in the sample holder (*ca* 5 cm diameter) to study the sample surface. For cross-section observation the samples were cryoscopically fractured. All the samples were vacuum coated with a thin Au−Pd layer before testing.

3.2.5. X-ray characterization

Wide angle X-ray Diffraction is an X-ray diffraction technique used to determine the crystalline structure of polymers. This technique refers to the analysis of Bragg peaks scattered to wide angles, which implies that they are caused by subnanometer-sized structures. The diffraction pattern generated allows to determine the chemical composition

or phase composition of the sample, the texture of the sample (preferred alignment of crystallites), the crystallite size and presence of film stress.

Wide angle XRD was acquired on a Bruker AXS D5005 diffractometer. The PUPH/EG composites were scanned at 4 $K \cdot min^{-1}$ using Cu Kα radiation (λ=0.15418 nm) at a filament voltage of 40 kV and a current of 20 mA. The diffraction scans were collected within the range 2θ =5°–80° with a 2θ step of 0.01°.

3.2.6. Differential Scanning Calorimetry Measurements

DSC is one of the most widely used techniques to characterize the thermal properties of polymers. The DSC measures the difference in the heat flow between a sample and inert reference as a function of temperature and time while the substance and reference are subjected to a controlled temperature program. DSC analyzer calculates the heat flow using the temperature difference generated between the sample and the reference. An exothermic heat flow indicates that the heat flows out of the sample, while an endothermic heat flow indicates that the heat flows into the sample. The samples are heated, cooled or held isothermally and the DSC analyzer measures the energy changes that occur at a specific temperature or over a temperature range. DSC can determine different parameters such as the glass transition temperature, the heat capacity jump at the glass transition, melting and crystallization temperatures, heat of fusion, heat of reactions, heat capacity measurements, kinetic evaluation of chemical reactions or of polymer crystallization, thermal degradation, etc (Gabbott, 2008; Menczel, et al., 2009). It should be noted that the abbreviation DSC is used to represent the technique (differential scanning calorimetry) and the instrument (differential scanning calorimeter).

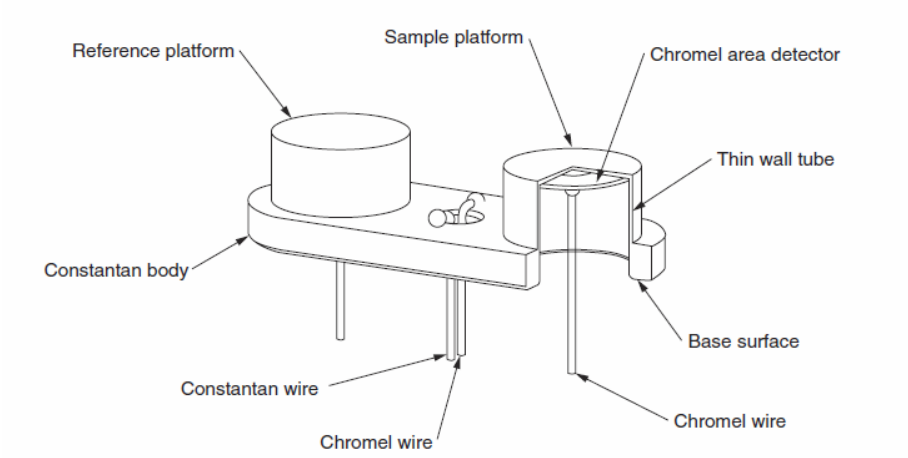

Figure 3.12. Schematic representation of the cell used in the DSC Q20 (Menczel, et al., 2009).

There are two types of DSC techniques: the standard DSC and the modulated DSC (MDSC). In the former, the temperature regime submitted to the sample and reference is linear heating rates from as fast as 200 K/min to 0 K/min (isothermal). However, in the MDSC a different temperature regime is applied to the sample and reference. In particular, a sinusoidal modulation (changing heating rate) is overlaid on the conventional linear heating rate to obtain a heating profile (solid green line in **Figure 3.13**), in which the average sample temperature still continuously increases with time but not linearly. Thus, the result is the same as if two different experiments were carried out at the same time: one experiment at the linear (average) heating rate (dashed pink line in **Figure 3.13**) and the other one at a sinusoidal (instantaneous) heating rate (dashed-dot brown line in **Figure 3.13**) (Thermal Analysis Review. Modulated DSC Theory).

The equation that describes the heat flow at any point and permits to deconvolute the different types of contributions to the heat flow is:

$$\frac{dQ}{dt} = C_p \cdot \frac{dT}{dt} + f(T,t) \tag{3.1}$$

where dQ/dt is the total heal flow, C_p is the heat capacity, dT/dt is the heating rate and *f(T,t)* is the heat flow from kinetic processes. Thus, the total heat flow, which is the only part measured by the standard DSC, is composed by two components: one of them is a function of the sample's heat capacity and heating rate (Heat capacity component), and the other one is a function of absolute temperature and time (Kinetic component) (Reading, et al., 2006).

The heat capacity component is referred to as the reversing heat flow and the kinetic component is referred to as the non-reversing heat flow. An MDSC experiment can separate the total heat flow into its reversing and non-reversing components. The events that contribute to the reversing heat flow are those which respond directly to changes in the heating rate and are fast enough to be reversing on the timescale of the modulation, such as glass transition and most melting. The events that contribute to the non-reversing heat flow are those which do not respond to changes in the heating rate, such as enthalpy relaxation at the glass transition, evaporation, crystallization, some melting and chemical reactions like decomposition or thermoset cure (Menczel, et al., 2009).

An MDSC experiment is dependent on three variables which are selected by the operator: the underlying heating rate (range 0-10 K/min), the period of modulation (range 10-100 s) and the temperature amplitude of modulation (range ±0.01-10K) (Thermal Analysis Review. Modulated DSC Theory).

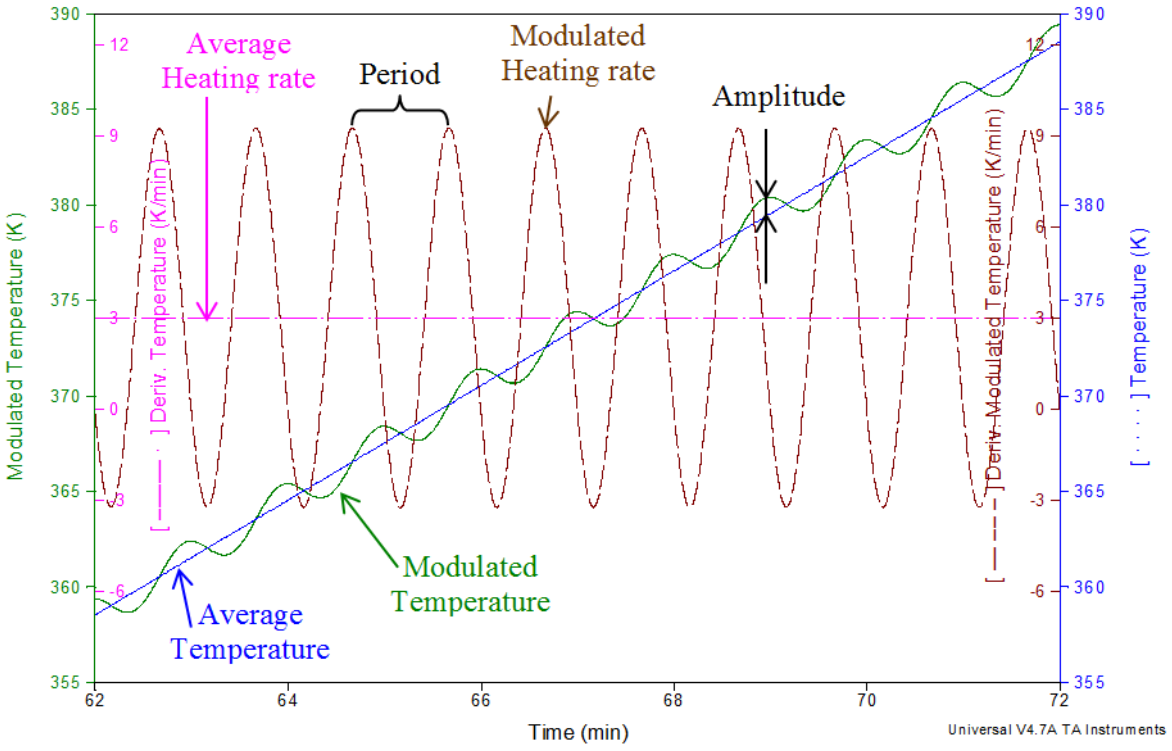

Figure 3.13. Example of MDSC Heating Profile of the *60*VP/*40*BA-*1*C sample with an underlying heating rate of 3 K·min^{-1}, a modulation period of 60 s and a modulation amplitude of ±1 K. Representation adapted from (Thermal Analysis Review. Modulated DSC Theory).

A TA Instruments DSC Q-20 with a refrigerated cooling system was employed to analyze all the samples in this thesis (see **Figure 3.14**). The DSC tests were performed under a 50 ml·min^{-1} flow of nitrogen to prevent oxidation. High-purity indium was used to calibrate the cell. The measurements were conducted in crimpled non-hermetic aluminium pans, using an empty crimpled aluminium pan as the reference cell.

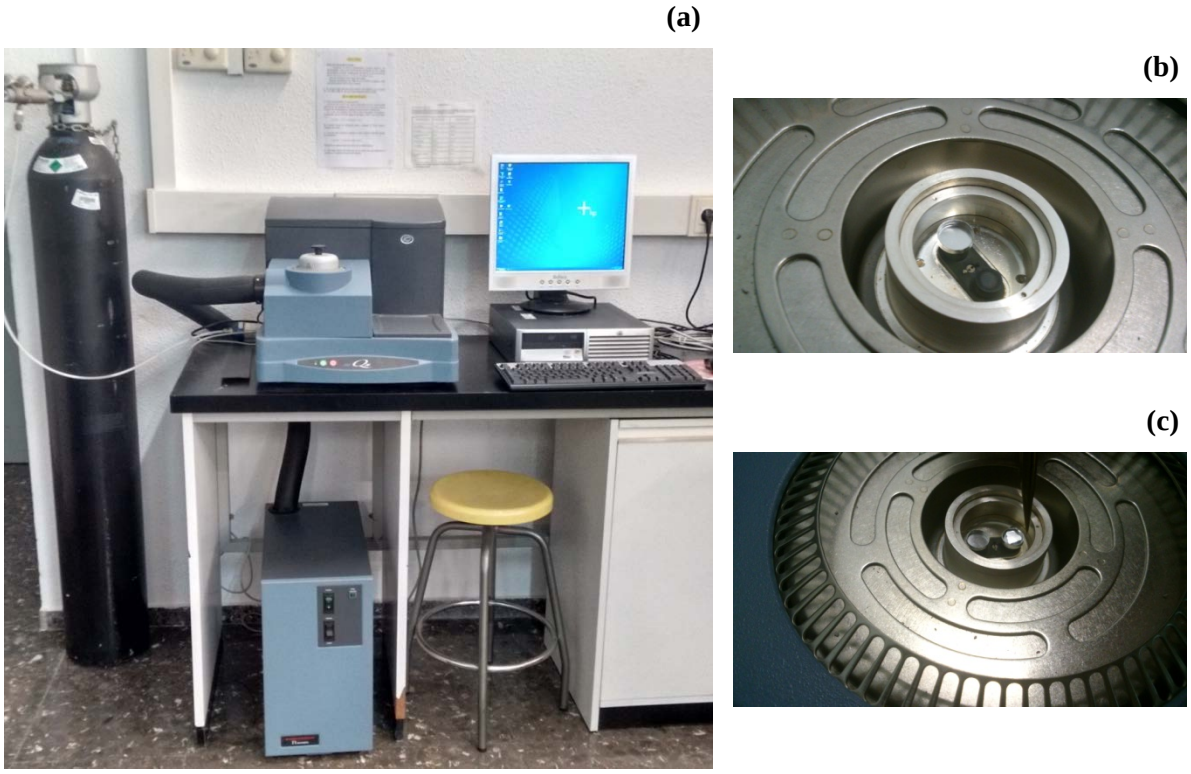

Figure 3.14. (a) Picture of the DSC TA Q-20 Instrument, the refrigerated cooling system and the dry nitrogen gas cylinder. Pictures of the measuring chamber (b) with only the reference pan and (c) with both the reference and the sample pan.

Modulated DSC (MDSC) measurements were carried out for the *X*VP/*Y*BA-*Z*C samples. The thin films were repeatedly stacked into a pan, with a weight of approx. 7.0 mg. The standard modulation conditions used were 1 K of amplitude and 60 s of period. Each measurement was taken in two cycles from 193 K to 473 K at a heating rate of 3 $K \cdot min^{-1}$. The first run was carried out in order to remove all the residual moisture and the thermal history.

Standard DSC measurements were performed for the PUPH/EG composites. The thin films were repeatedly stacked into a pan, with a weight of approx. 3.0 mg. Two heating cycles were carried out from 183 K to 493 K at a heating rate of 20 $K \cdot min^{-1}$ under nitrogen

atmosphere. The first run was performed in order to remove the thermal history of the sample.

The T_g was evaluated as the intersection of the base line of the glassy region with the tangent to the endotherm in the middle point.

3.2.7. Broadband Dielectric Relaxation Spectroscopy

Dielectric Relaxation Spectroscopy is a technique based on the interaction of a sample with a time-dependent electric field (Kremer, et al., 2003). The basis of DRS is the application of external perturbation field (electric field) $\vec{E}$ to the sample, so the molecular dipole system is perturbed from the equilibrium until the field is removed. Then, this dipole system returns to the equilibrium, so it is possible to obtain information about the spontaneous fluctuations in the system. The reorientation of dipoles and the translational diffusion of charged particles in this oscillating electric field provide the basis of the analysis based on the alternating current (ac) dielectric technique. Thus, DRS technique measures changes in different physical properties of a polar material, such as polarization, permittivity and conductivity as a function of temperature and the frequency of the external electric field. The changes in the dielectric constant and polarizability of a polymer are detected during phase transitions (the glass transition, melting or crystallization) and secondary transitions (localized relaxation mechanisms), as compared to the small changes in enthalpy, volume, or heat capacity measured by other more common thermal analytical techniques (Menczel, et al., 2009).

The relaxation signals are associated with movements of certain molecular/ionic species, which results in information about the composition, the microstructure and morphology of the sample. This technique has an advantage over other common thermal techniques, since its applicability is in a broad frequency range (10^{-6} Hz-10^{11} Hz) (Kremer, et al., 2003).

In order to measure the dielectric permittivity of a material, the sample is introduced between two electrodes, forming a capacitor. When the sinusoidal electric field $E^*(\omega) = E_0 \cdot \exp(i\omega t)$ is applied to this capacitor, the capacitance (C^*) increases due to the polarization of the sample. A sinusoidal voltage (U) is applied at fixed frequency (f) and the corresponding current (I) oscillates with the same frequency than that of the voltage. There is a phase shift between the current and the voltage which is described by the phase angle (φ) (see **Figure 3.15**). The expressions that relate these magnitudes are:

$$U(t) = U_0 \cdot \cos(\omega t) = \mathrm{Re}\left(U^* \exp(i\omega t)\right) \tag{3.2}$$

$$I(t) = I_0 \cdot \cos(\omega t + \varphi) = \mathrm{Re}\left(I^* \exp(i\omega t)\right) \tag{3.3}$$

$$\text{With } U^* = U_0 \text{ and } I^*(\omega) = I' + iI''; \; I_0 = \sqrt{I'^2 + I''^2} \; ; \; \tan(\varphi) = \frac{I''}{I'} \tag{3.4}$$

where ω is the angular frequency with $\omega = 2\pi f$ and the symbol * refers to the complex character of the quantity.

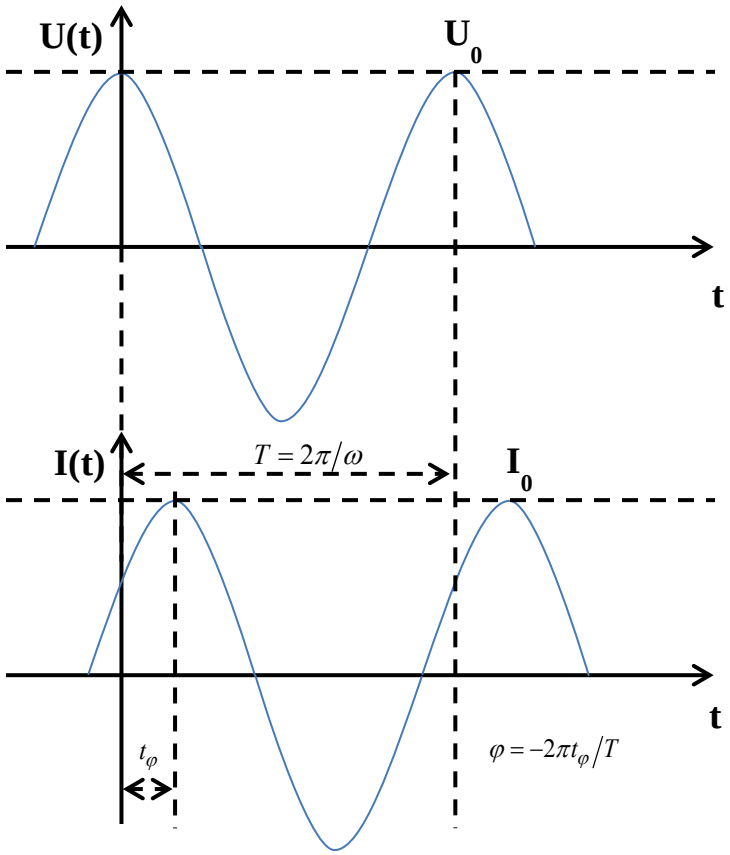

Figure 3.15. The time dependence of the voltage and current functions (T is the period and t_φ is the phase shift time).

Using the sinusoidal electric field $E^*(\omega)$ and at field strengths within linear response, the complex dielectric permittivity can be obtained by measuring the complex impedance $Z^*(\omega)$ of the sample.

$$Z^*(\omega) = Z' + iZ'' = \frac{U^*(\omega)}{I^*(\omega)} \tag{3.5}$$

The equation (3.5) is related to the complex dielectric permittivity $\varepsilon^*(\omega)$ and the capacitance by:

$$\varepsilon^*(\omega) = \varepsilon'(\omega) - i\varepsilon''(\omega) = \frac{C^*(\omega)}{C_0} = \frac{1}{i\omega Z^*(\omega) C_0} \tag{3.6}$$

where C_0 is the vacuum capacitance of the empty capacitor, ε_0 the permittivity of free space. $\varepsilon'(\omega)$ and $\varepsilon''(\omega)$ are the real and imaginary part of the complex dielectric function.

The experimental measurements depend on the sample geometry placed between the parallel plates of the capacitor with area A, being d the distance between plates ($A \ll d$):

$$C_0 = A \cdot \varepsilon_0 / d \tag{3.7}$$

To cover the frequency domain from 10^{-6} Hz to 10^{11} Hz four different systems based on different measurement techniques are employed: Fourier correlation analysis in combination with dielectric converters (10^{-6} Hz to 10^{7} Hz), impedance analysis (10^{1} Hz to 10^{7} Hz), RF-reflectometry (10^{6} Hz to 10^{9} Hz) and network analysis (10^{7} Hz to 10^{11} Hz). The Broadband dielectric spectrometers designed by Novocontrol, one of which was used in this thesis, are based on Broadband Dielectric Converter with either by an additional frequency response analyzer or lock-in amplifier.

The basic measuring principle is shown in **Figure 3.16**.

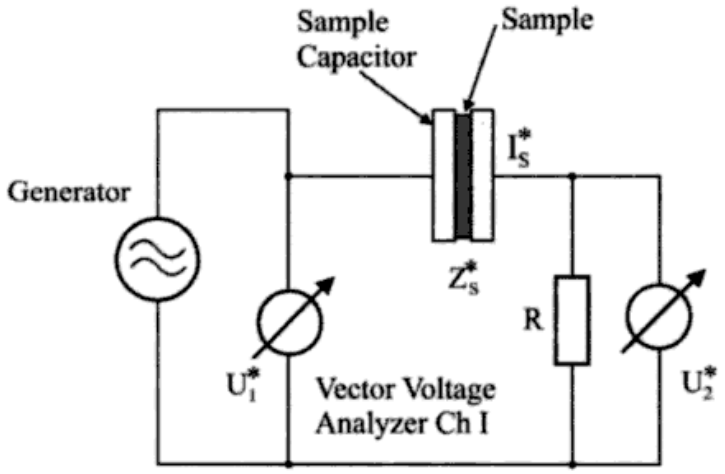

Figure 3.16. Scheme of a Fourier Correlation analyzer (Kremer, et al., 2003).

A sinusoidal voltage $U_1(t)$ with frequency $f = \omega/2\pi$ is applied to the sample by a generator, covering the frequency range from 10^{-6} Hz to 10^7 Hz. The resistor R converts the sample current I_S into a voltage $U_2(t)$. $U_1(t)$ and $U_2(t)$ are analyzed with respect to the amplitudes and phases of their armonic Fourier base waves $U_1^*(\omega)$ and $U_2^*(\omega)$ by two phase sensitive sine wave correlators. Thus, the complex sample impedance Z_S^* is calculated using the measured data by

$$Z_S^*(\omega) = \frac{U_S^*(\omega)}{I_S^*(\omega)} = R \cdot \left(\frac{U_1^*(\omega)}{U_2^*(\omega)} - 1 \right) \tag{3.8}$$

where $U_S^*(\omega)$ and $I_S^*(\omega)$ are the sample voltage and current.

However, the Fourier correlation analyzer of **Figure 3.16** with the resistor R suffers limitations. Therefore, the new instruments replaced the resistor R by a more sophisticated current to voltage converter in order to minimize these limitations (Kremer, et al., 2003).

All this is implemented in the Broadband Dielectric Spectrometer (Novocontrol Concept 80), from Novocontrol Gmbh (Hundsagen, Germany). Novocontrol instrument is composed of a system (Quatro Cryosystem) to control the temperature over a range from 113 K to 673 K, an impedance analyzer (Alpha Analyzer) to measure impedances from 10^{-5} Hz to 10 MHz and a network impedance analyzer (Agilent 4191A) to measure impedances from 1MHz to 3GHz.

The temperature controller (Quatro Cryosystem) has four circuits controlling the sample temperature, the gas temperature, the temperature of the liquid nitrogen in the dewar and the pressure in the dewar. The sample temperature is controlled by the heating of the N_2 (gas), achieving an accuracy of ±0.01 K.

The **Figure 3.17** and **Figure 3.18** show two pictures and the **Figure 3.19** shows a scheme of the Novocontrol Dielectric Spectrometer used in this thesis.

Figure 3.17. Picture of the Novocontrol Concept 80 instrument and the liquid nitrogen dewar.

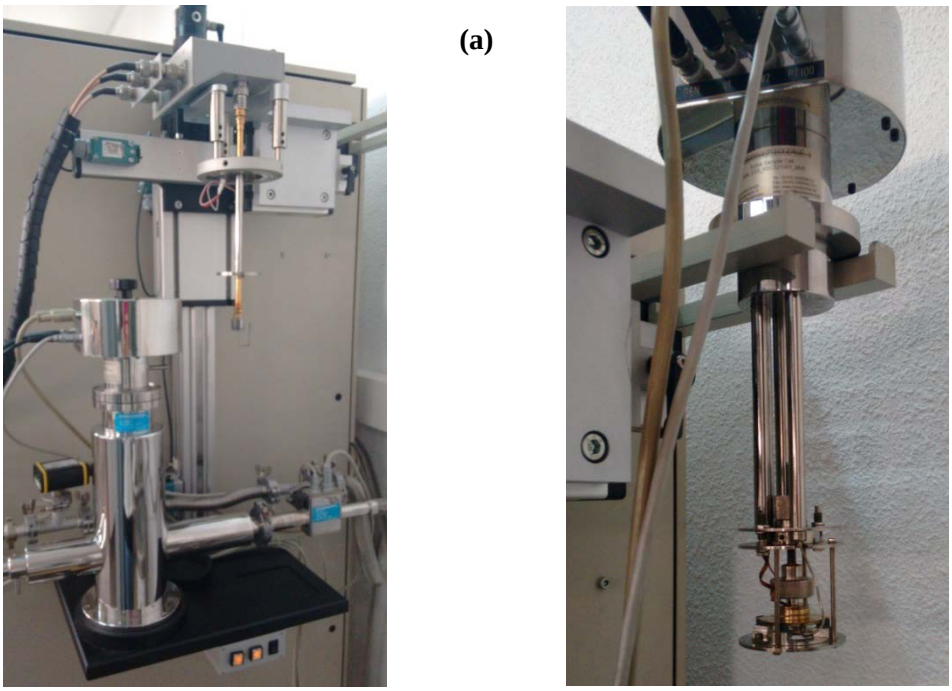

Figure 3.18. (a) View of the Alpha active cell inside the cryostat (left) and the RF extension line out of the cryostat (right). (b) Alpha active cell out of the cryostat with the sample between the gold-plated parallel electrodes.

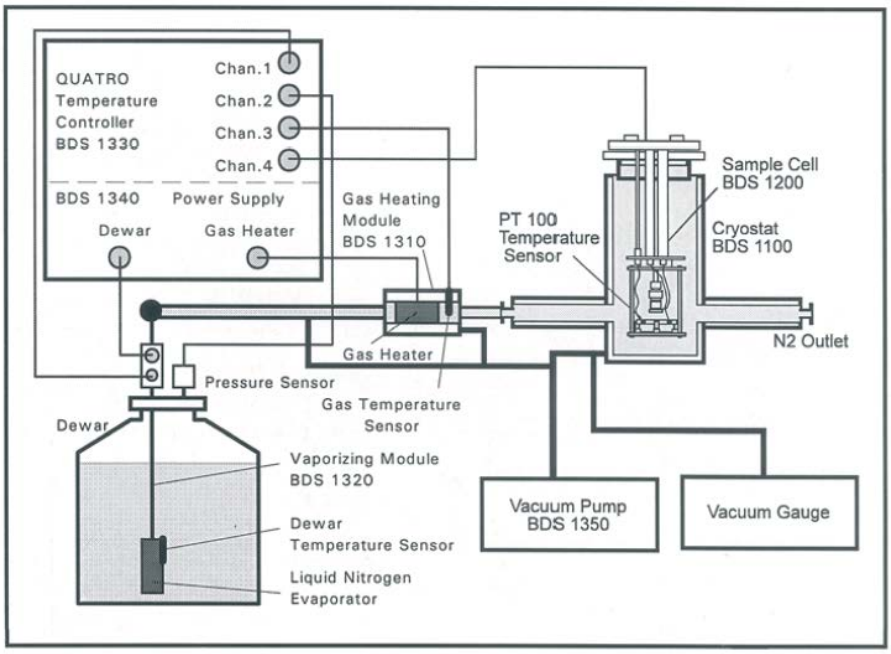

Figure 3.19. Scheme of the Novocontrol Concept 80 instrument.

Thus, the isothermal relaxation spectra of the samples were collected by using a Novocontrol Broadband Dielectric Spectrometer to carry out measurements from $5 \cdot 10^{-2}$ to $3 \cdot 10^{6}$ Hz. The measurements were performed in inert N_2 atmosphere. The temperature was controlled by a nitrogen jet with a temperature error of 0.1 K during every single sweep in frequency.

The measurements of the *X*VP/*Y*BA-*Z*C samples were performed in a temperature range from 423 K to 123 K. Molded disc shaped samples of about 100 μm thickness and 20 mm diameter were placed on two gold-plated electrodes forming a parallel plate capacitor. The experimental uncertainty was better than 5% in all cases.

The measurements of the PUPH/EG composites were carried out in a temperature range from 123 K to 423 K. Molded disc shaped samples of about 200 μm thickness and 20 mm diameter were placed on two gold electrodes forming a parallel plate capacitor. The experimental uncertainty was better than 5% in all cases.

3.2.8. Mechanical Properties

The mechanical properties of a sample can be tested using a universal testing machine (UTM). This machine is used to test the tensile stress and compressive strength of materials. UTM can carry out many standard tensile and compression tests, such as tensile tests, compression tests, peel tests, bend tests or puncture tests.

The tensile test consists in clamping a sample on each of its ends and pulling it apart until it breaks. Thus, the machine measures tensile properties of the sample: its strength (the tensile strength), its stretch (the elongation) and its stiffness (the tensile modulus).

Thus, the tensile properties of the *X*VP/*Y*BA-*Z*C samples were analyzed using a Hounsfield H10KM Universal Testing Dynamometer (see **Figure 3.20**). Strips were cut from the polymer films with 5 mm of width, 30 mm of length, and 100-120 μm of thick. The samples were weighed and dried in an air circulating oven at 363 K for 1h. This process was repeated until reaching constant weight. Then they were measured at 303 K with an extension rate of 5 or 10 mm·min^{-1} and a gauge length of 10 mm. At least six samples were tested for each polymer in order to average the data obtained.

Figure 3.20. Picture of a Hounsfield H10KM Universal Testing Dynamometer.

On the other hand, DMA allows measuring the mechanical properties of a sample as a function of time and temperature. The DMA measures mechanical stiffness (modulus) and

energy absorption by subjecting a specimen to oscillating mechanical stress or strain within the linear viscoelastic region. Thus, DMA imposes a small cyclic strain on a sample and measures the resulting stress response, or equivalently, it imposes a cyclic stress on a sample and measures the resultant strain response. There is a difference between the oscillatory input applied (stress or strain) to the sample response (strain or stress) measured. This difference is represented by the phase angle δ or phase shift between the input and the response (see **Figure 3.21**) (Menczel, et al., 2009). Materials respond to the applied field (stress or strain) by dissipating the input energy in a viscous flow (non-reversible response), by storing the energy elastically (reversible response), or through a combination of both of these two extremes. Thus, since the modulus is stress/strain, the complex modulus (E^*) can be calculated. From E^* and the measurements of δ, the storage modulus (E′) and loss modulus (E″) can be calculated:

$$\begin{aligned} E^* &= stress/strain \\ E' &= E^* \cdot \cos\delta \\ E'' &= E^* \cdot \sin\delta \\ \tan\delta &= E''/E' \end{aligned} \tag{3.9}$$

E′ is the storage modulus and is related to the samples stiffness. E″ is the loss modulus and is the viscous component, which is related to the samples abilitiy to dissipate mechanical energy through molecular motion. The tangent of phase difference, or tan δ is another common parameter that provides information on the relationship between the elastic and inelastic component. These parameters can be calculated as a function of time, temperature, frequency, or amplitude (stress or strain) depending on the application.

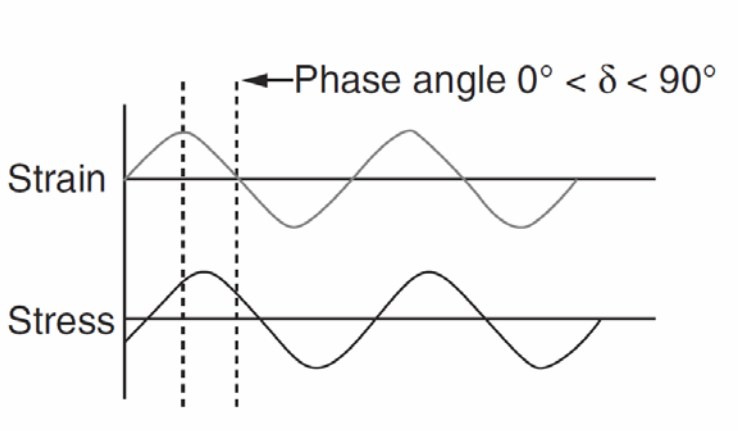

Figure 3.21. Basic principle of DMA technique. In this example, a sinusoidal strain is applied to a sample and the resulting sinusoidal stress is measured.

DMA is used both to study molecular relaxation processes in polymers and to determine inherent mechanical or flow properties as a function of time and temperature. The usual applications of DMA are to study: glass transition, secondary transitions, crystallinity, molecular mass/crosslinking, phase separation, composites, physical and chemical aging, curing of networks, orientation effect of additives (Menczel, et al., 2009).

DMA is technique very similar to DRS. DMA and DRS results, obtained in the same frequency range, are usually compared. Since the DMA has a narrower width of the frequency window available (broadest range 1 mHz- 1 kHz), dielectric analysis can add information on certain physical properties at much higher frequencies.

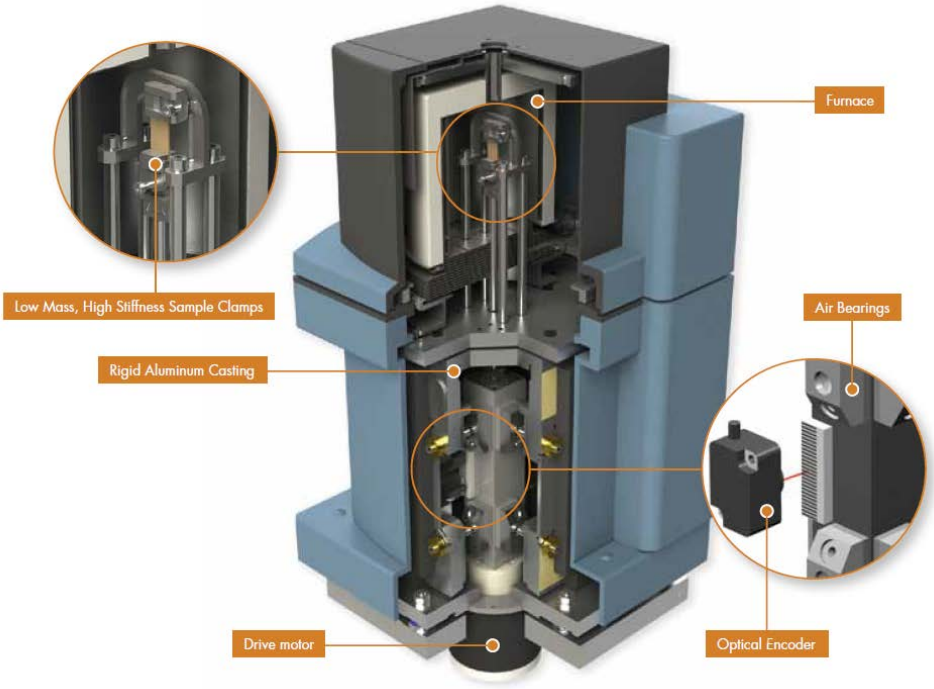

Figure 3.22. Picture of the different parts of a TA Instruments DMA Q800. Taken from TA Instruments.

The Dynamic Mechanical Analyser used in this thesis was a TA Instruments DMA Q800 (see **Figure 3.22** and **Figure 3.23**). The DMA Q800 is composed of different parts: (i) a non-contact drive motor, used to provide the oscillatory or static force required; (ii) rectangular air bearing slides, which receive directly the force from the non-contact drive motor; (iii) a high resolution linear optical encoder, used to measure displacement on the DMA Q800; (iv) a rigid aluminium casting, within which the drive motor, the air bearing slide assembly with optical encoder and air bearing are all mounted at a controlled temperature; (v) low mass, high stiffness sample clamps, which provide multiple modes of deformation; (vi) a furnace with automated movement, which combined with the Gas Cooling Accessory, provides efficient and precise temperature control.

Among all the different modes of deformation provided by the DMA Q800, the tension mode was the configuration used in this thesis. In this mode, the sample is placed in tension between a fixed and moveable clamp. In oscillation experiments, the instrument uses different methods for applying a static load to prevent buckling and unnecessary creep.

DMA of *60*VP-*40*BA sample was performed on molded probes of 6.5×8×0.09 mm, over the temperature range from 123 K to 413 K. Sample was dried in an air-circulating oven at 318 K for fifteen days in order to remove moisture or low molecular weight compounds and also was heated in the DMA oven, at 393 K for 10 minutes before the measurements. Measurements were carried out at 1 K ·min^{-1} heating rate, at frequencies of 0.3, 1, 3, 10 and 30 Hz.

DMA of the PUPH/EG composites was performed in a temperature range from 173 K to 453 K by using rectangular samples of dimension 16.54×6.00×0.25 mm. Measurements were carried out at 3 K·min^{-1} heating rate and at a frequency of 1 Hz.

Figure 3.23. Picture of the TA Instruments DMA Q800 (left) and the tension mode clamp used in the measurements (right).

Chapter 4:

Characterization of cross-linked Vinylpyrrolidone-Butyl Acrylate Copolymers

Results presented in this Chapter were published in: B. Redondo-Foj, M. Carsí, P. Ortiz-Serna, M. J. Sanchis, F. García and J. M. García, *J. Phys. D: Appl. Phys.,* vol. 46, pp. 295304-295315, **2013**. and B. Redondo-Foj, M. Carsí, P. Ortiz-Serna, M. Sanchis, S. Vallejos, F. García and J. García, *Macromolecules,* vol. 47(15), p. 5334–5346, **2014**.

Abstract

Poly(vinylpyrrolidone-co-butyl acrylate) samples with different proportions of monomers were prepared as tractable and hydrophilic materials. An analysis of the intermolecular interactions between the polymer groups was carried out by FTIR. The dependence of the C=O bands (lactam and pendant butyl ester) with the composition suggests a strong interaction between the lactam groups. They exert an important influence in the molecular mobility, which was studied by DSC, DRS and DMA. A single narrow glass transition temperature (T_g) is observed in each random copolymer, consistent with a single phase of low compositional nanoheterogeneity. The dependence of the T_g with the composition suggests significant interactions between polymer components. The dielectric and mechanical spectra show γ, β and α relaxations in increasing order of temperature, followed by conductive contributions. The apparent activation energies for secondary relaxations have similar values for all the samples. The γ process is related to the local motions of the butyl units and the β process is a Johari–Golstein secondary relaxation that is related to the local motions of the pyrrolidone group together with the motion of polymer backbone segments. The *dc* conductivity (σ_{dc}) was observed to increase with VP content. The temperature dependence of σ_{dc} followed a VFTH-like behavior, indicating that this process is governed by both the free volume and temperature. The temperature dependence of the decoupling index showed a decoupling of the segmental motion form the charge carrier motions at temperatures near glass transition

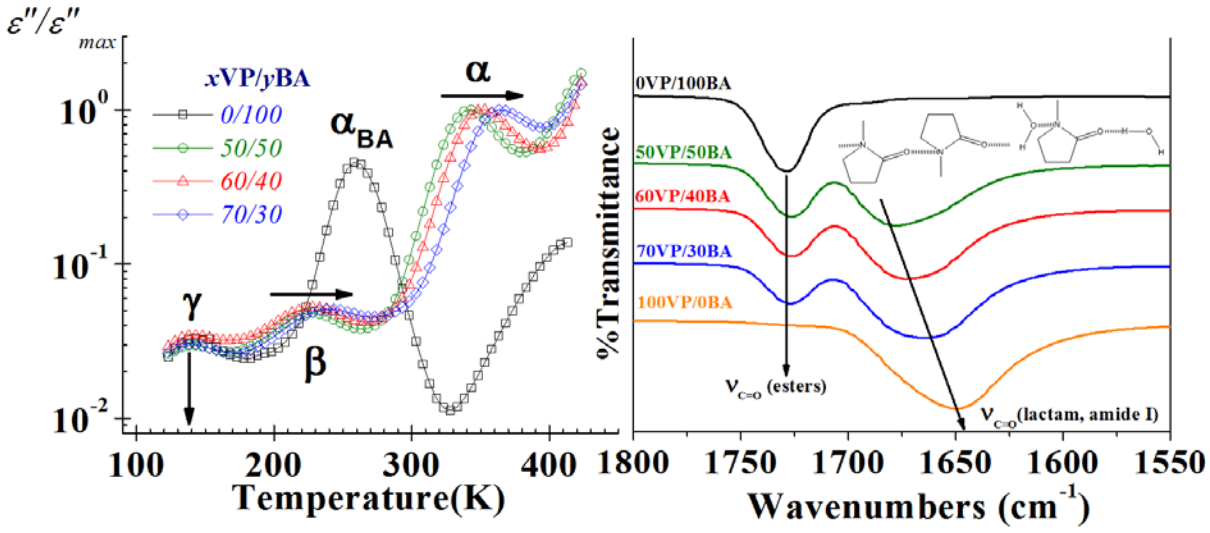

4. Characterization of cross-linked Vinylpyrrolidone/Butyl Acrylate Copolymers

4.1. Introduction

N-Vinyl-2-pyrrolidone (VP) is a cheap and widely available chemical, prepared industrially from acetylene and formaldehyde following the Reppe´s procedure (Reppe, 1954; Bühler, 2005). VP is a high boiling point liquid (365-368 K at 1.3 kPa), highly miscible in water and in organic solvents, and with other vinyl or acrylic monomers. VP linear polymerization, either in bulk, in solution or in suspension, gives rise to linear polyvinylpirrolidone (PVP). PVP is also known as Povidone, an amphiphilic polymer soluble in water and in polar organic solvents but insoluble in esters, ethers, ketones and hydrocarbons (Haaf, et al., 1985). It cannot be melt processed due to its low decomposition temperature. Its T_g reaches a constant value (approximately 448 K) when its average molecular weight is 100000 $g \cdot mol^{-1}$ (Tan, et al., 1976). The films prepared from PVP solution are brittle, clear and glossy. Its popcorn polymerization, *i.e.*, proliferous polymerization, gives rise to highly cross-linked PVP, called Crospovidone, completely insoluble, and of the great industrial importance. Both, linear and cross-linked PVP have a wide range of applications. Due to its biocompatibility, PVP is used in pharmacological and biomedical applications. Furthermore, it is also used in numerous industrial fields like adhesives, ceramic, coatings, food, etc (Bühler, 2005; Haaf, et al., 1985).

The relation between the structure of polymers and their properties has been widely studied in the literature. In this way, the copolymerization is presented as an effective

method to prepare macromolecules with specific chemical structures and to control some properties such as hydrophilic/hydrophobic balances, solubility, polarity, etc (Gallardo, et al., 1999). Hence, copolymers have attracted a great attention because they can be frequently used to tune the properties of a material between those of the corresponding homopolymers. Copolymers comprised of VP and acrylic or vinyl comonomers are commercially produced to modify, to improve and to adapt the properties of PVP to specific applications. In the same way, the water affinity of the PVP, or even the water solubility, which can be too high for certain applications, has been reduced by copolymerizing with vinyl acetate or vinyl propionate (Haaf, et al., 1985; Grigoraş, et al., 2008). Thus, acrylic chemicals are among the most versatile and inexpensive comonomers to prepare materials with specific properties.

The dynamic mechanical and dielectric properties are intrinsically correlated and they are associated with a structural polymer feature (McCrum, et al., 1991; Sanchis, et al., 1999; Carsí, et al., 2012; Carsí, et al., 2013; Deutsch, et al., 1954). The dynamic relaxation properties of cross-linked polymer networks are highly sensitive to network composition and polymer chain architecture. The cooperative segmental motions (T_g) and the more localized processes observed below T_g, can be dramatically affected by (i) changes in the backbone structure, (ii) crosslink density, or (iii) the introduction of pendant groups or branches. One of the most powerful and versatile methods for the study of molecular dynamics in polymer networks is the dielectric relaxation spectroscopy (DRS) (Kalakkunnath, et al., 2007). DRS is now widely used to investigate molecular dynamics of copolymers and nanocomposites (Kremer, et al., 2003).

Thus, in this thesis PVP-based copolymers have been prepared and characterized using the highly hydrophobic butyl acrylate as comonomer in different molar proportion. Some reasons for the use BA as the comonomer are: (i) the VP/acrylic copolymers have a known chemical microstructure, in terms of triad and tetrad composition sequences (Brar, et al., 2002; J. Mol. Struct., 2002); (ii) BA is fully miscible with VP; (iii) BA is a highly hydrophobic monomer which counterbalances the highly hydrophilic character of VP and (iv) the BA homopolymer is an extremely soft material (Miller, 1999), with T_g = 219 K, which permits to modulate the characteristic brittleness of VP homopolymer, thus obtaining more tractable materials.

The main aim of this chapter is to study the *X*VP/*Y*BA copolymer family behavior regarding several parameters, which permits to establish the structure-properties relationship and to optimize the performance according to a needed application. Thus, this chapter is focused on the analysis of the chemical and physical properties of a series of novel *X*VP/*Y*BA copolymer samples using several experimental techniques. In this part of the thesis, an in-depth comparative analysis between different characterization techniques and copolymer compositions is carried out.

4.2. Results and discussion

4.2.1. Sample hydrophilicity characterization

A gel is defined as a cross-linked polymeric or copolymeric network, which is characterized by a remarkable ability to absorb a considerable quantity of liquid up to swelling equilibrium, without being dissolved. When the swollen liquid is water, the gel

polymer is called hydrogel (Wichterle, 1971). On the other hand, when a hydrogel is dried, it is called xerogel, or simply a dried hydrogel. Thus, the gel polymer can be insoluble due to the presence of chemical or physical cross-links. The water swelling depends on the chemical composition and also on the cross-linking density. The higher the number of the hydrophilic groups, the higher the water holding capacity is. However, an increase in the cross-linking density produces a decrease in the swelling equilibrium.

Therefore, the hydrophilic character of the materials is related to the water uptake at given conditions. The water swelling percentage (WSP) was evaluated by means of dipping the samples in pure water at 293 K till constant weight. The WSPs of the samples are intimately related to the molar ratio of hydrophilic to hydrophobic monomers comprising the sample (see **Table 4.1**). **Figure 4.1** shows the influence of the VP content, which contains the highly hydrophilic lactam structure, on the WSP.

The influence of water in the physical properties of materials having 2-pyrrolidone moieties will be discussed in the next sections. Moreover, Tan *et al.* developed a study of the T_g depression of PVP in relation to the water uptake (Tan, et al., 1976).

Table 4.1. Film sample characteristics [thickness, water swelling percentage (WSP), and thermal resistance].

			TGA (N_2 atmosphere)	
Sample	**Sample thickness (μm)**	**WSP**	T_5 **(K)**	T_{10} **(K)**
*100*VP/*0*BA	115	> 200	651	668
*70*VP/*30*BA	123	92	623	640
*60*VP/*40*BA	115	60	622	643
*50*VP/*50*BA	111	37	626	640
*0*VP/*100*BA	290	<1	568	605

[#]Extension rate of 5^a or 10^b mm·min^{-1}

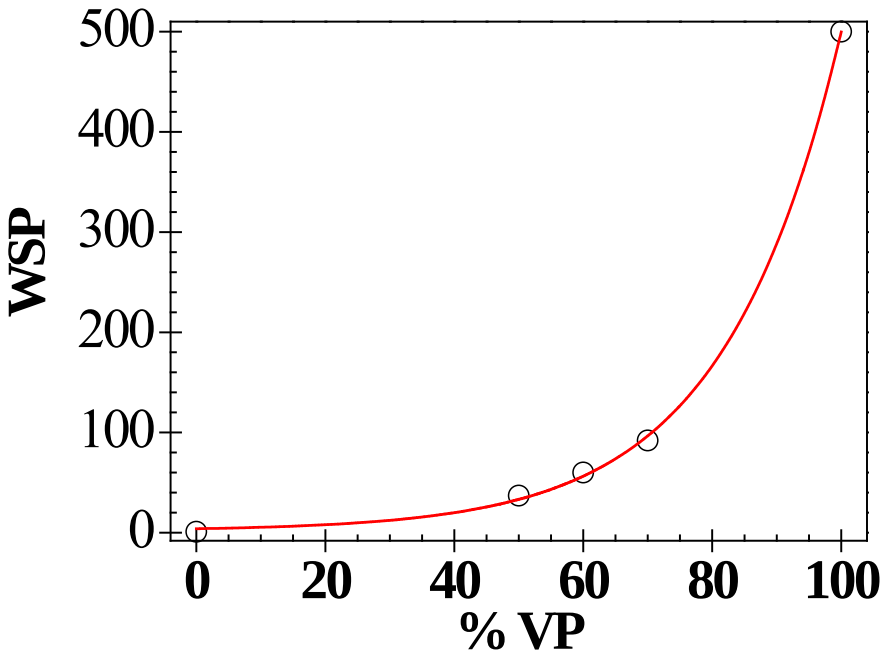

Figure 4.1. Influence of the mole percentage of the hydrophilic VP monomer (%VP) on the hydrophilic character of the samples, *i.e.* water swelling percentage (WSP).

4.2.2. Fourier Transform Infrared Measurements

The samples were used after the conditioning described in the subsection 3.1.1. The FTIR spectra of the *X*VP/*Y*BA samples showed the characteristic absorption bands corresponding to the functional groups present in the chemical structure of the material. The assignment of these bands is depicted in **Figure 4.2 a** and **b**. The band associated with the humidity in the samples is located about 3400 cm^{-1}. As expected, the intensity of this band increases with the VP content. The two $\nu_{C=O}$ bands were ascribed to (i) the majority pendant lactam structure (lower energy band, amide I), and (ii) the pendant butyl ester structure together with the cross-linker agent (higher energy band). According to the FTIR results, the chemical composition influences not only the intensity and energy of these two absorption bands, but also the transmittance ratio between the bands. While the higher

energy band absorption maxima (1727 cm^{-1}) was not affected by the copolymer composition, the absorption maxima of the amide I band shifted to higher energies with BA content. Thus, the amide I ($\nu_{C=O}$) absorption maxima of the *100*VP/*0*BA sample, observed at 1650 cm^{-1}, was shifted to 1678 cm^{-1} for the *50*VP/*50*BA sample. This shift showed a nearly linear correlation with the chemical constitution of the samples, as shown in **Figure 4.2 c**. These facts can be ascribed to the different nature of the ester and amide (lactam) groups. While the former does not establish strong interactions between them, the later establishes relatively strong permanent dipole-dipole interactions (see **Figure 4.3**). Hence, within the *100*VP/*0*BA sample structure there are strong and highly directional dipole-dipole bond interactions in-between the pendant lactam sub-groups (Grigoraş, et al., 2008). Upon random copolymerization, these permanent dipole-dipole interactions are impaired because these groups are moved away from each other giving rise to an increase in the C=O bond strength.

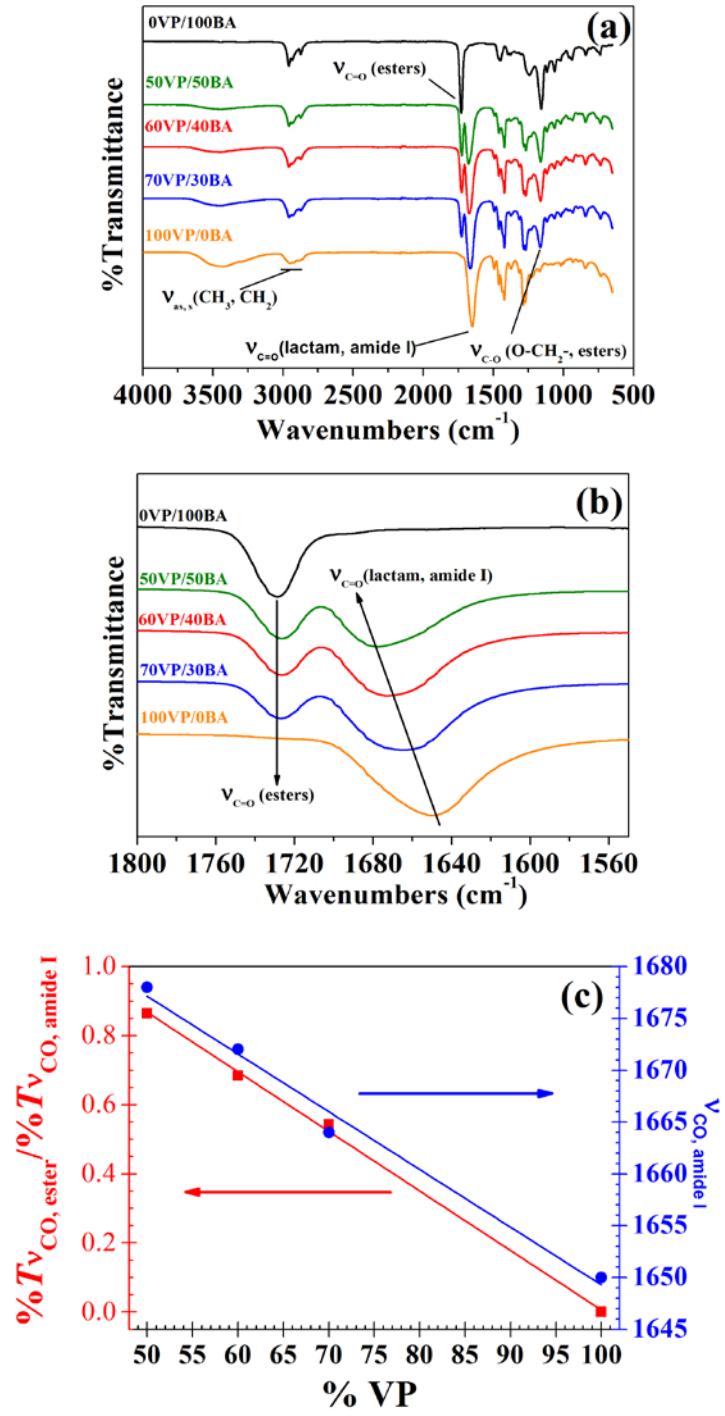

Figure 4.2. (a) and **(b)** Normalized FTIR spectra of the dried samples. **(c)** Correlation between the percentage of VP and: (i) Transmittance ratio of the peaks corresponding to the C=O of the pendant ester and lactam residues and (ii) Maximum wavenumber of the stretching band corresponding to the C=O of the lactam residue.

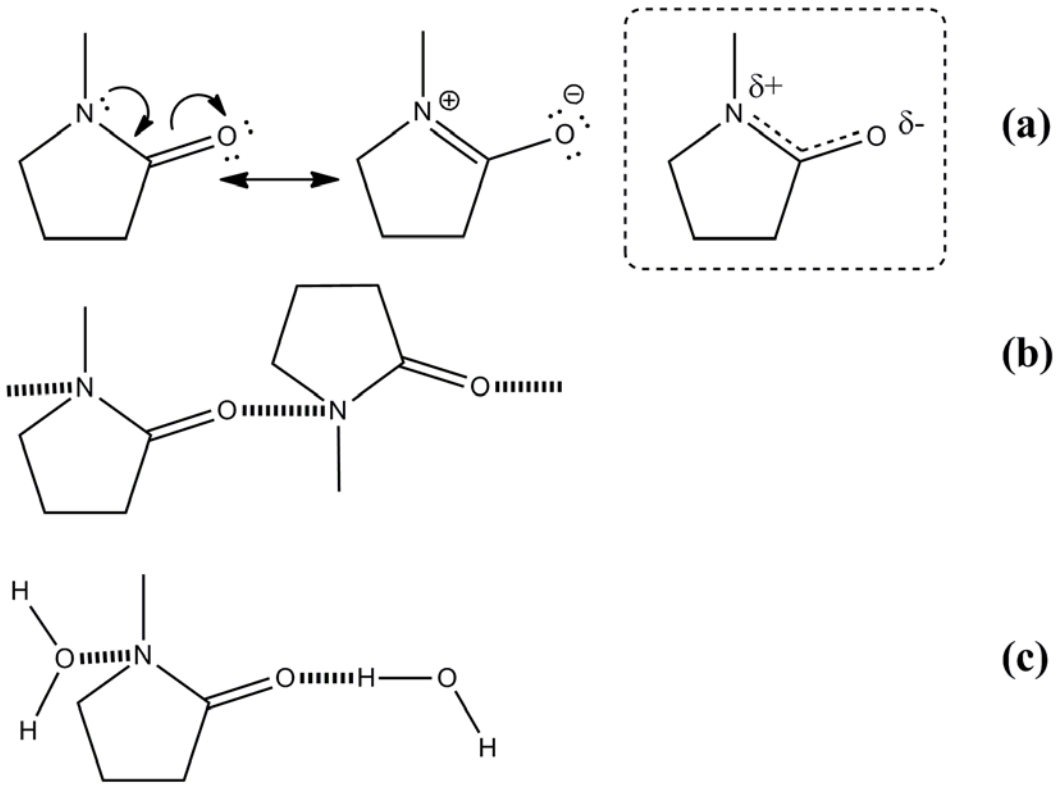

Figure 4.3 (a) Structure of 2-pyrrolidone moieties. **(b)** Model of 2-pyrrolidone/2-pyrrolidone interactions and **(c)** Model of 2-pyrrolidone/water interactions.

In order to deepen into the nature of water/sample interaction of our systems, a FTIR analysis of dry and swollen samples was carried out. Thus, **Figure 4.4a** shows the normalized FTIR spectra of dry and swollen *50*VP/*50*BA sample as an example. The experimental spectrum of water and the simulated spectrum of water *50*VP/*50*BA system are also represented. As it is observed, the $\nu_{C=O}$ (ester) band corresponding to the BA moieties does not shift upon swelling the samples, meaning a negligible interaction with water. On the other hand, the $\nu_{C=O}$ (lactam, amide I) band shifted to lower energy wavenumbers, pointing out a weakening of the C=O bond because of the hydrogen bonds formation with water (**Figure 4.3c**). The shift of this band to lower wavenumbers in the swollen samples, δ, is consistent with the hydrophilic character of the samples (δ = 24, 30

and 32 cm^{-1} for *50*VP/*50*BA, *60*VP/*40*BA, and *70*VP/*30*BA, respectively). This fact is clearly observed in **Figure 4.4b** where the composition *50*VP/*50*BA is represented.

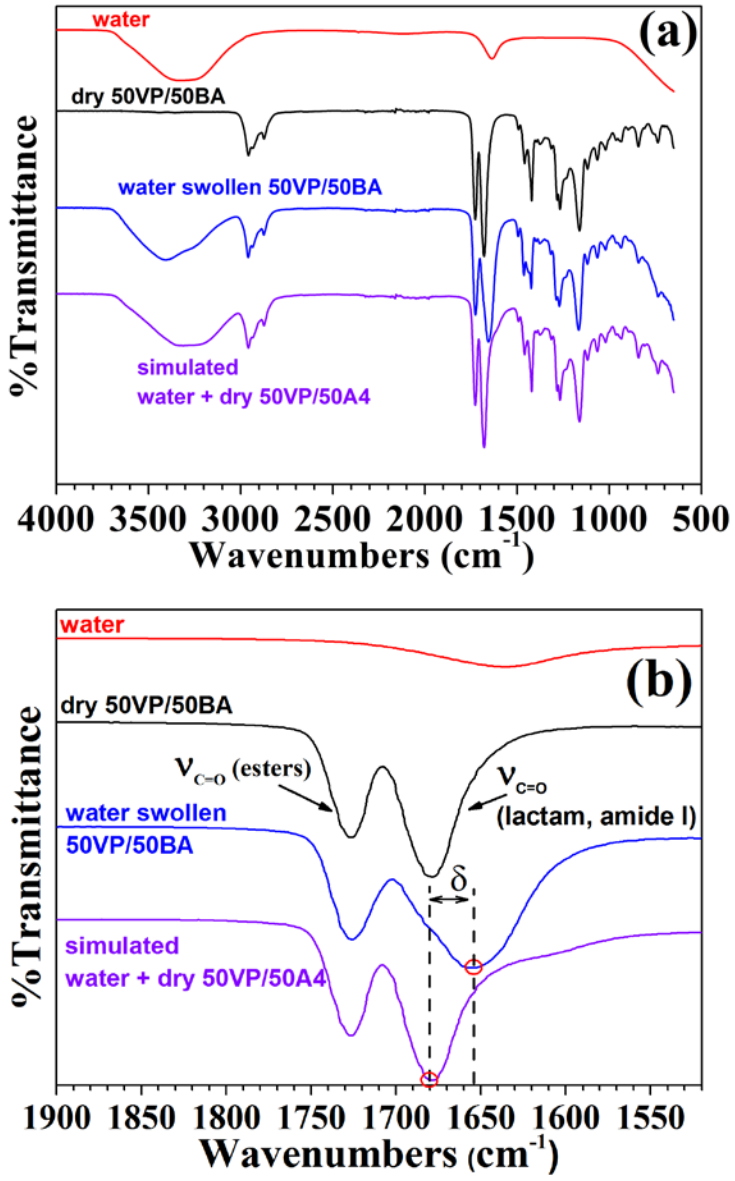

Figure 4.4. Normalized FTIR spectra of **(a)** pure water, *50*VP/*50*BA sample (dry and water swollen), and simulated water swollen FTIR spectra (addition of the water and the water swollen *50*VP/*50*BA spectra) and **(b)** zoom the $\nu_{C=O}$ of ester and lactam, amide I bands

4.2.3. Thermogravimetric analysis

The thermal stability of the *X*VP/*Y*BA samples was evaluated using TGA. **Figure 4.5a** shows the TGA spectra obtained for the *X*VP/*Y*BA samples. **Table 4.1** shows the thermal resistance under dynamic conditions, in terms of the temperature at which a weight loss of 5% and 10% is observed (T_5 and T_{10} respectively). The results clearly show the great influence of the copolymer structure. Thus, the best thermal performance is observed for *100*VP/*0*BA homopolymer, while the worst behavior was obtained for *0*VP/*100*BA homopolymer. This is probably because: (i) the amide bonds are stronger than the ester ones; (ii) the lactam structure is prone to establish relatively strong and highly directional inter and intra-chain dipole-dipole interactions and (iii) thermal breakage of a single bond of the lactam, which is a cycle, do not give rise to the loss of a detectable low-mass fragment.

Figure 4.5b shows the first derivative of the degradation curves ($\Delta_{\text{weight loss}}/\Delta_{\text{time}}$), where the different thermal resistance of the samples can be analyzed. This figure exhibits one peak for the homopolymers and two peaks for the copolymer samples. Each pendant residue gives rise to a well-defined maximum degradation rate. For the copolymer samples, the highest weight loss rate observed at about 673 K corresponds to the degradation of the ester residue and the second one observed about 706 K is attributed to the lactam sub-group degradation.

Figure 4.5c shows the relative weight loss rate of each sub-group (intensity first derivate), which is proportional to the molar rate of these structural units.

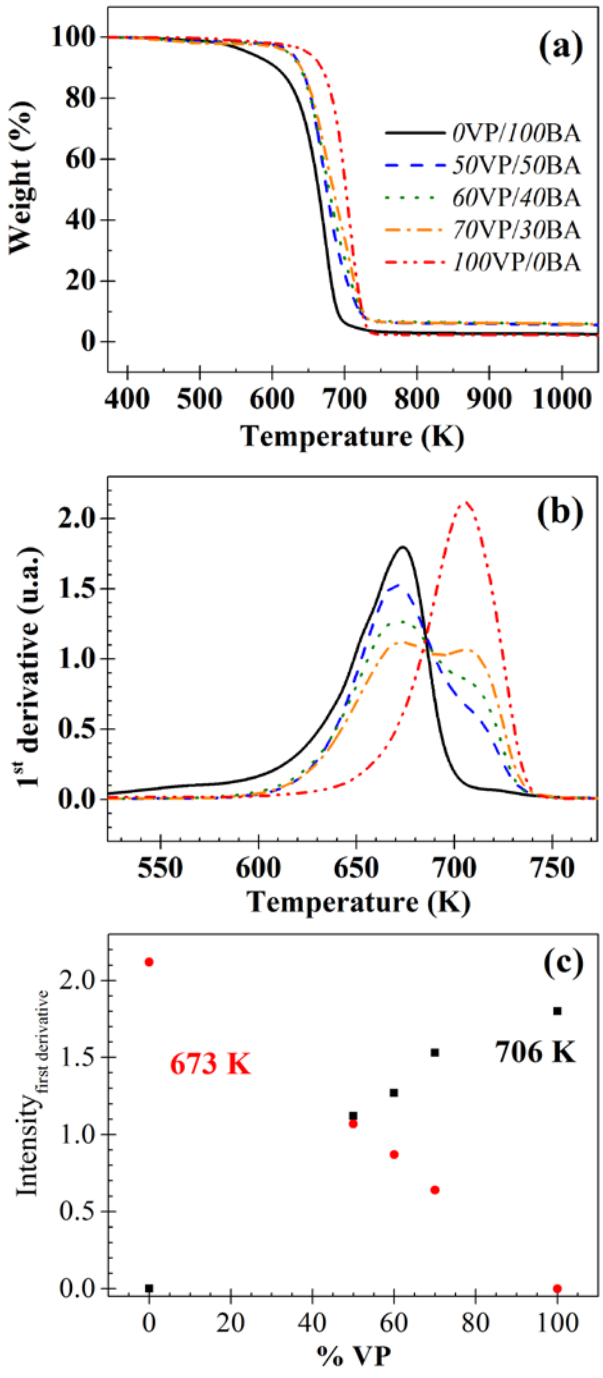

Figure 4.5. (a) TGA curves of the *X*VP/*Y*BA samples (weight loss as a function of the temperature under inert atmosphere, N_2). **(b)** First derivative of the TGA curves ($\Delta_{weight\ loss}/\Delta_{time}$) and **(c)** the % VP *vs.* the maxima intensity of the first derivative at 673 K (circle) and 706 K (square).

4.2.4. Differential scanning calorimetry measurements

The DSC thermograms (reversing curves) obtained for all the samples are plotted in **Figure 4.6**. The characteristic T_g's and their associated heat capacity changes are summarized in **Table 4.2**.

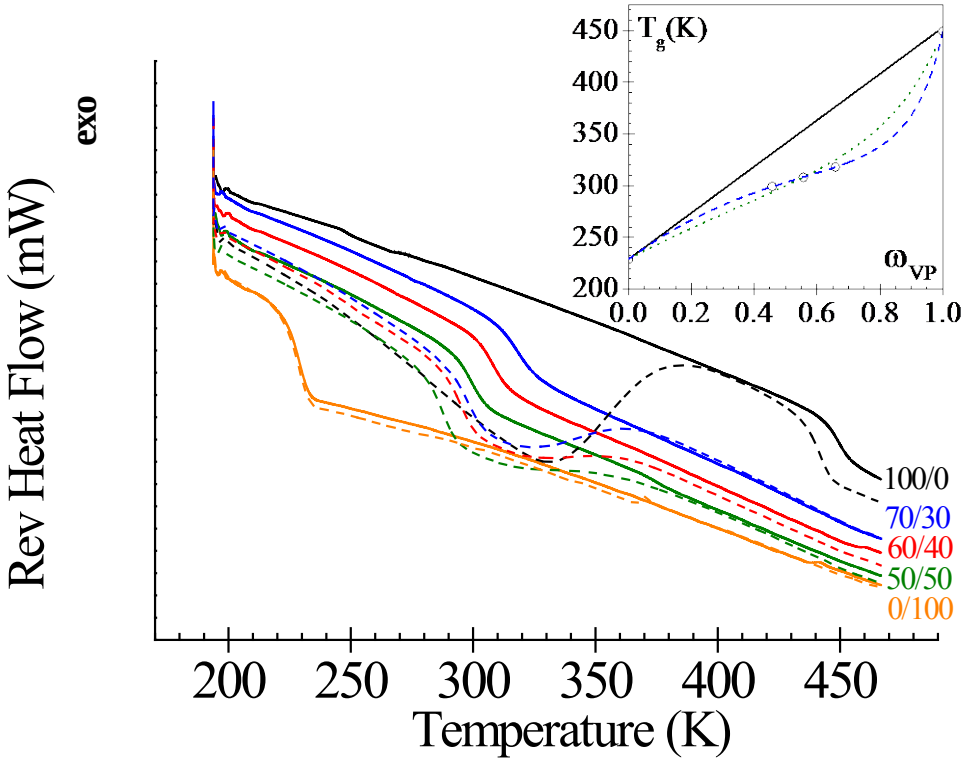

Figure 4.6. DSC experimental curves for *X*VP/*Y*BA samples: (i) 1st heating ramp (dashed lines) and (ii) 2nd heating ramp (continuous lines). Data are vertically shifted for a better visualization. Inset: Experimental T_g as a function of VP content (weight fraction of VP, ω_{VP}) (circle) and T_g values predicted by the behavior based on the simple weight function (—), by the Gordon-Taylor (– –) and by the Kwei (···) equations.

It is well known that hydrophilic polymers can absorb water (moisture) from the atmosphere. Thus, DSC was also used in order to monitor the drying process. Evaporation of the moisture gives rise to a broad endothermic peak in the non-reversing curve. This

peak is quite broad because water evaporation takes place over a wide range of temperatures. The presence of water in polymers is known to act as a plasticizer, decreasing the T_g values. For *X*VP/*Y*BA samples with x=100, 70, 60 and 50, the first heating ramp exhibits this endothermic peak at about 373 K. From the evaporation heat of bulk water (2400 $J \cdot g^{-1}$ at 373 K), the amount of moisture present in samples was estimated. The moisture percentages are collected in **Table 4.2**. As it is observed, the water content increases with the VP content, due to the formation of hydrogen bonds between water molecules and 2-pyrrolidone units (**Figure 4.3c**).

All DSC thermograms present a first step related to the glass rubber transition temperature. Prior to polymerization, the two monomers were visually miscible. Thus, the presence of one T_g in the copolymers is indicative of this miscibility (**Figure 4.6**). The observed step for each sample occurs at lower temperatures in the first heating ramp, due to the plasticizing effect of water. For all the analyzed copolymers, the obtained T_g's range between the homopolymers T_g values. These results obtained for the homopolymers match with the data acquired by conventional DSC, which were published in previous works (Feldstein, et al., 2003; Feldstein, et al., 2000; El-Begawy, et al., 1991; Huglin, et al., 1987; Lee, et al., 1966; John Wiley & Sons, March 2011). The T_g value for the copolymers decreases monotonously with the BA content, as expected due to the plasticizing effect of the butyl units on the *X*VP/*Y*BA mobility. Moreover, according to the FTIR results, the specific permanent dipole-dipole interactions between VP chains probably reduce the available free volume, decreasing the mobility in the *X*VP/*Y*BA samples. The inset of **Figure 4.6** shows the experimental dependence of T_g with the VP content, as well as the values predicted by different models. The most basic model is the so-called simple weight

function, defined as $T_g = \omega_{VP} \cdot T_{gVP} + \omega_{BA} \cdot T_{gBA}$, where T_g, T_{gVP}, T_{gBA} are, respectively, the T_gs of the copolymer sample, VP homopolymer and BA homopolymer and ω_{VP}, ω_{BA} are the corresponding weight fractions. As it is observed in **Figure 4.6**, the experimental behavior was not adequately predicted by this model. The dependence of the T_g with composition in *X*VP/*Y*BA samples shows a negative deviation respect to this simple weight function.

When there are deviations from the simple weight function, several classical equations can correlate and/or predict the dependence between the T_g of a miscible system and its composition. One of them is the Gordon-Taylor equation, $T_g = \frac{\omega_{VP} \cdot T_{gVP} + k\omega_{BA} \cdot T_{gBA}}{\omega_{VP} + k \cdot \omega_{BA}}$ (Gordon, et al., 1952), where *k* is the ratio between the volume expansion coefficients of the homopolymers. Another one is the Kwei empirical equation $T_g = \frac{\omega_{VP} \cdot T_{gVP} + k\omega_{BA} \cdot T_{gBA}}{\omega_{VP} + k \cdot \omega_{BA}} + q \cdot \omega_{VP} \cdot \omega_{BA}$ (Kwei, 1984), where the quadratic term, $q \cdot \omega_{VP} \cdot \omega_{BA}$, is assumed to be proportional to the number of specific interactions between the polymer chains (Kwei, 1984; Anshyang, et al., 1989; Song, et al., 1999). So, the *q* value from the Kwei equation can be used to estimate the strength of the interchain interactions. The values k =7.2± 0.1 and q =189.6± 2.4 of the Kwei equation were determined by the least-square procedure to obtain the best fit to the experimental points. Only the model of Kwei could fit the experimental data, since it takes into account the inter-chain interactions occurring in the samples and supported by the FTIR results. Therefore, the negative deviation of the simple weight function is indicative of interchain interactions, which decrease the mobility of the polymer chains. Negative deviation was already previously encountered in copolymer samples presenting very strong dipoles-dipole and hydrogen

bonding interactions (Kwei, 1984; Slark, 1999; Chee, 1995; Chee, 1991; Chee, 1987; Kwei, et al., 1987; Schneider, 1989).

The width of the glass transition may reflect the magnitude of local compositional fluctuations in the copolymer samples, giving a qualitative implication of the relative homogeneity of the system (Bershtein, et al., 2002). In our case, the broadening of the glass transition ($\Delta T = T_{end} - T_{on}$) is lower for the extreme compositions (homopolymer samples). However, for the intermediate compositions, ΔT is only slightly higher and increases with the VP content. This broadening of the glass transition is due to small-scale compositional fluctuations in the copolymer.

On the other hand, the heat capacity jump at T_g, ΔC_p, for the *X*VP/*Y*BA copolymer samples ranges between the ΔC_p values of the homopolymers. Moreover, these values are similar to that obtained for the *100*VP/*0*BA sample. As T_g, the ΔC_p versus composition showed negative deviation from the linear behavior. This tendency has been observed in systems which exhibit segmental interactions (Anshyang, et al., 1989; Chee, 1995). Thus, the composition dependence of the ΔC_p can be related to the presence of orderly packing of polymer molecules, which lowers the mobility at T_g. The ΔC_p value might include enthalpy contribution from the breaking of dipole-dipole bonds during heating.

Table 4.2. Characteristic Temperatures, Heat Capacity Change and Moisture of *X*VP/*Y*BA samples.

	***0*VP/*100*BA**	***50*VP/*50*BA**	***60*VP/*40*BA**	***70*VP/*30*BA**	***100*VP/*0*BA**
T_g^{DSC}, K	229	299	308	318	449
T_{on}, K	223.78	293.49	301.76	309.97	443.72
T_{end}, K	232.87	304.47	314.87	326.21	453.83
ΔT, K	9.09	10.98	13.11	16.24	10.11
ΔC_p, J·(g·K)$^{-1}$	0.2751	0.1634	0.1627	0.1588	0.1572
$T_g^{DRS}, K(\tau = 100s)$ [#]	218	292	298.6	315.6	–
Moisture (%)	0.0	3.0	3.8	6.3	12.2

[*]Values of Characteristic temperatures and heat capacity change corresponding to the 2nd heating ramp.
[**]Percentage of moisture corresponding to the 1st heating ramp.
[#] At which τ_{max} (α^{DRS}) = 100s For *0*VP/*100*BA homopolymer, the value was taken of D. Fioretto, A. Livi, P.A. Rolla, G. Socino, L. Verdini, 1994 *J. Phys.: Condens. Matter* **6** 5295-5302

4.2.5. Dielectric measurements

Figure 4.7 shows the temperature and frequency dependence of the dielectric permittivity and loss factor for the *X*VP/*Y*BA copolymer samples. For all samples, the dielectric permittivity ε' displays the same pattern for all isochrones. It is observed a low temperature step associated with the glass rubber transition, or α relaxation process, followed by an important increase of the permittivity. This increase is related to the electrode polarization (EP), coming from the accumulation of charges at the electrode-polymer interface.

On the other hand, the dielectric loss factor spectra clearly present two relaxation zones. In the low-temperature zone, it is observed two secondary relaxations, labeled as γ

and β processes, presumably associated with local side chain motions. In the high-temperature zone, the spectra present an ostensible α relaxation and a process associated with the EP conductivity phenomenon.

As previously introduced in the Chapter 1 of this thesis, the analysis of the dielectric spectra, in the frequency domain, was made by using the empirical equation of Havriliak-Negami (HN) (Havriliak, et al., 1967; Havriliak, et al., 1966; Havriliak, et al., 1997), which relates the complex permittivity (ε^*) to the frequency by Eq. (1.23). For secondary absorptions, the b_{HN} parameter is equal to one. The fit was carried out in two different zones in order to facilitate the characterization of the dipolar and conductive processes. As examples, the deconvolution procedure of the three copolymer samples is depicted in **Figure 4.8** to **Figure 4.10** for the low (conductivity and α processes) and high (β and γ processes) frequency zones.

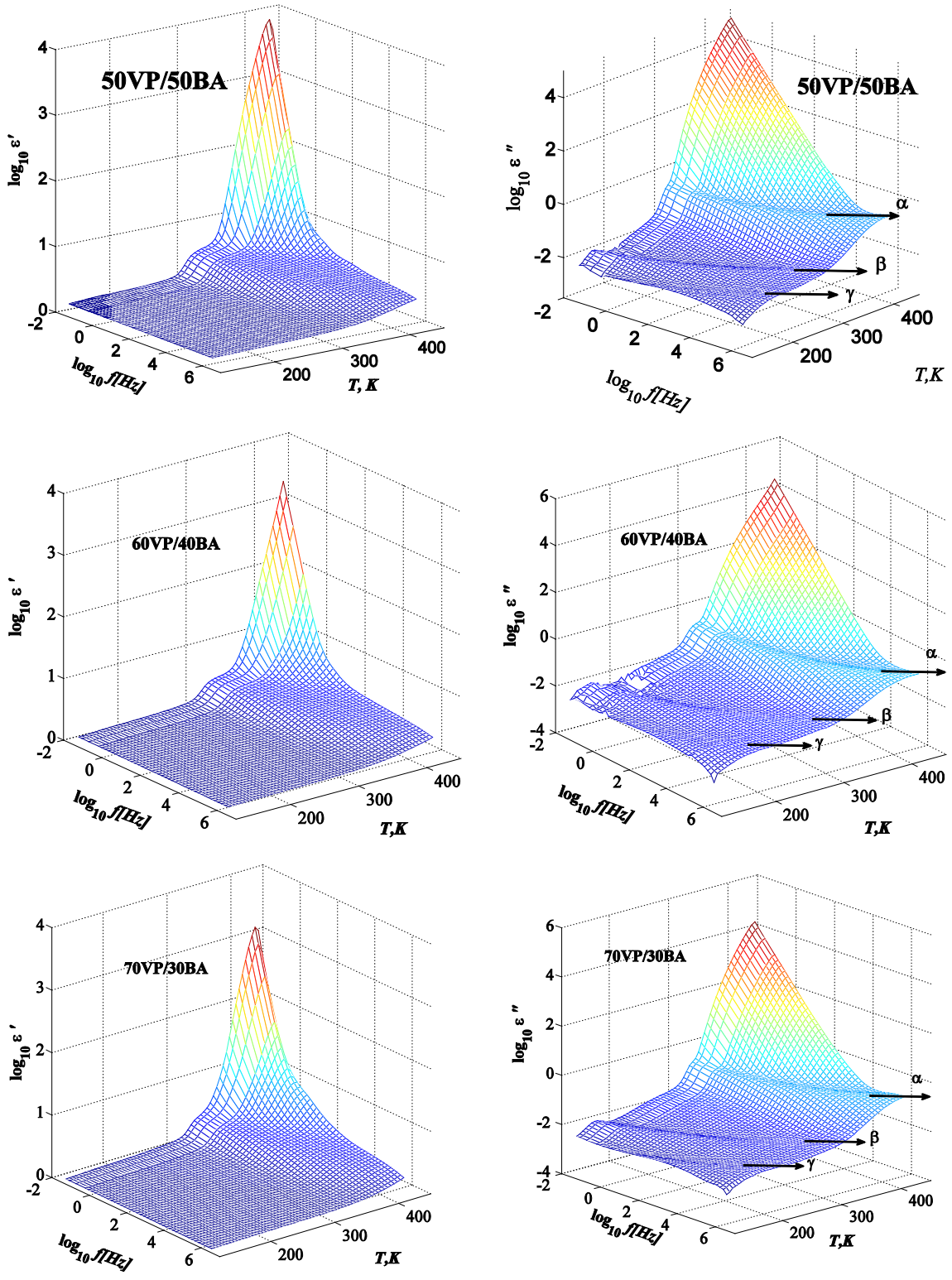

Figure 4.7. 3D representation of the dielectric permittivity of *x*VP-*y*BA copolymer samples in the temperature range of 423 K to 123 K at 5 K steps.

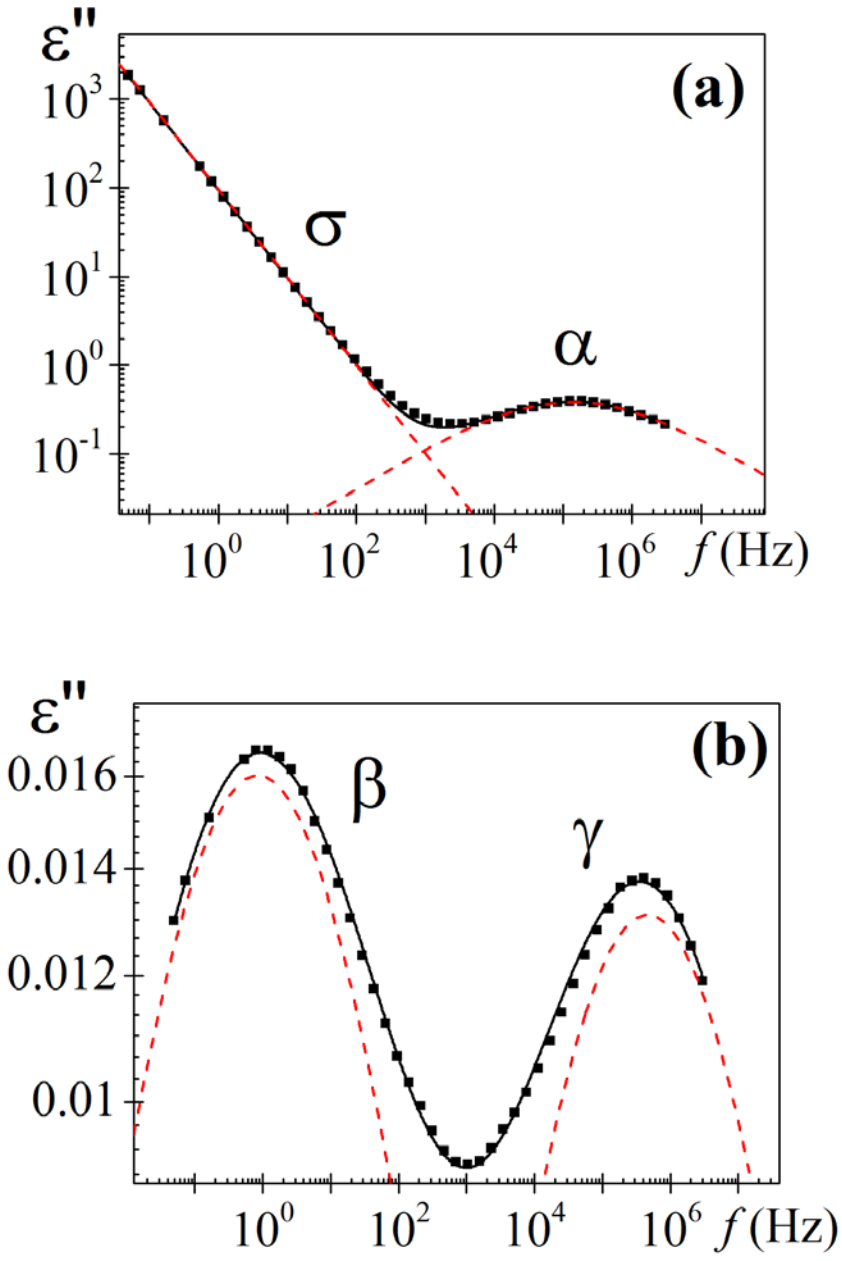

Figure 4.8. Deconvolution of loss factor for *50*VP/*50*BA **(a)** conductivity and α processes at 363 K; and **(b)** β and γ processes at 163 K. Squares represent the experimental data, continuous line the HN fitting curve, and dashed lines the individual processes.

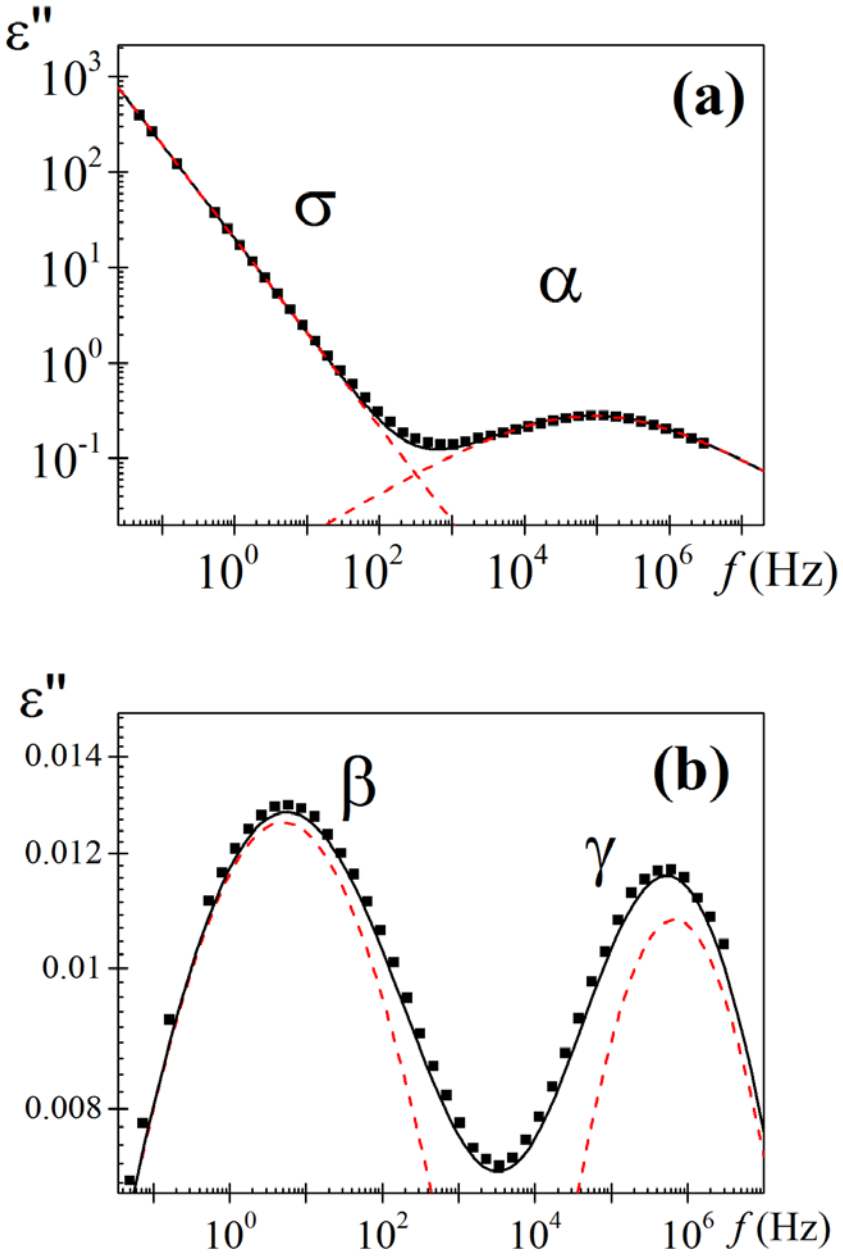

Figure 4.9. Deconvolution of loss factor for *60*VP/*40*BA **(a)** conductivity and α processes at 368 K; and **(b)** β and γ processes at 173 K. Squares represent the experimental data, continuous line the HN fitting curve, and dashed lines the individual processes.

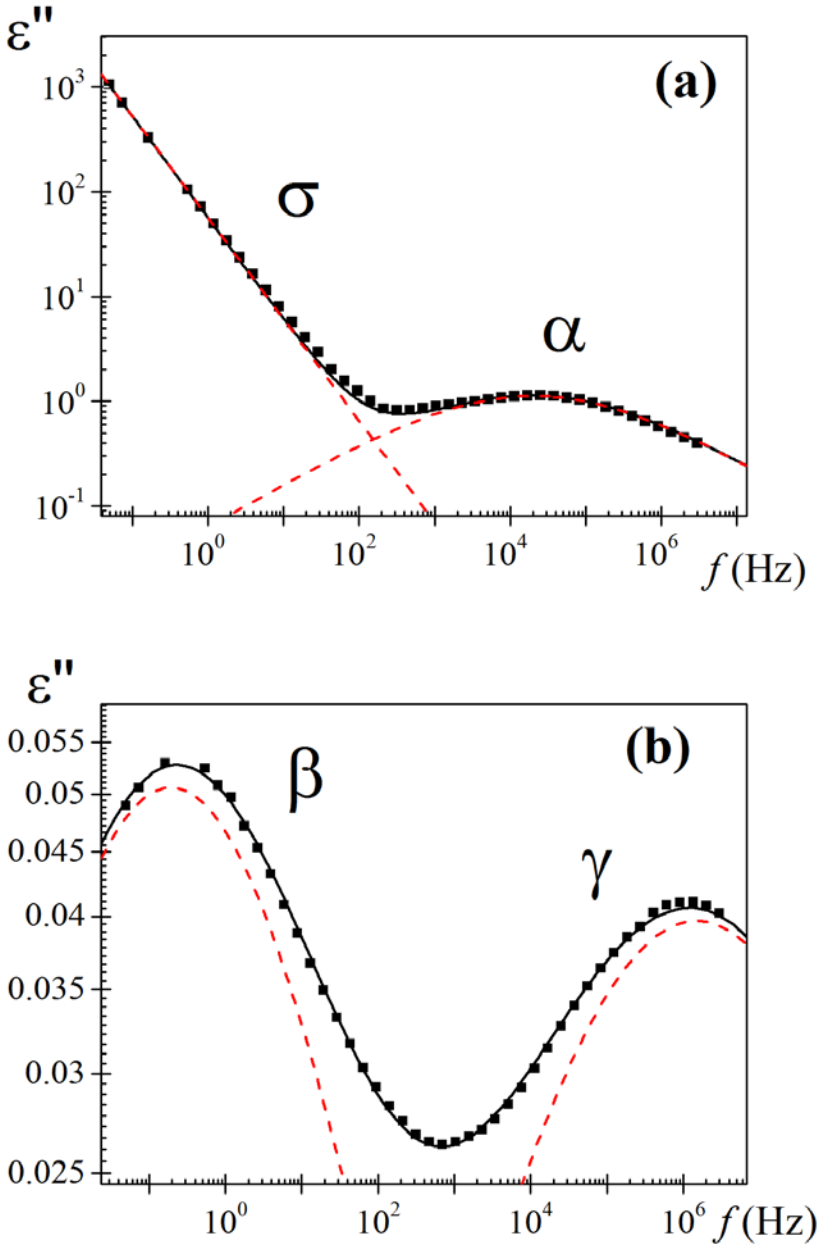

Figure 4.10. Deconvolution of loss factor for 7*0*VP/3*0*BA **(a)** conductivity and α processes at 368 K; and **(b)** β and γ processes at 163 K. Squares represent the experimental data, continuous line the HN fitting curve, and dashed lines the individual processes.

In the high frequency zone, an additive rule for the permittivity was assumed for the analysis of the dielectric loss spectra of the secondary processes (Donth, 1996).

$$\varepsilon''_{dip}(\omega) = \mathrm{Imag}\left[\sum_{i=1}^{2} \frac{\Delta\varepsilon_{HN,i}}{\left[1+\left(i\omega\tau_{HN,i}\right)^{a_{HN,i}}\right]^{b_{HN,i}}}\right] \tag{4.1}$$

The HN parameters of the two secondary relaxations were determined at several temperatures from a multiple non-linear regression analysis of the experimental data. The three characterizing peak parameters ($\Delta\varepsilon_{HN,i}$; $\tau_{HN,i}$; $a_{HN,i}$) were allowed to vary and are plotted in **Figure 4.11** to **Figure 4.13**.

In the high temperature zone, where the conductive process is dominant, we have included a new term in order to characterize the spectra: $\varepsilon^*(\omega) = \varepsilon^*_{dip} + \varepsilon^*_{cond}$ with $\varepsilon^*_{cond} = \left(i\sigma/e_0\omega\right)^s$ where e_0 is the permittivity of free space (e_0= 8.854 pF·m^{-1}), σ is the conductivity arising from charges transport at the liquid-electrode interface and s is a constant ($s \leq 1$). The fit parameters determined at several temperatures from a multiple nonlinear regression analysis are summarized in **Figure 4.11** to **Figure 4.13**.

Figure 4.11 shows the temperature dependence of the shape parameters associated with all relaxation processes present in the *X*VP/*Y*BA samples. The a_{HN} parameter is a function of temperature and composition. For the α relaxation, the value of a_{HN} parameter increases with temperature, which is an indication of the decrease of the homogeneity. The shape parameters of the *0*VP/*100*BA homopolymer were taken of the Fioretto paper (Fioretto, et al., 1994). The a_{HN} parameter values increase with the VP content, but they are similar after normalization by $T_{ref}=T_g$ (inset **Figure 4.11**). This is an indication of both, the

homogeneity and the insignificance of the concentration fluctuation effect on the *X*VP/*Y*BA series. Moreover, the value of b_{HN} parameter was near one at all temperatures investigated for the copolymer samples. Thus, the Eq. (1.23) reduces to the Cole-Cole equation (Cole, et al., 1941) that describes a relaxation with a symmetric distribution of relaxation times. For amorphous polymers, a non-symmetric distribution of times is expected for the α relaxation, associated with macromolecular segmental motion at temperatures immediately above the T_g. But for semi-crystalline polymers and more generally for heterogeneous systems, a symmetrical distributions were observed for the α relaxation processes (Boyd, 1985; Laredo, et al., 2003; Huo, et al., 1992; Noda, 2005; J. Polym. Sci. Part B Polym. Phys., 2003; Janik, et al., 2001; Feldman, et al., 2002; Ortiz-Serna, et al., 2010; Ortiz-Serna, et al., 2011). This symmetric distribution can be due to the fact that dipole fluctuations associated to slower mechanisms than the segmental relaxation can be presented.

On the other hand, the a_{HN} parameter for the β process is very similar for all *X*VP/*Y*BA copolymers samples, and slightly decreases with the increase of temperature. Finally, for the γ process, the a_{HN} parameter increases with temperature.

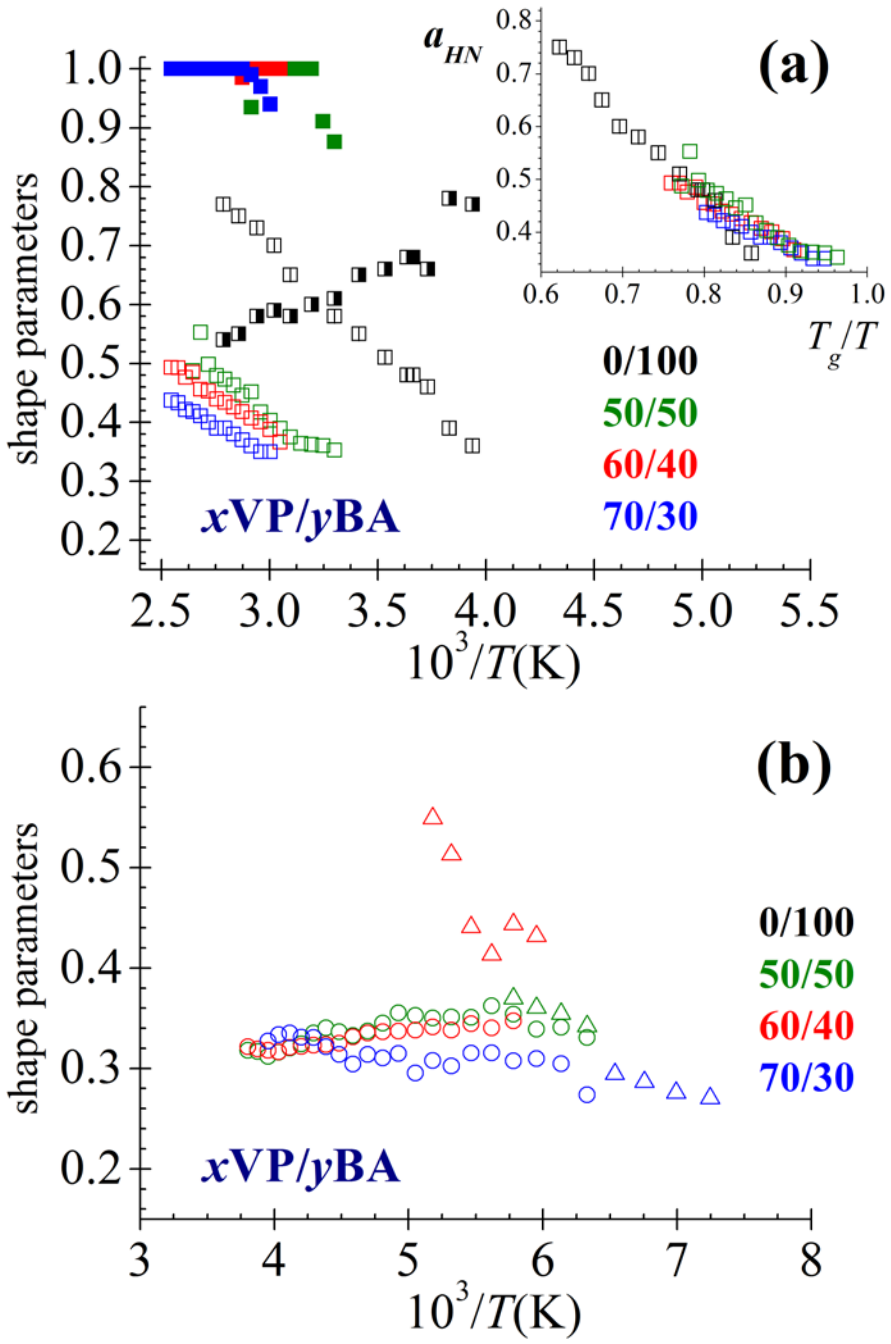

Figure 4.11. **(a)** Temperature dependence of the shape parameters a_{HN} (open symbol) and b_{HN} (full symbol) for α relaxation (squares). For the *0*VP/*100*BA: a_{HN} (◫) and b_{HN} (◨). Inset: a_{HN} parameter for α process as a function of normalized temperature [T_g is the temperature which the $\tau_{max}(\alpha)$=100 s]. **(b)** Temperature dependence of the shape parameter a_{HN} for β (circles) and γ (triangles) relaxations.

The temperature dependence of the relaxation strength is shown in **Figure 4.12**. For β and γ processes this dependence follows the classical trends, that is, the dielectric strength increase or nearly remain constant with the temperature. This fact is consistent with a thermally activated mechanism because the dipole mobility rises with the temperature, associated with the free volume increase. Non-significant changes in the dielectric strength for the β and γ absorptions with the composition are observed. Nevertheless, the α relaxation strength decreases with temperature. The thermal energy disturbs the alignment of the molecule dipoles that intervene in the cooperative motions and give rise to the relaxation. One should expect that the dielectric strength increases with VP content, reflecting the increasing polarity of the polymer chains. However, the experimental trend of the dielectric strength is at odds with this last assumption. This behavior can be related to the reduction in the molecular mobility as the VP content increases. As mentioned before (FTIR results), the mobility impairment can be caused by the presence of dipole-dipole interactions between the lactam groups present in the structural unit of VP.

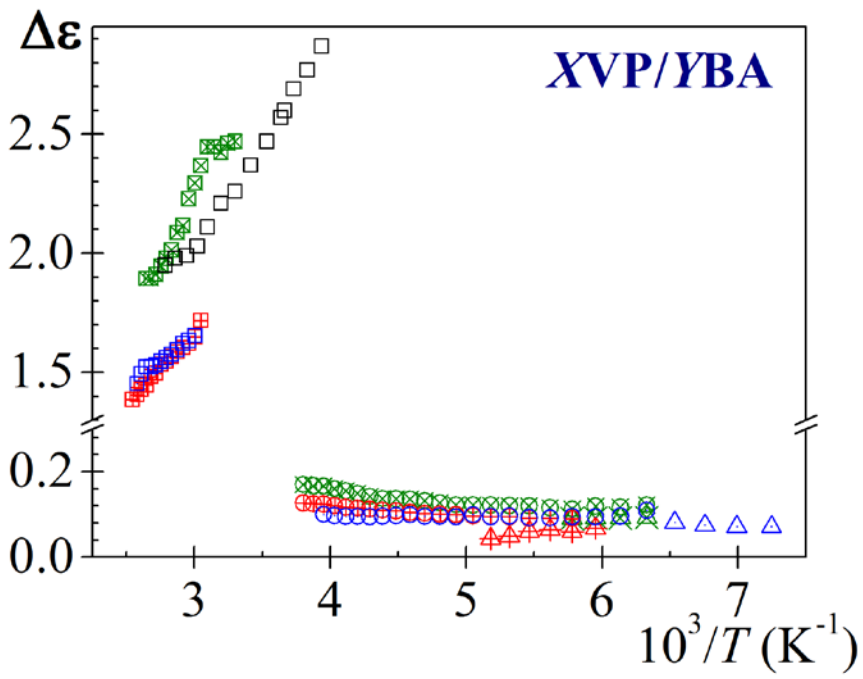

Figure 4.12. Temperature dependence of the strengths of the α (squares) (50/50 (⊠), 60/40 (⊞), 70/30 (⊡),100/0 (□)), β (circles) (50/50 (⊗), 60/40 (⊕), 70/30 (○))and γ (triangles) (50/50 (⊠), 60/40 (⊞), 70/30 (△)) relaxations of *X*VP/*Y*BA samples

The temperature dependence of the relaxation times, which is associated with the peak maxima of the primary and secondary absorptions, is shown in **Figure 4.13a**. According to our results, the increase of VP content results in an increase of the T_g and segmental relaxation times of the *X*VP/*Y*BA samples. As usual, the average relaxation time associated with the α relaxation is described by VFTH equation (Eq. (1.2)) (Riande, et al., 2004; Vogel, 1921; Fulcher, 1925; Tamman, et al., 1926; Lunkenheimer, et al., 2000). Values of the τ_0, T_v and D_0 parameters that fit Eq. (1.2) to the experimental results are collected in **Table 4.3** for all *X*VP/*Y*BA copolymer samples. As usual, the values of T_v are nearly 50 K below those of T_g. Moreover, the strength parameter obtained for these samples are lower than 10, the frontier that separates fragile ($D_0 < 10$) from strong ($D_0 > 10$) glasses (Angell, 1995; Angell, 1996; Rubi, et al., 1997).

By comparing Eq. (1.2) with the Doolittle expression (Doolittle, 1951; Doolittle, 1952), the relative free volume $\phi_g / B = \left(T_g - T_v\right) / \left(D_0 \cdot T_v\right)$ and the expansion coefficient of the free volume $\alpha_f = 1 / \left(D_0 \cdot T_v\right)$ at T_g were evaluated (see **Table 4.3**). Free volume theories require that the ratio of the activation energy at constant volume to that at constant pressure is zero. However, this ratio for polymers is not zero (Mpoukouvalas, et al., 2009), which questions the applicability of these theories to the α relaxations. Even so, it is an experimental fact that the values of the ϕ_g/B and α_f for most flexible polymers lie in the vicinities of $2.5 \cdot 10^{-2} \pm 5.0 \cdot 10^{-3}$ and (4-6) $\cdot$ 10^{-4} K^{-1}, respectively. It is worth noting that the values of ϕ_g/B are slightly higher than the values reported for this parameter for most flexible polymers. On the other hand, the thermal expansion coefficients of the free volume α_f at T_g are similar to the ones reported for the most flexible polymers. (Ferry, 1961) In **Table 4.3**, the VTFH parameters corresponding to *0*VP/*100*BA homopolymer were taken from the literature (Fioretto, et al., 1994; Encinar, et al., 2008). We don't have any evidence of available data regarding α relaxation process for dry PVP in the literature.

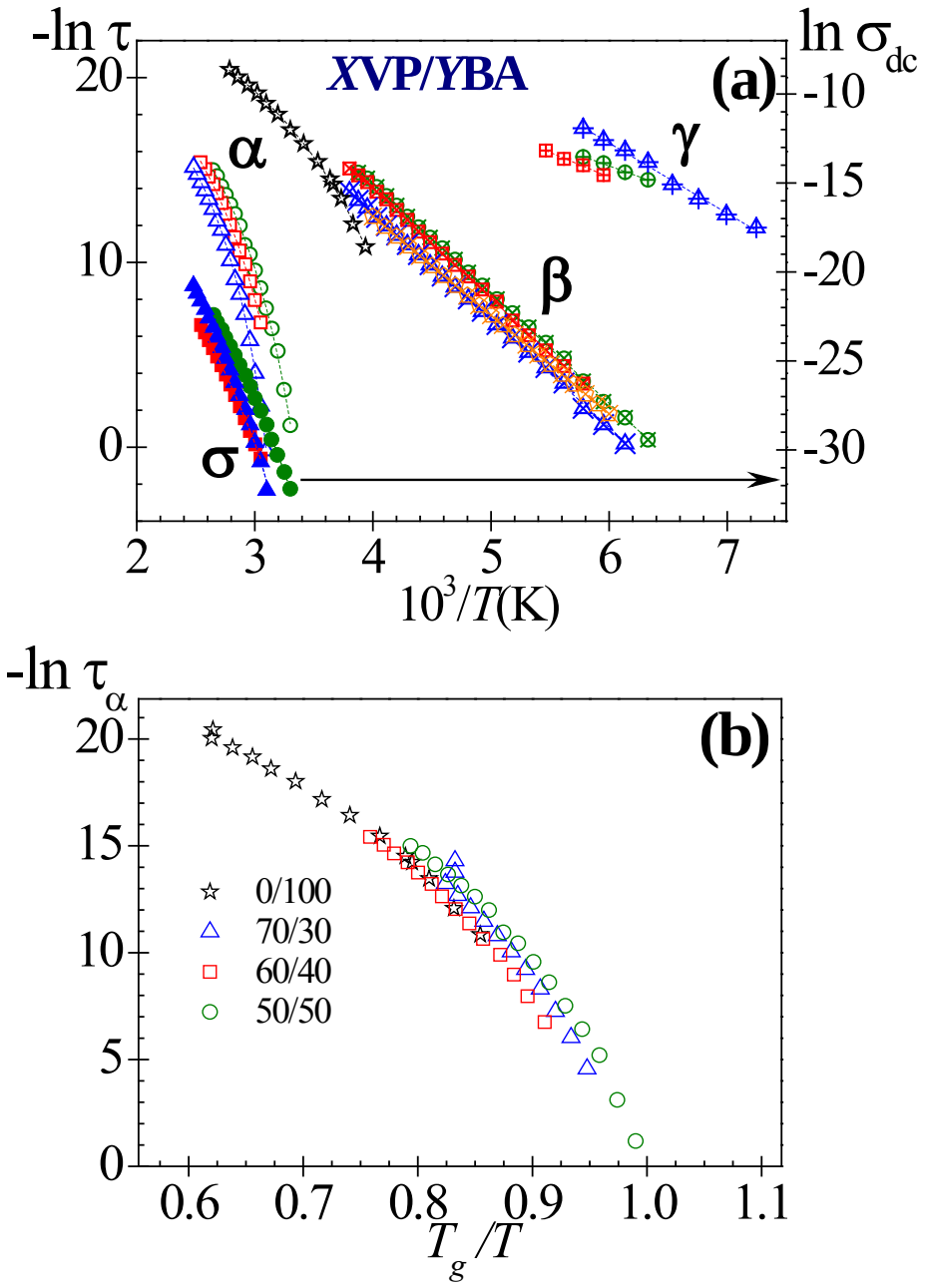

Figure 4.13. (a) Temperature dependence of the relaxation times for *X*VP/*Y*BA samples in the left Y-axis: α (0/100(☆), 50/50 (○), 60/40(□), 70/30(△)), β (50/50 (⊠), 60/40(⊠), 70/30(⊠), 100/0(⊠)) and γ (50/50 (⊕), 60/40(⊞), 70/30(⊞)) dipolar relaxations. Temperature dependence of the ionic conductivity for *X*VP/*Y*BA samples in the right Y-axis [50/50 (●), 60/40 (■), 70/30 (▲)]. Lines represent the fitting. **(b)** The relaxation time for α process as a function of normalized temperature.

Table 4.3. Characteristic parameters of the segmental process of the *X*VP/*Y*BA samples.

	0VP/100BA	**50VP/50BA**	**60VP/40BA**	**70VP/30BA**	**100VP/0BA**
			α process		
$log_{10}\ \tau_0,\ s$	-12.0±0.5[a]	-10.9±0.2	-11.2±0.1	-10.5±0.1	—
D_0	7.2±1.3[a]	5.5±0.4	5.9±0.2	4.2±0.1	—
$T_v,\ K$	178±7[a]	246.5±2.8	249.5±1.8	275.3±1.1	—
ϕ_g/B[b]	0.040±0.004	0.033±0.003	0.033±0.003	0.034±0.002	—
$\alpha_f \times 10^4$[b], K^{-1}	7.8±1.1	7.4±0.4	6.8±0.6	8.6±0.4	—
m[b]	49.2±5.0	83.0±4.0	79.2±4.5	97.5±4.0	—
m^*[b]	73.1	90.7	92.6	97.4	134.8
$E_a^{\alpha}\left(T_g\right)$[b], $kJ{\cdot}mol^{-1}$	216±23	464±28	452±26	589±24	—
$E_a^{*\alpha}\left(T_g\right)$[b], $kJ{\cdot}mol^{-1}$	279	476	499	563	1176
β_{KWW} [at T_g][b]	0.25	0.23	0.24	0.25	—

[a]D. Fioretto, A. Livi, P.A. Rolla, G. Socino, L. Verdini, 1994 *J. Phys.:Condens. Matter* **6** 5295-5302

[b]The T_g was obtained for τ=100s.

As previously introduced in Chapter 1, Angell (Angell, 1985) introduced in the 1980s the concept of dynamic fragility. This parameter rationalizes the deviation of supercooled liquids from Arrhenius behavior in the vicinity of the T_g, for the α relaxation. The dynamic fragility index, *m*, is an index of the cooperative motions in polymers that are influenced by intermolecular interactions. It characterizes how rapidly the properties vary when the temperature of a supercooled liquid approaches its T_g and it is defined by the Eq. (1.5). Taking T_g as reference and considering the temperature dependence of the α relaxation for

flexible polymers and liquids governed by Eq. (1.2), the fragility parameter can be written as

$$m = \frac{D_0 \cdot T_v}{2.303 \cdot T_g \cdot \left(1 - T_v / T_g\right)^2} \tag{4.2}$$

Fragility values typically range between m=16, for strong systems, and m=200 for the fragile ones (Merino, et al., 2011). The values of m, collected in **Table 4.3** , show that, for the *X*VP/*Y*BA copolymer samples the dynamic fragility index increases with the respective T_g. This trend is in agreement with Angell's energy landscape model (Angell, 1995; Angell, 1991). If the density of minimum energy is high in the hypersurface, the material will have a larger probability of finding a new conformation and thus will exhibit higher fragility. Fragile materials usually have a higher degree of intermolecular coupling (*i.e.* high cooperativity) which is quickly lost with rising temperature, so that the relaxation process changes rapidly. The rapid change of conformation suggests a larger entropy change, or large ΔC_p. However, correlation between dynamic fragility index and ΔC_p is not present in all polymeric systems (Cangialosi, et al., 2006; Roland, et al., 1999). In fact, this correlation between m and ΔC_p is not observed for the *X*VP/*Y*BA copolymer samples. The dynamic fragility index increases with the VP content, but ΔC_p values are kept practically constant. Moreover, the VP and BA homopolymers also show a different behavior.

The BA homopolymer shows the lowest fragility but it has the highest ΔC_p. This behavior has been observed in some systems where the formation of nanodomains, integrated by the side chains flanked by the backbone, is produced (Carsí, et al., 2012; Carsí, et al., 2013). This effect can be understood due to a decrease in the free volume. Thereby, larger ΔC_p values does not necessary imply higher fragility. ΔC_p might include

enthalpy contribution associated with rearrangement of the molecular chains, which leads to the formation of side chain nanodomains.

On the other hand, due to the fact that fragility is proportional to the T_g, VP homopolymer should show the highest fragility. Nevertheless, this sample has the lowest value of ΔC_p (Qin, et al., 2006), tendency observed in some hydrogen-bonded systems (Santangelo, et al., 1998). There is no information about the *m* parameter for the *100*VP/*0*BA sample because the conductive contribution to permittivity masks the α relaxation process (see **Figure 4.7**). Thus, it is not possible to see properly the PVP spectrum and there is not available data regarding α relaxation process for dry PVP in the literature.

Figure 4.13b shows the normalized temperature dependence of τ_α, also called fragility plot, for *X*VP/*Y*BA samples. As it is observed, their temperature dependence is equivalent, namely, non-significant differences in fragility are produced between the copolymer samples. Since the fragility is related to the cooperativity, these results point out that the VP composition does not produce significant changes in cooperativity of the samples.

Qin and McKenna (Qin, et al., 2006) compiled literature data for dynamic fragility of different types of glass forming liquids. They found a roughly linear increase of *m* with T_g for the various types of systems analyzed. The pertinent expressions were $m^* \approx 0.28(\pm 0.067)T_g + 9(\pm 20)$ for polymers and $m^* \approx 0.25(\pm 0.059)\cdot T_g + 16(\pm 10)$ for organic and inorganic ionic glasses and hydrogen bonding organics. The values of *m** calculated by the former expression for all *X*VP/*Y*BA samples, are summarized in **Table 4.3**. As we can

observe, an increase tendency with T_g is reproduced and the dynamic fragility values are similar to those obtained from Eq. (4.2). The analysis of the fragility in terms of the structure, carried out by Qin and McKenna, suggests that the more flexible the polymer, the less brittle the material is and therefore, the fragility parameter (m) is lower. As it is known, the *0*VP/*100*BA sample presents more conformational versatility that the *100*VP/*0*BA ones, and consequently, a lower fragility parameter is expected. Thus, it is observed that *X*VP/*Y*BA samples become more fragile with the VP content.

The apparent activation energy associated with the relaxation dynamics of the chains at T_g can be obtained from the dynamic fragility index as

$$m = \left[\frac{d \log \tau_A}{d\left(T_g / T\right)} \right]_{T=T_g} = \left[\frac{d \log \tau_{VFTH}}{d\left(T_g / T\right)} \right]_{T=T_g} \tag{4.3}$$

where the subscripts A and VFTH indicate, respectively, Arrhenius and Vogel relaxation times. These expressions lead to the following equation for the activation energy, $E_a^{\alpha}\left(T_g\right)$, at the T_g

$$E_a^{\alpha}\left(T_g\right) = \frac{R \cdot D_0 \cdot T_v}{\left(1 - T_v / T_g\right)^2} \tag{4.4}$$

where R is the gas constant. By comparing Eqs. (4.2) and (4.4), the activation energy can be expressed by the alternative form: $E_a^{\alpha}\left(T_g\right) = 2.303 \cdot R \cdot m \cdot T_g$. This relation suggests that $E_a^{\alpha}\left(T_g\right)$ raises with the increase of T_g. Values of $E_a^{\alpha}\left(T_g\right)$ for all *X*VP/*Y*BA samples are collected in **Table 4.3**, and it is observed that these values indeed increase with the glass transition temperature. Moreover, Rössler and co-workers (Rössler, et al., 1998) predicted

the following expression $E_a^{\alpha^*}\left(T_g\right)=\left[0.006\left(\pm 6.5\cdot 10^{-4}\right)T_g^2\left(K\right)-35\left(\pm 66\right)\right]$ *kJ/mol* for a wide variety of polymers. In general, $E_a^{\alpha}\left(T_g\right)$ values are similar to those predicted by $E_a^{\alpha^*}\left(T_g\right)$ equation. However, $E_a^{\alpha^*}\left(T_g\right)$ is higher for *50*VP/*50*BA and *60*VP/*40*BA samples, but it is slightly lower for *70*VP/*30*BA than $E_a^{\alpha}\left(T_g\right)$.

The temperature dependence of the relaxation times associated with the secondary relaxations in the glassy state is also shown in **Figure 4.13**. According to our results, the increase in VP content results in an increase in the temperature of the maximum and in the relaxation times of the *X*VP/*Y*BA samples. It can be seen that both relaxation processes follow Arrhenius behavior (ARRH) ($\tau_{\max}=\tau_{\infty}\cdot\exp\left[E_a/RT\right]$) and their activation energies (E_a) and pre-exponential factors (τ_{∞}) are summarized in **Table 4.4**. The parameters associated to the β process for *100*VP/0BA sample are those ones corresponding to the PVP with low water content (1% wt) reported by Cerveny and co-workers (Cerveny, et al., 2008).

As explained in the introduction chapter, it is well known that different molecular mechanisms can be responsible for secondary processes in glass-forming materials. One type of sub-T_g relaxations involve the motion of pendant groups or an isolated part of the molecule and would be mainly controlled by intramolecular potentials. However, there is another type of sub-T_g relaxations labeled as Johari and Goldstein relaxations (JG) (Johari, et al., 1970; Johari, et al., 1972) that involve the motion of the whole molecule, having therefore an origin similar to that of the α-relaxation. These secondary relaxations are defined as intermolecular in character. One way to distinguish between both types of sub-T_g

relaxation is to carry out the analysis proposed for Ngai, known as the Coupling Model (CM), which was introduced in subsection 1.2.2.3. Ngai et al. found that the JG secondary relaxation obeys the following criteria: $\tau_{\beta,\gamma}\left(T_{g\alpha}\right) \approx \tau_0^{CM}\left(T_{g\alpha}\right) = t_c^n \cdot \tau_\alpha^{1-n}$, where t_c is the crossover time in the CM, which is about 2 *ps* and n = 1 - β_{KWW} is the coupling parameter, being β_{KWW} the stretch exponent of the KWW equation (Eq. (1.31)).

For this purpose, the normalized α relaxation in the time domain was calculated from the retardation loss spectra (Tamman, et al., 1926; Kohlrausch, 1854) evaluated from the HN fit parameters as follows

$$\phi(t) = \frac{\int_{-\infty}^{\infty} L_\alpha\left(\ln\tau\right) e^{-t/\tau} d\ln\tau}{\int_{-\infty}^{\infty} L_\alpha\left(\ln\tau\right) d\ln\tau} \tag{4.5}$$

The KWW decay functions at different temperatures are shown in the **Figure 4.14**. In the case of the *0*VP/*100*BA homopolymer, the decay function was obtained from the HN fit parameters taken from the literature (Fioretto, et al., 1994).

In the **Figure 4.15**, the respective temperature (**Figure 4.15a**) and normalized temperature (**Figure 4.15b**) dependence of the characteristic relaxation times and the stretch exponents are shown. Moreover, the τ_{KWW} dependence of β_{KWW} is also represented (**Figure 4.15c**). As usual, an increase of temperature produces a decrease in the characteristic relaxation time and an increase in the β_{KWW} value. The evolution of the τ_{KWW} with the temperature obeys the VFTH equation. The tendency of the stretch exponent can be related to the decreasing of intermolecular constraints (or coupling) between the relaxing units with increasing temperature. According to our results, the stretch exponent (β_{KWW})

decreases as the VP content increases at high temperatures. However, the β_{KWW} values for the three samples are approaching at T_g and even the β_{KWW} slightly increases with the VP content. On the other hand, according to **Figure 4.15c,** the β_{KWW} decreases with the increase of τ_{KWW}. The coupling between the relaxing units, *i.e.* the increase of intermolecular constraints, leads to higher relaxation times of the α process.

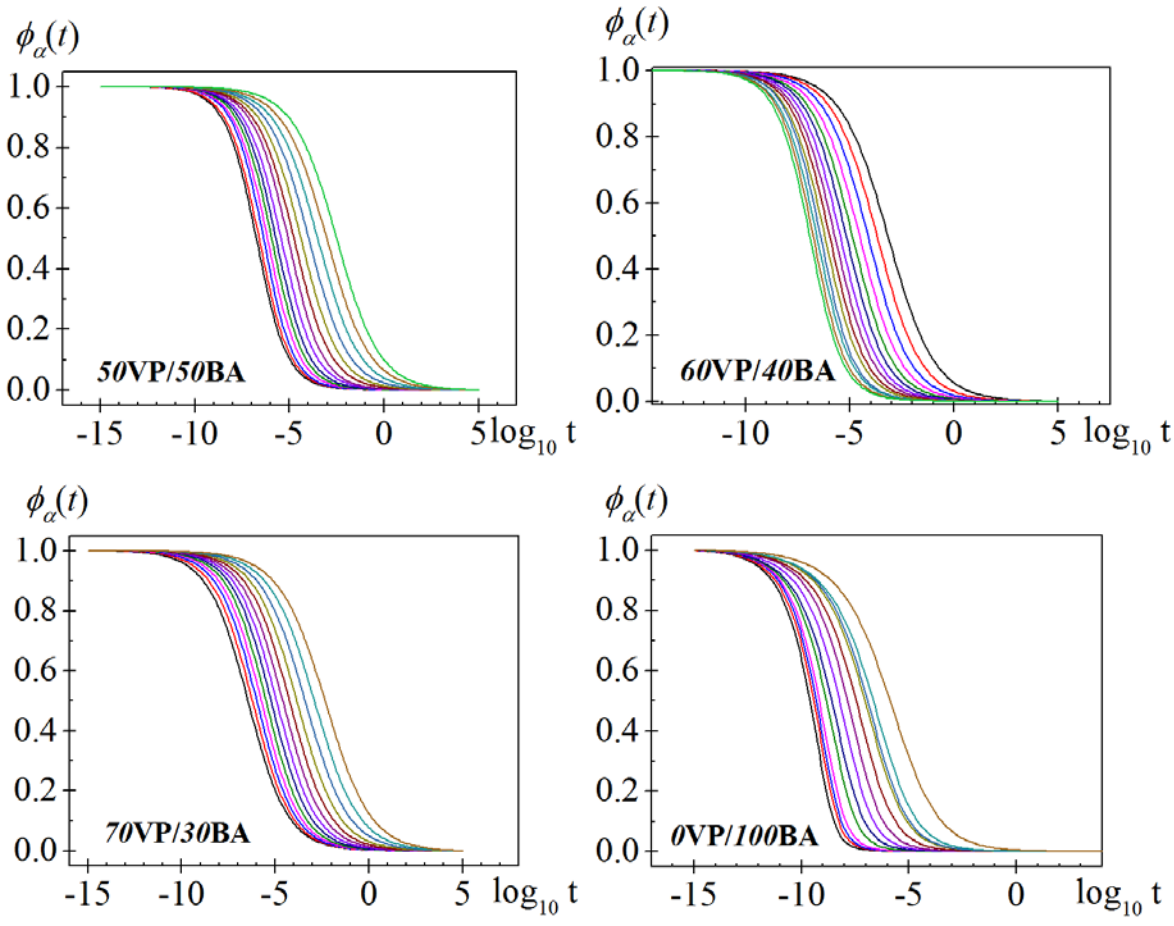

Figure 4.14 Normalized relaxation curves in the time domain for the α relaxation of *X*VP/*Y*BA samples.

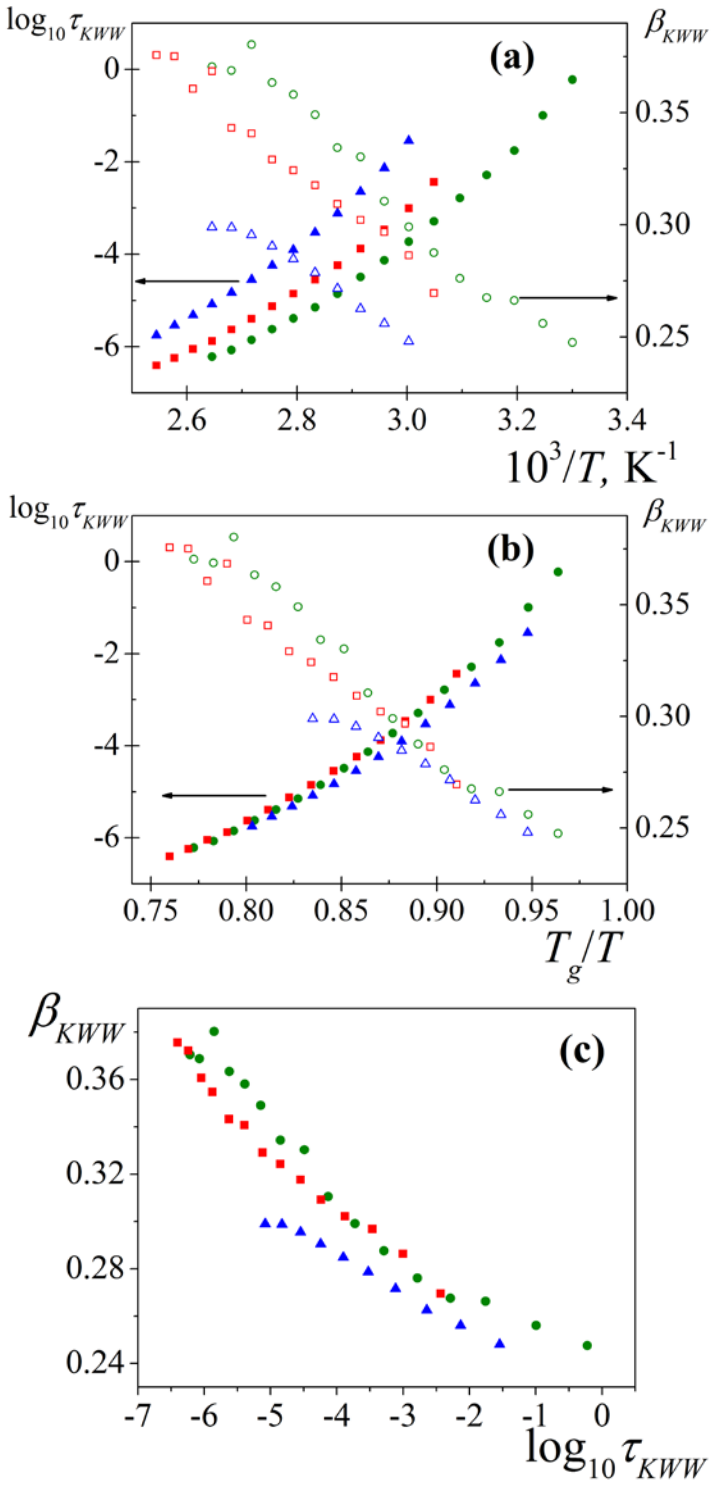

Figure 4.15. **(a)** The temperature and **(b)** the normalized temperature dependence of the stretch exponent β_{KWW} (open symbols) and the characteristic relaxation times τ_{KWW} (full symbols) for the *50*VP/*50*BA (circles), *60*VP/*40*BA (squares) and *70*VP/*30*BA (triangles) samples. **(c)** β_{KWW} as function of τ_{KWW} .

According to the CM and taking into account that (i) the T_g is conveniently defined as the temperature at which the dielectric relaxation time $\tau_\alpha \approx 100s$ and (ii) in the Arrhenius temperature dependence of the secondary relaxations, the ratio $\left(E_a^{\beta,\gamma}/RT_g\right)$ can be evaluated as a function of n and τ_∞ parameters as follows (Ngai, et al., 2004) $\left(E_a^{\beta,\gamma}/RT_g\right)_{cal} = 2.303\left[(1-n)\log_{10}\tau_\alpha\left(T_g\right) + n\log_{10}t_c - \log_{10}\tau_\infty^{\beta,\gamma}\right]$. In **Table 4.4** are collected the values of the ratio $\left(E_a^{\beta,\gamma}/RT_g\right)$ evaluated by using the CM theory and from experimental data. According to our results, there is only good agreement between the experimental value of ratio $\left(E_a^{\beta,\gamma}/RT_g\right)_{\text{expt}}$ and the calculate value $\left(E_a^{\beta,\gamma}/RT_g\right)_{\text{cal}}$ for the slower process. This means that, the β relaxation process is a JG process, and therefore, has intermolecular character. On the other hand, the γ process has an intramolecular character and it is related to local motions of side chains. According to the values of the energy activation parameters (**Table 4.4)**, the γ process is related to motions of the terminal butyl units (Fulcher, 1925; Sanchis, et al., 2004). However, the β process is related to the local motions of the pyrrolidone group accompanied by the segments motions of the polymer backbone (Zhang, et al., 2004). The butyl unit motions responsible of the γ relaxation can be restricted by the presence of the VP units, so an increase in the activation energy of the process is observed by increasing the VP content. On the other hand, the activation energy of the β process slightly diminishes with VP content. Due to the molecular origin of β process, the motion of pyrrolidone group is restricted to the BA increasing content. However, as β relaxation is a cooperative motion, the influence of VP content in the activation energy is lower than in the γ process.

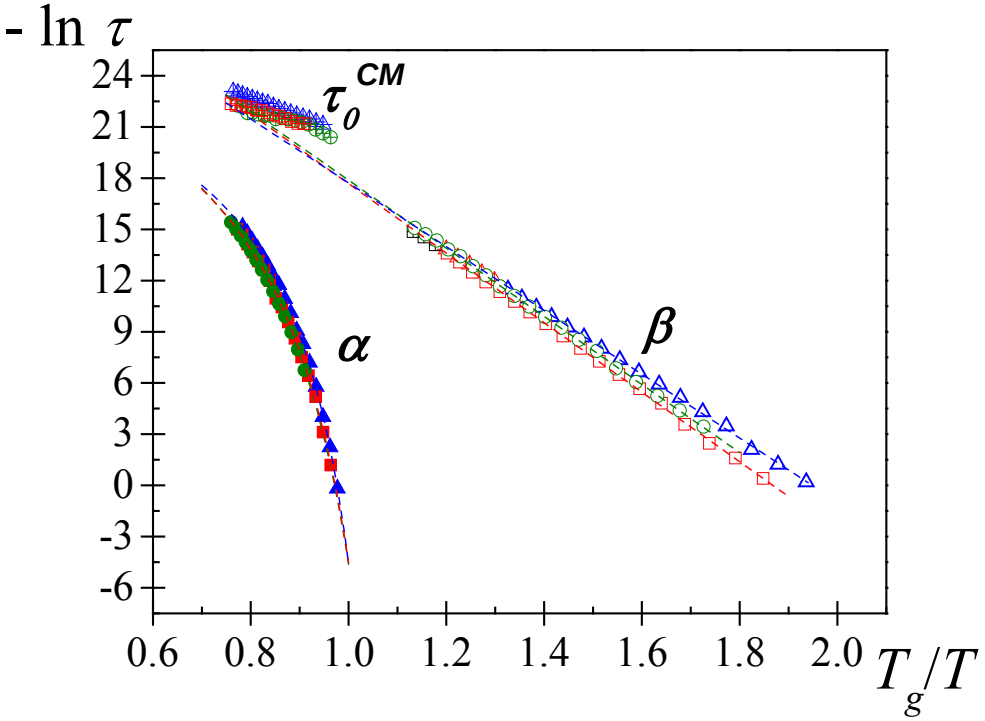

Figure 4.16. Angell plot of the α and β relaxations of *50*VP/*50*BA (circles), *60*VP/*40*BA (squares) and *70*VP/*30*BA (triangles) samples. The symbols with a cross represent τ_0 values obtained according to the CM. Dashed lines correspond to the fitting. The glass transition temperatures used to scale the data are collected in **Table 4.2**.

Using the τ_{KWW} and β_{KWW} values obtained from the retardation time spectra (**Figure 4.15**), the τ_0^{CM} parameter was calculated for each copolymer and for each temperature. Thus, the values of $-\ln(\tau_0^{CM})$ parameters for each sample are represented in **Figure 4.16**. As it is observed, τ_0^{CM} values are superimposed to the obtained values of τ_β for all the samples, fulfilling the condition of the Eq. (1.34): $\tau_\beta \approx \tau_0^{CM}$. Hence, it is confirmed that the β process is a JG relaxation. The disagreement between τ_β and τ_0^{CM} close to T_g could be related to the error associated to the fitting procedure.

Table 4.4. Characteristic parameters of the secondary processes of the *X*VP/*Y*BA samples.

	0VP/100BA	**50VP/50BA**	**60VP/40BA**	**70VP/30BA**	**100VP/0BA**
			γ process		
$\log_{10}\ \tau_\infty, s$	-11.5±0.4[a]	-12.6±0.3	-13.3±0.3	-15.6±0.5	—
E_a^γ , $kJ{\cdot}mol^{-1}$	12.1±0.3[a]	19.2±0.8	22.1±1.0	27.6±1.3	—
$\left(E_a^\gamma/RT_g\right)_{\text{expt}}$ [c]	4.4	7.7	8.6	10.4	—
$\left(E_a^\gamma/RT_g\right)_{\text{cal}}$		9.4	11.2	16.8	
			β process		
$\log_{10}\ \tau_\infty, s$	—	-16.5±0.1	-16.4±0.1	-15.6±0.1	-14.7±0.1[b]
E_a^β , $kJ{\cdot}mol^{-1}$	—	49.4±0.2	49.5±0.2	47.7±0.4	44.4±0.9
$\left(E_a^\beta/RT_g\right)_{\text{expt}}$ [c]	—	19.8	19.3	18.0	—
$\left(E_a^\beta/RT_g\right)_{\text{cal}}$		18.4	18.5	17.0	

[a] M. Encinar, E. Guzmán, M.G. Prolongo, R.G. Rubio, C. Sandoval, F. González-Nilo, L. Gargallo, D. Radic, *Polymer* 2008 **49(26)** 5650-5658
[b] Cervery S., Alegría A. Colmenero J., 2008 *J. Chem. Phys.* **128** 044901
[c] The glass transition temperature used was the calorimetric T_g.

On the other hand, the *ac* conductivity has been calculated from the dielectric permittivity according to the relation: $\sigma^*(\omega) = j{\cdot}\omega{\cdot}e_0{\cdot}\varepsilon^*(\omega)$. In general, at a constant temperature *ac* conductivity can be expressed as (Böttger, et al., 1985; Jonscher, 1992)

$$\sigma'(\omega) = \sigma_{dc} + A\omega^s \tag{4.6}$$

where σ_{dc} is the frequency-independent conductivity ($\omega \to 0$), A is a temperature dependent factor and s is the frequency exponent ($0 \leq s \leq 1$) also depending on the temperature. The Eq. (4.6) is often called *"the ac universality law"* since it has been found to satisfactorily

describe the *ac* response of numerous different types of materials, which can be classified as disordered solids (Jonscher, 1992; Dyre, et al., 2000; Dyre, 1988).

Figure 4.17 depicts the dependence of the *ac* conductivity from the frequency of the applied field at several temperatures in the range from 308 K to 423 K (step 5 K). In the low frequencies and high temperatures zone, a frequency independent conductivity is recorded (first term of Eq. (4.6)), which is attributed to resistive conduction through the bulk of polymer. On the other hand, when frequency is raised, the main displacement of the charge carriers is reduced. At this point the real part of conductivity, after reaching a certain frequency, ω_c, become proportional to frequency following the law $\sigma'_{ac}(\omega) \sim \omega^s$ with $0 \leq s \leq 1$ (second term of Eq. (4.6)). For all *X*VP/*Y*BA copolymers and tested temperatures, the value of the *s* parameter was in the range of 0.98 to 1. However, the influence of temperature is more pronounced in the low frequency range, while at high frequencies, the *ac* conductivity values are approaching.

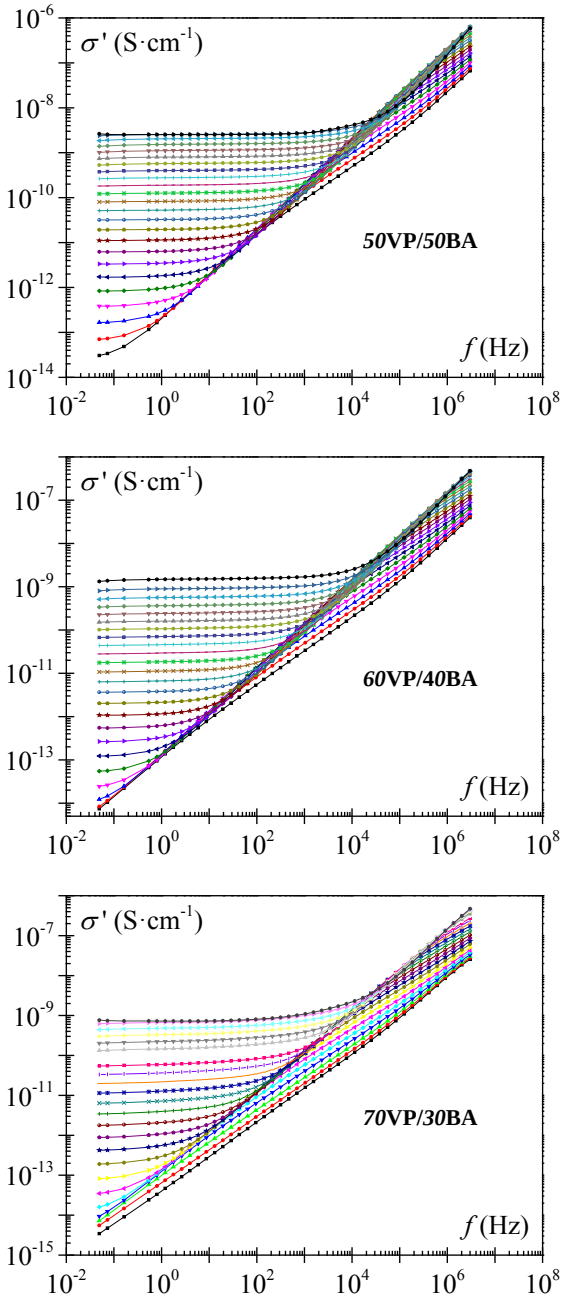

Figure 4.17. Frequency dependence of the σ' ($S \cdot cm^{-1}$) from 308 K to 423 K for *X*VP/*Y*BA copolymers.

According to the Continuous-Time-Random Walk (CTRW) approximation (Montroll, et al., 1965), the real part of the complex conductivity can be expressed as (Dyre, 1988; Kremer, et al., 2003):

$$\sigma'(\omega) = \frac{\sigma_0 \cdot \omega \cdot \tau_\sigma \cdot \arctan(\omega \cdot \tau_\sigma)}{\frac{1}{4} \cdot \ln^2\left(1 + \omega^2 \cdot \tau_\sigma^2\right) + \left[\arctan(\omega \cdot \tau_\sigma)\right]^2} \tag{4.7}$$

where τ_σ is the relaxation time for conductivity process and σ_0 is the plateau or *dc* conductivity. According to Dyre (Dyre, 1988; Sangoro, et al., 2011), charge carriers hop in a random spatially varying potential landscape. Thus, the transport process is governed by the ability of charge carriers to overcome the randomly distributed energy barriers. The highest barrier that must be overcome to achieve an infinite cluster of hopping sites determines the onset of *dc* conductivity. Therefore, the time corresponding to the rate to overcome the highest barrier determining the *dc* conductivity (σ_0) is one of the characteristic parameters of the model, which was previously defined as τ_σ.

Thus, the values of the *dc* conductivity have been obtained by four different methods: (i) from the fitting of the $\varepsilon^*(\omega)$ experimental data $\left(\varepsilon^*_{cond}(\omega) = i\left(\sigma / e_0 \omega^s\right)\right)$, (ii) from the extrapolation of the *ac* conductivity at low frequencies (from the plateau), (iii) from the fitting of σ' experimental data to the CTRW equation (Eq. (4.7)) and (iv) from the Nyquist plot ($Z''(\omega)$ *vs* $Z'(\omega)$).The plots are arcs that intersect the abscissa axis at the extreme frequencies in such a way that $Z''(\infty) = 0$ and $Z''(0) = R_p$, being R_p the polarization resistance, which strongly decreases with increasing temperature. The values of *dc* conductivity were estimated from the R_p values by means of the relationship $\sigma_{dc} = 1/R_p A_s$, where A_s is the area of the sample. The different values of σ_{dc} obtained by the four methods are plotted as a function of the reciprocal of temperature in **Figure 4.18**. As observed in this figure, the *dc* conductivity values obtained from the four methods are in good agreement. The temperature dependence of the *dc* conductivity follows VFTH behavior

$\left(\sigma_{dc} = \sigma_0 \cdot \exp\left(-D_0 \cdot T_v / \left(T - T_v\right)\right)\right)$, which was found in a variety of materials (Merino, et al., 2011). Moreover, according to the results, the σ_{dc} increases with the VP content.

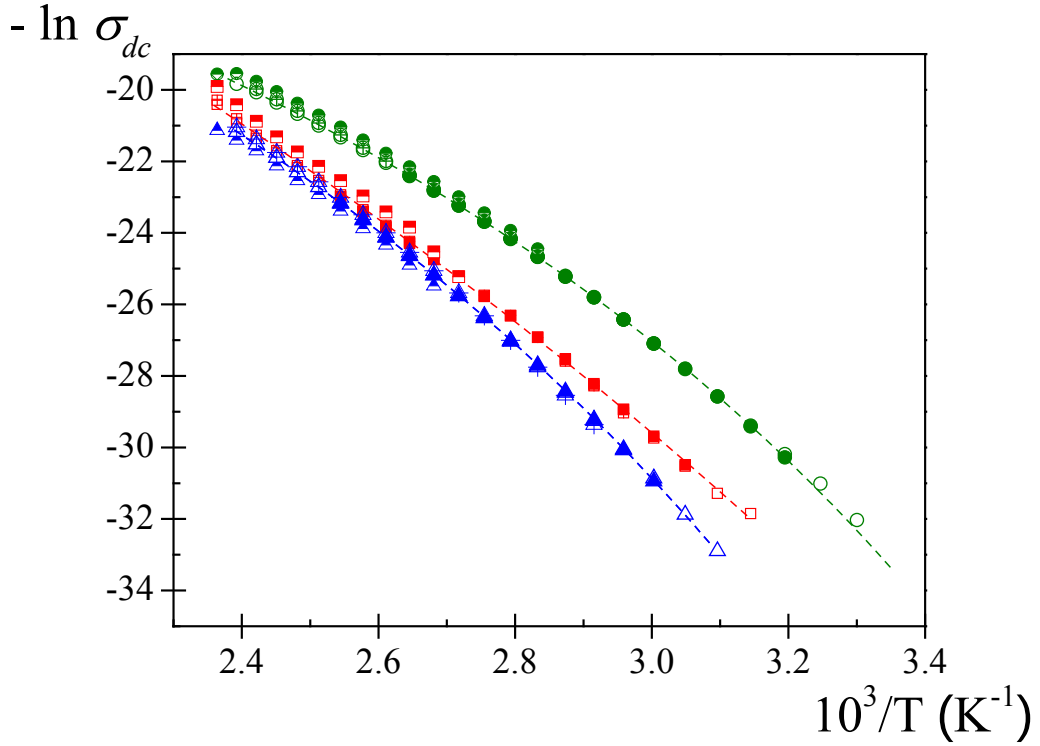

Figure 4.18. Temperature dependence of the ionic conductivity for *50*VP/*50*BA (circles), *60*VP/*40*BA (squares) and *70*VP/*30*BA (triangles) copolymers evaluated by (i) the fitting of the experimental ε^* (full symbols), (ii) the extrapolation of the ac conductivity at low frequencies (open symbols), (iii) the fitting of σ' to the CTRW equation (cross symbols) and (iv) the Nyquist plot *Z′ vs Z″* (half full symbols). The dashed lines correspond to the fit to the VFTH equation.

On the other hand, the values of the characteristic conduction time $\left(\tau_\sigma\right)$ can also be obtained by different methods. The first method is by the fitting of the data to the CTRW equation Eq. (4.7). The τ_σ values can also be obtained by reading the maxima of the imaginary part of $M^*(\omega)$ at low frequencies. Finally, the *M″(ω)* data at low frequencies can be fit to the following expression (Kremer, et al., 2003):

$$M''(\omega) = M_{\infty} \cdot \frac{\omega\tau_{\sigma}}{1+(\omega\tau_{\sigma})^2} \tag{4.8}$$

where $M_{\infty} = 1/\varepsilon_{\infty}$. The τ_{σ} values obtained from the methods described above are collected in **Figure 4.19** and compared with the σ_{dc}. As expected, τ_{σ} values also follow a VFTH - like behavior, whose tendency is practically the same as that of σ_{dc} values.

The fact that both σ_{dc} and τ_{σ} values follow a VFTH-like behavior can suggest the existence of a possible coupling between conductive and segmental dynamics. This possible coupling will be studied below. Moreover, the VFTH-like behavior is an indication that the origin of charge carrier transport is the segmental motions of the polymer chains (Neagu, et al., 1997; Lu, et al., 2006; Smaoui, et al., 2010). The *dc* charge transport is governed by both, the free volume and the temperature.

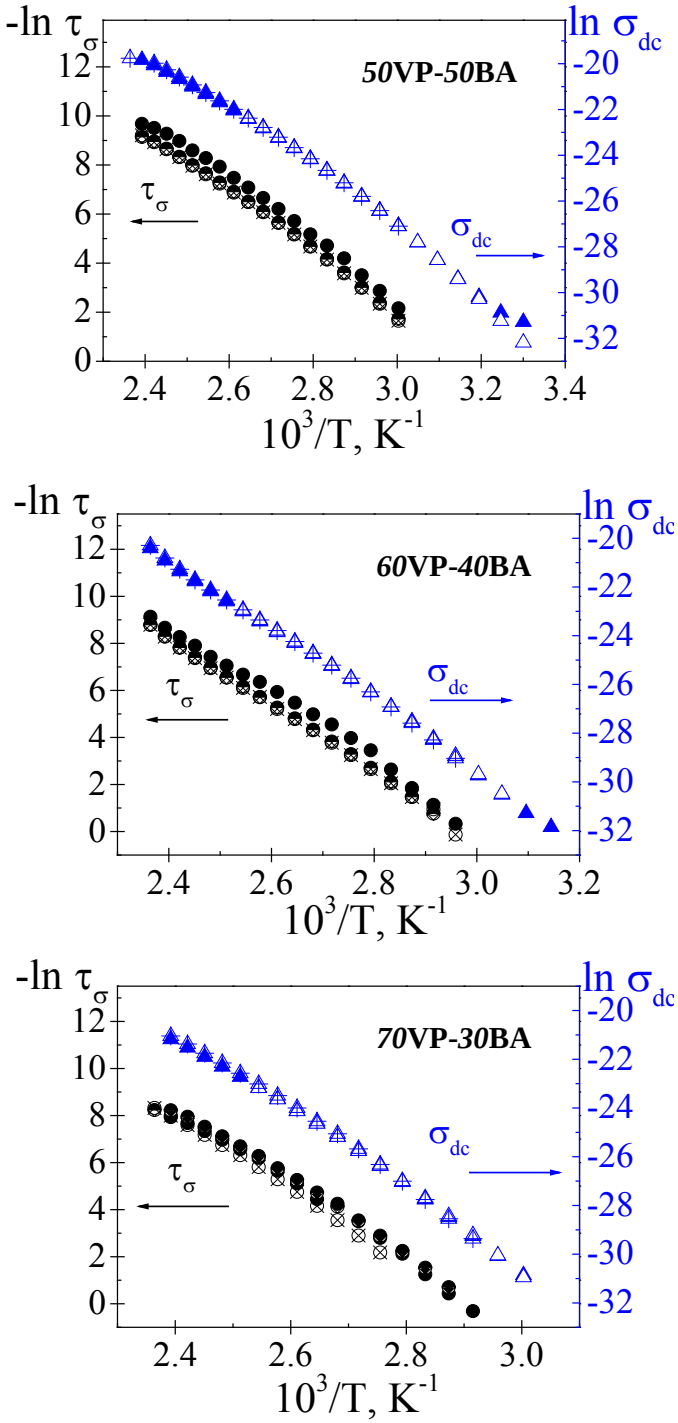

Figure 4.19. Temperature dependence of the *dc* conductivity (triangles) and the characteristic conduction time (circles) and for *50*VP/*50*BA, *60*VP/*40*BA and *70*VP/*30*BA copolymers evaluated by (i) the fitting of σ' to the CTRW equation (full circles), (ii) reading the maxima of $M''(\omega)$ (cross circles) and (iii) the fitting of $M''(\omega)$ to Eq. (4.8) (half full circles).

In **Table 4.5** the fit parameters of the VFTH equation for the conductive process are summarized. As observed, the D_0 and T_v fit parameters for the VFTH fitting of τ_σ and σ_{dc} values are similar, confirming that the tendency is approximately the same.

Table 4.5. Characteristic parameters of the conductivity process of the *X*VP/*Y*BA samples.

	50VP/50BA	**60VP/40BA**	**70VP/30BA**
	VFTH fitting to *dc* Conductivity		
$\log_{10}\ \sigma_0$, S/cm	-2.8±0.4	-2.8±0.2	-2.2±0.3
D_0, K	16.8±1.8	18.5±0.4	14.7±1.6
T_v, K	182.9±5.6	185.2±1.2	208.0±5.9
	VFTH fitting to Conductivity Relaxation Time		
$\log_{10}\ \tau_0$, s	-9.73±0.1	-10.0±0.7	-10.1±0.5
D_0, K	16.8±0.7	18.6±3.5	15.0±2.7
T_v, K	183.7±2.6	187.8±13	208.9±11.0

The *dc* conductivity in a polymer can be related to its segmental relaxation time τ_α by (Wang, et al., 2012; Agapov, et al., 2011):

$$\sigma \propto \frac{1}{\tau_\alpha \cdot T} \tag{4.9}$$

This relationship has been observed for many flexible polymers, and in particular in Poly(ethylene oxide) (PEO) (Killis, et al., 1982; Ratner, et al., 1988). Thus, the structural relaxation time slows down upon cooling close to the glass transition, which leads to significant decrease of *dc* conductivity.

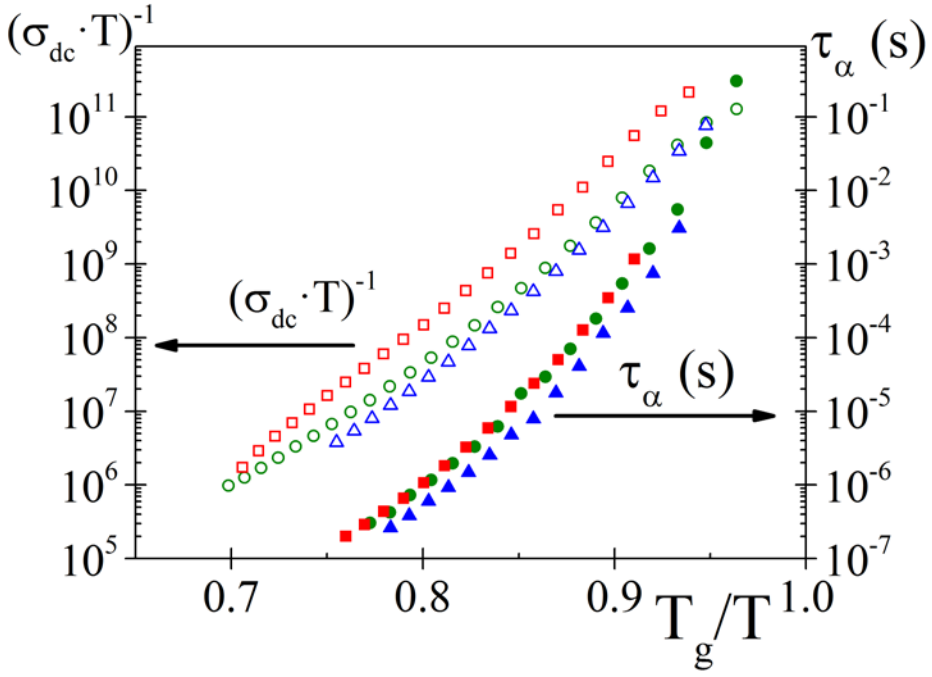

Figure 4.20. Inverse ionic conductivity $(\sigma_{dc} \cdot T)^{-1}$ (open symbols) and segmental relaxation time τ_α (full symbols) *vs* T_g/T for *50*VP/*50*BA (circles), *60*VP/*40*BA (squares) and *70*VP/*30*BA (triangles) copolymers. (Agapov, et al., 2011)

If the ion transport is coupled to the polymer segmental motion (Eq. 4.9), then, the inverse conductivity $(\sigma_{dc} \cdot T)^{-1}$ and τ_α should have the same temperature dependence (Wang, et al., 2012). **Figure 4.20** shows the temperature dependence of the *dc* conductivity and the segmental relaxation time for the *X*VP/*Y*BA samples. As observed, the temperature dependence of $(\sigma_{dc} \cdot T)^{-1}$ is not exactly the same as τ_α, which shows a certain degree of decoupling. For the three samples, it seems that the tendency is similar at high temperatures, but the $(\sigma_{dc} \cdot T)^{-1}$ shows weaker temperature dependence than τ_α when the temperature approximates to T_g. This difference in the temperature dependence of σ_{dc} and τ_α can also be observed in the VFTH parameters collected in **Table 4.3** and **Table 4.5**.

Moreover, the charge carrier motions can also be correlated with the dynamics of the structural relaxation using the so-called *decoupling index* (R_τ) (Angell, 1983; Angell, 1992):

$$R_\tau = \frac{\tau_\alpha}{\tau_\sigma} \tag{4.10}$$

where τ_α is the structural relaxation time and τ_σ is the conductivity relaxation time. R_τ gives a physical idea of the relation between the conductivity and the structural relaxation processes (Mizuno, et al., 2006). This index describes the extent to which the charge carrier conducting motions in a given glass can be considered decoupled/coupled from the polymeric chains motions of the glassy matrix (Merino, et al., 2011). At high temperatures, R_τ was calculated using τ_α as the α relaxation time obtained from the HN fitting ($\tau_{HN,\alpha}$) and τ_σ as the conductivity relaxation time from $M''(\omega)$ fitting (Eq. 4.8). At temperatures near T_g, where there is not experimental data, τ_α and τ_σ were approximated using the VFTH parameters of the α and conductivity processes respectively (**Table 4.3** and **Table 4.5**).

The decoupling index is plotted as a function of the normalized temperature in **Figure 4.21** for the copolymer samples. As observed, the decoupling index is practically the same for the three copolymer samples. Moreover, for the three copolymer samples, R_τ remains constant at higher temperatures and increases for temperatures near T_g. As described before, this is due to the fact that at high temperatures, the temperature dependence of both relaxation times τ_α and τ_σ is similar (see the same slope of both curves in inset of **Figure 4.21**). However, both relaxation times increase differently as temperatures approximates to T_g, since τ_α increases more than τ_σ (see the different slope of both curves in inset of

Figure 4.21). Thus, the slowing down of the segmental motions is more intense than that of the charge carrier conducting motions at temperatures near glass transition.

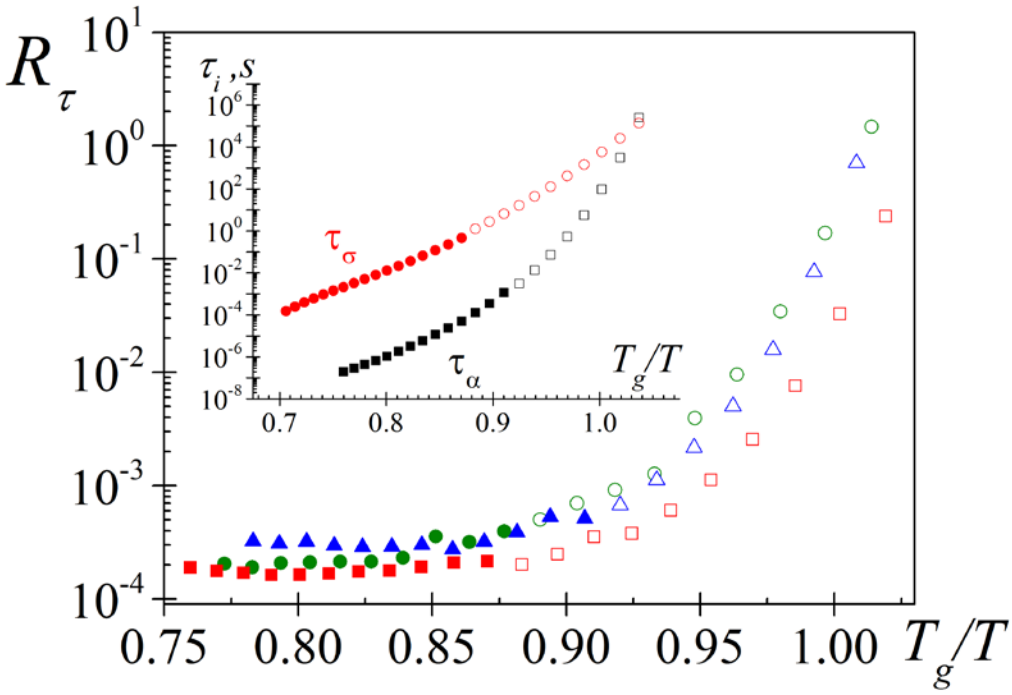

Figure 4.21. The ratio R_τ as a function of T/T_g for the *50*VP/*50*BA (circles), *60*VP/*40*BA (squares) and *70*VP/*30*BA (triangles) copolymers. R_τ was calculated from experimental relaxation times (full symbols) and from relaxation times obtained with the VFTH equation (open symbols), using the VFTH parameters collected in **Table 4.3** and **Table 4.5**. Inset: The normalized temperature dependence of the conductivity and α relaxation times for *60*VP/*40*BA.

During cooling, all systems show enormous increases in viscosity, but favorable systems show only small increases in conductivity relaxation time. Thus, a high conductivity is preserved in the glassy state. Thus, according to Angell (Angell, 1992), the decoupling index is interesting to be studied at the point in temperature at which the structure becomes fixed on cooling. This point is closely related to T_g. Thus, the values of R_τ at T_g are of the order of 10^{-1}, which are much lower values than other conducting

polymers (Burmistr, et al., 2005). This fact together with the VFTH dependence of the σ_{dc} and τ_{σ} indicates that the charge carrier motion is significantly influenced by the dynamics of the α process.

4.2.6. Mechanical properties

There is always a relationship between the mechanical properties and the chemical constitution of every material. In our case, the *100*VP/*0*BA sample was hard and brittle. However, the *0*VP/*100*BA sample was soft, and it had to be prepared with a thickness three times higher than the others in order to obtain a manageable material. The copolymer samples showed a mechanical behavior in-between the properties presented by *100*VP/*0*BA and *0*VP/*100*BA homopolymers. Moreover, from a macroscopically point of view, they were highly tractable materials. The properties of the samples are shown in **Table 4.6**. The Young´s modulus and the tensile strength increase with the VP content, whereas the elongation (%) decreases with the VP content. These tendencies are related to the increase of the hardness and brittleness of the samples with the VP content.

On the other hand, it is also interesting to evaluate the dependence of the mechanical properties with the time and the temperature. The dynamic mechanical analysis (DMA) is used both to study molecular relaxation processes in polymers and to determine inherent mechanical or flow properties. The DMA and DRS results, obtained in the same frequency range, are usually compared. The DMA has a narrow width of the frequency window (broadest range 1mHz-1kHz), so the DRS can add information on certain physical properties at lower and much higher frequencies. However, sometimes the conductivity processes observed at low frequencies in the DRS spectra can overlap or mask the α

relaxation. In these cases, the DMA allow a better visualization and analysis of the α relaxation.

Table 4.6. Mechanical properties of the *X*VP/*Y*BA samples.

Sample	Mechanical properties		
	Young modulus (MPa)	Tensile strength (MPa)	Elongation (%)
*100*VP/*0*BA	1476[a]	31[a]	7[a]
*70*VP/*30*BA	455[a]	20[a]	458[a]
*60*VP/*40*BA	200[a]	15[a]	540[a]
*50*VP/*50*BA	60[b]	15[b]	780[b]
*0*VP/*100*BA	--[c]	--[c]	--[c]

[a]Extension rate of 5 mm·min^{-1}. [b] Extension rate of 10 mm·min^{-1}. [c] The mechanical analysis could not be carried out because of the softness of the material, even with a thickness of 290 μm.

As a result of the mechanical properties obtained in the tensile test (see **Table 4.6**), it is observed that the *60*VP/*40*BA sample is the copolymer that has the most balanced properties. Its stiffness, which is reflected in the Young modulus and the tensile strength, is lower compared with the 7*0*VP/*30*BA sample. However, the *60*VP/*40*BA sample is less brittle (or more ductile) than the 7*0*VP/*30*BA sample, which is observed in the elongation value.

Therefore, as a representative sample of the copolymer family, the *60*VP/*40*BA copolymer was analyzed using the DMA. **Figure 4.22** shows the storage and loss modulus isochrones for *60*VP-*40*BA sample, over the temperature window 123 K–423 K at 0.3, 1, 3, 10 and 30Hz. The loss isochrones show three distinct relaxation peaks (α, β and γ) in a decreasing temperature order. Around 310 K (1Hz), the dynamic mechanical response is dominated by the α peak related to the glass-rubber relaxation, and at lower temperatures, in the glassy state, a broad absorption centered around 176 K appears. This absorption is

labeled β relaxation. Finally, the loss isochrones show the presence of a γ relaxation process below 133 K, but unfortunately this process is not fully defined in the experimental range of temperature. As expected, the location of both, α and β peaks, is shifted to higher temperatures as frequency increases, and the intensity of the peaks remains nearly constant as the frequency of the isochrones increases. As observed, the obtained spectrum is very similar to the one obtained from the dielectric measurements. In order to compare both spectra, in **Figure 4.23** are plotted the mechanical (E'') and the dielectric loss modulus ($M''=\varepsilon''/(\varepsilon'+\varepsilon'')$) as a function of temperature at 1 Hz. E'' is compared with M'' because both parameters are modulus, while the loss factor ε'' should be compared with the loss compliance (J'').

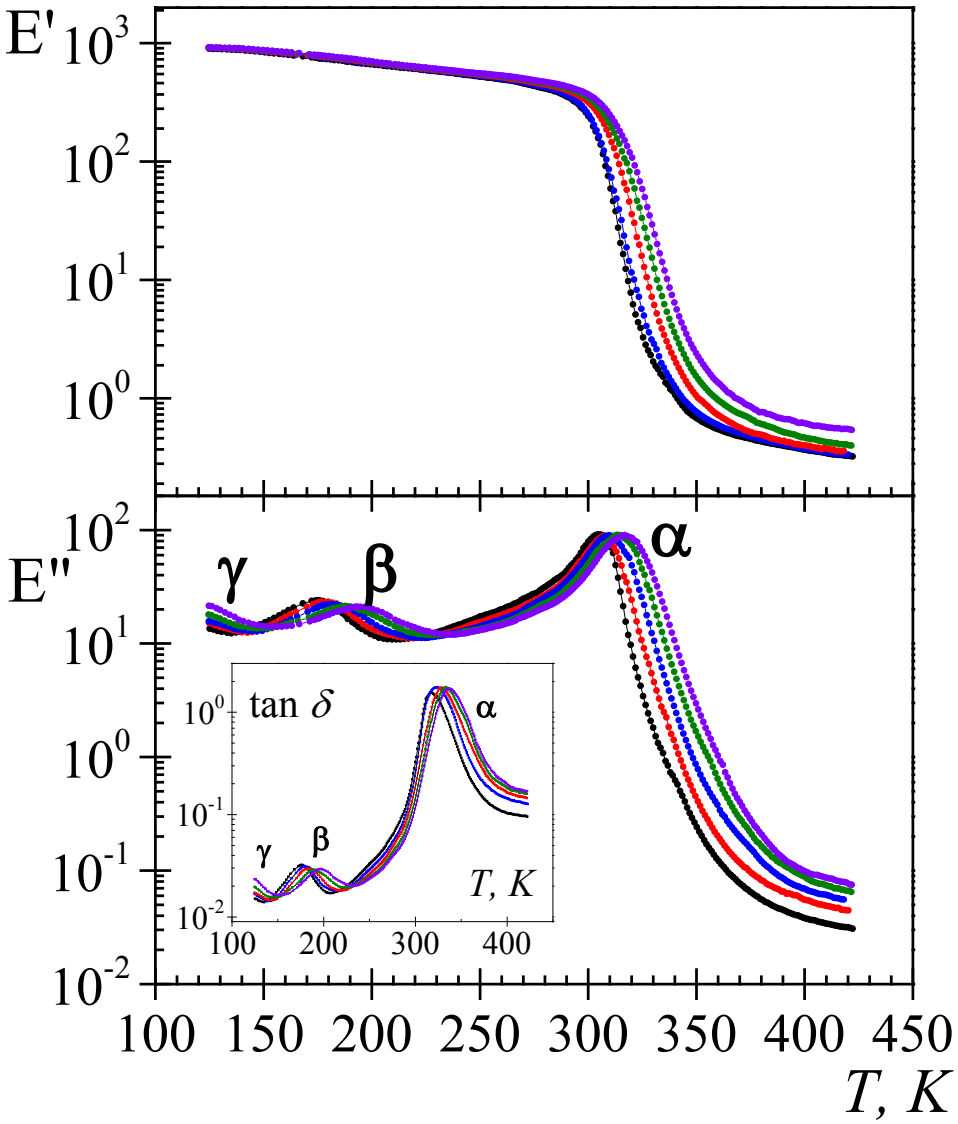

Figure 4.22. Temperature dependence of storage and loss modulus for *60*VP-*40*BA sample at 0.3, 1, 3, 10 and 30 Hz. Inset: Temperature dependence of tan δ for *60*VP-*40*BA sample at 0.3, 1, 3, 10 and 30 Hz

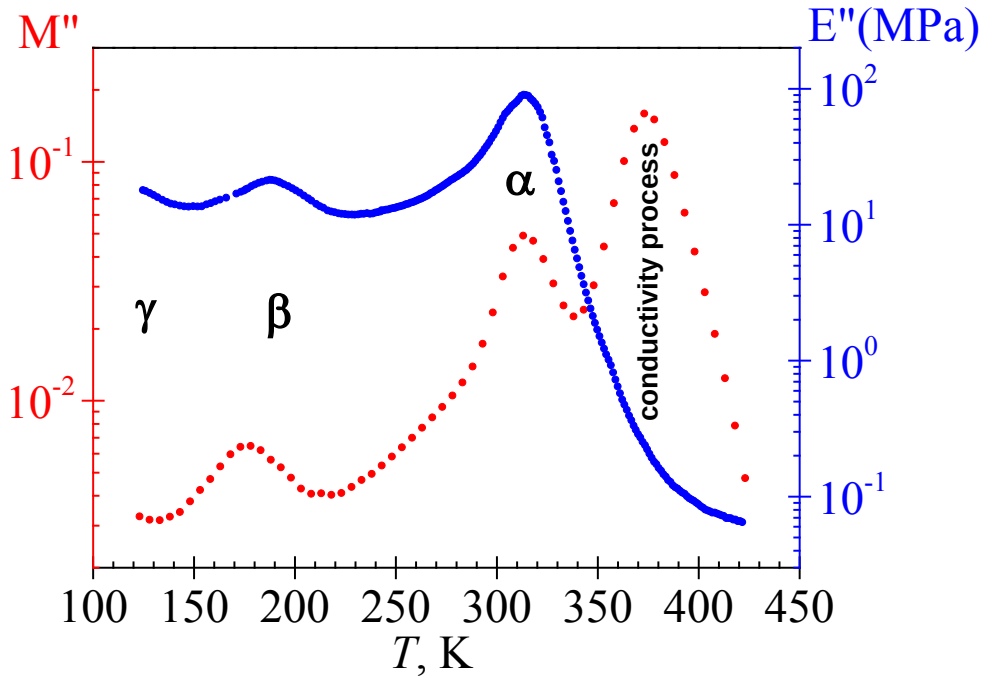

Figure 4.23 Temperature dependence of loss dielectric modulus and loss mechanical modulus at 1 Hz, for 60VP-40BA sample.

In order to characterize and analyze the observed relaxations in the mechanical spectrum, it is convenient to choose a model which appropriately reproduces the experimental data. A reliable model to represent the secondary relaxations in polymers is the Fuoss and Kirkwood equation (Eq. (1.25) (Fuoss, et al., 1941), which was introduced in the Chapter 1. This semi-empirical model has extensively been used in the representation of the mechanical relaxations and can be rewritten in terms of the temperature dependence of E'' as:

$$E'' = E''_{\max} \cdot \operatorname{sech}\left[\frac{m_{FK} \cdot E_a}{R}\left(\frac{1}{T} - \frac{1}{T_{\max}}\right)\right] \tag{4.11}$$

where E'' represents the mechanical loss, E''_{max} is the value of this quantity at the peak maximum, T_{max} is the temperature of the peak maximum, E_a is the apparent activation

energy, R is the gas constant, and m_{FK} is a parameter ($0<m_{FK}<1$) related to the broadness of the relaxation in the sense that the lower m_{FK}, the wider the distribution is. The value of $m_{FK}=1$ corresponds to a single relaxation time (Debye peak). The strength of the mechanical relaxation peak can be calculated from the relationship (McCrum, et al., 1991), $E''_{max} = m_{FK} \cdot \Delta E/2$, where ΔE represents (E_0-E_∞).

The function was determined from a multiple nonlinear regression analysis of the experimental data, allowing the three characterizing peak parameters (*i.e.* E''_{max}, ($m_{FK} \cdot E_a/R$), T_{max}) to vary. **Table 4.7** compiles the fit parameters corresponding at all the experimental frequencies studied and the corresponding values of m_{FK}. The variation of the relaxation times with temperature for the β process is shown in **Figure 4.24**. It can be seen that the relaxation times follows an Arrhenius behavior with activation energy of 59.8 ±0.1 $kJ \cdot mol^{-1}$, which is approximately 20% higher than that obtained by DRS measurements, 49.5±0.2 $kJ \cdot mol^{-1}$ (see **Table 4.4**). This difference can be associated to the different experimental frequency range covered for DRS and DMA measurements.

Table 4.7. Fuoss and Kirkwood fit parameters of β relaxation for 60VP-40BA sample.

***f*, Hz**	E''_{max}, ***MPa***	$m_{FK,\beta} E_a/R$, ***K***	$T_{max,\beta}$, ***K***	$m_{FK,\beta}$	***ΔE*, *MPa***
0.3	24.2±0.2	1804.9±44.0	171.8±0.2	0.25±0.01	193.0±3.4
1	23.4±0.1	1954.6±60.1	176.8±0.2	0.27±0.01	172.2±4.5
3	22.1±0.1	1705.0±21.7	181.2±0.1	0.24±0.01	187.0±2.0
10	21.1±0.1	1618.1±25.9	186.9±0.1	0.22±0.01	187.9±2.3
30	21.0±0.1	1646.2±42.2	193.2±0.2	0.23±0.01	183.3±3.9

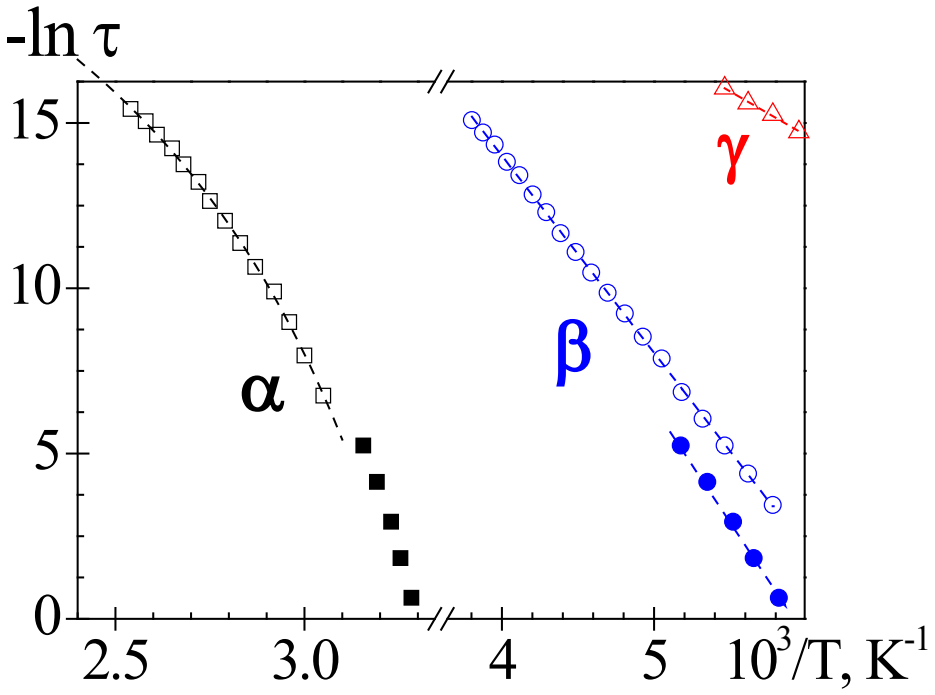

Figure 4.24. Arrhenius plot for the α (squares), β (circles) and γ (triangles) relaxations for *60*VP-*40*BA sample. Open symbols for dielectric results and full symbols for mechanical results.

As it is observed in **Table 4.7**, the values of $m_{FK,\beta}$ parameter do not show a noticeable dependence on the frequency of the isochrones. The low values obtained for this parameter seem to be an indication of the distributed character of the process. According to our results, the ΔE_β value remains nearly constant with the increasing frequency.

As stated in the previous section, the relaxations associated with the glass transition follow a behavior defined by the VFTH equation. In particular, for DMA measurements, Eq. (1.2) can be expressed as (McCrum, et al., 1991; Kremer, et al., 2003; Riande, et al., 2004; Vogel, 1921; Fulcher, 1925; Tamman, et al., 1926; Lunkenheimer, et al., 2000; Angell, 1995):

$$ln\, f = A - \left[\frac{M}{T_{max} - T_v}\right] \tag{4.12}$$

where A and M are constants, T_{max} is the temperature of the E'' maximum peak and T_v is the Vogel Temperature. The parameters of Eq (4.12) that fit the Arrhenius plots (see **Figure 4.24**) are A = (25.1±0.6), M = (1510.9±35.9) K and T_v = (247.0±0.1) K. As usual, the result for T_v is nearly 50 K below that of T_g, and is very similar to the T_v obtained by DRS (T_v = 249.5±1.8 K) (see **Table 4.3**). Besides, the M parameter, which corresponds to the product ($D_0 \cdot T_v$) of the equation Eq. (1.2), is very similar to the ($D_0 \cdot T_v$)=1472.05± 3.6 obtained by DRS.

Moreover, the activation energy of the α relaxation $E_a^{\alpha}\left(T_g\right)$ is also obtained using the Eq. (4.4). Thus, the $E_a^{\alpha}\left(T_g\right)$ value is 420.65±15 $kJ \cdot mol^{-1}$, which is slightly lower (~7.5% lower) than that obtained by DRS ($E_a^{\alpha}\left(T_g\right)$=452±26 $kJ \cdot mol^{-1}$) (see **Table 4.3**). As for the activation energy of the β process, this difference can be associated to the different experimental frequency range covered for DRS and DMA measurements.

As stated in the dielectric section, by comparing Eq. (4.12) with the Doolittle expression (Doolittle, 1951; Doolittle, 1952), the fraction of free volume at the glass transition temperature, ϕ_g/B, and the free volume expansion coefficient $\alpha_f = (1/V)(\partial V/\partial T)_p$ can be estimated. According to the Cohen-Turbull theory, B is a parameter close to the unit related to the ratio between the critical volume for a relaxation process to take place and the volume of the segments involved in the process (Bueche, 1959; Cohen, et al., 1959). The value of the relative free volume ϕ_g/B at T_g was 0.034±0.001, whereas the value of the thermal expansion coefficient of the free volume α_f at T_g amount to (6.6±0.2)×10^{-4} K^{-1}. As observed, the values obtained are in good agreement with those obtained from the dielectric measurements.

4.3. Conclusions

The copolymers with different contents of VP and BA were chemically designed in order to improve the properties of the homopolymers. The samples were characterized by means of FTIR, TGA, DSC, Mechanical and DRS techniques. The characterization carried out shows a correlation between the properties and the chemical composition.

According to TGA and mechanical results, thermal and mechanical stability is enhanced with the VP content. The WSPs of the samples are intimately related to the molar ratio of the highly hydrophilic lactam structure (VP) to the highly hydrophobic ester residue (BA). For all samples, the DRS spectra showed three dipolar relaxations (γ, β and α) and a conductive process specially important at low frequency and high temperatures. The DMA spectrum for the *60*VP/40BA is in good agreement to the one obtained from the dielectric measurements.

The dipole-dipole interactions between amide functions (Grigoraş, et al., 2008), which are verified by FTIR characterization, affected significantly several parameters related to the molecular mobility:

(i) The glass transition temperature. The evaluated T_gs for the *x*VP-*y*BA copolymer samples from DSC and DRS techniques are in agreement and show that the T_gs increase with the VP content due to a reduction of the molecular mobility.

(ii) The heat capacity at T_g. The highest value of the heat capacity at T_g is the corresponding to the *0*VP/*100*BA, whereas the lowest value of ΔC_p (T_g) is the obtained for the *100*VP/*0*BA. This is related to the reduction of mobility associated with the strong dipole-dipole interactions between VP units. For the *X*VP/*Y*BA

copolymer samples, the ΔC_p (T_g) values are practically constant and similar to the value obtained for *100*VP/*0*BA sample.

(iii) The α dielectric strength values for the *50*VP/*50*BA sample are higher than those ones obtained for the other two copolymers. This fact can be related to the dipole-dipole interactions between lactam groups that hindered the molecular motion.

(iv) The activation energy values. The activation energy of the γ process, related to local butyl units motions, increases with the VP content. Whereas, the activation energy of the β relaxation, which is a JG process related to the motions of the pyrrolidone group together with the polymer backbone segments, remains nearly constant with the composition. Finally, the E_a for the α process at T_g mainly increases for the highest VP content. Again, these tendencies can be related to the effect of the dipole-dipole interactions in the molecular mobility.

(v) The fragility values, which are influenced by intermolecular interactions, increases with the VP content. The obtained fragility parameters indicated that these copolymers are fragile glasses.

The conductivity measurement carried out was also analyzed by different procedures and the values obtained are in good agreement. Moreover, the σ_{dc} is observed to increase with the VP content. According to the ARRH plot, the *dc* charge transport is governed by both, the free volume and the temperature.

Finally, the temperature dependence of the decoupling index shows two tendencies at temperatures higher and close to T_g. Thus, at $T>>T_g$, the temperature dependence of the relaxation times of both α and σ processes is similar, but this dependence is different when

T is near T_g. Thus, the slowing down of the segmental motions is more intense than that of the charge carrier conducting motions at temperatures near glass transition.

Chapter 5:

Effect of Cross-linking on the Molecular Dynamics of the Vinylpyrrolidone- Butyl Acrylate Copolymers

Results presented in this Chapter have been collected in: **B. Redondo-Foj**, M. J. Sanchis, P. Ortiz-Serna, M. Carsí, J. M. García and F. García, *Soft Matter*, vol. 11, p. 7171–7180, **2015**.

Abstract

The effect of the cross-link density on the molecular dynamics of copolymers composed of VP and BA was studied using DSC and DRS. A single glass transition was detected by DSC measurements. The dielectric spectra exhibit conductive processes and three dipolar relaxations labeled as α, β and γ in decreasing order of temperatures. The cross-linker content affects both α and β processes, but the fastest γ process is relatively unaffected. An increase of the cross-linking produces a typical effect on the α process dynamics: (i) the glass transition temperature is increased, (ii) the dispersion is broadened (iii) its strength is decreased and (iv) the relaxation times are increased. However, the β process, which possesses typical features of a pure Johari-Goldstein relaxation, unexpectedly loses the intermolecular character for the highest cross-linker content.

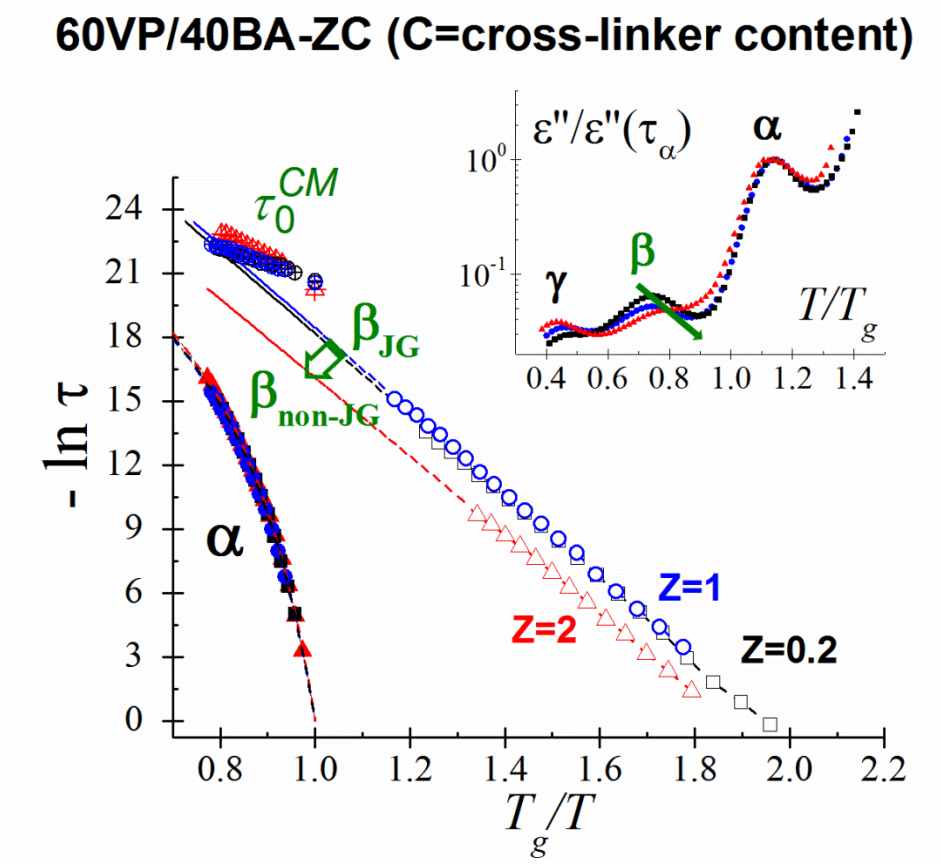

5. Effect of Cross-linking on the Molecular Dynamics of the Vinylpyrrolidone-Butyl Acrylate Copolymers

5.1. Introduction

As stated in Chapter 4, copolymers comprised of VP and acrylic or vinyl comonomers are commercially produced to modify, to improve and to adapt the properties of PVP to specific applications (Haaf, et al., 1985; Devine, et al., 2005; Devine, et al., 2006; Grigoraş, et al., 2008). Hence, acrylic chemicals are presented as versatile and inexpensive comonomers to prepare materials with specific properties. In particular, butyl acrylate is presented as a valuable acrylic comonomer for tuning the properties of PVP. The homopolymer from BA (PBA) is hydrophobic and has a glass transition of 219 K, while the PVP is an extremely hydrophilic polymer (uncross-linked PVP is water soluble), with glass transition of 448 K. Thus, copolymers comprised of VP and BA can be presented as tractable materials with moderate hydrophilicity and good mechanical and thermal properties.

In addition to analyzing the copolymerization effect on the polymer properties, the study of the cross-linking also results in interesting effects on the properties. The dynamics of cross-linked polymers is influenced by the network composition and the polymer chain architecture. As it is well-known, both the glass-rubber and the sub-glass transitions are highly sensitive to changes in the backbone structure, the cross-link density, and the introduction of pendant groups or branches. As a result, the relationship between network structure, chain dynamics and bulk properties of cross-linked polymers has been widely

studied in the literature using different techniques for a wide range of material systems (Borns, et al., 2007; Qazvini, et al., 2005; Cook, et al., 2004; Viciosa, et al., 2007; Jobish, et al., 2012; Bekin, et al., 2014). In particular, the dielectric relaxation spectroscopy (DRS) is presented as one of the most powerful techniques to study the chain dynamics of solid polymers with temperature and frequency. This technique enables the analysis of the chains response over more than 10 decades in the frequency domain (Kremer, et al., 2003).

As previously reported, the introduction of network junctions due to cross-linking is reflected in the increase in the glass transition temperature (T_g) (Roland, 1994; Patil, et al., 2013). The effect of cross-linking in the segmental transition, also called α relaxation, usually broadens the dispersion and makes its relaxation time more sensitive to temperature, that is, the material becomes more fragile. On the other hand, it is found that the cross-linking may produce different effects in the sub-glass transitions, which may be related to their molecular origin (Casalini, et al., 2010; Carsí, et al., 2012; Carsí, et al., 2013; Kalakkunnath, et al., 2007; Sabater i Serra, et al., 2009). Thus, as previously introduced in subsection 1.2.2.3, the secondary relaxations can have an intramolecular origin or an intermolecular origin (JG relaxations). Thus, to know whether the secondary relaxations have an intra- or intermolecular origin, Ngai et al proposed the comparison of the JG secondary relaxation time, τ_{JG}, and the primitive (non-cooperative) relaxation time, τ_0^{CM}, of the Coupling Model (CM). A secondary relaxation is considered a JG relaxation when its relaxation time, τ_β, obeys the Eq. (1.37).

At any temperature, τ_0^{CM} can be calculated by the CM as $\tau_0^{CM} = t_c^n \cdot (\tau_\alpha)^{1-n}$, where t_c is about 2 ps and n is the coupling parameter. The coupling parameter can be evaluated as n =

(1-β_{KWW}), where β_{KWW} parameter is the stretch exponent of the KWW equation (Eq. (1.31)), that lies in the range 0–1 and quantifies the extent of deviation from pure exponentially, *i.e.* the degree of the relaxation time dispersion. The case $\beta_{KWW} = 1$ refers to simple exponential behavior.

In the previous chapter, the effect of copolymer composition in a family of VP and BA copolymers with a different proportions of monomers and a fixed cross-linker molar ratio of 1% was studied using different characterization techniques. The dielectric spectra showed three relaxations, γ, β and α, followed by conductive processes. It was observed dipole-dipole interactions between the lactam groups of VP, which was found to exert an important influence in the molecular mobility. A single T_g was detected by DSC measurements showing the copolymer miscibility, and it was found to be strongly dependent of the composition. The γ process was related to local motions while the β process was assigned to a JG process.

In this chapter, the effect of the cross-linking on the dynamics of 60VP/40BA copolymer is examined. This copolymer ratio was chosen because this sample has the most balanced properties compared with other compositions. The study is mainly focused on the segmental and the JG processes due to their intermolecular character. A detailed comparative analysis between the samples with different cross-link densities will be carried out.

5.2. Results and Discussion

5.2.1. Sample hydrophilicity characterization

As stated in the subsection 4.2.1, the water-swelling percentage of the samples at a given conditions can be related to its hydrophilic character. The WSP values obtained for 60VP/40BA-0.2C, 60VP/40BA-1C and 60VP/40BA-2C samples were 70, 60 and 50%, respectively. As observed, the WSP is intimately related to the cross-linker agent content. Thus, the increase of the cross-link density physically impairs the water uptake and hinders the interactions between the 2-pyrrolidone units and water.

5.2.2. MDSC Measurements

The DSC thermograms (reversing curves) obtained for all the samples are plotted in **Figure 5.1**, and their characteristic temperatures (T_g, T_{on}, T_{end}) and the associated Heat Capacity changes (ΔC_p) and moisture percentages of *60*VP/*40*BA-*Z*C (*Z*=0.2, 1 and 2) samples are summarized in **Table 5.1**.

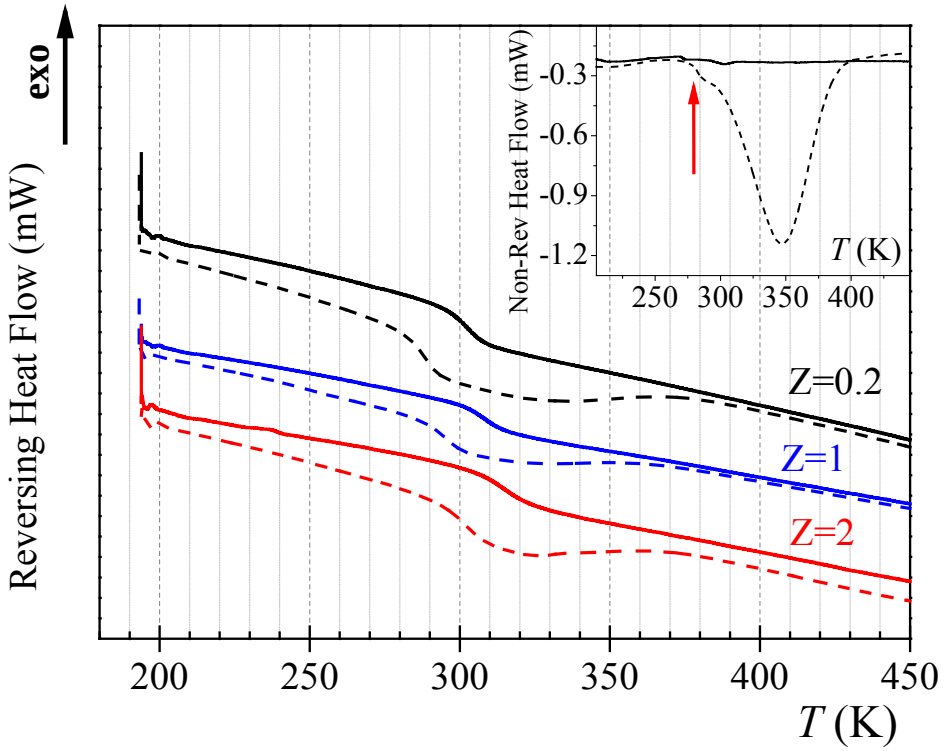

Figure 5.1. MDSC thermograms (reversing curves) for *60*VP/*40*BA-*Z*C samples: (i) 1st heating ramp (dashed lines) and (ii) 2nd heating ramp (continuous lines). Data are vertically shifted for a better visualization. Inset: Non-reversing curve for the *60*VP/*40*BA-*0.2*C sample.

All DSC thermograms present a first step related to the glass rubber transition temperature, which is well-defined in both the first and the second reversing curves. A single T_g is observed showing the copolymer miscibility. This first step is well-defined in both the first and the second reversing curves but appears at lower temperatures in the first heating ramp, due to the plasticizing effect of water. On the other hand, it is observed an increase of the T_g value of about 12K with the increase of cross-linking. This is due to the decrease in the mobility imposed by the cross-links to segmental motion. Moreover, the width of the glass transition ($\Delta T=T_{end}-T_{on}$) also increases with the cross-linker content. ΔT parameter gives a qualitative indication of the relative homogeneity of the system because it may reflect the magnitude of local compositional fluctuations (Bershtein, et al., 2002).

Hence, this broadening is due to an increase in small-scale compositional fluctuations in the copolymer related to the cross-linking. Additionally, the constraints imposed by the cross-links also results in a decrease in ΔC_p (T_g), related to the presence of orderly packing of polymer molecules, which lowers the mobility at T_g (Alves, et al., 2005; Scott, et al., 2002). It is noteworthy that the ΔC_p value may include enthalpy contribution from the breaking of dipole-dipole bonds during heating.

Table 5.1. Characteristic Temperatures and Heat Capacity Change and Moisture of *60*VP/*40*BA-*Z*C (*Z*=0.2, 1 and 2) samples.

Sample	***Z*=0.2**	***Z*=1**	***Z*=2**
	First Heating Ramp (wet samples)		
$T_g^{MDSC}(K)$	288.7	295.2	302.2
$T_{on}(K)$	282.1	289.3	295.4
$T_{end}(K)$	293.8	301.7	310.3
$\Delta T(K)$	11.7	12.4	14.9
$\Delta C_p(J/gK)$	0.264	0.242	0.231
Moisture (%)	4.5	3.8	3.5
	Second Heating Ramp (dry samples)		
$T_g^{MDSC}(K)$	302.4	308	314.6
$T_{on}(K)$	296.0	301.8	308.3
$T_{end}(K)$	307.9	314.9	322.9
$\Delta T(K)$	11.9	13.1	14.6
$\Delta C_p(J/gK)$	0.201	0.163	0.158
$\Delta T_g(K)$	26.8	34	46.29
$^{\#}T_g^{DRS}(K)$	291.5	298.6	310.5

$^{\#}T_g^{DRS}(K)$ evaluated at τ=100 s

The thermograms, in the non-reversing curves, also present a small endothermic peak related to the enthalpy relaxation and located next to the step of the glass rubber transition. While the T_g is well-defined in both the first and the second reversing curves, the endothermic peak is only partially observed in the first non-reversing curve. Furthermore, this peak is more clearly detected for the sample containing a 0.2% of cross-linker (see arrow in the inset of **Figure 5.1**). The enthalpy relaxation or physical aging may appear when a sample has been storage below its glass transition temperature during a certain period of time and it only appears as an endothermic relaxation peak in the first measurement (Cugini, et al., 2014; Odegard, et al., 2011; Hodge, 1983; Modulated DSC® Paper #5 Measurement of Glass Transitions and Enthalpic Recovery, 2005). On the other hand, the endothermic peak can also be produced due to the relaxation of internal stresses, like those originated in the processing conditions to get films. Hence, the previously stressed molecules are able to rearrange in the T_g region, absorbing energy in the process (Gabbott, 2008). For this reason, the first heating ramp was performed in order to remove the possible thermal and mechanical history of the samples.

Additionally, the non-reversing curve in the first heating ramp also exhibits a broad endothermic peak at about 373 K, related to the evaporation of the moisture. This is due to the hydrophilic character of the *60*VP/*40*BA-*Z*C samples, which are able to absorb water from the atmosphere (moisture) as reported for *X*VP/*Z*BA copolymer samples in Chapter 4. The broadness of the evaporation peak partially hides the enthalpy relaxation placed next to the glass transition. From the evaporation heat of bulk water (2400 *J/g* at 100 ºC), the amount of water present in the samples was estimated and the moisture percentages are collected in **Table 5.1**. As it is observed, the amount of moisture decreases with the cross-

linker content. This may be due to the fact that the cross-linking hinders the formation of hydrogen bonds between water molecules and 2-pyrrolidone units. As explained above, there is a difference between the T_g values calculated in the first (T_{g1}) and second (T_{g2}) heating ramps ($\Delta T_g = T_{g2} - T_{g1}$), due to the plasticizer effect of water. Thus, ΔT_g increases with the moisture content, confirming the influence of water in the T_g value.

5.2.3. Mechanical properties

As stated in Chapter 4, the mechanical properties are related to the chemical composition of every material. As it is expected, the increase of the cross-linker content, from *Z*=0.2 to *Z*=2 (*60*VP/*40*BA-*Z*C), involves a reduction in the elongation, along with a concomitant hardening of the materials showing by the increase of the Young´s modulus (**Table 5.2**).

Table 5.2. Thickness and mechanical properties of the 60VP/40BA copolymer as a function of the cross-linker agent content.

Sample	***Z*=0.2**	***Z*=1**	***Z*=2**
sample thickness (μm)	115	115	115
Young modulus[#] (MPa)	187^b	200^a	286^a
Tensile strength[#] (MPa)	15^b	15^a	19^a
Elongation[#] (%)	900^b	540^a	390^a

[#]Extension rate of 5^a or 10^b mm·min^{-1}

5.2.4. DRS measurements

This chapter is focused on the analysis of the cross-linker content effect on the dynamic mobility of the *60*VP/*40*BA copolymer. Previously in the Chapter 4, a detailed

analysis of the sample with 1% of cross-linked (*60*VP/*40*BA-*1*C) was already reported. Therefore, additionally other two *60*VP/*40*BA-*Z*C copolymers with a lower (Z = 0.2) and a higher (Z=2) cross-linker content are analyzed in this chapter.

Figure 5.2a shows the temperature dependence of the dielectric permittivity [inset of **Figure 5.2a**] and loss factor, at 1.13 10^4 Hz, for the three samples analyzed. As it is observed, the position of the peaks shifts to higher temperatures with the increase of cross-linker content and the relaxation curves tend to broaden. This shift indicates the increase of the T_g with the cross-link density. In addition, a decrease in the intensity of the loss peaks is observed as the cross-linking increases. It is especially remarkable the case of β relaxation, whose intensity decreases significantly with the cross-linking. In a previous work (Carsí, et al., 2012), a significant effect of the cross-linking on the β relaxation was also observed. In that work, when the poly(2-ethoxyethyl methacrylate) was cross-linked using 2.5% (mol) of ethylene glycol dimethacrylate, the β peak completely disappeared from the spectra.

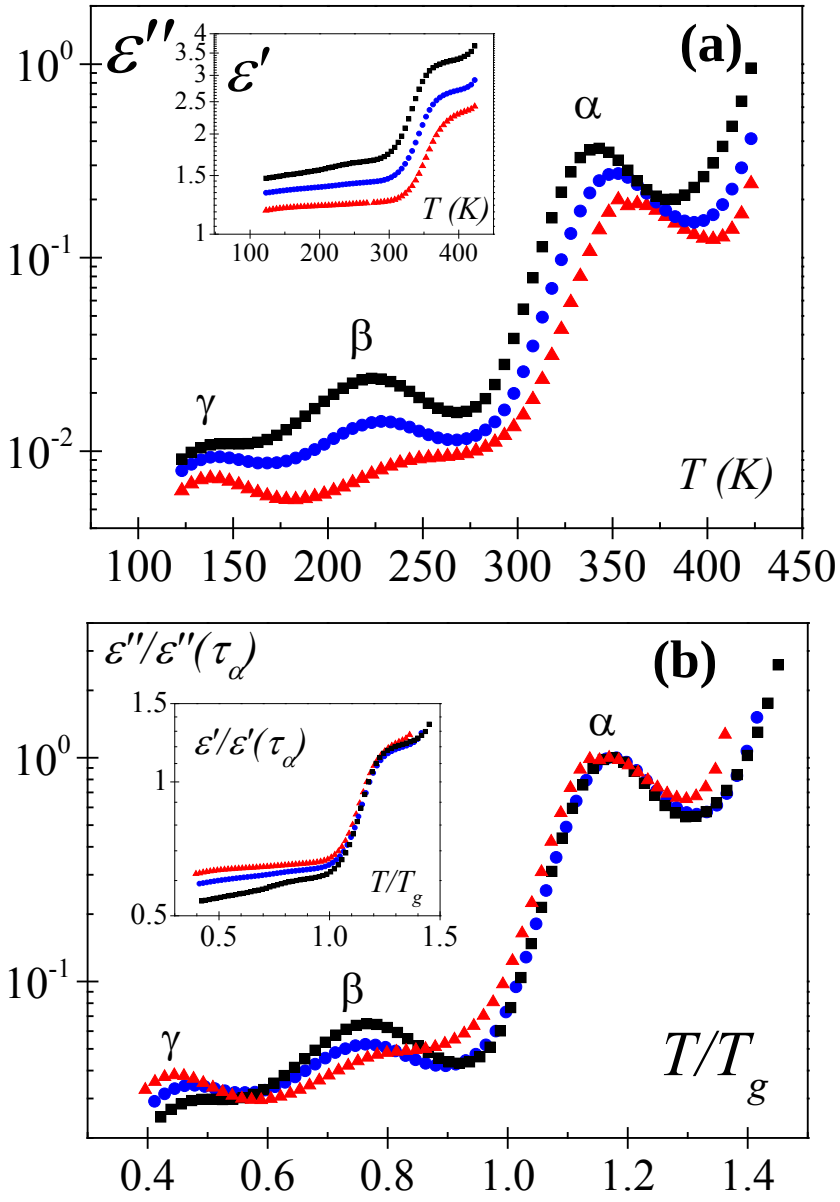

Figure 5.2. (a) Temperature dependence of the dielectric and loss permittivity at $1.13 \cdot 10^4$ Hz for *60*VP/*40*BA-*ZC* samples with Z=0.2 (square), Z=1 (circle) and Z=2 (triangle). **(b)** Temperature dependence of the normalized permittivity at $1.13 \cdot 10^4 Hz$ ($\varepsilon''(\tau_\alpha)$ is the permittivity at the characteristic time (τ_α=100s) for α relaxation).

On the other hand, in order to establish a better comparison of the samples, the normalized curves are also represented in **Figure 5.2b**. The growth in the breadth indicates qualitatively a broader distribution of relaxation times. It is also observed a significant

increase of the loss factor at high temperatures that is associated with the conductivity contribution. The conductive processes can be originated not only by the migration of mobile charge carriers across the medium, but also by the trapping of charges at interfaces and boundaries. Thus, this additional polarization is the result of (i) accumulation of charges at the electrode-sample interface, called "electrode polarization" (EP) (Kremer, et al., 2003) and/or (ii) the separation of charges at internal phase boundaries referred to as Maxwell-Wagner-Sillars (MWS) polarization (Wagner, 1914; Sillars, 1937).

In order to obtain a better visualization of the effect of the cross-linker content on the conductive processes, it is advisable to use other formalisms for the data representation: (i) the dielectric loss modulus $M''(\omega)$ evaluated from $M^*(\omega) = M'(\omega) + iM''(\omega) = 1/\varepsilon^*(\omega)$ (Hodge, et al., 2005), where $\omega = 2\pi f$ is the angular frequency, (ii) the $\tan\delta(\omega) = \varepsilon''(\omega)/\varepsilon'(\omega)$ and (iii) the real part of the complex conductivity, $\sigma'(\omega) = \omega\varepsilon_0\varepsilon''(\omega)$, since the EP and MWS contributions are better visualized. The normalized isochrones of ε'', M'', $tan\ \delta$ and σ' at 75K above T_g for the three samples are represented in **Figure 5.3**. In the low frequency zone, the sample with the highest cross-linker content shows a more complicate spectrum. Thus, the slope of the loss factor is reduced, whereas the breadth of the loss modulus peak is increased with the cross-linker content. On the other hand, two overlapping conductive processes appear in the spectrum when the dielectric data are plotted in terms of *tan δ*. The same effect is visualized when the real part of the complex conductivity is represented. In **Figure 5.3**, the high frequency conductive process is noted as MWS. This process is generally evident in non-homogenous materials like multiphase polymers, blends and colloids, crystalline or liquid crystalline polymers, composites, etc. and occurs across smaller size scales when comparing to the electrode polarization. The

MWS effects are more pronounced for conductive materials and, in certain cases, this large-scale polarization can mask the dielectric orientation response of the material.

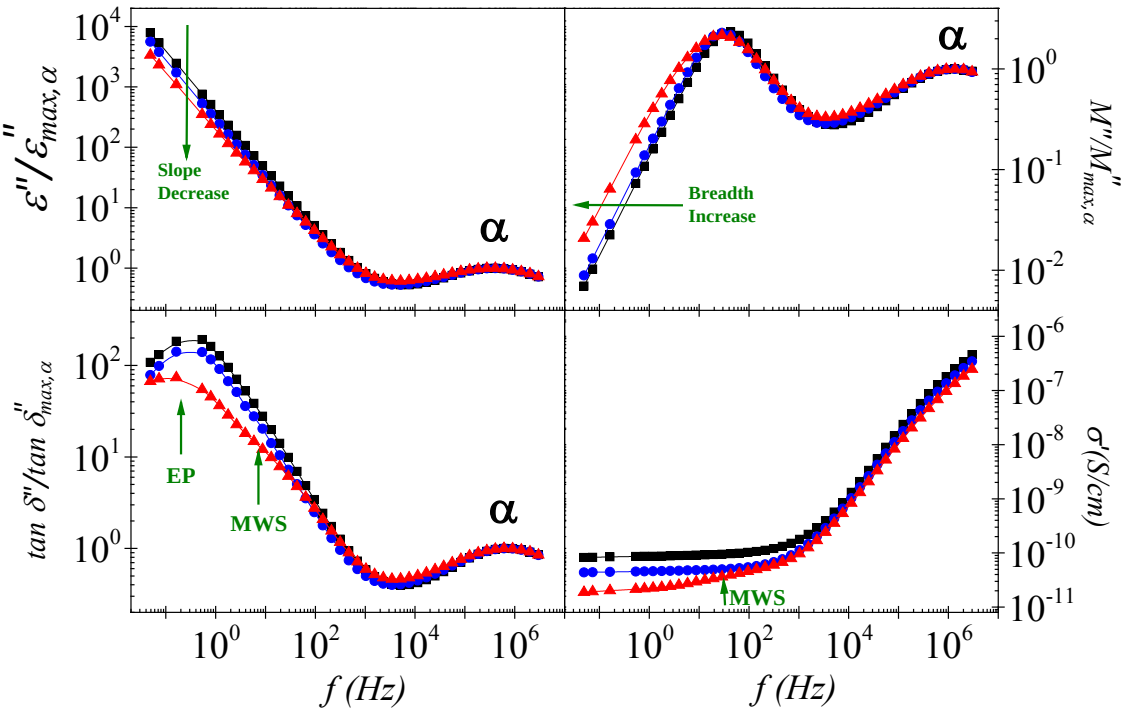

Figure 5.3. Frequency dependence of ε'', M'', *tan* δ and σ' at (T_g+75K) for *60*VP/*40*BA-*Z*C samples with Z=0.2 (square), Z=1 (circle) and Z=2 (triangle).

Although the Kohlrausch-William-Watts (KWW) (Williams, et al., 1970; Williams, et al., 1971) and the Havriliak-Negami (HN) (Havriliak, et al., 1967; Havriliak, et al., 1966) formalisms are equally able to fit the experimental data for the uncross-linked copolymer, the HN formalism provided superior fits at high levels of cross-linking.(Glatz-Reichenback, et al., 1994) For this reason, the analysis of the dielectric spectra was made in the frequency domain by using the empirical equation of HN, which relates the complex permittivity (ε*) to the frequency by Eq. (1.23). The HN fit was carried out in two different zones in order to facilitate the characterization of the dipolar and conductive processes. As an example, the deconvolution procedure is depicted in **Figure 5.4** for two isothermals, one of them in the

high temperature zone (conductivity and α processes) and the other one in the low temperature zone (β and γ processes).

In the low temperature zone, an additive rule for the permittivity was assumed for the analysis of the dielectric loss spectra of the secondary processes(Donth, 1996).

$$\varepsilon^*_{dip}(\omega) = \mathrm{Imag}\left[\sum_{i=1}^{2} \frac{\Delta\varepsilon_i}{\left[1+\left(i\omega\tau_{HN,i}\right)^{a_{HN,i}}\right]^{b_{HN,i}}}\right] \tag{5.1}$$

The HN parameters of the two secondary relaxations were determined at several temperatures from a multiple non-linear regression analysis of the experimental data. The four characterizing peak parameters ($\Delta\varepsilon_i$, $\tau_{HN,i}$, $a_{HN,i}$, $b_{HN,i}$) were allowed to vary and the obtained values are plotted in **Figure 5.5** to **Figure 5.7**.

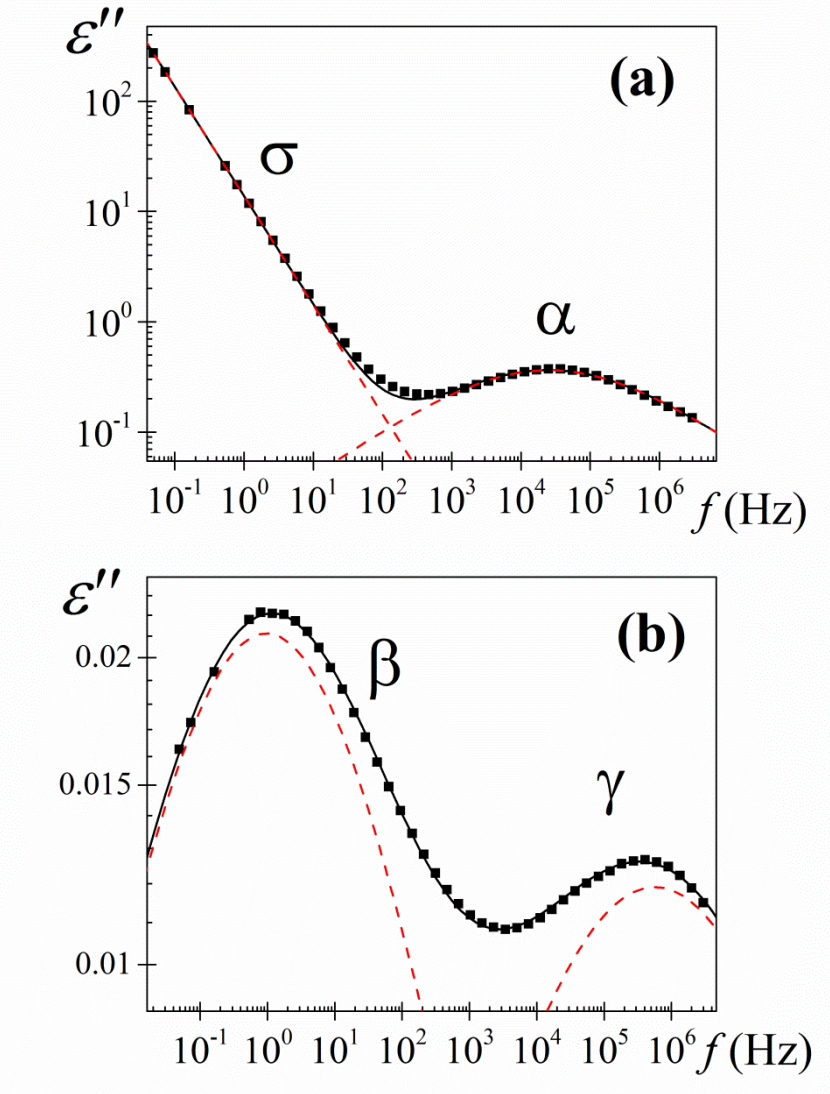

Figure 5.4. Deconvolution of loss factor for 60VP/40BA-0.2C **(a)** conductivity and α processes at 348K and **(b)** β and γ processes at 163K. Squares represent the experimental data, continuous line the HN fitting curve, and dashed lines the individual processes.

In the high temperature zone, where the conductive process is dominant, we have included a new term in order to characterize the spectra: $\varepsilon^*(\omega)=\varepsilon^*_{dip}+\varepsilon^*_{cond}$ with $\varepsilon^*_{cond}(\omega)=(i\sigma/e_0\omega)^s$ where e_0 is the permittivity of free space (e_0= 8.854 pF·m^{-1}), σ is the conductivity arising from charges transport at the liquid-electrode interface and s is a constant ($s\leq1$), which was approximately one for all the samples. For the Z=2 sample, it

was necessary to limit the fitting parameters due to the presence of MWS process at intermediate frequencies between the α and conductivity processes. However, it was not possible to characterize the MWS process because it is not clearly defined in our spectra (see **Figure 5.3**).

The temperature dependence of the relaxation strength, for all relaxation processes, is shown in **Figure 5.5**. For β and γ processes this dependence follows the classical trends, that is, the dielectric strength increase or nearly remain constant with the temperature. This fact is consistent with a thermally activated mechanism because the dipole mobility rises with the temperature, associated with the free volume increase. Non-significant changes in the dielectric strength for the γ absorption with the cross-linker content are observed. However, for the β absorption a significant reduction in the relaxation strength is observed for the samples with a Z=1 and Z=2 cross-linker content.

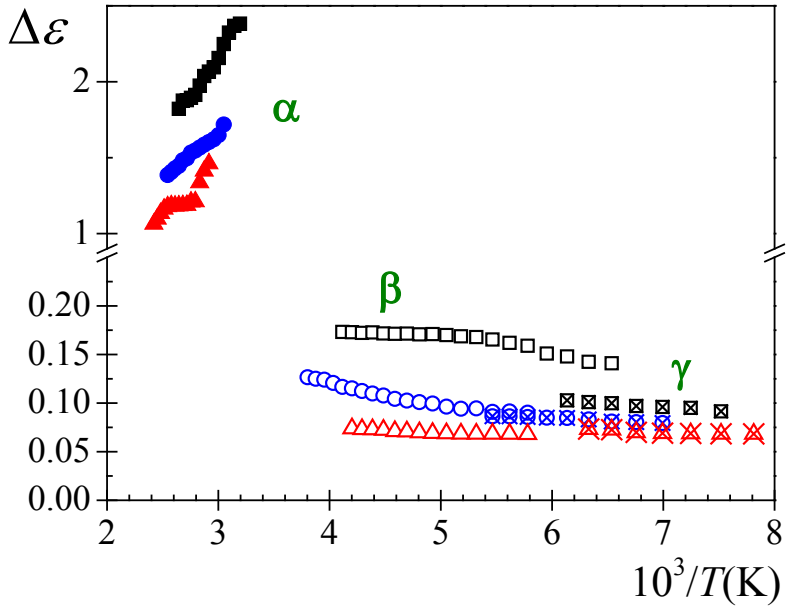

Figure 5.5. Temperature dependence of the strengths of the *60*VP/*40*BA-*Z*C samples (*Z*=0.2 squares, *Z*=1 circles and *Z*=2 triangles) for α (full symbol), β (open symbol) and γ (cross symbol) relaxations.

On the other hand, the α relaxation strength decreases with both temperature and cross-linker content. This is due to the fact that the thermal energy disturbs the alignment of the molecule dipoles that intervene in the cooperative motions and the cross-linking produces a reduction in the molecular mobility, as observed in other polymers (Glatz-Reichenback, et al., 1994; Roland, 1994).

Figure 5.6 shows the temperature dependence of the a_{HN} shape parameters associated with all relaxation processes present in the *60*VP/*40*BA-*Z*C samples (*Z*=0.2, 1 and 2). For the α process the a_{HN} parameter increases with temperature, that is, the dielectric loss peak narrows. However, a_{HN} parameter decreases with the cross-linker content. The chains may experience different motions depending on their environment. Thus, the ones near the cross-link sites are in restricted environments, while those between cross-link sites will

have a relaxation behavior similar to the uncross-linked polymer. Accordingly, a higher distribution in the local environment of the single relaxing segments with cross-linking content may lead to a broadening of the relaxation (Roland, 1994). On the other hand, a non-defined tendency is observed in the temperature dependence of the a_{HN} parameter for the β and γ processes.

The value of b_{HN} shape parameter was one at all temperatures investigated for all the processes independently of the cross-linker content. Thus, the Eq. (1.23) reduces to the Cole-Cole equation (Donth, 1996) that describes a relaxation with a symmetric distribution of relaxation times. Although for amorphous polymers, a non-symmetric distribution of times is expected for the α relaxation, associated with macromolecular segmental motion at temperatures immediately above the T_g, symmetrical distributions have been observed for several heterogeneous systems (Boyd, 1985; Laredo, et al., 2003; Huo, et al., 1992; Noda, 2005; J. Polym. Sci. Part B Polym. Phys., 2003; Janik, et al., 2001; Feldman, et al., 2002; Ortiz-Serna, et al., 2010; Ortiz-Serna, et al., 2011).

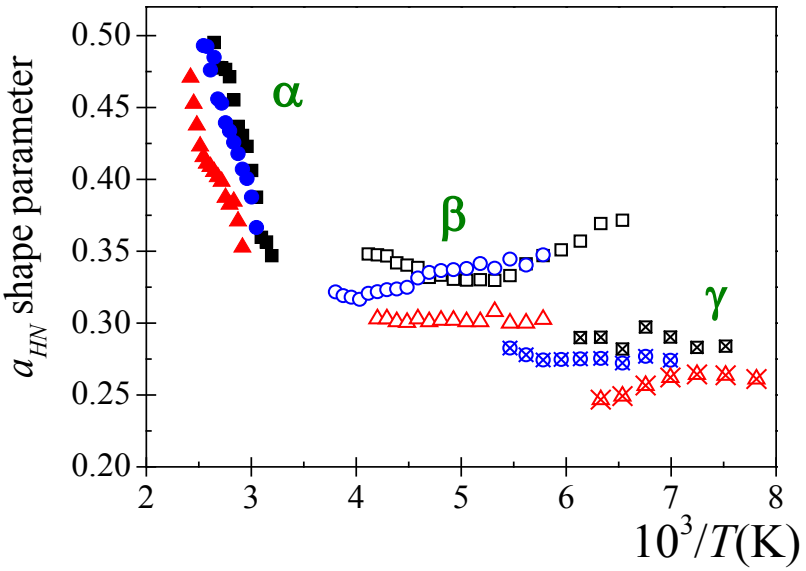

Figure 5.6. Temperature dependence of the shape parameters a_{HN} of the *60*VP/*40*BA-*Z*C samples (*Z*=0.2 squares, *Z*=1 circles and *Z*=2 triangles) for α (full symbol), β (open symbol) and γ (cross symbol) relaxations. For all processes, b_{HN} =1.

The temperature dependence of the relaxation times, which is associated with the peak maxima of the primary and secondary absorptions, is shown in **Figure 5.7**. According to our results, the relaxation time increases with the increase of cross-link density. This is reflected in the increase of T_g due to the molecular motion slowdown of the polymer chains. **Figure 5.7** also shows the temperature dependence of dc-conductivity (σ_{dc}). It is observed that σ_{dc} at a constant temperature diminishes with the cross-linker content. Thus, the constraints imposed by cross-linking could hinder the diffusion of charge carriers and, consequently, the conductivity decreases.

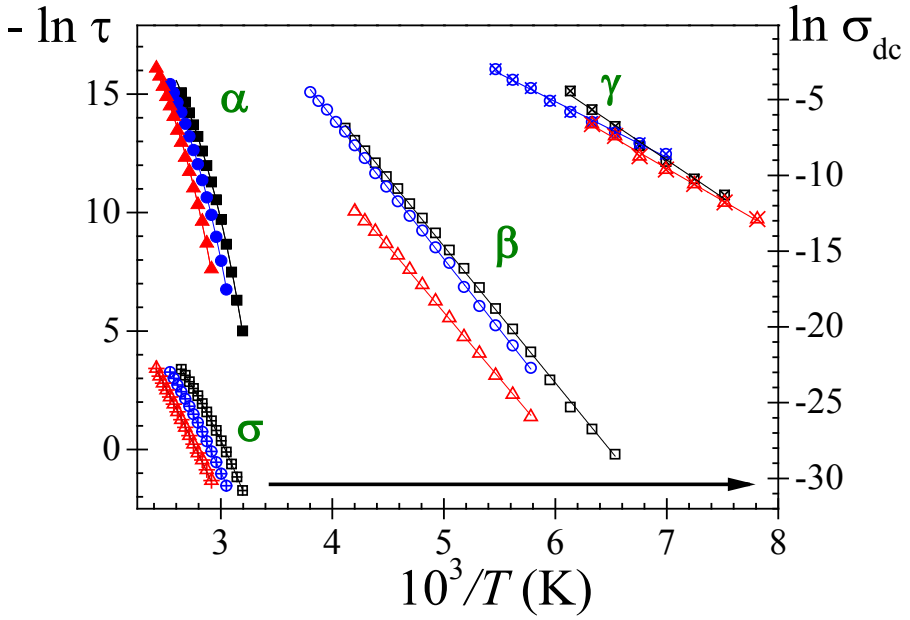

Figure 5.7. Temperature dependence of the relaxation times (left-Y axis) and ionic conductivity (σ) (right-Y axis), for *60*VP/*40*BA-*Z*C samples with *Z*=0.2 (square), *Z*=1 (circle) and *Z*=2 (triangle). Continuous lines represent the VFTH fitting for α and σ processes and the Arrhenius fitting for β and γ processes.

As usual, the average relaxation time associated with the α relaxation is described by VFTH equation (Eq. (1.2)). Values of the τ_0, T_v and D_0 parameters, obtained by fitting the Eq. (1.2) to the experimental results, are collected in **Table 5.3**. The values of T_v are nearly 50K below those of T_g. Moreover, the strength coefficient obtained for these samples are lower than 10, the frontier that separates fragile ($D_0 < 10$) from strong ($D_0 > 10$) glasses (Angell, 1995; Angell, 1996; Bermejo, et al., 1997).

The deviation from the Arrhenius behavior can be quantified by the strength coefficient (D_0) of Eq. (1.2) or by determining the slope at T_g of the curves in the Angell plot (Bohmer, et al., 1993; Bohmer, et al., 1992; Bohmer, et al., 1993; Williams, 1979) (see **Figure 5.9**). Thus, the dynamic fragility index, *m*, can be evaluated by the expression

previously reported in Chapter 4:

$$m = \frac{D_0 \cdot T_v}{2.303 \cdot T_g \cdot \left(1 - T_v / T_g\right)^2} \tag{5.2}$$

Fragility values typically range between m=16, for strong systems, and m=200 for the fragile ones.(Merino, et al., 2011) The values of m, collected in **Table 5.3**, show that, for the *60*VP/*40*BA-*Z*C copolymer samples the dynamic fragility index slightly increases with the T_g. This trend is in agreement with the Angell's energy landscape model (Angell, 1995; Angell, 1991).

As explained in Chapter 4, the apparent activation energy associated with the relaxation dynamics of the chains at T_g can be obtained from the dynamic fragility index as $E_\alpha\left(T_g\right) = 2.303 \cdot R \cdot m \cdot T_g$. Values of $E_\alpha\left(T_g\right)$ are shown in **Table 5.3**. Within the uncertainty of calculated values, it can be observed an increase of the $E_\alpha\left(T_g\right)$ with the cross-linker content.

The obtained values of m and $E_\alpha\left(T_g\right)$ were found slightly lower when comparing with the ones calculated by using the empirical expressions proposed by Qin and McKenna(Qin, et al., 2006) for polymers: $m^* \approx 0.28\left(\pm 0.067\right)T_g + 9\left(\pm 20\right)$ and $E_a^{\alpha *}\left(T_g\right) = \left[0.006\left(\pm 6.5 \cdot 10^{-4}\right)T_g^2\left(K\right) - 35\left(\pm 66\right)\right]$ (kJ·mol^{-1}) (see **Table 5.3**). However, the same tendency in the values was observed for both methods.

On the other hand, for the γ and β absorptions, the temperature dependence of the relaxation times follow Arrhenius (ARRH) behaviour ($\tau_{\max} = \tau_\infty \cdot \exp\left[E_a / RT\right]$). The

activation energies (E_a) and pre-exponential factors (τ_∞) obtained are summarized in **Table 5.3**. The $\left(E_{a\gamma}/RT_g\right)$ is not significantly affected by the cross-linker content. However, the $\left(E_{a\beta}/RT_g\right)$ value is similar for the Z=0.2 and Z=1 samples, but it decreases with the highest cross-link density.

According to the previous results of Chapter 4, the slower β relaxation for the sample with Z=1 is a JG process, whereas the faster γ relaxation is related to the local motions. So, the γ and β processes have intra- and intermolecular origin, respectively.

In order to analyze the effect of the cross-linker content on the intra/intermolecular origin of both secondary relaxation processes, the CM analysis proposed for Ngai et al. (Ngai, 1998; Ngai, et al., 2004; Ngai, et al., 2007; Paluch, et al., 2005; Casalini, et al., 2003) is carried out, which is briefly described in the introduction part. We have analyzed two samples with lower (Z=0.2) and higher (Z=2) cross-linker content than the previously analyzed (Z=1). For this purpose, the normalized α relaxation in the time domain, $\phi(t)$, was calculated from the retardation time spectra (Tamman, et al., 1926; Kohlrausch, 1854) by using the HN fit parameters (Kremer, et al., 2003; Reiner Zorn, 1999). for each sample (**Figure 5.8 (a)** to **(c)).** From the fitting of $\phi(t)$ to the Eq. (1.31), the α characteristic relaxation time (τ_{KWW}) and the stretch exponent (β_{KWW}) for the three samples analysed were obtained (see inset **Figure 5.9**). The evolution of the τ_{KWW} with the temperature obeys the VFTH equation, whereas β_{KWW} increase with temperature. This can be related to the decrease of intermolecular constraints (or coupling) between the relaxing units. On the other hand, this parameter, within the uncertainty of calculated values, is nearly independent of the cross-linker content at temperatures near T_g. So, the cross-linking does

not affect significantly the strength of the intermolecular constraints on segmental relaxation at temperatures near T_g (see **Table 5.3**). However, at higher temperatures the β_{KWW} parameter decreases with the cross-linker content (Roland, 1994; Casalini, et al., 2010). As the cross-linking content increases, the heterogeneity is higher, so the β_{KWW} parameter decreases. Furthermore, the temperature dependence of β_{KWW} parameter exhibits a slope change for the Z=2 sample at high temperatures. This change could be related to the possible effect of the MWS process presence in the HN fitting of the α-process.

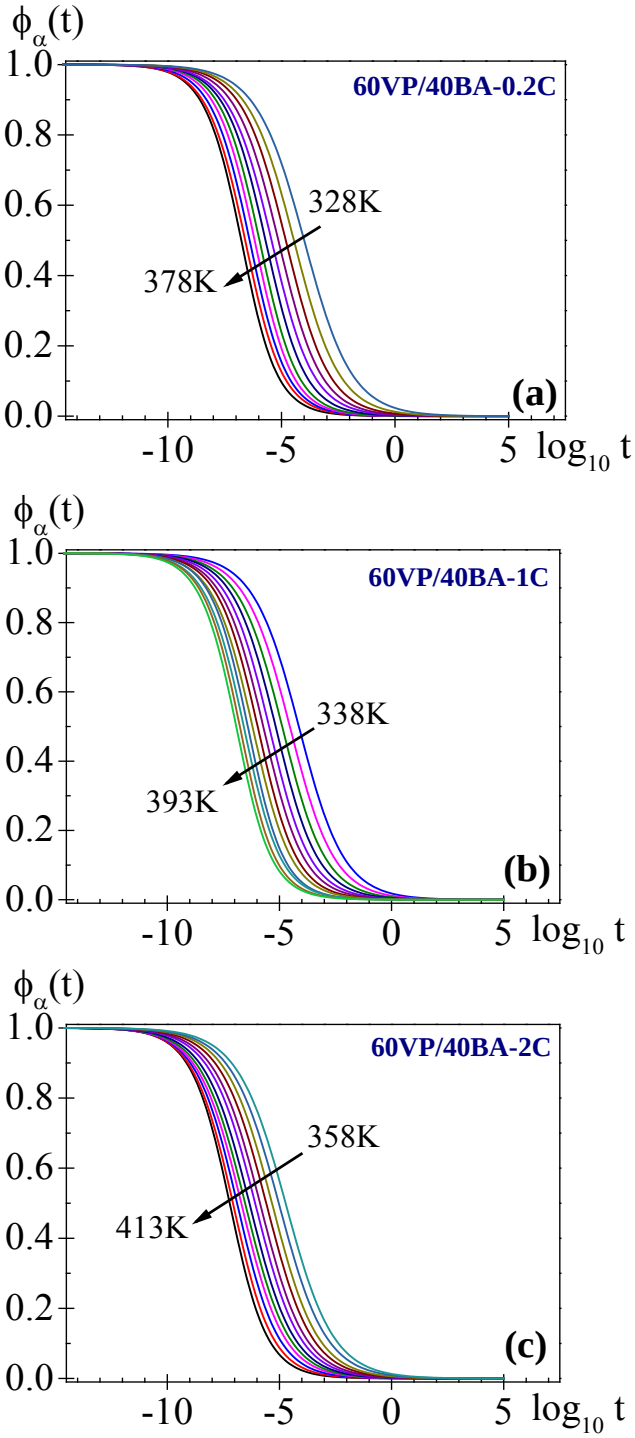

Figure 5.8. Normalized relaxation curves in the time domain for the α relaxation of *60*VP/*40*BA-*Z*C samples **(a)** *Z*=0.2, **(b)** *Z*=1 and **(c)** *Z*=2

According to the CM [Eq. (1.37) and Eq.(1.38)] and taking into account that (i) the T_g

is defined as the temperature at which the dielectric relaxation time $\tau_{KWW} \approx 100s$ and (ii) the secondary relaxations have Arrhenius temperature dependence, the ratio $\left(E_a^i/RT_g\right)$, with *i*=β and γ, can be evaluated as a function of *n* and τ_∞ parameters as follows: $\left(\frac{E_a^i}{RT_g}\right) = 2.303\left[(1-n)\log_{10}\tau_\alpha\left(T_g\right) + n\log_{10}t_c - \log_{10}\tau_{\infty i}\right]$(Ngai, et al., 2004). In **Table 5.3** are collected the values of the ratio $\left(E_a^i/RT_g\right)$ evaluated by both the CM and the experimental data. Thus, the $\left(E_a^\gamma/RT_g\right)_{\text{expt}}$ values are lower than $\left(E_a^\gamma/RT_g\right)_{CM}$ values for the three samples, which confirm that the γ process has an intramolecular character. On the other hand, $\left(E_a^\beta/RT_g\right)_{\text{expt}}$ value is similar to $\left(E_a^\beta/RT_g\right)_{CM}$ value for the samples with *Z*= 0.2 and 1, but these values are different for the *Z*=2 sample. These results confirm that the β process is a JG relaxation for *Z*=0.2 and 1, but it changes its behaviour for Z=2. Moreover, the $\left(E_a^\beta/RT_g\right)$ value for *Z*=2 is lower than those obtained for *Z*=0.2 and *Z*=1.

In order to analyze the inter/intramolecular character of the α and β processes the Angell plots(Angell, 1991) are represented in **Figure 5.9**. The increase in cross-linking only leads to a faintly increase in the cooperativity inherent to the α process related to the glass transition (Roland, 1994; Kalakkunnath, et al., 2007; Ngai, et al., 1993). Many authors have assumed a strong connection between fragility and cooperativity (Ngai, et al., 1993; Ngai, 2011; Ikeda, et al., 2010; Patkpwski, et al., 2003; Delpouve, et al., 2014), with some evidence of a linear relation between them at the glass transition. In our case, both parameters do not change significantly with the cross-linker content. On the other hand, **Figure 5.9** evidences for the β process differences between the samples with *Z*=0.2 and 1

respect to that with Z=2. This behavior can be related to the effect of the cross-linker agent on the inter/intramolecular character of the β process, evidenced previously for the CM.

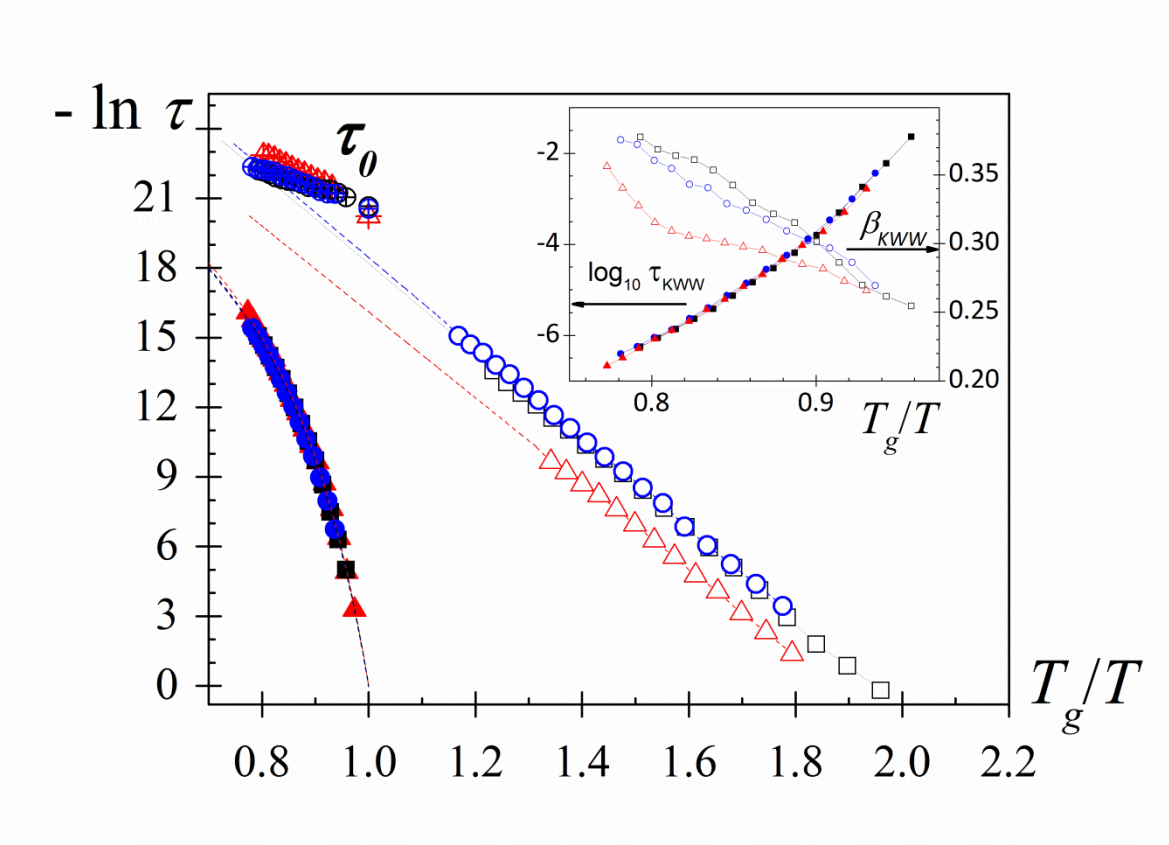

Figure 5.9. Angell plot of the α and β relaxations of *60*VP/*40*BA-*Z*C samples with Z=0.2 (square), Z=1 (circle) and Z=2 (triangle). The symbols with a cross represent τ_0^{CM} values obtained according to the CM. Dashed lines correspond to the fitting. The glass transition temperatures used to scale the data are collected in **Table 5.1**. Inset: temperature dependence of the β_{KWW} (open symbols) and τ_{KWW} (full symbols).

Table 5.3. Characteristic parameters of the dipolar and conductivity processes of the 60VP/40BA–ZC samples (Z=0.2, 1 and 2).

sample	***Z*=0.2**	***Z*=1**	***Z*=2**
	γ relaxation		
$\ln \tau_\infty (s)$	-31.2±0.4	-30.6±0.1	-30.9±0.5
$E_a^\gamma \left(kJ \cdot mol^{-1}\right)$	22.7±1.0	22.1±1.0	22.6±0.5
$\left(E_a^\gamma / RT_g\right)_{\text{expt}}$	9.4	8.9	8.8
$\left(E_a^\gamma / RT_g\right)_{CM}$	11.9	11.2	11.5
	β relaxation		
$\ln \tau_\infty (s)$	-37.4±0.2	-37.8±0.5	-33.63±0.2
$E_a^\beta \left(kJ \cdot mol^{-1}\right)$	47.9±0.3	49.5±0.2	46.3±0.6
$\left(E_a^\beta / RT_g\right)_{\text{expt}}$	19.8	19.9	17.9
$\left(E_a^\beta / RT_g\right)_{CM}$	18.1	18.4	14.3
	α relaxation		
$-\ln \tau_0 (s)$	25.8±0.3	25.8±0.3	25.9±0.4
D_0	5.8±0.3	5.9±0.2	5.8±0.3
T_v (K)	244.5±2.0	249.5±1.8	261.1±2.0
m	81.8±1.6	80.4±1.3	83.4±1.5
m*	88.9	90.6	93.6
$E_a(T_g)$ (kJ·mol^{-1})	456±47	460±40	496±46
$E_a^*(T_g)$ (kJ·mol^{-1})	475	500	544
β_{KWW} [at T_g]	0.24	0.24	0.24

The most useful feature of the CM is the Eq. (1.38), since it connects the cooperative α relaxation time ($\tau_{KWW} \equiv \tau_\alpha$) with the intermolecularly uncorrelated (non-cooperative)

relaxation time (τ_0^{CM}) (Ngai, et al., 2007; Casalini, et al., 2003). Using the τ_{KWW} and β_{KWW} values obtained from the retardation time spectra (inset **Figure 5.9**), the τ_0^{CM} parameter was calculated for each copolymer and for each temperature. Thus, the values of τ_0^{CM} parameters for each sample are represented in **Figure 5.9**. As it is observed, τ_0^{CM} values only are superimposed to the obtained values of τ_β for Z=0.2 and 1, fulfilling the Eq. (1.37): $\tau_\beta = \tau_{JG} \approx \tau_0^{CM}$. Hence, it is shown how β relaxation ceases to possess typical features of a pure JG relaxation for Z=2.

Moreover, if the expressions of the CM are rewritten, a JG process should also fulfill the following criteria: $\log_{10}\left(\frac{\tau_\alpha}{\tau_\beta}\right) \approx \log_{10}\left(\frac{\tau_\alpha}{t_c}\right)^n$. Thus, **Figure 5.10** represents the temperature dependence of the ratios of $\log_{10}\left(\frac{\tau_\alpha}{\tau_\beta}\right)$ and $\log_{10}\left(\frac{\tau_\alpha}{t_c}\right)^n$ for all the samples. If a secondary process is a JG relaxation, both ratios should be superimposed. However, only these ratios are practically superimposed for the samples with Z=0.2 and 1. Besides, the value of the quotient between both ratios should be one for a JG relaxation. This quotient is approximately one only for the samples with Z=0.2 and 1 (inset of **Figure 5.10**), showing again that the β relaxation for the sample with Z=2 does not have the typical characteristics of a JG process.

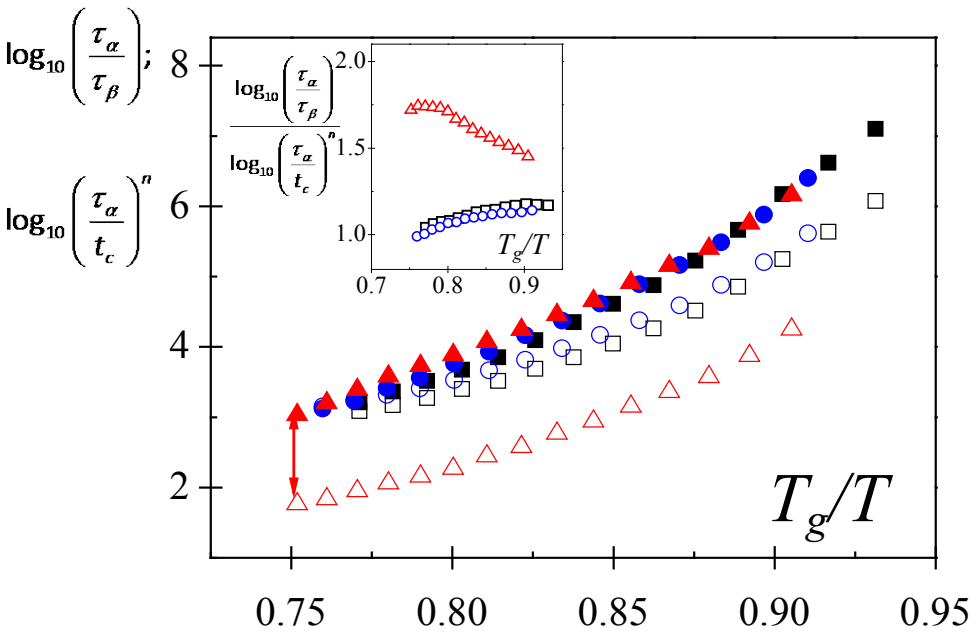

Figure 5.10. Temperature dependence of $\log_{10}\left(\frac{\tau_\alpha}{\tau_\beta}\right)$ (full symbols) and $\log_{10}\left(\frac{\tau_\alpha}{t_c}\right)^n$ (open symbols) for the *60*VP/*40*BA-*Z*C samples with Z=0.2 (square), Z=1 (circle) and Z=2 (triangle). Inset: Temperature dependence of the ratio $\log_{10}\left(\frac{\tau_\alpha}{\tau_\beta}\right) \Big/ \log_{10}\left(\frac{\tau_\alpha}{t_c}\right)^n$ for the samples with Z=0.2 (square), Z=1 (circle) and Z=2 (triangle).

5.3. Conclusions

This chapter is focused on analyzing the influence of the cross-link density on the molecular dynamics of the *60*VP/*40*BA copolymer. The molar ratios of the ethylene glycol dimethacrylate cross-linker were varied between 0.2 and 2%. As expected, the increase in cross-link density affects significantly most of the properties analyzed throughout this work:

(i) The mechanical stability is enhanced.

(ii) The sample hydrophilicity decreases.

(iii) The glass transition temperature increases due to the reduction of the segmental motion imposed by the cross-links. The T_g values were evaluated by MDSC and DRS techniques and a good agreement was observed between both techniques.

(iv) The ΔC_p (T_g) diminishes, related to the decrease in mobility imposed by cross-links.

(v) Regarding to the dielectric properties, the effect on the α peak was: (a) a shift to higher temperatures, related to the increase of the T_g, (b) a decrease in the strength due to the reduction in the molecular mobility, (c) an increase in the breadth, as showing by the increase of a_{HN} parameter, which qualitatively indicates a broader distribution of relaxation times and (d) an increase of the relaxation times due to the slowdown of the molecular motions imposed by the constraints on the polymer chains. However, only it is observed a faintly increase in the cooperativity inherent to the α process.

(vi) The nature of the β relaxation, including both amplitude and rate, strongly depends on the cross-linker content. According to our results, for lower cross-linker contents the β process is a JG relaxation whereas this process ceases to have the typical behaviour of a pure JG relaxation for Z=2. Thus, the cross-linker agent produces a decoupling between the main chain and the local chain motions. Nevertheless, molecular dynamic simulations would be useful for a definitive assignment of the origin of this relaxation.

(vii) The local motion of the polymer (γ relaxation) is essentially unaffected.

Chapter 6:

Characterization of Expanded Graphite-Polycarbonatediol Polyurethane Composites

The results collected in this chapter were publised in: C.M. Gómez, M. Culebras, A. Cantarero, **B. Redondo-Foj**, P. Ortiz-Serna, M. Carsí and M. Sanchis, *Appl. Surf. Sci,* vol. 275, pp. 295-302, 2013.**B. Redondo-Foj**, P. Ortiz-Serna, M. Carsí, M. Sanchis, M. Culebras, C.M. Gómez and A. Cantarero, *Polym. Int.,* vol. 64, pp. 284-292, 2015.; P. Ortiz-Serna, M. Carsí, **B. Redondo-Foj**, M. Sanchis, M. Culebras, C.M. Gómez and A. Cantero, *J. Appl. Polym. Sci.,* DOI:10.1002/APP.42007, 2015.

Abstract

Segmented polycarbonatediol polyurethane (PUPH) has been synthesized and modified with different amounts of expanded graphite (EG) conductive filler (from 0 to 50 wt %). SEM, X-ray diffraction measurements and FTIR analysis demonstrated a homogeneous dispersion of the EG filler in the matrix. Thermal and dynamical thermal analysis of the composites clearly indicates changes in the polyurethane relaxations upon addition of graphite. DRS has been used to study the dielectric properties of the PUPH/EG composites in the frequency and temperature ranges from 10^{-2} to 10^{7} Hz and from -140 to 170ºC, respectively. The dielectric permittivity of the composites showed an insulator to conductor percolation transition with the increase of the EG content. Significant changes in the dielectric permittivity take place when the weight fraction of EG is in the range of 20–30 wt%. Specially, the dependence of the conductivity with the frequency, temperature and EG content has been studied. The addition of expanded graphite to the matrix causes a dramatic increase in the electrical conductivity of ten orders of magnitude, which is an indication of percolative behavior. A percolation threshold of ~30 wt% was evaluated by using the scaling law of the percolation theory.

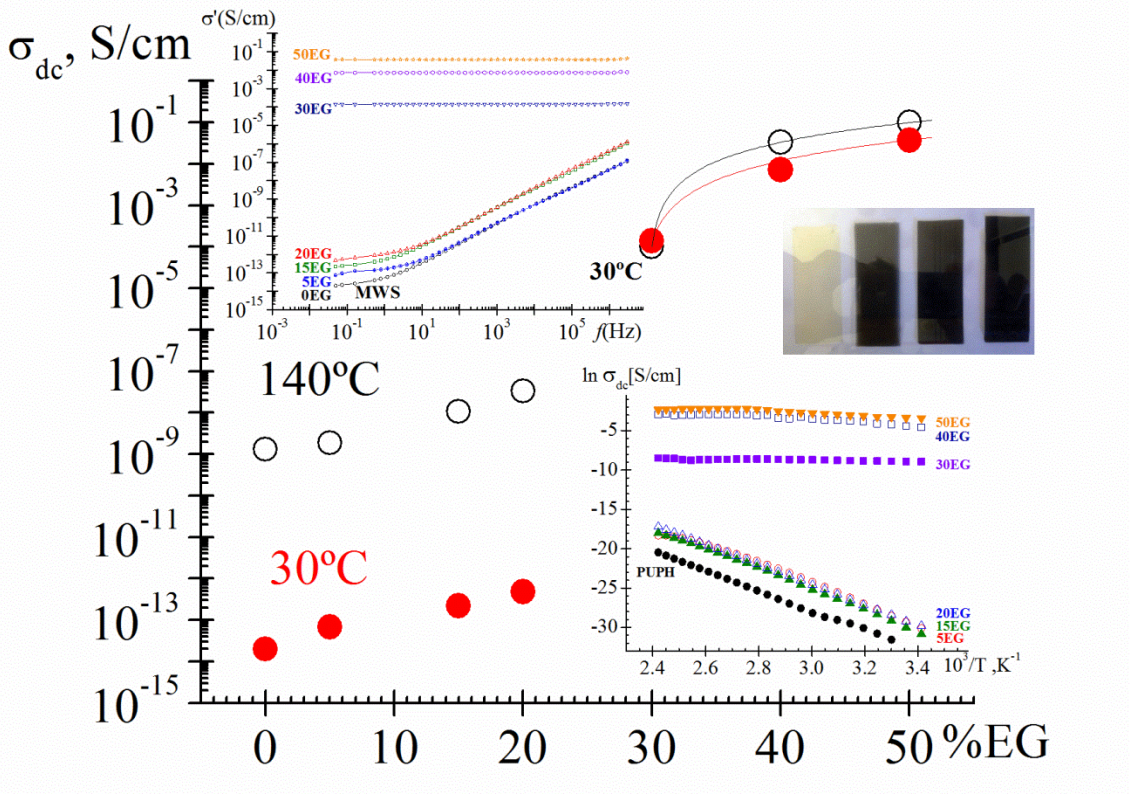

6. Characterization of Expanded Graphite-Polycarbonatediol Polyurethane Composites

6.1. Introduction

Polyurethanes are one of the most versatile materials since they can behave as elastomers, thermoplastics or thermoset polymers depending on the different reactants and synthesis conditions selected. They are extensively used as foams, elastomers, coatings, sealants and adhesives in different applications (Lee, 1998; Szycher, 1999; Oertel, 1993; Priscariu, 2011; Król, 2007). Segmented polyurethane elastomers (TPU) are linear block copolymers formed by thermodynamically incompatible segments named as soft and hard domains. The soft segment is a polyol of molecular mass between 500 and 3000 $g \cdot mol^{-1}$ that provides high flexibility at room temperature. The hard segment is formed by a diisocyanate and a low-molecular-weight diol which provides physical crosslink sites through strong intermolecular hydrogen bonding (Strawhecker, et al., 2013; Costa, et al., 2012). The morphological, physical, chemical and mechanical properties of TPUs range in a wide spectrum, which depends on the hard segment formulation and content, molecular structure of soft segment and manufacturing conditions. Polyether and polyester macrodiols are commonly used in a wide range of commercial applications due to their affordable price. In contrast, polycarbonatediol (PCD) derived TPUs depict improved water and organic solvent resistance, high mechanical strength and high heat-resistance, at the expense of an increase in the price (Eceiza, et al., 2008; Kojio, et al., 2004; Tanaka, et al., 2002). Due to their inherent properties they are used for specific applications as artificial

and synthetic leathers, thermoplastics, elastomers, paints and adhesives, where high reliability is required. The wide range of properties attained is directly related to the chemical composition reflected by the different hard-hard and hard-soft segments interactions. Demand for PCD is growing in the World as the polyurethane market increasingly shifts toward higher-performance materials.

The polyurethanes, like most of the polymers, are electrically insulating materials. However, they can be specifically modified in order to increase its conductivity by dispersing conductive fillers (Otieno, et al., 2008; Chang, et al., 2010). Conductive metals lack of properties such as elasticity and corrosion resistance. In contrast, insulating polymeric materials, which behave as conductive ones by addition of conductive particles, show good mechanical properties and are easy to mold. Carbon materials such as Carbon Nanotubes (CNTs) have been used to increase the electrical properties of polymer matrices (Sandu, et al., 2011). However, CNTs are very expensive for large-scale applications. Other conductive fillers such as graphite and its variants are being used to provide electrical conductive properties to polymeric matrices (Konwer, et al., 2011; He, et al., 2008). Graphite is very cheap, abundant, has an elevated electrical conductivity (10^4 $S \cdot cm^{-1}$) and increases the mechanical properties of polymers having a reinforcing effect on the polymeric material (He, et al., 2008). The drawback is the difficult dispersion of the graphite in the polymer matrix. This fact can be overcome by modifying its surface. For example, graphite can be expanded by chemical oxidation and thermal shock in order to increase the size of channels, improving thus the interaction with the polymer matrix (Dhakate, et al., 2008).

Thus, when a conducting constituent is added to a polymer matrix, which has a low concentration of free charge carriers, new contributions can be presented. Their electrical response is mainly associated with relaxation phenomena occurring under the influence of the alternated current (ac). The ac electrical response of disordered systems to electric perturbations results in the superposition of different contributions (Kremer, et al., 2003; Carsí, et al., 2013). These contributions are related to: (i) the hopping process of localized charge carriers, (ii) the response produced by the molecular structure deformation, following on the diffusion of charges through percolation paths, and (iii) the dispersive response of the bound charges (dipolar response). The dipolar response presents at high frequencies one or more secondary relaxations. These processes are followed in decreasing order of frequency by the glass–rubber relaxation.

The conducting polymer–based composites are considered as heterogeneous disordered systems (Strümpler, et al., 1999; Dyre, et al., 2000) and their electrical performance is directly related to the permittivity/conductivity of the all constituent's phases and to other parameters related to the filler component, as the size, shape and volume fraction of the filler. Because of the small dimensions of the filler component and the resulting high surface–to–volume ratio, composites typically have, even at low filler concentrations, a high fraction of interfacial regions (interphase) with a major influence on the electrical properties. When an electric field is applied inside a heterogeneous system, containing different constituents with dissimilar conductivities and permittivities, interfacial polarization mechanisms take place due to the accumulation of electric charges at the interfaces of these materials. Thus, new contributions associated with the separation of charges at internal phase boundaries, referred to as Maxwell–Wagner–Sillars (MWS)

polarization (Maxwell, 1893; Wagner, 1914; Sillars, 1937), should be taking into account. The MWS effects are more pronounced for conductive materials and, in certain cases, this large–scale polarization can mask the dielectric orientation response of the material. Recently, there is evidence that this process is not unique for heterogeneous systems, since their presence has been detected in some complex homopolymers (Arbe, et al., 2010; Sanchis, et al., 2010; Hempel, et al., 2002). An example of this kind of complex homopolymers is the family of poly(n–alkyl methacrylates). Structural studies based on X–ray diffraction have shown the aggregation of side groups of different monomeric units, forming self–assembled alkyl nanodomains, their sizes being related to the length of the side group (Beiner, 2001; Beiner, et al., 2003).

For the conducting polymer–based composites, the conducting filler content results a crucial parameter that determine their electrical behavior. When the conducting filler content is low, the mean distance between conducting particles is sufficiently large and the conductivity is restricted by the presence of the dielectric matrix. However, by increasing the conductive filler content, a physical path is formed, through which the current can flow by percolating the whole system. According to the percolation theory, a transition exists from a state of limited and spatially restricted connections of conductive particles to a state of an infinite network of connections (insulator–conductor transition). The transport properties exhibit, in the vicinity of the transition, strongly non–linear behavior which in the case of electrical conduction is expressed as a power law transition (Bunde, et al., 1991; Zallen, 2004; Stauffer, 1984; Lux, 1993). The percolation threshold represents the critical concentration of the conductive particles content which is necessary for the onset of conductive behavior to take place.

Frequency dependent studies are very useful in order to obtain better understanding of the charge transport mechanism. In this sense, dielectric spectroscopy (Kremer, et al., 2003; McCrum, et al., 1991; Riande, et al., 2004) represents a powerful tool for investigating the polymer dynamics as well as the polymer–filler interaction in composites materials. This technique allows studying the temperature and frequency dependence of the electrical conductivity. In order to investigate the physical origin of the occurring charge transport, different hopping models (the variable range hopping (Mott, 1987; Mott, 1990) and the random free–energy barrier models (Dyre, 1988; Dyre, et al., 2002)) have been employed and applied to analyze the ac data.

In this thesis, PUPH has been synthesized and modified with different amounts of EG as a conductive filler. The composites characterization has been carried out by means of FTIR, morphological analysis, thermogravimetric analysis, differential scanning calorimetry, wide angle X-ray diffraction, dynamic mechanical analysis and dielectric relaxation spectroscopy.

Thus, the main goal of this chapter is the chemical and physical characterization of segmented PUPH/EG composites. This chapter reports (i) the effect of the hard/soft domains in the molecular dynamics of polycarbonatediol polyurethane, (ii) the effect of the EG on the thermal, mechanical and dielectric properties of PUPH, and (iii) the phenomenological description and interpretation of the conductivity behavior of PUPH/EG composites as a function of the EG content, temperature and frequency.

6.2. Results and Discussion

6.2.1. Fourier Transform Infrared Spectroscopy

Figure 6.1 shows the FTIR spectra of PUPH/EG composites at different EG contents. The FTIR spectrum of the unfilled PUPH exhibits the typical bands for polyurethanes based on polycarbonatediol: N–H stretching vibration at 3200–3500 cm^{-1} (Jiao, et al., 2013), –C=O stretching vibration in the amide I region associated with free and H–bonded carbonyl groups at 1640–1800 cm^{-1} (Hu, et al., 2005; Mondal, et al., 2006), the carbonyl C=O stretching vibration in the amide region (–NH–CO–O) at 1621 cm^{-1}, C=C aromatic stretching band at 1510 cm^{-1}, $–CH_2–$ deformation vibration at 1406 cm^{-1}, C–O carbonate group stretching band at 1226 cm^{-1}, –C–O–C– stretching band in ether group at 1056 cm^{-1} and the peak of the rolling band of the group $–CH_2–$ detected at 760 cm^{-1} (Jiao, et al., 2013). The NCO stretching band of MDI at 2270 cm^{-1} has disappeared indicating that the reaction between OH and NCO groups has been completed (Meuse, et al., 1992). Polyurethanes are capable of forming several kinds of hydrogen bonds due to the presence of a donor N–H group and a C=O acceptor group in the urethane linkage (Lan, et al., 1996; Mondal, et al., 2006). This is why hard segment–hard segment or hard segment–soft segment hydrogen bonding can exist. In the case of PUPH, the appearance of a N–H band at 3310 cm^{-1} and a small one at 3000 cm^{-1} are attributed to “free” and H–bonded N–H groups, respectively. These bands decrease with the EG content suggesting that the filler disrupt the ordered structure of hard–hard and hard–soft interactions. On the other hand, the stretching vibration of the C=O groups in the hard segments (Seymour, et al., 1970;

Seymour, et al., 1973) give rise to: (i) a main peak centered at 1735 cm^{-1}, associated with C=O groups that are free (non–hydrogen bonded); and (ii) the peak at 1700 cm^{-1} that resulted from hydrogen bonding with urethane N–H groups (Hu, et al., 2005; Sadeghi, et al., 2011). Significant suppression in hydrogen bonding can be inferred from the diminished peak intensity at 1700 cm^{-1} as the amount of EG increases. These results suggest that the carboxyl groups in EG contribute to the interfacial interaction between the PUPH backbone and the EG layers. In other words, the C=O groups of the hard segments of PUPH may form hydrogen bonds with the hydroxyl groups of few–layered graphene. It is observed a decrease in the intensity of 1730 cm^{-1} and 1700 cm^{-1} bands when the EG concentration is higher than 15 wt%, being this decrease more noticeably for the last one. This fact implies that addition of EG disrupt the carbonyl interactions indicating a good dispersion of the EG in the thermoplastic polyurethane. Furthermore, the difficulty to detect the characteristic signals of PUPH chains as the EG content increases could be related to the existence of some type of interaction between both components.

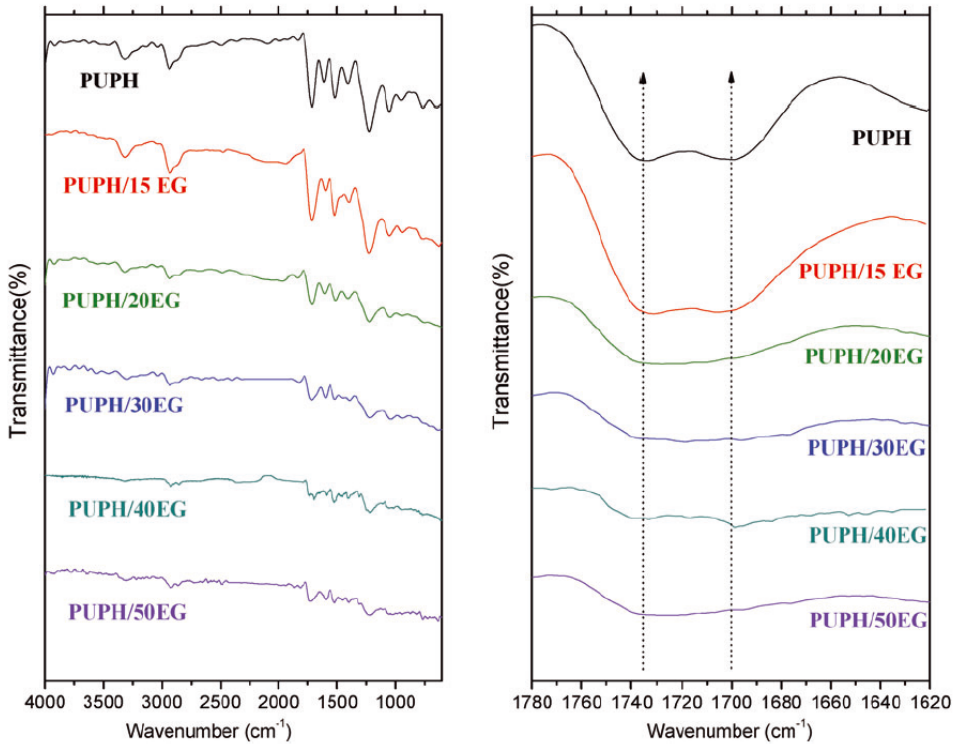

Figure 6.1. FTIR spectra for PUPH and PUPH/EG composites. Right: The spectra were scaled in the carbonyl absorbance region for better visualization

6.2.2. Morphological Analysis

Figure 6.2 shows SEM images of EG, PUPH, PUPH/15EG, and PUPH/50EG. Graphite is formed by carbon atoms sp^2 bonded in flat planes that keep together due to van der Waals forces. Graphite can be intercalated with a convenient solvent, as in this work, and later with fast heating to a high temperature leads to exfoliation consisting of an increase in the dimension perpendicular to the carbon layers of the intercalated graphite. Expanded graphite, as shown in **Figure 6.2 (A)**, shows a structure based on parallel boards resulting in many pores. The spacing between the graphite layers increases during exfoliation giving a porous structure consisting of numerous graphite sheets, so that the polymer can be easily intercalated among them. **Figure 6.2 (B)**, **(D)** and **(F)** show the

surface of the PUPH/EG composites with 0, 15 and 50 wt% EG content, respectively. Obviously, in contrast to the PUPH surface, a certain roughness was appreciated in presence of expanded graphite. This is evident when comparing the last two images, being the roughness higher in the sample with higher EG content. **Figure 6.2 (C), (E)** and **(G)** correspond to the cross section of the PUPH, PUPH/15GE and PUPH/50EG films, respectively. A good affinity of the EG for the PUPH is observed as the EG layers become absorbed by the polyurethane leading to a continuous composite structure.

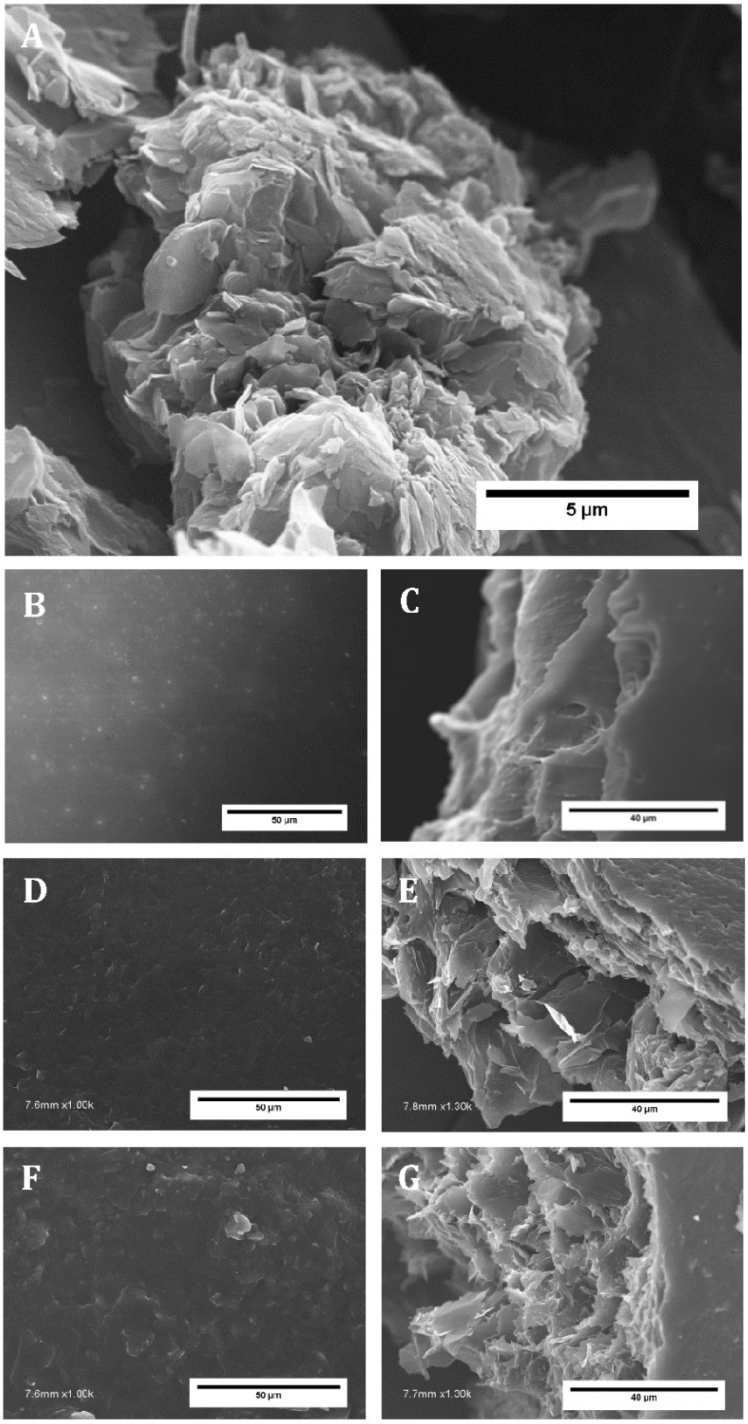

Figure 6.2. SEM images of: (A) EG; (B) PUPH, (D) PUPH/15EG and (F) PUPH/50EG are surface images; and (C) PUPH, (E) PUPH/15EG and (G) PUPH/50EG are a cross section of the cryoscopic fracture.

6.2.3. X-ray Diffraction

The position of the peaks can be expressed by the scattering angle (2θ) or by the scattering wave vector (q). Both magnitudes are correlated by the Bragg's Law:

$$2 \cdot d \cdot \sin\theta = 2 \cdot \left[\frac{2\pi}{q} \right] \cdot \sin\theta = \lambda \tag{6.1}$$

where d is the Bragg's spacing of the repeating domain unit, which is related to q by $d = 2 \cdot \pi / q$; 2θ is the scattering angle and λ is the wavelength of incident wave.

Figure 6.3 shows the X–ray patterns of EG, PUPH and PUPH/EG composites. EG shows a two sharp peaks at q=18.7 nm^{-1} (2θ=26°) corresponding to diffraction in the (002) plane and at q=37.5 nm^{-1} (2θ=54°) corresponding to the diffraction in the (110) plane (Li, et al., 2007). The spectrum of PUPH shows the presence of a broad peak centered in the vicinity of q=14.5 nm^{-1} (2θ=20.65°) and a small shoulder at q=8.9 nm^{-1} (2θ=12.6°). These peaks are ascribed to the micro–phase separated morphology into "soft" and "hard" segments occurring during polymerization and are an indication of short range order, commonly observed in polyurethanes (Ryan, et al., 1992). The composites show a narrow diffraction peak at q=18.7 nm^{-1} (2θ=26°) associated with the EG filler. The intensity of the peaks related to PUPH at 2θ=20.65° decreases significantly, whereas that at 2θ=12.6° increases with the addition of EG. The intensity reduction reflects, in some way, an eventual reduction in the number of existing nanodomains in the film. The interdomain spacing d, which only depends on the molecular weight of the macrodiol was estimated using the Bragg's law (Eq. (6.1)) to be equal to 0.5 nm.

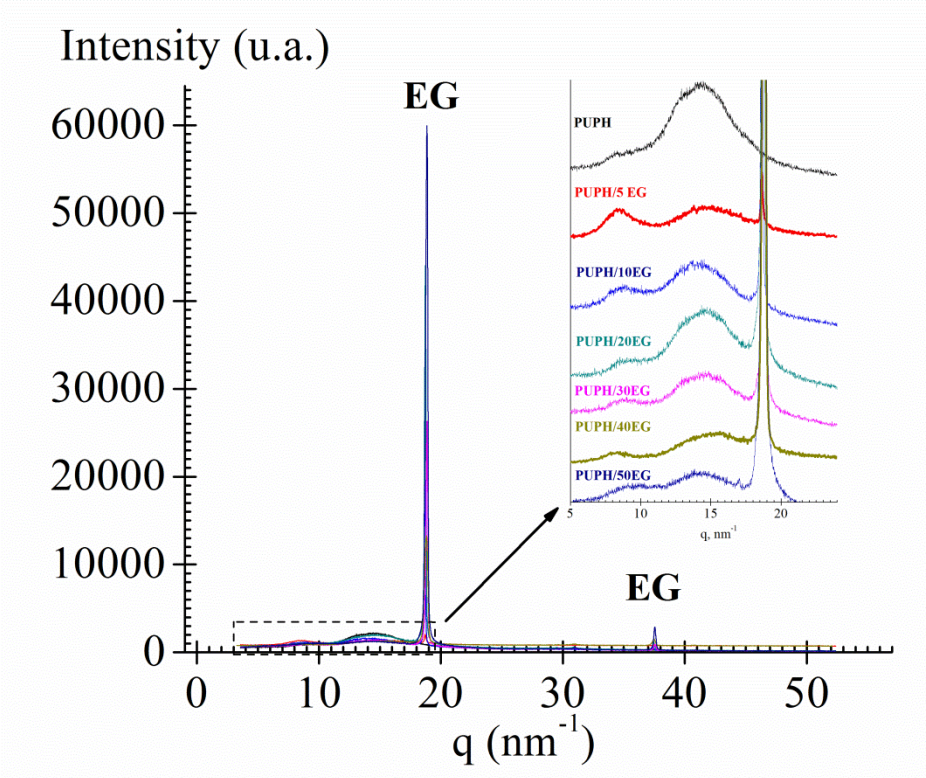

Figure 6.3. X–ray diffraction patterns of EG, PUPH and PUPH/EG composites at different EG contents. Inset: zoom of the X–ray pattern in the 0 to 23 nm^{-1} region. The spectra were scaled for better visualization.

6.2.4. Thermogravimetric Analysis

Thermogravimetric analysis was carried out in order to analyze the effect of expanded graphite insertion on the thermal stability of the polyurethane films. This analysis allows the evaluation of changes in weight as a function of temperature in a controlled atmosphere. **Figure 6.4** shows the TGA thermograms obtained for each film and **Table 6.1** collects the characteristic temperatures of the degradation processes in the materials under study. T_{on} is the temperature related to the beginning of the decomposition process, T_p is the temperature of the maximum rate of weight loss and T_{end} is the temperature related to the ending of the decomposition process. For PUPH films two degradation processes have been

observed. The first starts around 312 ºC and is due to urethane bound decomposition. The second process that appears near 486 ºC is related to a weight loss associated with other segments of the remaining structure or with a probable C-C bound cleavage (Pielichowski, et al., 1998; Petrovic, et al., 1994). In the case of EG particles only one degradation process has been observed. This process begins at 609 ºC and is related to the carbon atoms oxidation in the EG particles. In PUPH/EG films three degradation processes can be observed. The two first are related to the degradation of the polymer matrix and the last process is due to the degradation of the EG particles. According to our results, the EG particles have not a significant effect on the PUPH/EG composites stability, since the characteristic temperatures of degradation processes are very similar in the films with and without EG. Instead, the presence of polymer chains decreases the degradation temperature of EG particles, as shown in **Table 6.1**. A similar effect has been observed in other composites (Wang, et al., 2010).

Table 6.1. Thermogravimetric characteristic temperatures of PUPH and PUPH/EG composites.

%EG	T_{on1} (ºC)	T_{p1} (ºC)	T_{end1} (ºC)	T_{on2} (ºC)	T_{p2} (ºC)	T_{end2} (ºC)	T_{on3} (ºC)	T_{p3} (ºC)	T_{end3} (ºC)
0	312	349	370	486	501	537			
15	308	341	361	460	503	538	578	610	676
30	311	345	363	470	507	531	562	588	680
50	310	352	368	486	510	532	555	580	693
100							609	649	755

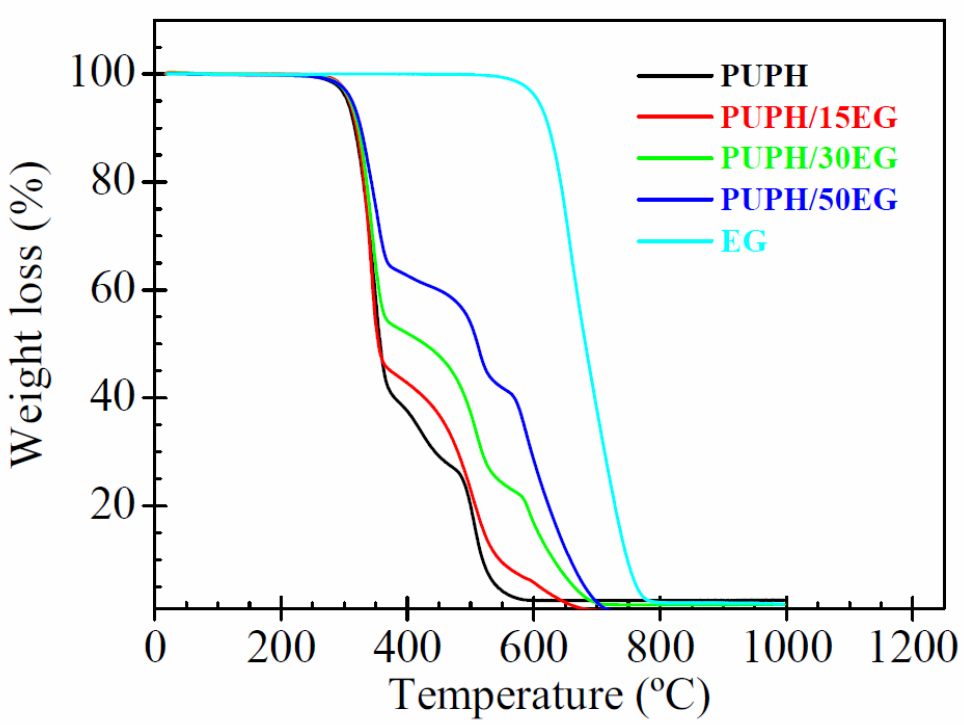

Figure 6.4. Weight loss as a function of temperature for PUPH and PUPH/EG composites.

6.2.5. Differential Scanning Calorimetry Measurements

In order to study the thermal behavior of the PUPH and the PUPH/EG composites, DSC measurements were carried out in the temperature range from -90 to 220ºC. The DSC thermograms obtained for PUPH/EG samples are shown in **Figure 6.5** and the characteristic parameters obtained are summarized in **Table 6.2**. These parameters are: the glass transition temperature (T_g), the variation of the heat capacity (ΔC_{pnor}), the melting temperature (T_m), and the degree of crystallinity (χ_c). The last parameter was determined from the enthalpy of crystallization normalized using $\chi_c = \Delta H_c / \Delta H_{100\%}$, where ΔH_c is the enthalpy of fusion of every sample, taking into account the weight of the PUPH in the sample and $\Delta H_{100\%}$=25.85 J/g is the enthalpy of fusion of the hard segment. For all the

analyzed samples, the T_g, evaluated as the midpoint of the specific heat capacity increment, appears in the temperature range from -20 to 10 ºC, and the melting peak is visible around 187 ºC.

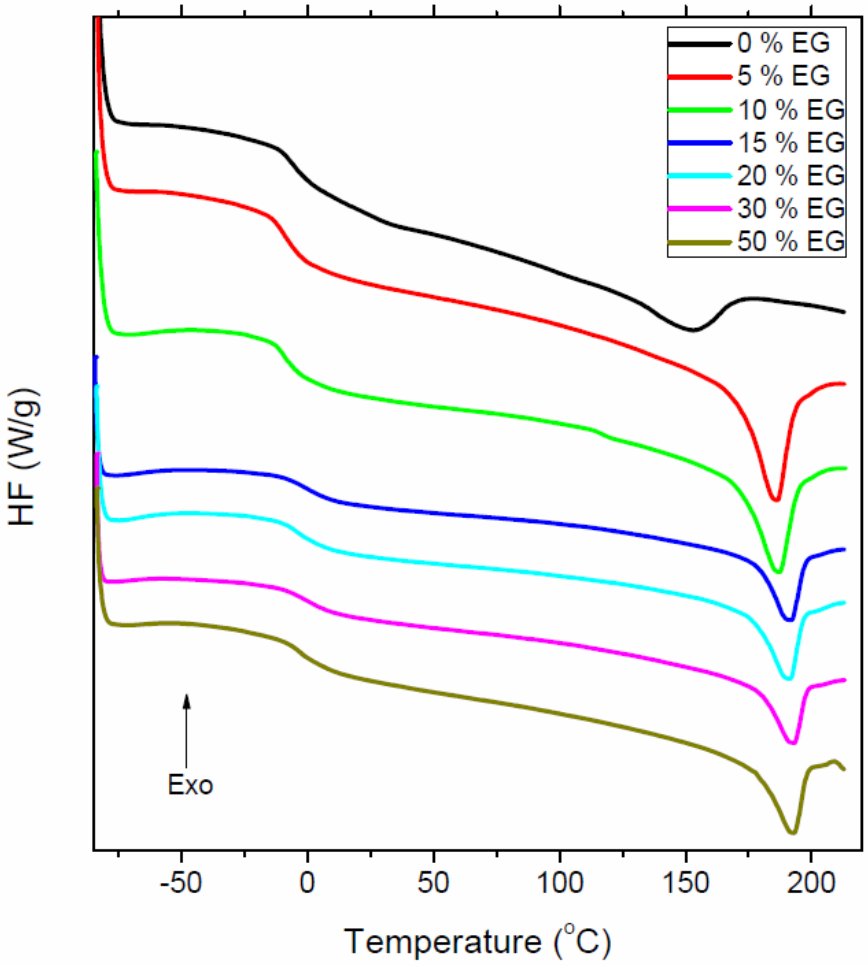

Figure 6.5. DSC curves taken at 20ºC/min of the PUPH and PUPH/EG composites.

Depending on the EG content two different trends are observed in the values of the glass transition temperatures. Thus, for low EG particles content (5 and 10 *wt*%) , a decrease of T_g is observed, which indicates that the EG addition tends to increase the mobility. This tendency is probably associated with an increase of the free volume due to a decrease in the molecular packing of the chain. So, the presence of EG particles, at a

relative smaller content, reduces the dipole-dipole interactions of PUPH molecules and plays an inert diluent role decreasing the self-association interaction of PUPH molecules. Similar tendency has been observed in other composites (Xu, et al., 2002; Ash, et al., 2002; Bershtein, et al., 2002; Arrighi, et al., 2003; Ash, et al., 2004). However, for high content (15 to 50 *wt*%) of EG, the T_g is similar for all these samples, but higher than that corresponding to PUPH matrix. This can be associated with the reduction of molecular mobility of the polyurethane chains imposed by the EG particles. Therefore, a fraction of polymer could be immobilized on the surface of the EG particles. (Chen, et al., 2002; Liu, et al., 2001; Sargsyan, et al., 2007; Privalko, et al., 1979; Huang, et al., 2001; Lipatov, et al., 1972; Kalogeras, et al., 2004)

Table 6.2. Parameters obtained from DSC of PUPH/EG composites.

%EG	T_g (ºC)	ΔC_{pnor} (J/gºC)	T_m (ºC)	χ_c (%)
0	-8.10	0.2145	164.8	42.6
5	-12.91	0.3470	185.4	36.1
10	-13.87	0.2890	186.3	34.2
15	-2.3	0.3040	191.4	28.6
20	-2.7	0.2854	191.5	27.1
30	-3.23	0.2070	191.7	21.9
50	-3.1	0.1823	191.9	11.0

On the other hand, the composites heat capacity jump at T_g (ΔC_{pnor}), normalized to the fraction of PUPH, which is a measure of the fraction polymer participating in the glass transition. This parameter is affected by two different factors: (i) the crystallization degree of the matrix and (ii) the effect of the EG particles in the polymer mobility. Thus, for the PUPH sample, which has the highest χ_c degree, the ΔC_{pnor} is lower than those

corresponding to the composites with the lower %EG. The addition of the EG tend to reduce the crystallinity degree increasing the amount of the amorphous polymer, which can contribute to the glass transition. However, a fraction of polymer is immobilized on the EG particles surface (Bershtein, et al., 2002; Klonos, et al., 2010), which reduces the amount of the amorphous polymer that participates to the T_g. This last effect is relevant for the highest %EG content. On the other hand, in the PUPH/EG composites, the ΔC_{pnor} decreases with the EG content. Similar results have been also obtained for other polymer composites (Fragiadakis, et al., 2007).

The analysis shows that the melting temperature, T_m, increases with the EG content. Finally, the degree of crystallinity is 42.6% for the pure PUPH and decreases with the filler content. This is an indication that the EG particles restrict the chain ordering.

6.2.6. Dynamic Mechanical Analysis

DMA analysis was performed in order to determine the viscoelastic properties of PUPH and PUPH/EG films. **Figure 6.6** shows the storage modulus, E', and loss modulus, E'', as a function of temperature. The storage modulus increases with the EG content, suggesting that the particles of expanded graphite have a reinforcing effect on the polyurethane matrix. The temperature of the E'' maximum is related to the T_g of the material and shifts to higher values with the addition of the EG particles. This tendency is in agreement with that observed in DSC measurements.

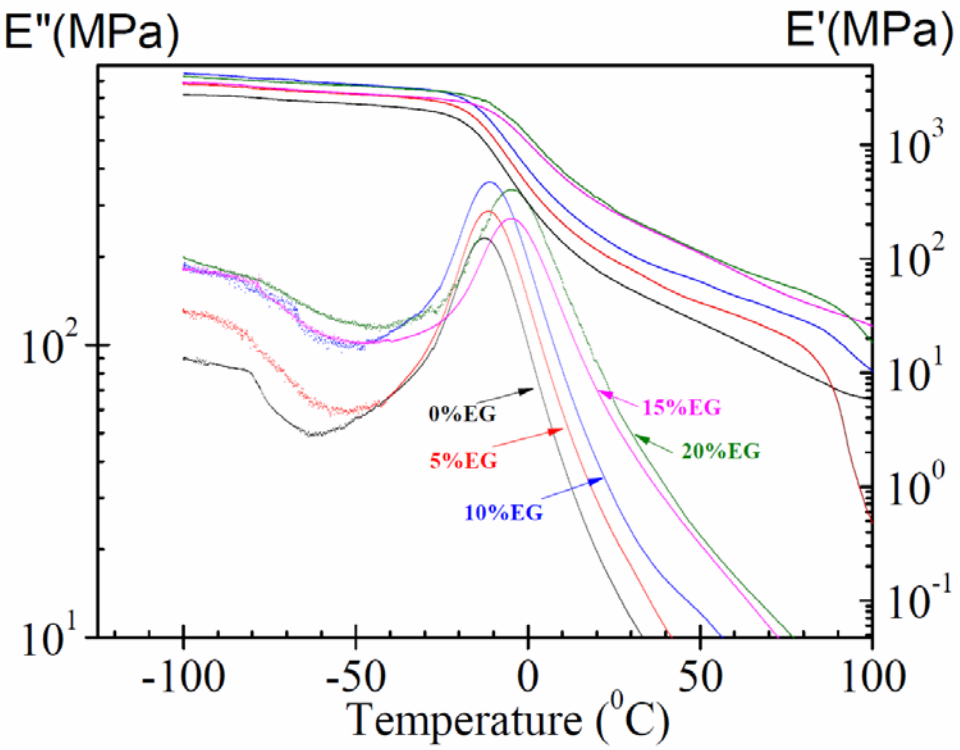

Figure 6.6. Temperature dependence of storage and loss modulus for the PUPH/EG composites at 1 Hz.

6.2.7. Dielectric Measurements

DRS analysis was carried out in order to analyze the effect of the EG particles in the dielectric dipolar and conductivity processes.

Figure 6.7 shows three-dimensional (3D) representations of the real and imaginary components of the complex dielectric permittivity for the PUPH film, in the range of $5 \cdot 10^{-2}$ to 10^9 Hz and temperature window of -120 ºC to 140 ºC.

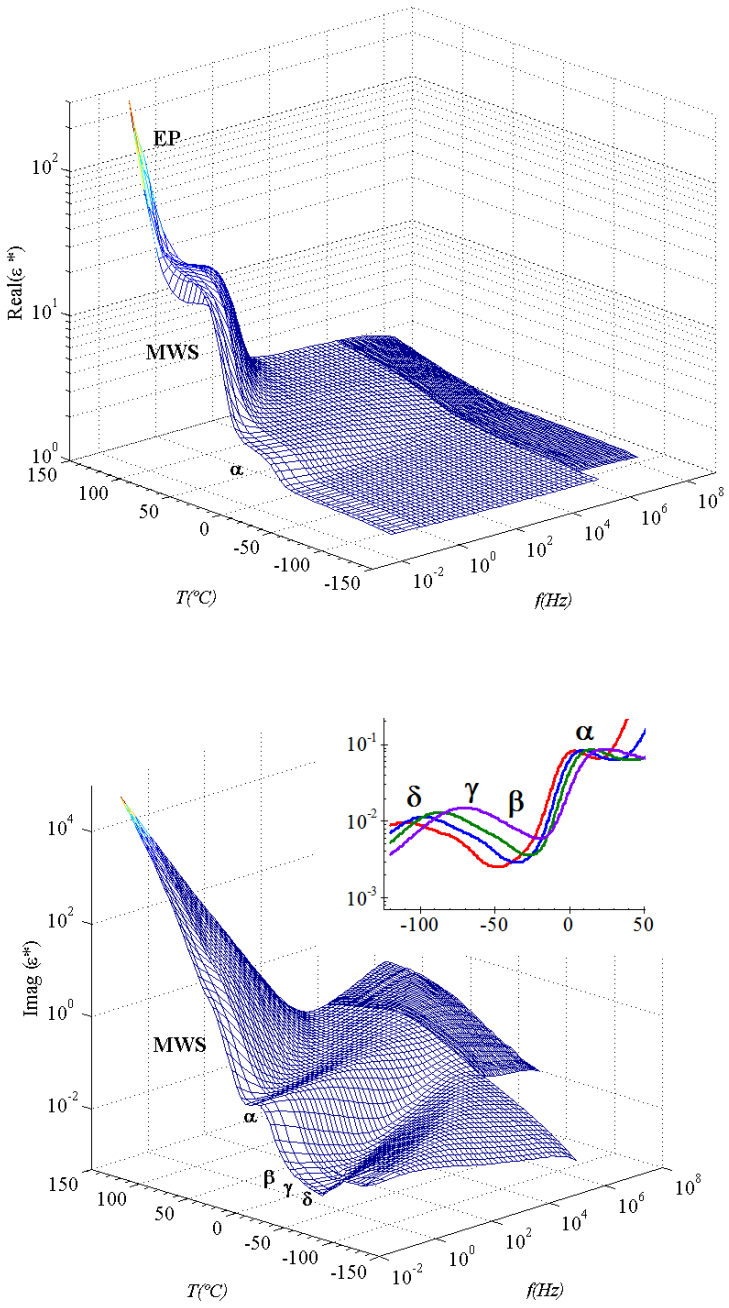

Figure 6.7. 3D representation of the dielectric permittivity of PUPH in the temperature range of -120 ºC to 140 ºC, step 5 ºC. Inset: zoom of the low temperature region.

The isochrones corresponding to the dielectric loss ε'' clearly present two relaxational zones. In the low-temperature region, three secondary relaxations, labelled as δ, γ and β

processes, are observed, presumably associated with side chain motions (see inset in **Figure 6.7**). In the high-temperature zone the spectrum present an ostensible α relaxation associated with the glass transition temperature followed by a rather sharp increase as temperature increases as a result of the strong contribution of the conductivity. The contribution of the polarization, produced at the electrode-polymer interface, to the dielectric loss scales with frequency dependence as ω^{-s}, where usually *s* is a parameter close to unity.

PUPH is a typical system in which charge contributions to the dielectric permittivity are important at low frequencies. Therefore, it is also convenient to analyze the results in terms of the complex dielectric modulus $\left(M^* = 1/\varepsilon^*\right)$, a variable very sensitive to charge transport (Hodge, et al., 2005). This formalism has several advantages (Pathmanathan, et al., 1991): (i) it allows the determination of the *dc* conductivity from the M'' spectra, (ii) electrode polarization effects usually do not mask the features of the spectra, and (iii) the results of the dielectric analysis are seemingly analogous to the mechanical modulus of solids. **Figure 6.8** plots the mechanical (E'') and dielectric loss modulus (M'') as a function of temperature at 1Hz. Both spectra clearly present two relaxational zones. In the low-temperature region, the presence of several secondary relaxations is observed, presumably associated with local motions. In the high-temperature region, both spectra show an ostensible α relaxation. Moreover, only in the dielectric spectrum two processes associated with the conductivity phenomena (MWS and ohmic conductivity) are observed.

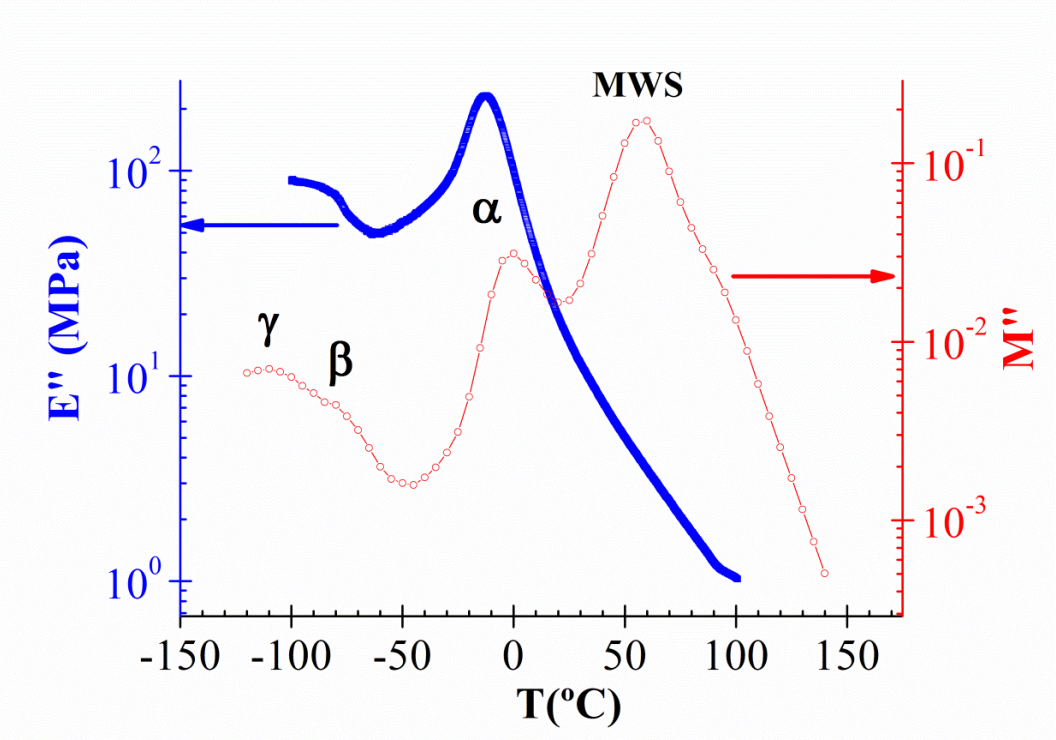

Figure 6.8. Temperature dependence of the dielectric loss modulus and loss mechanical modulus at 1 Hz for PUPH film.

The pertinent loss modulus in the frequency and temperature experimental range is shown in **Figure 6.9a**. As observed, the loss modulus exhibits two ostensible peaks corresponding to the α relaxation and the MWS process, in decreasing order of frequency. This last process is overlapped with the EP process in the low frequency region. In the tan δ representation (**Figure 6.9b**), a peak is observed at lower frequencies than that of the glass-rubber relaxation. This peak is associated with the EP phenomenon that is dominant in the low frequency range.

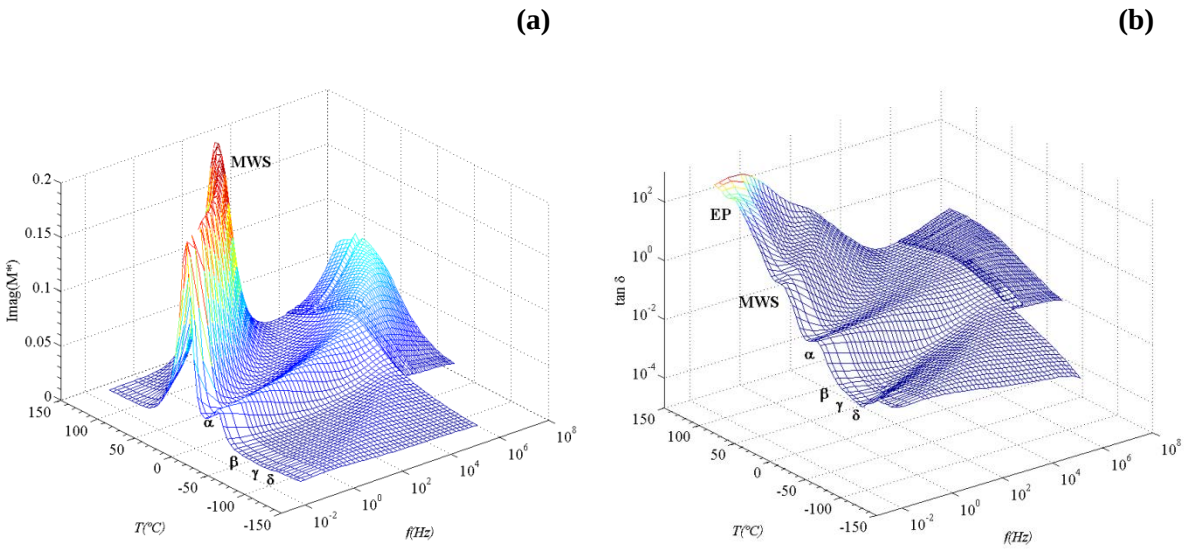

Figure 6.9. (a) Values of M'' in the frequency domain for PUPH at several temperatures (-120 ºC to 140 ºC, step 5 ºC). **(b)** Loss tan δ in the frequency domain for PUPH at several temperatures (-120 ºC to 140 ºC, step 5 ºC).

In order to analyze the effect of the EG particles in the dielectric dipolar and conductivity processes, the dielectric spectrum of PUPH sample is compared with the spectra of PUPH/EG samples at different compositions.

Figure 6.10 shows the temperature dependence of the dielectric permittivity and loss factor at several frequencies for the PUPH and PUPH/15EG films, which was taken as a representative sample of the PUPH/EG composites. The isochrone that shows the temperature dependence of ε′ presents two steps. At low temperatures a first step associated with the glass rubber or α relaxation is followed by a second step at higher temperatures, associated with the Maxwell-Wagner-Sillars (MWS) relaxation. Finally, at the higher temperatures an important increase of the permittivity related to the electrode polarization (EP) effect is observed. The second step is more clearly visualized for the PUPH film, since for the PUPH/EG composite the magnitude of the EP process hinders the MWS process

definition. EP process proceeds from the accumulation of charges at the electrodes-polymer interface, whereas the interfacial polarization, or MWS process, is due to the build-up of charges at the interfaces of the heterogeneous systems components. The PUPH is a heterogeneous system due to the existence of micro-phase separation associated with the *soft* and *hard* micro-domains (Bates, et al., 1990; Ryan, et al., 1992). The polarization of these micro-domains, a process that can be attributed to the different conductivity between them, can cause the accumulation of charges. Probably these micro-domains are the responsible of the observed MWS process. The α relaxation shifts to high temperatures with the addition of EG particles, indicating a decrease in the mobility of the polymer chains. This result is in agreement with the DSC and DMA results reported in previous chapters, which show an increase in the T_g with the addition of 15% wt of EG particles. Low temperature spectrum shows the presence of almost two secondary processes. These processes seem to be unaffected by the addition of EG, as can be expected due to their local character.

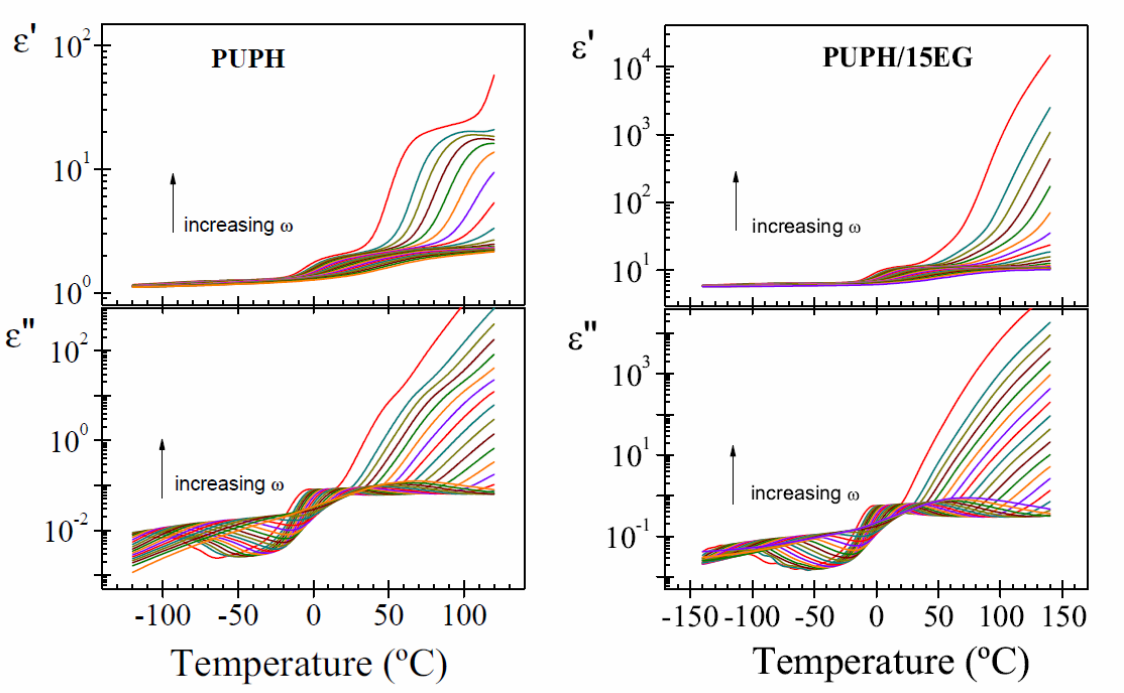

Figure 6.10. Temperature dependence of the permittivity (ε′) and loss factor (ε″) for PUPH and PUPH/15EG at several frequencies.

As stated before, to get insight of the complex conductive behavior of the films, it is advisable to use the complex modulus formalism ($M^* = 1/\varepsilon^*$) for the data representation. As observed in **Figure 6.11a**, better definitions of the loss peaks are obtained by plotting the dielectric results in terms of the dielectric loss modulus, M''. The isochrone of M'' exhibits three ostensible peaks corresponding in increasing order of temperature to the overlapped secondary relaxations (β and γ), the α relaxation and the MWS process, overlapped with the ohmic conduction process in the high temperature region. The EP process is better visualized, as a peak, in the tan δ representation, as observed in **Figure 6.11b**. As seen in **Figure 6.11c**, the relaxation strength significantly increases in the composite ($\Delta\varepsilon_{PUPH} \sim 1.3$ versus $\Delta\varepsilon_{PUPH/15EG} \sim 4.9$). Taking into account that $\Delta\varepsilon$ is

proportional to (i) the number of entities that participates in the process and (ii) dipolar moment, this result is in accordance with the ΔC_{pnor} values obtained by DSC.

Also, a significant effect of EG content is observed on the definition of the MWS process, pointing out that the micro-phase separated morphology of the PUPH matrix is significantly modified with the EG addition.

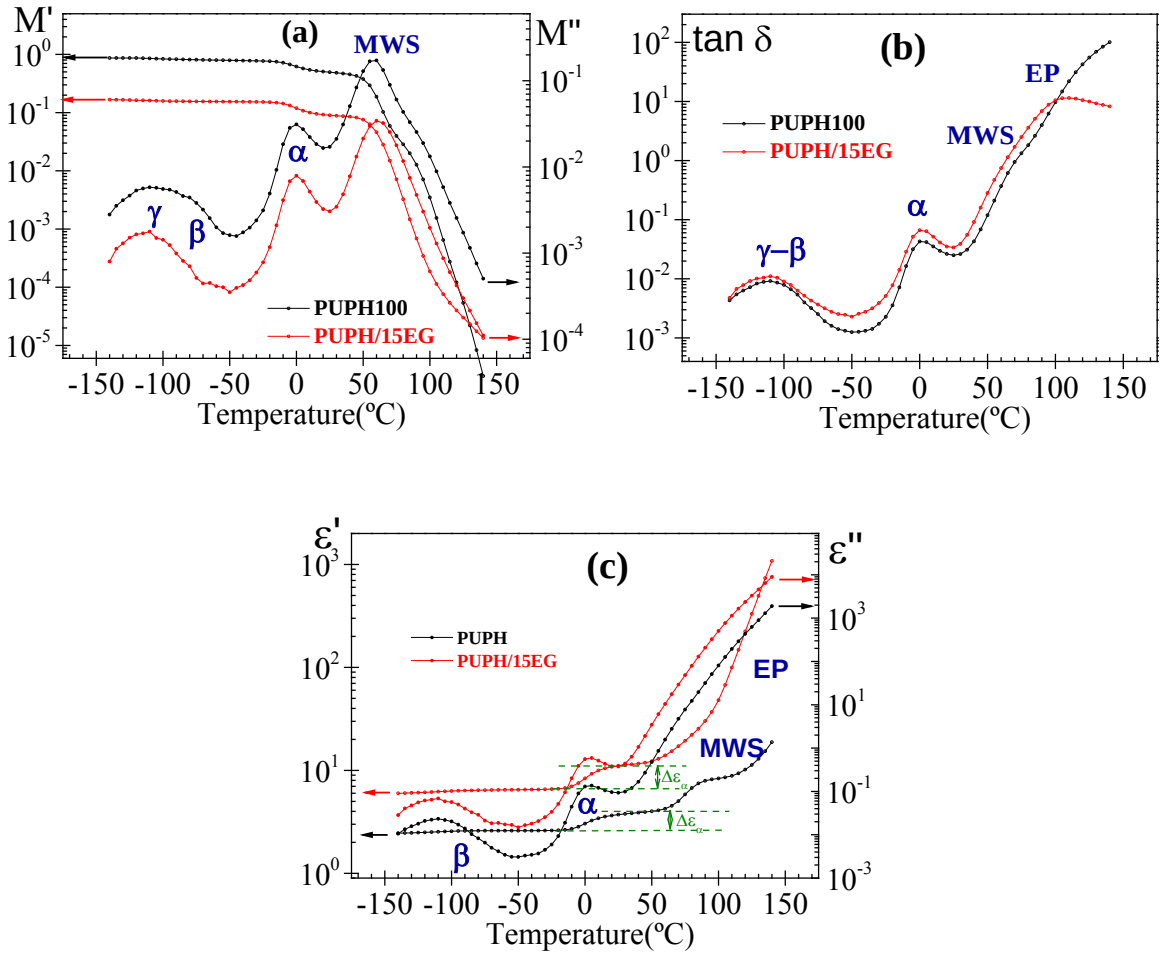

Figure 6.11. Temperature dependence of **(a)** the modulus (M′) and loss modulus (M″), **(b)** tan δ and **(c)** the permittivity (ε′)/loss factor (ε″) for PUPH (black curve) and PUPH/15EG (red curve) at 1Hz.

For a clear visualization, the dielectric permittivity and loss factor of PUPH and PUPH/15EG, as a sample of PUPH/EG composites, were also plotted in the frequency

domain in **Figure 6.12**. The dielectric constant of the composites is a function of its capacitance, which is proportional to the quantity of charge stored on their surface of the sample under an applied electric field. In the PUPH/EG composites, which are filled with conducting fillers, the quantity of the accumulated charge will increase because the polarization of the PUPH/EG interfaces. The polarization makes an additional contribution to the charge quantity. From this point of view, the dielectric constant of the composites will be higher than that of the pure PUPH; and it will also increase with increasing the concentration of fillers. The experimental results in **Figure 6.12** just support this explanation. Moreover, according to the DSC results, the crystallinity degree of the film increases with the introduction of EG filler, which affects the dipole polarization of the groups and segments. The crystallinity of the polymer matrix is also considered an important factor influencing the dielectric properties of the composite. As observed, the MWS process related to the nanodomains formation of *soft* and *hard* segments is hindered by the inclusion of EG filler. According to the WAXRD results (**Figure 6.3**), incorporation of EG governs the polymer chain movements and consequently, molecule polarization. This is reflected in the dielectric spectra by a reduction of the MWS process.

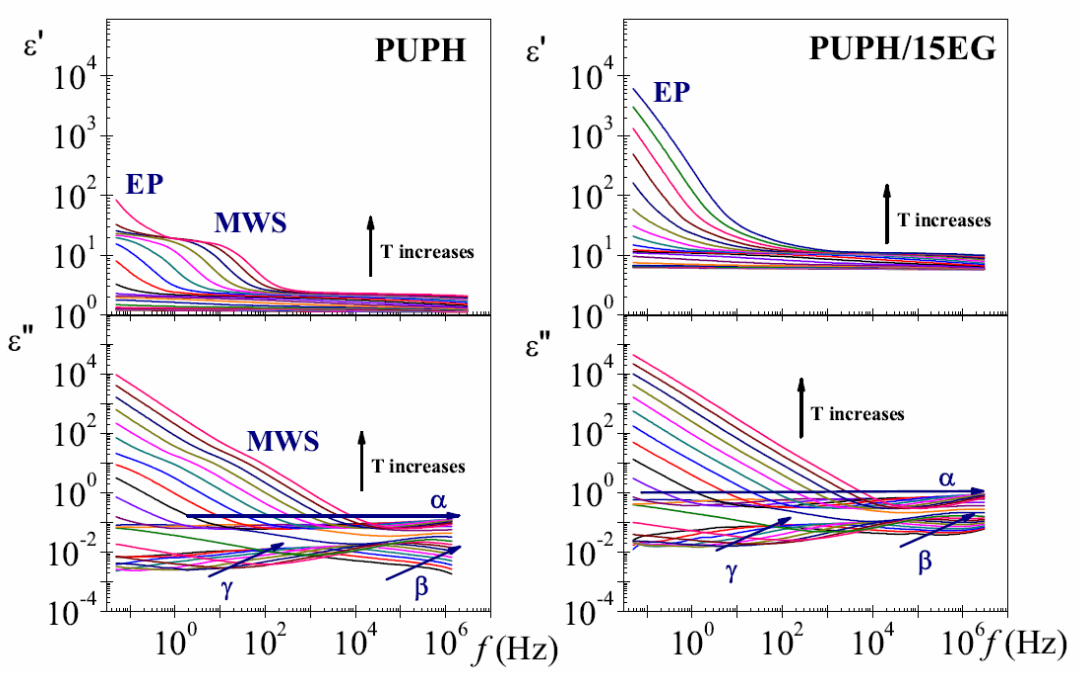

Figure 6.12. Dielectric Permittivity (ε′) and loss factor (ε″) as a function of frequency for PUPH and PUPH/15EG films in the temperature range -100 ºC to 120ºC (step 10 ºC).

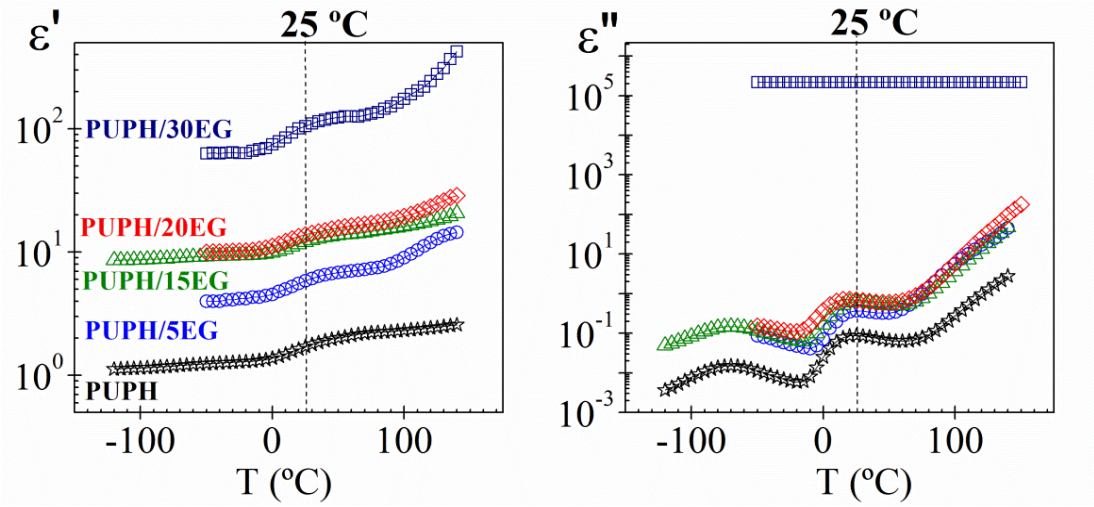

Figure 6.13. Temperature dependence of the complex permittivity, at 1 kHz, for PUPH (●) and PUPH/EG composites with different EG weight fractions (wt%).

Figure 6.13 shows the temperature dependence of the dielectric permittivity and loss factor of PUPH and PUPH/EG composites. As observed, an abrupt variation is produced when 30 wt% of EG filler is added. For lower EG contents, the segmental dynamics of the PUPH matrix seems to be slightly affected by the presence of the EG filler, which is in agreement with previous observations reported for other composites (Cangialosi, et al., 2012; Otegui, et al., 2013).

The EG particles effect on the PUPH conductivity was also studied. The *ac* conductivity was calculated from the dielectric permittivity according to the relationship

$$\sigma^* = i\omega\varepsilon_0\varepsilon^*(\omega) \tag{6.2}$$

So, the real and imaginary part of $\sigma^*(\omega)$ are given, respectively, by $\sigma'(\omega)=\sigma'_{ac}(\omega)=\omega\cdot\varepsilon_0\cdot\varepsilon''(\omega)$ and $\sigma''(\omega)=\omega\cdot\varepsilon_0\cdot\varepsilon'(\omega)$.

In general, at a constant temperature, the *ac* conductivity can be expressed as (Böttger, et al., 1985; Jonscher, 1996)

$$\sigma(\omega) = \sigma_{dc} + A\omega^s \tag{6.3}$$

where σ_{dc} is the $\omega \to 0$ limiting value of $\sigma(\omega)$ and A, s are parameters depending on the temperature. Eq. (7.3) is often called “the *ac* universality law" since it has been found to satisfactorily describe the *ac* response of numerous different types of materials, which can be classified as disordered solids (Dyre, et al., 2000; Dyre, 1988).

Figure 6.14 shows in double logarithmic plots the real component of the complex conductivity, $\sigma'=\sigma_{ac}$ (S cm^{-1}), in the frequency domain for pure PUPH and PUPH/EG composites, measured at several temperatures. According to **Figure 6.14**, the dc

conductivity of the analyzed samples increases with increasing temperature and EG content. The conductivity exhibits a frequency dependence that follows the Eq. (6.3), and it becomes stronger as the concentration of EG decreases. For low EG content, it is evident that the ac conductivity, $\sigma_{ac}(\omega)$ increases with frequency and temperature, being dependent of both magnitudes. The change of the conductivity at high frequencies is due to the increasing importance of the polarization effects on the macroscopic conductivity. As usual, in the frequency domain, the isotherms corresponding to high temperatures exhibit a plateau in the low frequency region, reflecting a frequency independent conductivity, *i.e.*, dc conductivity. The frequency range corresponding to the plateau increases with temperature. The bulk conductivity of the pure PUPH increases with temperature, as expected for an insulator material, with a value at 30 ºC and 10^{-1} s^{-1} of about $2 \cdot 10^{-14}$ S cm^{-1}. The conductivity value of the PUPH sample increases to ~ $4 \cdot 10^{-10}$ S cm^{-1} at 120 ºC and 10^{-1} s^{-1}, that is, four orders of magnitude. As observed, for samples with EG content less or equal to 20 wt%, the frequency dependence of $\sigma'(\omega)$ is nearly linear [$\sigma'(\omega) \sim \omega^s$] in the high frequency range (second term Eq. (6.3)). However, for EG content equal or higher than 30 wt%, a frequency independent conductivity is obtained in all the experimental frequency range (first term Eq. (6.3)).. This absence of a frequency dependence for high EG contents could be related to the occurrence of a highly interconnected filler network with almost the absence of electrical barriers. It is also observed that the *dc* conductivity significantly increases for EG content equal to or higher than 30 wt%. This observation suggests that the critical filler content, *i.e.*, the percolation threshold, should be near 30 wt% for this particular PUPH/EG composite series. On the other hand, in the PUPH sample it is observed that the MWS–relaxation creates a 'knee'–like increase of the σ–curve in the

middle part of the isotherm, which is uniformly shifted with the temperature. The MWS process is related to the build–up of charges at the interfaces of components of heterogeneous systems. The charges can migrate under the influence of the applied field contributing to the electrical response of the systems. (Psarras, 2006; Aharony, et al., 1993) In this case, this phenomenon is related to the micro–phase separation of the "soft" and "hard" segments. The reduction of the MWS process definition with the EG content reflects a probable reduction in the number of existing nanodomains imposed by the EG filler. This result is in agreement with that of X–ray. Thus, the incorporation of EG filler governs the polymer chain movement and, consequently, the molecule polarization, which is reflected in the dielectric spectra by the reduction of the MWS process intensity.

In order to study the effect of the EG content on the electrical conductivity of PUPH/EG composites, **Figure 6.15** shows the electrical conductivity σ_{ac} as a function of the EG weight percentage. As observed, the conductivity increases continuously with the EG content in all the studied temperatures. Moreover, for constant conductive filler content, the conductivity considerably increases as the temperature is raised. According to these results, the temperature dependence of the conductivity is more significant for EG contents lower than 30 wt%. The increase of EG content is beneficial to form conductive networks. As the EG content increases, the conductivity is gradually improved, and a sharp transition occurs at EG content of 30 wt%. Finally, for EG content higher than 40 wt%, non–significant changes are observed in the conductivity values.

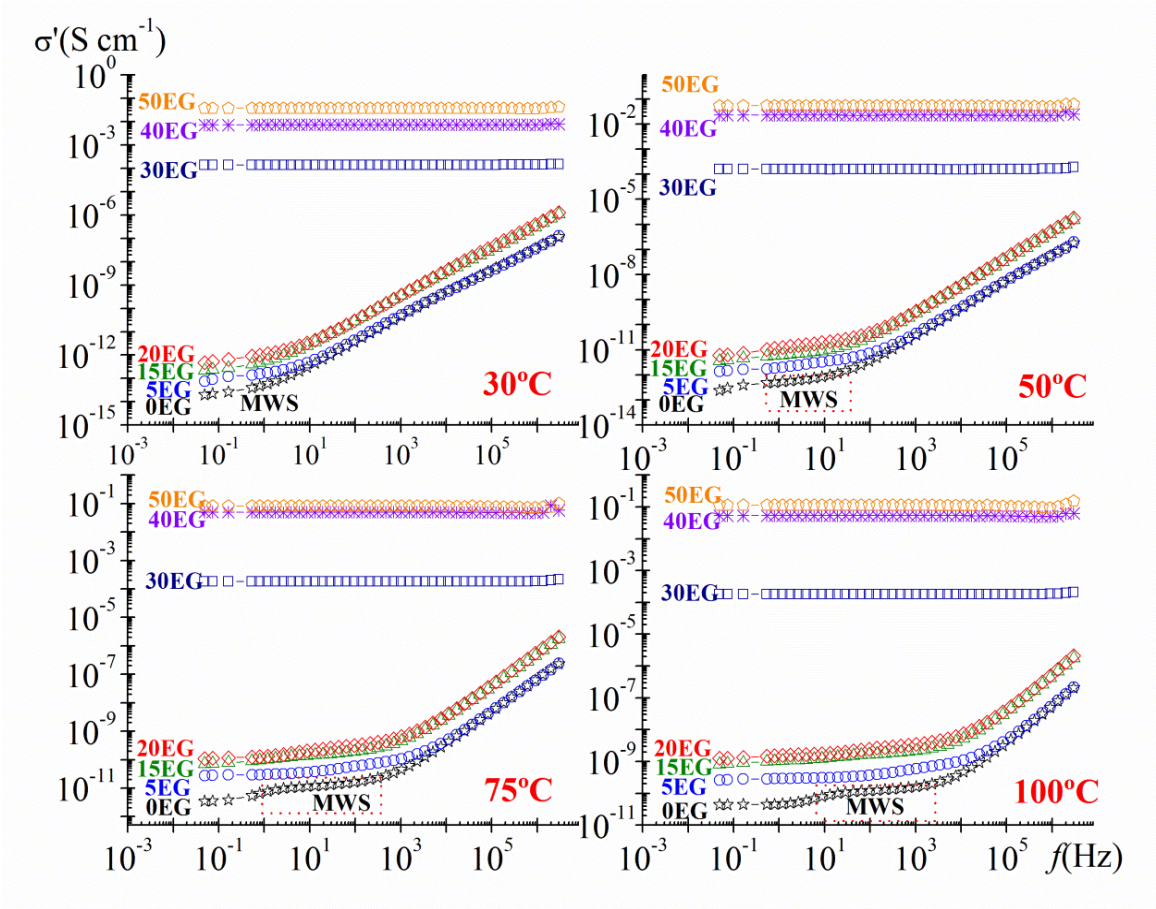

Figure 6.14. Frequency dependence of the ac conductivity, at several temperatures, for pure PUPH polymer and PUPH/EG composites films, with an EG weight fraction (wt%).

Figure 6.16 shows *dc* conductivity at 30 and 140 ºC, evaluated from the $\sigma'(\omega)$ value when $\omega \rightarrow 0$, as a function of the EG mass fraction. At both temperatures a sharp increase in the electrical conductivity is observed when the EG content reaches 30 wt%. This increase is more pronounced at 30ºC.

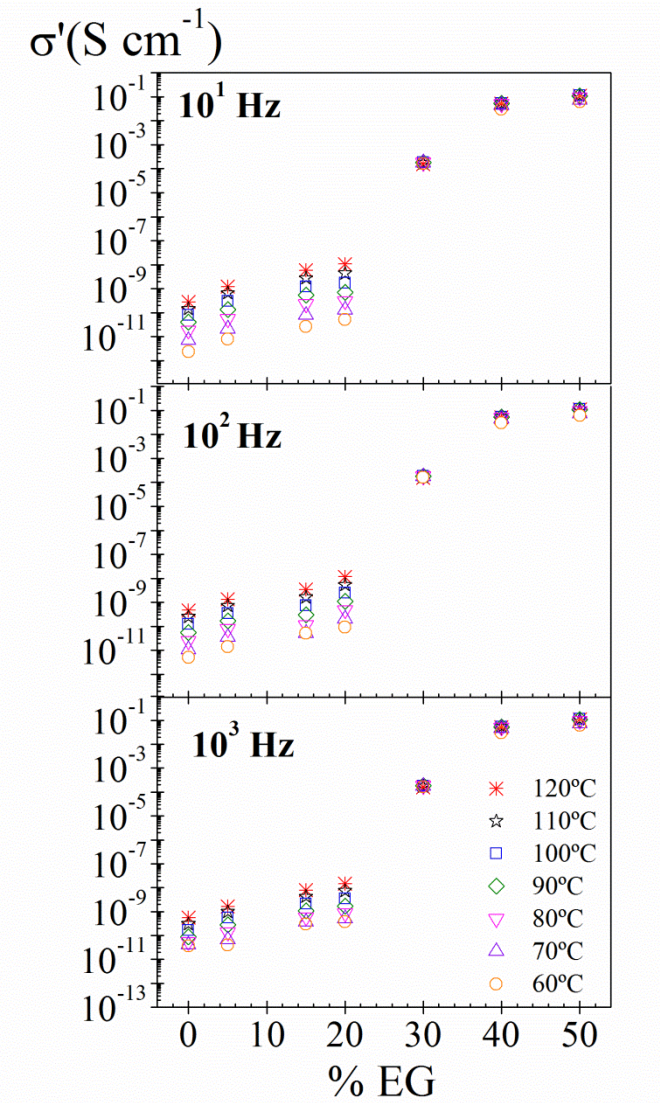

Figure 6.15. The EG content dependence of the conductivity for PUPH/EG composites at various temperatures between 60 and 120 ºC at several frequencies: 10^3, 10^2 and 10^1 Hz.

In order to calculate the percolation threshold, the data were fitted to the scaling law of the percolation theory. This theory defines an insulation–conductor transition and a corresponding threshold of the conductive filler concentration via the equation (Aharony, et al., 1993; Krupa, et al., 2001; Novák, et al., 2002; Lux, 1993):

$$\sigma_{dc} = C \cdot \left(p - p_c\right)^t \qquad p > p_c \tag{6.4}$$

where C is a constant, p_c is the weight fraction of filler or percolation threshold and t is the scaling critical exponent. The critical t exponent is related to the dimensionality of the system (1.3 and 2 in two and three dimensional materials, respectively) (Lux, 1993). The data were fitted to the scaling law and the values of C, p_c and t, evaluated by multiple non−linear regression analysis, are listed in **Table 6.3**.

According to our results, the percolation threshold, p_c, is nearly temperature independent (**Figure 6.15**). Thus, the p_c values obtained for both analyzed temperatures are very similar. Moreover, these values are higher than those reported for other composites with EG (Chao Li, et al., 2010). This fact is directly related to the morphology of the filler, which clearly depends on the processing conditions (Piana, et al., 2013; Eceiza, et al., 2008).

Furthermore, the scaling critical exponent, t, decreases slightly with the temperature and the obtained value is somewhat smaller than the universal value of three−dimensional percolating systems (t = 2). On the one hand, the increase of t with decreasing temperature could be then associated with the reduction in the dimensionality of the conductive network, which occurs when temperature increases. On the other hand, the measurement of more samples with EG contents in the vicinity of p_c would have allowed a more accurate analysis of the percolation threshold. Thus, since values of p much higher than p_c have been into account in the Eq.(6.4), this could lead to obtain a lower value of the t exponent.

In all composites analyzed, the conductivity did not exceed 10^{-1} S cm^{-1}, which is 13 orders of magnitude higher than PUPH, but much lower than the corresponding to EG filler. Moreover, extrapolation to p=100% using Eq.(6.4) gives a conductivity of 0.32 and 0.73 S cm^{-1} for 30 ºC and 140 ºC, respectively. These values are 3 orders of magnitude

lower than the conductivity measured in EG pure filler (Marinho, et al., 2012). This result could be related to the coating of the individual EG particles by the PUPH insulating surface, resulting in a poor electrical contact between the EG particles. Therefore, for low EG content, the matrix acts as an electrical barrier, avoiding the direct contact between the EG particles.

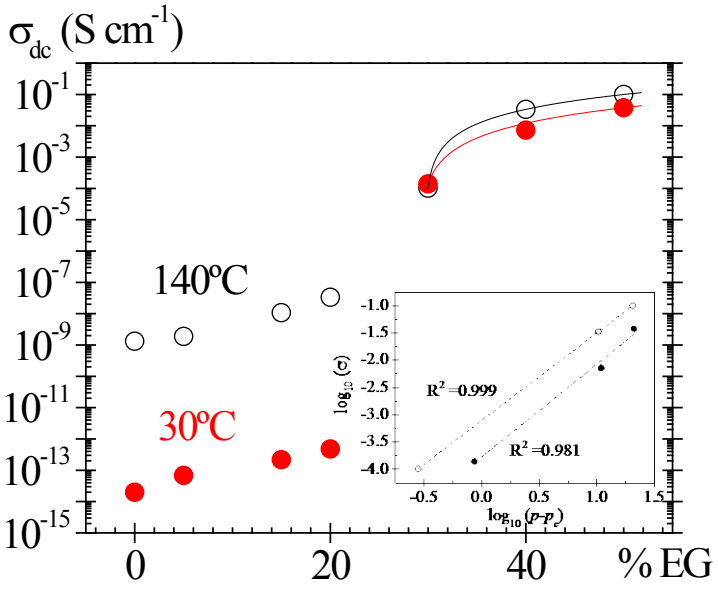

Figure 6.16. Dependence of the *dc* conductivity on the EG weight mass fraction, *p,* at 30 ºC and 140 ºC (1 kHz). The solid line is a fit to the scaling law of the percolation theory.

Table 6.3. Percolation scaling law parameters at 30 ºC and 140 ºC.

	30 ºC	**140 ºC**
t	1.76±0.01	1.61±0.01
p_c **(wt%)**	29.14±0.02	29.72±0.02
C **(S cm^{-1})**	$1.82 \cdot 10^{-4} \pm 1.07 \cdot 10^{-13}$	$7.88 \cdot 10^{-4} \pm 1.37 \cdot 10^{-8}$

Figure 6.17 shows the *dc* conductivity values, obtained at several temperatures from extrapolations to low frequencies, as a function of the reciprocal temperature for all the examined composites. As seen, the *dc* conductivity is a thermally activated process and can be described by $\sigma_{dc} = \sigma_0 \cdot \exp(-E_a/RT)$. The experimental data were satisfactorily linear fitted to an Arrhenius plot, and the evaluated activation energy (E_a) and pre–factor (σ_0) values are summarized in **Table 6.4**. According to our results, the reduction of the inter–particle separation, by increasing the weight mass fraction of the EG, results in the reduction of the corresponding activation energy values.

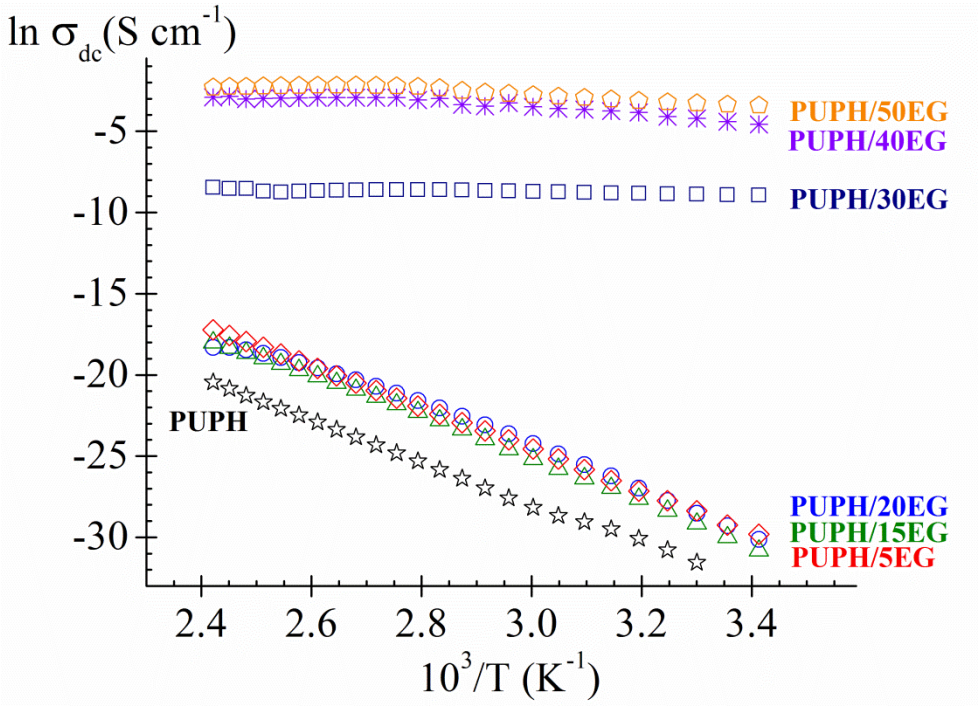

Figure 6.17. Plot of neperian logarithmic of the *dc* conductivity as a function of the reciprocal temperature.

Table 6.4. Sample name and the corresponding values of the conductivity activation energy and pre–factor parameters of all the analyzed films.

Sample name	ln σ_0 (S cm^{-1})	E_a^{σ} (kJ mol^{-1})
PUPH	10.7±0.2	107.3±0.5
PUPH/5EG	12.5±0.2	108.6±1.2
PUPH/15EG	13.7±0.3	107.6±0.9
PUPH/20EG	13.9±0.1	106.6±0.3
PUPH/30EG	—	—
PUPH/40EG	—	—
PUPH/50EG	—	—

6.3. Conclusions

Composites of polycarbonatediol polyurethane and expanded graphite have been synthesized with different EG compositions, mainly to study its effect on the PUPH properties.

FTIR, X–Ray diffraction and SEM of the composites indicate a good average dispersion of EG in the polyurethane matrix with good filler–polymer interactions.

The obtained results from the thermogravimetric analysis indicate that inclusion of EG particles does not significantly increases the thermal stability of the polyurethane matrix. However, expanded graphite reduces its temperature of decomposition in presence of polyurethane.

In this case, only one T_g was observed in the analyzed films. For low EG content a decrease of the T_g value of the composites is observed. This behavior is associated with a

raise of the free volume due to a decrease in the molecular packing of the chain, resulting in an increase of the molecular mobility. Instead, for high EG contents, the interaction between PUPH-EG produces a reduction of the molecular mobility and therefore an increase in T_g. This tendency is in agreement with the results obtained from DMA measurements.

The higher value of the ΔC_{pnor} for the PUPH/15EG composite, associated with an increase of the fraction of polymer contributing to the glass transition, is in accordance with the dielectric/mechanical results.

The electrical conductivity and dielectric properties of PUPH/EG composites were studied in a wide range of frequencies and temperatures. These measurements show that the dielectric permittivity and electrical conductivity of the composites increase with the addition of EG, as expected. An insulator–to–conductor transition is observed with the EG content. Thus, an abrupt variation of both, dielectric permittivity and ac conductivity, is observed at EG content near to 30 wt%. Only in the PUPH sample or in the low EG content compositions, the interfacial polarization or MWS process, is good defined. This result, together with the X–ray analysis, indicates that the EG produces a reduction in the number of formed nanodomains, directly responsible of this conductive process.

For low contents of EG conducting filler (10–20 wt%), the conductivity of the composites is temperature and frequency dependent and remains at the level of the polymeric PUPH matrix (~10^{-14} S cm^{-1}). As the EG filler content increases, a critical concentration of p_c~30wt% is reached. Above this p_c it is observed that conductivity is nearly frequency and temperature independent and a sharp increase, of several orders of

magnitude, takes place. From these results it can be concluded that the conduction comes about percolation paths. The percolation theory has been used to describe the insulator–to–conductor transition.

Finally, the existence of percolation paths at high EG content it is also supported by the observed Arrhenius conductivity behavior and by the activation energy dependence on the EG content. The higher activation energy values observed for the low filler contents can be rationalized if we consider that the mean distance between filler particles increases with decreasing filler content.

Chapter 7:

Conclusions and Future Lines of Research

7. Conclusions and Future Lines of Research

This dissertation set out to analyze two families of polymers in order to determine their properties as function of their chemical structure. In this final chapter, the main conclusions of this thesis will be summarized, and also the directions for future research will be discussed.

7.1. Conclusions

The main research conclusions of this dissertation are compiled in this subsection. These conclusions are grouped into two parts, according to the two families of polymers analyzed.

The first polymeric materials characterized were a series of chemically cross-linked copolymers, which are composed of VP and BA monomers. The object of the analysis was to study both the effect of the monomer composition and the cross-linking content on the properties of the copolymers.

Thus, the specific conclusions obtained for the *X*VP/*Y*BA copolymers with a fixed cross-link density were:

- The samples were chemically and physically characterized by FTIR and TGA, DSC, DMA and DRS techniques. The results obtained from these analyses were found to be in good agreement.
- FTIR analysis verified the chemical structure and showed the existence of dipole-dipole interactions between amide functions.
- According to TGA and mechanical results, thermal and mechanical stability was increased with the VP content.

- DSC results mainly showed a single glass transition and water evaporation peak in the first cycle. Both T_g values and the moisture absorbed from the atmosphere increased with the VP content.
- The dipole-dipole interactions affected significantly several parameters related to the molecular mobility:
  - The T_g values, obtained from DSC and DRS results, increased with the VP content due to a reduction of the molecular mobility.
  - The values of ΔC_p (T_g) were lower for the copolymers and the *100*VP/*0*BA than that obtained for the *0*VP/*100*BA. This is also related to the reduction of mobility associated with the dipole-dipole interactions between VP units.
  - The α dielectric strength values were also lower for higher VP content due to the fact that dipole-dipole interactions hinder the molecular motion.
  - The activation energy of the γ process and α process at T_g increased with the VP content due to the limitation of the chains mobility. However, the E_a for the β process remained nearly constant with the VP content.
  - The fragility values, which are influenced by intermolecular interactions, increased with the VP content.
- The σ_{dc} values obtained by different procedures were in good agreement and increased with the VP content. The temperature dependence of the *dc* conductivity followed a VFTH-like behavior, which indicated that this process is governed by both, the free volume and temperature. The temperature dependence of the decoupling index showed a decoupling of the segmental motion form the charge carrier motions at temperatures near glass transition.

On the other hand, from the analysis of the effect of cross-linking on the *60*VP/*40*BA copolymers, the following conclusions were derived:

- The T_g, evaluated by MDSC and DRS, increased with cross-linking due to the reduction of the segmental motion imposed by the cross-links.
- The ΔC_p (T_g) diminished, which is also related to the decrease in the mobility due to the cross-linking.
- The DRS characterization showed the effect of cross-linking on different parameters:
    - The α peak: (i) shifted to higher temperatures, related to the increase of the T_g, (ii) decreased its strength due to the reduction in the molecular mobility, (iii) increased its breadth, as showing by the increase of a_{HN} parameter, which qualitatively indicates a broader distribution of relaxation times and (iv) increased their relaxation times due to the slowdown of the molecular motions imposed by the constraints on the polymer chains. However, only it is observed a faintly increase in the cooperativity inherent to the α process
    - The β relaxation was found to be a JG relaxation for lower cross-linker contents, whereas this process ceased to be JG relaxation for Z=2. Thus, the cross-linker agent limits the motion related to β relaxation to a more localized motion.
    - The local motion of the polymer (γ relaxation) is essentially unaffected.

The second family of polymers analyzed was a series of polymer matrix composites composed by PUPH reinforced with EG. The object of the analysis was to study the effect of the EG content on the thermal, mechanical and electric properties.

Thus, the specific conclusions obtained for the PUPH/EG composites were:

- FTIR, XRD and SEM indicated a good average dispersion of EG in the PUPH.
- TGA analysis showed a non-significant increase of the thermal stability of PUPH with the EG content.

- XRD results showed a micro-phase separation related to the presence of the soft and hard segments, which was affected by the EG filler.
- Two tendencies of the T_g with the EG content were observed:
    - A decrease of the T_g value was observed for low EG, associated with a raise of the free volume.
    - An increase of the T_g value was observed for high EG, associated with the reduction of the molecular mobility due to the interaction between PUPH-EG. This tendency is in agreement with the results obtained from DMA measurements.
- DSC, DMA and DRS results indicated that the fraction of polymer contributing to the glass transition is dependent of both the EG and crystalline fraction content.
- DRS results showed that the electrical conductivity and dielectric properties of PUPH/EG composites increased with the EG addition:
    - An insulator–to–conductor transition is observed with the EG content. The percolation threshold, p_c, was nearly 30%. Above this p_c value, the conductivity was nearly frequency and temperature independent.
    - The MWS process associated with the microphase separation is good defined only for the PUPH and PUPH/EG composites with low EG content.

7.2. Research Limitations & Future Lines of Research

The future research suggestions generally arise out of the limitations identified during the development of the research. Therefore, the results obtained in the present thesis for each family of polymers, as well as the conclusions derived from them, can serve as a starting point for different future lines of research.

7.2.1. Cross-linked VP/BA copolymers

Due to the characteristics of the cross-linked VP-BA copolymers, some desirable analysis was not able to carry out, which lead to different limitations in the characterization:

- The DRS characterization of the cross-linked homopolymers.
    - The VP homopolymer couldn't be analyzed properly due to its water affinity, which increased the conductivity contribution. Therefore, this water content impeded the characterization of the dipolar processes. In fact, it is not possible to see completely the pure PVP spectrum. Despite this fact, some data was collected from literature (Cerveny, et al., 2008).
    - The BA homopolymer was very difficult to handle and the data obtained from its analysis was not reliable. So, as in the case of VP homopolymer, some data was collected from literature (Fioretto, et al., 1994; Encinar, et al., 2008)
- The analysis of the uncross-linked *60*VP/*40*BA copolymer. The characterization of this sample would have been interesting for comparative purposes in the study of the cross-linking effect. However, the uncross-linked *60*VP/*40*BA copolymer was very unmaneagable and it was not possible its characterization.
- The DMA analysis for all the *X*VP/*Y*BA-*Z*C copolymers. This mechanical characterization was only carried out for the composition of *60*VP/*40*BA-*1*C.

Due to the difficulty to handle these samples, the analysis of the films in the DMA instruments became very complicated. Thus, the composition of *60*VP/*40*BA was chosen because of their most balanced properties.

– A complementary analysis for a better understanding of JG β relaxation. In Chapter 5, the β relaxation was found to be a JG relaxation for lower cross-linker contents, whereas this process ceased to fulfill the typical conditions of a JG relaxation for Z=2. Due to the fact that this result is unexpected, it would be interesting to carry out different analysis to a better understanding of this behavior.

Thus, taking into account the difficulties found in the experimental characterization, the analysis of the cross-linked VP-BA copolymers could be completed with:

– High Pressure Dielectric Measurements. When a glass former is cooled from the high temperature liquid state towards vitrification into the glassy state, the α relaxation time τ_α, the viscosity or diffusion coefficient increase rapidly. The dramatic loss of molecular mobility on decreasing temperature is not only due to a decrease in thermal energy for temperature activation, but also to an increase of density (ρ) and molecular packing (Capaccioli, et al., 2012; Ngai, et al., 2012). Since ρ varies with temperature, the study of molecular mobility of glass-formers would have into account the effect of both ρ and temperature T. Therefore, studies of the effect of temperature and pressure (P) on the molecular mobility of glass formers would be interesting. Thus, Capaccioli et al. (Capaccioli, et al., 2012; Ngai, et al., 2012) propose that the dynamics

could be studied by (i) varying the temperature while ρ is kept constant, (ii) altering ρ while T is kept constant and (iii) varying the combinations of P and T but keeping τ_α the same. These authors saw that the τ_α, n and τ_{JG} are coinvariant to sizable changes in T and P. Hence, it would be interesting to study the effect of P on the JG β relaxation for all the samples and especially for *60*VP/*40*BA-*2*C sample.

- Molecular Dynamics Simulations. These simulations would be useful for a definitive assignment of the origin of the JG β relaxation.

7.2.2. PUPH/EG Composites

During the development of the research on the PUPH/EG composites, the main difficulties identified were:

- The selection of the matrix for the composites. The complicated microstructure of the PUPH polymer makes it difficult to analyze the properties of the PUPH/EG composites.
- The selection of the compositions for PUPH/EG composites. In order to carry out a more accurate analysis of the percolation threshold, it would be desirable to measure more samples with EG contents in the vicinity of p_c.

The future lines of research will remain focused on polymers modified with different conductive fillers to increase its conductivity. However, both the matrix and conductive fillers will have different characteristics:

- The polymeric matrix will be chosen to have an easier microstructure.

- The size of the filler will be nanoscale (less than 100 nm in at least one dimension), so the composites obtained will be *nano*-composites. The small size of nanofillers results in a large surface area, thus increasing the amount of polymer in contact with the filler, which will improve the composite properties.
- Different filler morphologies will be studied in order to analyze their effect on the composite properties.

References

References

Adachi, A., Fukunaga, A., Hayashi, K., Kunisada, M., & Horikawa, T. (2003). *Contact Dermatitits, 48*, 133-136.

Agapov, A., & Sokolov, A. (2011). *Macromolecules, 44*, 4410-4414.

Aharony, A., & Stauffer, D. (1993). *Introduction to Percolation Theory* (2nd Edn. ed.). London: Taylor and Francis.

Ahn, S., Kasi, R., Kim, S., Sharmaa, N., & Zhoub, Y. (2008). *Soft Matter, 4*, 1151–1157.

Alegría, A., Guerrica-Echevarría, E., Goitiandía, L., Tellería, I., & Colmenero, J. (1995). *Macromolecules, 28(5)*, 1516-1527.

Alvarez, C., Lorenzo, V., & Riande, E. (2005). *J. Chem. Phys., 122*, 194905.

Alves, N., Gomez-Ribelles, J., & Mano, J. (2005). *Polymer, 46*(491–504).

Angell, C. (1983). *Solid State Ionics, 9-10*, 3-16.

Angell, C. (1988). *Relaxation in Complex Systems.* (K. Ngai, & G. Wright, Edits.) Springfield: US Dept. Commerce.

Angell, C. (1991). *J. Non-Cryst. Solids, 131-133,* 13-31.

Angell, C. (1992). *Annu. Rev. Phys. Chem., 43*, 693-717.

Angell, C. A. (1985). *J. Non-Cryst. Solids, 73*, 1-3.

Angell, C. A. (1995). *Science, 267*, 1924-1935.

Angell, C. A. (1996). *Complex Behavior of Glassy Systems.* Sitges, Barcelona, Spain: Proceedings of the XIV Sitges Conference.

Anshyang, A., Lin, T., Kwei, K., & Reiser, A. (1989). *Macromolecules, 22*, 4112-4119.

Arbe, A., Genix, A., Arrese-Igor, S., Colmenero, J., & Richter, D. (2010). *Macromolecules, 43*, 3107-3119.

Arrighi, V., McEwen, I., Qian, H., & Prieto, M. (2003). *Polymer, 44*, 6259-6266.

Ash, B., Schadler, L., & Siegel, R. (2002). *Mater. Lett., 55*, 83-87.

Ash, B., Siegel, R., & Schadler, L. (2004). *J. Polym. Sci., Part B: Polym. Phys., 42*, 4371-4383.

Atkins, P. (1990). *Physical Chemistry.* Oxford: Oxford University Press.

Bates, F., & Fredrickson, G. (1990). *Annual Review of Physical Chemistry, 25*, 525-557.

Beiner, M. (2001). *Rapid Commun., 22*, 869-895.

Beiner, M., & Huth, H. (2003). *Nat. Matter, 2*, 595-599.

Bekin, S., Sarmad, S., Gürkan, K., Keçeli, G., & Gürdag, G. (2014). *Sens. Actuators B: Chem., 202*, 878-892.

Bergman, R., Alvarez, F., Alegría, A., & Colmenero, J. (1998). *J. Chem. Phys., 109*, 7546.

Bermejo, F., Fischer, H., Ramos, M., de Andrés, A., Dawidowski, J., & Fayos, V. (1997). *Complex Behaviour of Glassy Systems.* (M. Rubí, & C. Pérez-Vicente, Eds.) Berlin-Heidelberg: Springer Lecture Notes in Physics (Springer).

Bershtein, V., Egorova, L., Yakushev, P., Pissis, P., & Sysel, P. B. (2002). *J Polym. Sci., Part B: Polym. Phys , 40*, 1056–1069.

Blythe, A., & Bloor, D. (2005). *Electrical properties of polymers.* New York: Cambridge University Press.

Bohmer, R., & Angell, C. A. (1992). *Phys. Rev. B, 45*, 10091-10094.

Bohmer, R., & Angell, C. A. (1993). *Phys. Rev. B, 48*, 5857-5863.

Bohmer, R., Ngai, K. L., Angell, C. A., & Plazek, D. J. (1993). *J. Chem. Phys., 99*, 4201-4209.

Borns, M., Kalakkunnath, S., Kalika, D., Kusuma, V., & Freeman, B. (2007). *Polymer, 48*, 7316-7328.

Böttger, H., & Bryskin, U. (1985). *Hopping conduction in solid.* Berlin: Akademie Verlag.

Bower, D. (2002). *An Introduction to Polymer Physics.* Cambridge University Press.

Boyd, R. H. (1985). *Polymer, 26*, 323-347.

Brar, A. S., & Kumar, R. (2002). *J. Appl. Polym. Sci., 85*, 1328-1336.

Brar, A. S., & Kumar, R. (2002). *J. Mol. Struct.*, *616*, 37-47.

Brar, A., & Kumar, R. (2002). *J Mol Struct, 616*, 37-47.

Bueche, F. (1959). *J. Chem. Phys., 30*, 748-752.

Bühler, V. (2005). Polyvinylpyrrolidone Excipients for Pharmaceuticals: Povidone, Crospovidone and Copovidone. Berlin: Springer.

Bunde, A., & Havlin, S. (1991). *Fractal and Disordered Systems.* Berlin: Springer.

Burmistr, M., Sukyy, K., Shilov, V., Pissis, P., Polizos, G., Spanoudaki, A., & Gomza, Y. (2005). *Solid State Ionics, 176*, 1787-1792.

Cangialosi, D., Alegría, A., & Colmenero, J. (2006). *J. Chem. Phys., 124*, 024906-024909.

Cangialosi, D., Boucher, V., Alegría, A., & Colmenero, J. (2012). *Polymer, 53*, 1362.

Capaccioli, S., Paluch, M., Prevosto, D., Wang, L.M., Ngai, K.L. (2012). *J. Phys. Chem. Lett., 3*, 735-743

Carsí, M., Sanchis, M. J., Díaz-Calleja, R., & Nugent, M. J. (2013). *Eur. Polym. J., 49*, 1495–1502.

Carsí, M., Sanchis, M. J., Díaz-Calleja, R., Riande, E., & Nugent, M. J. (2012). *Macromolecules, 45*, 3571−3580.

Casalini, R., & Roland, C. (2003). *Phys Rev Lett, 91*, 015702.

Casalini, R., & Roland, C. (2010). *J. Polym. Sci., Part B: Polym. Phys.*, *48*, 582-587.

Casalini, R., Ngai, K., & Roland, C. (2003). *Phys. Rev. B: Condens. Matter, 68*, 014201.

Cerrada, M., de la Fuente, J., Fernández-García, M., & Madruga, E. (2001). *Polymer, 42*, 4647-4655.

Cerveny, S., Alegría, A., & Colmenero, J. (2008). *J. Chem. Phys., 128*, 044901-044907.

Chang, H., Yeh, Y., & Huang, K. (2010). *Mater. Trans., 51*, 1145-1149.

Chao Li, Y., Yiu Li, R., & Chin Tjong, S. (2010). *J. Nanomat.* DOI:10.1155/2010/261748

Chee, K. (1987). *Polymer, 28*, 977-979.

Chee, K. (1991). *J. Appl Polym. Sci., 43*, 1205-1208.

Chee, K. (1995). *Polymer, 36*, 809-813.

Chen, K., & Yang, S. (2002). *J. Appl. Polym. Sci., 86*, 414-421.

Cohen, M., & Turnbull, D. (1959). *J. Chem. Phys., 31*, 1164-1169.

Cole, K. S., & Cole, R. (1941). *J. Chem. Phys., 9*, 341-351.

Colmenero, J., Alegría, A., Alberdi, J., Alvarez, F., & Frick, B. (1991). *Phys. Rev. B, 44(14)*, 7306.

Cook, W., Scott, T., Quay-Thevenon, S., & Forsythe, J. (2004). *J Appl Polym Sci, 93*, 1348-1359.

Costa, V., Nohales, A., Félix, P., Guillem, C., & Gómez, C. (2012). *J. Elastomers Plast., 45*, 217-238.

Costa, V., Nohales, A., Félix, P., Guillem, C., Gutiérrez, D., & Gómez, C. (2015). *J. Appl. Polym. Sci.* DOI:10.1002/APP.41704

Craig, D. (1995). Dielectric Analysis of Pharmaceutical Systems. London: Taylor&Francis.

Cugini, A., & Lesser, A. (2014). *Polym. Eng. Sci*.

Czech, P., Okrasa, L., Mechin, F., Boiteux, G., & Ulanski, J. (2006). *Polymer, 47*, 7207.

Davidson, D., & Cole, R. (1950). *J. Chem. Phys., 18*, 1417-1418.

Debye, P. (1929). *Polar Molecules.* New York: Chem. Catalog.

Debye, P. (1945). *Polar Molecules.* New York: Dover Publications.

Delpouve, N., Delbreilh, L., Stoclet, G., Saiter, A., & Dargent, E. (2014). *Macromolecules, 47*, 5186-5197.

Deutsch, K., Hoff, E. A., & Reddish, W. (1954). *J. Polym. Sci., 13*, 565-582.

Devine, D., & Higginbotham, C. (2003). *Polymer, 44*, 7851-7860.

Devine, D., & Higginbotham, C. (2005). *Eur. Polym. J., 41*, 1272–1279.

Devine, D., Devery, S.M., Lyons, J.G., Geever, L.M., Kennedy, J.E., & Higginbotham, C.L. (2006). *Int. J. Pharm.*, *326*, 50-59.

Dhakate, S., Sharma, S., Borah, M., Mathur, R., & Dhami, T. (2008). *Int. J. Hydrogen Energy, 33*, 7146-7152.

Dominguez-Espinosa, G., Ginestar, D., Sanchis, M., Díaz-Calleja, R., & Riande, E. (2008). *J. Chem. Phys., 129*, 104513.

Donth, E. (1996). *J. Polym. Sci., Part B: Polym. Phys., 34(17)*, 2881–2892.

Doolittle, A. (1951). *J. Appl. Phys., 22(12)*, 1471-1975.

Doolittle, A. K. (1952). *Appl. Phys., 23(2)*, 236-423.

Dyre, J. (1988). *J. Appl. Phys., 64(5)*, 2456-2468.

Dyre, J. (1988). *Phys. Rev. B, 37*, 10143-10149.

Dyre, J. (1998). *J. Non-Crystal. Solids, 235-237*, 142-149.

Dyre, J., & Shrøder, T. (2000). *Rev. Mod. Phys., 72(3)*, 873-892.

Dyre, J., & Schrøder, T. (2002). *Phys. Stat. Sol. B, 230*, 5-13.

Eceiza, A., Larrañaga, M., de la Caba, K., Kortaberria, G., Marieta, M., Corcuera, M., & Mondragon, I. (2008). *J. Appl. Polym. Sci., 108*, 3092-3103.

Eceiza, A., Martin, M., de la Caba, K., Kortaberria, G., Gabilondo, N., Corcuera, M., & Mondragon, I. (2008). *Polym Eng Sci, 48*, 297.

Ediger, M., & Angell, C. (1996). *J. Phys. Chem, 100*, 13200-13212.

Ediger, M., Angell, C., & Nagel, S. (1996). *J Phys Chem, 100(31)*, 13200-13212.

El-Begawy, S. E., & Huglin, M. B. (1991). *Eur. Polym. J., 27*, 1023-1027.

Encinar, M., Guzmán, E., Prolongo, M., Rubio, R., Sandoval, C., González-Nilo, F., Gargallo,L., Radic, D. (2008). *Polymer, 49 (26)*, 5650-5658.

Feldman, Y., Puzenko, A., & Ryabov, Y. (2002). *Chem. Phys., 284*, 139-168.

Feldstein, M. M., Roos, A., Chevallier, C., Creton, C., & Dormidontova, E. (2003). *Polymer, 44*, 1819-1834.

Feldstein, M. M., Shandryuk, G., Kuptsov, S., & Platé, N. (2000). *Polymer, 41(4)*, 5327-5338.

Ferry, J. (1961). *Viscoelastic Properties of polymers, 2nd ed.* New York: John Wiley&Sons.

Fioretto, D., Livi, A., Rolla, P., Socino, G., & Verdini, L. (1994). *J. Phys.: Condens. Matter, 6*, 5295-5302.

Floudas, G., Placke, P., Stepánek, P., Brown, W., Fytas, G., & Ngai, K. (1995). *Macromolecules, 28*, 6799-6807.

Folttmann, H., & Quadir, A. (2008). *Drug Del. Tech, 8*(22-27).

Fox, T., & Flory, P. (1950). *J. Appl. Phys., 21*, 581-91.

Fragiadakis, D., & Pissis, P. (2007). *J. Non-Crystal. Solids, 353*, 4344-4352.

Fröhlich, H. (1958). Theory of Dielectrics. Dielectric Constant and Dielectric Loss. Oxford University Press.

Fulcher, G. (1925). *J Am Ceram Soc., 8*, 339-340.

Fuoss, R., & Kirkwood, J. (1941). *J Am Chem Soc, 63* , 385-394.

Fuoss, R., & Kirkwood, J. (1941). *J Am Chem Soc, 63*, 385-394.

Gabbott, P. (2008). Principles and Applications of Thermal Analysis. . Blackwell Publishing Ltd.

Gallardo, A., Lemus, A., San Roman, J., Cifuentes, A., & Diez-Masa, J. (1999). *Macromolecules, 32*, 610-617.

Glatz-Reichenback, J., Sorriero, L., & Fitzgerald, J. (1994). *Macromolecules, 27*, 1338.

Goldstein, J., Newbury, D., Joy, D., Lyman, C., Echlin, P., Lifshin, E., Sawyer, L., Michael, J. (2003). *Scanning Electron Microscopy and X-Ray Microanalysis*. New York: Springer.

Gómez, C., Culebras, M., Cantarero, A., Redondo-Foj, B., Ortiz-Serna, P., Carsí, M., & Sanchis, M. (2013). *Appl. Surf. Sci, 275*, 295-302.

Gordon, M., & Taylor, J. S. (1952). *J. Appl. Chem., 2*, 493-500.

Grassi, M., Colombo, I., & Lapasin, R. (2000). *J. Controlled Release, 68*, 97-113.

Grigoraş, V. C., & Bărboui, V. (2008). *Rev. Roum. Chim., 53*, 127-131.

Gupta, A., Chen, G., Joshi, P., Tadigadapa, S., & Eklund, P. (2006). *Nano Lett, 6*, 2667-2673.

Haaf, F., Sanner, A., & Straub, F. (1985). *Polym. J., 17*, 143-152.

Hart, E., & Waxman, B. (1983). *Encyclopedia of Chemical Technology* (Vol. 23). (H. Mark, D. Othmer, C. Overberger, & G. Seaborg, Eds.) New York: Interscience.

Havriliak, S., & Negami, S. (1966). *J. Polym. Sci., Part B: Polym. Symp., 14*, 99-117.

Havriliak, S., & Negami, S. (1966). *J. Polym. Sci., Part C: Pol. Symp., 14(1)*, 99-117.

Havriliak, S., & Negami, S. (1967). *Polymer, 8(4)*, 161-210.

Havriliak, S., & Negami, S. (1997). *Dielectric and Mechanical Relaxation in Materials.* Munich: Hanser.

He, F., Fan, J., & Lau, S. (2008). *Polym. Test., 27*, 964-970.

Hempel, E., Beiner, M., Huth, H., & Donth, E. (2002). *Thermochim Acta, 391*, 219-225.

Hodge, I. (1983). *Macromolecules, 16(6)*, 898–902.

Hodge, I., Ngai, K., & Moynihan, C. (2005). *J. Non-Cryst. Solids, 351(2)*, 104-115.

Hu, J., & Mondal, S. (2005). *Polym. Int., 54*, 764-771.

Huang, X., & Brittain, W. (2001). *Macromolecules, 34*, 3255-3260.

Huglin, M. B., & Rehab, M. M. (1987). *Polymer, 28(13)*, 2200-2206.

Huglin, M., & Zakaria, M. (1986). *J. Appl. Polym. Sci., 31*, 457-475.

Huo, P., & Cebe, P. (1992). *J. Polym. Sci., Part B: Polym. Phys., 30*, 239-250.

Ikeda, M., & Aniya, M. (2010). *Intermetallics, 18*, 1796-1799.

Jablonski, A., Lang, A., & Vyazovkin, S. (2008). *Thermochim Acta, 474*, 78-80.

Janik, P., & Paluch, M. (2001). *Phys. Rev. E.: Stat. Phys., Plasmas, Fluids, 64*, 042502.

Jin-Chao, Z., Fei-Peng, D., Xing-Ping, Z., Wei, C., Xiao-Mei, W., Hong, Z., Xiao-Lin, X., Yiu-Wing, M. (2011). *Compos. B, 42*, 2111.

Jobish, J., Charoen, N., & Praveen, P. (2012). *J. Non-Crystal Solids, 358*, 1113-1119.

Johari, G. P., & Goldstein, M. (1970). *J. Chem. Phys., 53*, 2372.

Johari, G. P., & Goldstein, M. (1972). *J. Chem. Phys., 56*, 4411.

Johari, G., & Goldstein, M. (1971). *J. Chem. Phys., 55(9)*, 4245-4252.

Johari, G., & Pathmanathan, K. (1986). *J. Chem. Phys., 85(11)*, 6811-6812.

John Wiley & Sons, L. (March 2011). *Properties and Behavior of Polymers, Two Volume Set.* (J. W. Ltd., Ed.) Wiley.

Jonscher, A. (1992). *Universal relaxation law.* London: Chelsea Dielectric Press.

Jonscher, A. (1996). In A. Jonscher, *Universal Relaxation LAw: A Sequel to Dielectric Relaxation in Solids.* London: Chelsea Dielectrics Press.

Ju, H., Ki, S., & Lee, Y. (2002). *J. Appl. Polym. Sci., 83*, 1128-1139.

Kahle, S., Korus, J., Hempel, R., Unger, R., Höring, S., & Schröter, K. (1997). *Macromolecules, 30*, 7214.

Kalakkunnath, S., Kalika, D. S., Lin, H., Raharjo, R. D., & Freeman, B. D. (2007). *Macromolecules, 40*, 2773-2781.

Kalogeras, I., & Neagu, E. (2004). *Eur. Phys. J. E, 14*, 193-204.

Kaoutit, H. E., Estevez, P., Ibeas, S., Garcia, F., Serna, F., Benabdelouahab, F., & Garcia, J. (2013). *Dyes Piments., 96*, 414-423.

Khursheed, A. (2011). *Scanning Electron Microscope Optics and Spectrometers.* London: World Scientific Publishing Co. Pte. Ltd.

Killis, A., LeNest, J., Cheradame, H., & Gandini, A. (1982). *Makromol. Chem., 183*, 2853.

Klonos, P., Panagopoulou, A., Bokobza, L., Kyritsis, A., Peoglos, V., & Pissis, P. (2010). *Polymer, 51*, 5490-5499.

Kohlrausch, F. (1854). *Pogg Ann Phys Chem, 91*, 179-214.

Kojio, K., Nonaka, Y., Masubuchi, T., & Furukawa, M. (2004). *J Polym Sci., Part B: Polym Phys, 42*, 4448.

Konwer, S., Maiti, J., & Dolui, S. (2011). *Mater. Chem. Phys., 128*, 283-290.

Kovacs, A. (1963). *Adv. Polym. Sci., 3*, 394.

Kovacs, A., Aklonis, J., Hutchinson, J., & Ramos, A. (1979). *J. Pol. Sci., 17(7)*, 1097-1162.

Kremer, F., & Schönhals, A. (2003). *Broadband Dielectric Spectroscopy.* Berlin: Springer.

Król, P. (2007). *Prog. Mater. Sci., 52*, 915.

Krupa, I., & Chodák, I. (2001). *Eur. Polym. J., 37*, 2159-2168.

Ku, C., & Liepens, R. (1987). *Electrical Properties of Polymers. Chemical Principles.* Munich-Vienna-New York: Hanser Publishers.

Kwei, T. K. (1984). *J. Polym. Sci. Polym. Lett. Ed*., 22 (6), 307–313.

Kwei, T. K., Pearce, E. M., Pennacchia, J. R., & Charton, M. (1987). *Macromolecules, 20 (5)*, 1174–1176.

Laredo, E., & Grimau, M. (2003). *Macromolecules, 36*, 9840-9850.

Lee, S. (1998). *Thermoplastic Polyurethane Markets in the EU-Production, Technology, Applications and Trends a Report from Rapra's Industry Analysis and Publishing Group.* Uitgewer : iSmithers Rapra Publishing.

Lee, W. A., & Knight, G. J. (1966). *The Glass Transition of Polymers, Polymer Handbook.* (J. I. Brandrup, Ed.) New York: Wiley- Interscience Publishers.

Lewis, I., & Edwards, H. (2001). *Handbook of Raman Spectroscopy.* New York: Marcel Dekker.

Li, Z., Lu, C., Xia, Z., Zhou, Y., & Luo, Z. (2007). *Carbon, 45*, 1686-1695.

Lindsay, C., & Patterson, G. (1980). *J. Chem. Phys., 73*, 3348.

Lipatov, Y., & Privalko, V. (1972). *Polym. Sci., 14*, 1843-1848.

Liu, X., & Wu, Q. (2001). *Polymer, 42*, 10013-10019.

Lopérgolo, L., Lugao, A., & Catalani, L. (n.d.). *Polymer, 44*, 6217-6222.

Lovel, R. (1974). *J. Phys. C: Solid State Phys.,* 7(23), 4378-4384.

Lu, H., Zhang, X., & Zhang, H. (2006). *J Appl Phys, 100(5)*, 054104.

Lunkenheimer, P., Schneider, U., Brand, R., & Loidl, A. (2000). *Contemp. Phys., 41*, 15-36.

Lux, F. (1993). *J. Mater. Sci., 28*, 285-301.

Marinho, B., Ghislandi, M., Tkalya, E., Koning, C.E.,& de With, G. (2012). *Powder Technol., 221*, 351-358.

Mark, J. (2007). *Physical Properties of Polymer Handbook*. Springer.

Maxwell, J. (1893). *Electricity and Magnetism.* Oxford: Clarendon.

McCrum, N., Read, B., & Williams, W. (1991). *Anelastic and Dielectric Effects in Polymeric Solids.* New York: Dover Publications.

Menczel, J., & Bruce Prime, R. (2009). *Thermal Analysis of Polymers. Fundamentals and Applications.* Hoboken, New Jersey: John Wiley & Sons.

Merino, E., Atlas, S., Raihane, M., Belfkira, A., Lahcini, M., Hult, A., Dionísio, M., Correia, N. (2011). *Eur. Polym. J., 47*, 1429-1446.

Meuse, C., Yang, X., Yang, D., & Hsu, S. (1992). *Macromolecules, 25*, 925-932.

Michler, G. (2008). *Electron Microscopy of Polymers.* Berlin Heidelberg: Springer-Verlag.

Miller, R. L. (1999). *Glass transition Temperatures of Polymers* (4th Ed. ed.). (J. Brandrup, E. H. Immergut, & E. A. Grulke, Eds.) Hoboken: Polymer Handbook; Wiley-Interscience.

Mizuno, F., Belieres, J., Kuwata, N., Pradel, A., Ribes, M., & Angell, C. (2006). *J. Non-Crystal Solids, 352*, 5147-5155.

Montroll, E., & Weiss, G. (1965). *Math. Phys., 6*, 167.

Mott, N. (1987). *Conduction in Non-Crystalline Materials.* Oxford: Clarendon Press.

Mott, N. (1990). *Metal Insulator Transitions.* London: Taylor and Francis.

Mpoukouvalas, K., Floudas, G., & Williams, G. (2009). *Macromolecules, 42*, 4690-4700.

Neagu, E., Pissis, P., Apekis, L., & Gomez Ribelles, J. L. (1997). *J Phys D: Appl Phys, 30(11)*, 1551–60.

Ngai, K. (1979). *Comments Solid State Phys, 9*, 141-155.

Ngai, K. (1998). *J. Chem. Phys, 109*, 6982.

Ngai, K. (2003). *J. Phys. Condens. Matter, 15*, S1107-S1125.

Ngai, K. (2011). Relaxation and diffusion in complex systems. Berlin: Springer.

Ngai, K. L., & Paluch, M. (2004). *J. Chem. Phys., 120*, 857-873.

Ngai, K., & Capaccioli, S. (2004). *Phys. Rev. E, 69*, 031501.

Ngai, K., & Capaccioli, S. (2007). *J. Phys.-Condens. Mat., 19(20)*, 205114.

Ngai, K.L., Habasaki, J., Prevosto, D., Capaccioli, S., Paluch, M. (2012). *J. Chem. Phys., 137*, 034511.

Ngai, K., & Roland, C. (1993). *Macromolecules, 26*, 2688-2690.

Ngai, K., & Tsang, K. (1999). *Phys Rev E, 60*, 4511.

Nguyen, K., & West, J. (2002). *Biomaterials, 23*, 4307-4314.

Nicholson, J. (1994). *The chemistry of Polymers*. Cambridge: RSC Paperbacks.

Noda, N. (2005). *Polymer, 46*, 7201-7217.

Novák, I., Krupa, I., & Chodák, I. (2002). *J. Mater. Sci. Lett., 21*, 1039-1040.

Odegard, G., & Bandyopadhyay, A. (2011). *J. Polym. Sci. Part B: Polym. Phys., 49(24)*, 1695-1716.

Odian, G. (2004). *Principles of Polymerization* (4th ed.). Hoboken: John Wiley & Sons, Inc.

Oertel, G. (1993). *Polyurethane Handbook, 2nd ed.* New York: Hanser.

Okrasa, L., Czech, P., Boiteux, G., Mechin, F., & Ulanski, J. (2008). *Polymer, 49*, 2662.

Ortiz-Serna, P., Carsí, M., Redondo-Foj, B., Sanchis, M., Culebras, M., Gómez, C., & Cantero, A. (2015). *J. Appl. Polym. Sci.*(DOI:10.1002/APP.42007).

Ortiz-Serna, P., R., D.-C., Sanchis, M. J., Riande, E., Nunes, R., Martins, A., & Visconte, L. (2010). *Macromolecules, 43*, 5094–5102.

Ortiz-Serna, P., R., D.-C., Sanchis, M. J., Riande, E., Nunes, R., Martins, A., & Visconte, L. (2011). *J. Non-Cryst. Solids, 357*, 598–604.

Otegui, J., Schwartz, G., Cerveny, S., Colmenero, J., Loichen, J., & Westermann, S. (2013). *Macromolecules, 46*, 2407-2416.

Otieno, G., & Kim, J. (2008). *J. Ind. Eng. Chem., 14(2)*, 187-193.

Paluch, M., Pawlus, S., Hensel-Bielowka, S., Kaminska, E., Prevosto, D., Capaccioli, S., Rolla, P. A., Ngai, K. L. (2005). *J. Chem. Phys., 122(23)*, 234506-234506-6.

Pathmanathan, K., & Johari, G. (1991). *J. Chem. Phys., 95*, 5990.

Patil, P., Rath, S., Sharma, S., Sudarshan, K., Maheshwari, P., Patri, M., Khandelwal, P., Pujari, P. (2013). *Soft Matter, 9*, 3589-3599.

Patkpwski, A., Paluch, V., & Gapinski, J. (2003). *J. Non-Crystal. Solids, 330*, 259-263.

Peppas, N. (1987). *Hydrogels in medicine and pharmacy.* Florida: CRC Press.

Peppas, N., Bures, P., Leobandung, W., & Ichikawa, H. (2000). *Eur. J. Pharm. Biopharm., 50*, 27-46.

Petrovic, Z., Zavargo, Z., Flynn, J., & Macknight, W. (1994). *J. Appl. Polym. Sci., 51(6)*, 1087-1095.

Piana, F., & Pionteck, J. (2013). *Compos. Sci. Technol., 80*, 39-46.

Pielichowski, K., Pielichowski, J., & Prociak, A. (1998). *J. Appl. Polym. Sci., 67 (8)*, 1465-1471.

Pissis, P., Georgoussis, G., Bershtein, V., Neagu, E., & Fainleib, A. (2002). *J. Non-Cryst. Solids, 305*, 150.

Plazek, D., & Ngai, K. (1996). The glass temperature. In J. E. Mark, *Physical properties of polymers handbook* (p. 139). Woodbury, N.Y.: AIP Press.

Polizos, G., Kyritsis, A., Pissis, P., Shilov, V., & Schevchenko, V. (2000). *Solid State Ionics, 136*, 1139.

Priscariu, C. (2011). *Polyurethane Elastomers. From Morphology to Mechanical Aspects*. New York: Springer.

Privalko, V., & Titov, G. (1979). *Polym. Sci., RSSR 21*, 380-387.

Psarras, G. (2006). *Compos. Part A Appl. Sci. Manuf., 37*, 1545-1553.

Qazvini, N., & Mohammadi, N. (2005). *Polymer, 46*, 9088-9096.

Qin, Q., & McKenna, B. (2006). *J. Non-Cryst. Solids, 352*, 2977-2985.

Ratner, M., & Shriver, D. (1988). *Chem. Rev., 88*, 109-124.

Reading, M., & Hourston, D. J. (2006). *Modulated-Temperature Differential Scanning Calorimetry. Theoretical and Practical Applications in Polymer Characterization*. (m. Reading, & D. J. Hourston, Eds.) Dordrecht, The Netherlands: Springer.

Reiner Zorn, A. (1999). *J. Polym. Sci. Part B: Polym. Phys., 37*, 1043.

Reppe, W. (1954). *Polyvinylpyrrolidon.* Weinheim: Verlag Chemie.

Riande, E., & Díaz-Calleja, R. (2004). *Electrical Properties of Polymers.* The United States of America: Dekker, M.

Riande, E., Díaz-Calleja, R., Prolongo, M., Masegosa, R., & Salom, C. (2000). *Polymer Viscoelasticity: Stress and Strain in Practice.* New York: Marcel Dekker.

Roberts, G., & White, E. (1973). Relaxation processes in amorphous polymers. In R. Haward (Ed.), *The Physics of Glassy Polymers.* London: Applied Science.

Roland, C. (1994). *Macromolecules, 27*, 4242-4247.

Roland, C., Santangelo, P., & Ngai, K. (1999). *J. Chem Phys, 111(12)*, 5593-5598.

Rönnau, A., Wulferink, W., Unver, E., Ruzicka, T., Krutmann, J., & Grewe, M. (2000). *Br. J. Dermatol., 143*, 1055-1058.

Rössler, E., Hess, K. U., & Novikov, V. (1998). *J. Non-Cryst.Solids, 223*, 207-222.

Rubi, M., & Pérez-Vicente, C. (1997). Berlin: Springer.

Ryabov, Y., & Nuriel, H. (2003). *J. Polym. Sci. Part B: Polym. Phys. 41(3)*, 217-223.

Ryan, A., Macosko, C., & Bras, W. (1992). *Macromolecules, 25*, 6277-6283.

Sabater i Serra, R., Escobar-Ivirico, J., Meseguer-Dueñas, J., Andrio-Balado, A., & Gomez-Ribelles, J. (2009). *Journal of Polymer Science: Part B: Polymer Physics, 47*, 183-193.

Sanchis, M. J., Díaz-Calleja, R., Gargallo, L., Hormazábal, A., & Radic, D. (1999). *Macromolecules, 32*, 3457-3463.

Sanchis, M. J., Díaz-Calleja, R., Pelissou, O., Gargallo, L., & Radic, D. (2004). *Polymer, 45*, 1854-55.

Sanchis, M., Carsí, M., Ortiz-Serna, P., Domínguez-Espinosa, G., Díaz-Calleja, R., Riande, E., Alegría, L., Gargallo, L. Radic, D. (2010). *Macromolecules, 43*, 5723–5733.

Sandu, I., Brasoveanu, M., Morjan, I., Voicu, I., Dumitrache, F., Teodor, C.F., Gavrila-Florescu, L. (2011). *Thin Solid Films, 519(12, SI)*, 4128-4131.

Sangoro, J., & Kremer, F. (2011). *Acc. Chem. Res., 45*(4), 525-532.

Santangelo, P., & Roland, C. (1998). *Phys. Rev B, 58(21)*, 14121-14123.

Sargsyan, A., Tonoyan, A., Davtyan, S., & Schick, C. (2007). *Eur. Polym. J., 43*, 3113-3127.

Schlessinger, M. (1995). *Infrared technology fundamentals.* New York: Marcel Dekker, Inc.

Schneider, H. A. (1989). *Polymer, 30(5)*, 771-779.

Schönhals, A. (1997). In J. Rung, & J. Fitzgerald, *Dielectric Spectroscopy of Polymeric Materials. Fundamentals and Applications.* Washington: American Chemical Society.

Schröter, K., Unger, R., Reissig, S., Garwe, F., Khale, S., Beiner, M., & Donth, E. (1998). *Macromolecules, 31*, 8966.

Scott, T., Cook, W., & Forsythe, J. (2002). *Eur Polym J, 38*, 705-716.

Seymour, R., Allegrezza, A., & Cooper, S. (1973). *Macromolecules, 6*, 896-902.

Sillars, R. (1937). *Inst. Elect. Eng., 80*, 378.

Slark, A. (1999). *Polymer, 40*, 1935-1941.

Smaoui, H., Arous, M., Guermazi, H., Agnel, S., & Toureille, A. (2010). *J. Alloys Compd., 489*, 429-436.

Song, M., Hourston, D., Pollock, H. M., & Hammiche, A. (1999). *Polymer, 40*, 4763-4767.

Sperling, L. (2006). *Introduction to Physical Polymer Science.* Hoboken: Wiley-Interscience.

Stauffer, D. (1984). *Introduction to Percolation Theory.* London: Taylor&Francis.

Stephan, A. (2006). *Eur. Polym. J., 42*, 21-42.

Strawhecker, K., Hsieh, A., Chantawansri, T., Kalcioglu, Z., & Van Vliet, K. (2013). *Polymer, 54*, 901.

Strümpler, R., & Glatz-Reichenbach, J. (1999). *Electroceram, 3*, 329-346.

Szycher, M. (1999). *Handbook of Polyurethanes.* Washington DC: CRC Press.

TAInstruments. (n.d.). Thermal Analysis Review. Modulated DSC Theory. *TA Instruments. Thermal Analysis & Rheology, TA-211B*.

Tamman, G., & Hesse, W. (1926). *Z Anorg Allg Chem., 156*, 245-247.

Tan, Y. Y., & Challa, G. (1976). *Polymer, 17*, 739-740.

Tanaka, H., & Kunimura, M. (2002). *Polym. Eng. Sci., 42*, 1333.

Thomas, L. (2005). Modulated DSC® Paper #5 Measurement of Glass Transitions and Enthalpic Recovery. *TA Technical Paper (TP010)*.

Vallejos, S., El Kaoutit, H., Estévez, P., García, F., de la Peña, J., Serna, F., & García, J. (2011). *Polym. Chem., 2*, 1129-1138.

Vallejos, S., Estevez, P., Ibeas, S., Garcia, F., Serna, F., & Garcia, J. (2012). *Sensors, 12*, 2969-2982.

Vallejos, S., Estevez, P., Ibeas, S., Muñoz, A., García, F., Serna, F., & Garcia, J. (2011). *Sens. Actuators: B. Chem., 157*, 686-690.

Vallejos, S., Munoz, A., Garcia, F., Serna, F., Ibeas, S., & Garcia, J. (2012). *J. Hazard. Mat., 227-228*, 480-483.

Vandenbeele, P. (2013). *Practical Raman Spectroscopy-An Introduction*. Ghent: Wiley.

Viciosa, M., Rouzé, N., Dionísio, M., & Gomez-Ribelles, J. (2007). *Eur. Polym J., 43*, 1516-1529.

Vogel, H. (1921). *Z Phys., 22*, 645-646.

Wagner, K. (1914). *Arch. Electrotech., 2*, 371.

Wang, Y., Agapov, A., Fan, F., Hong, K., Yu, X., Mays, J., & Sokolov, A. (2012). *Phys. Rev. Lett., 108*, 088303.

Weinmüller, C., Langel, C., Fornasiero, F., Radke, C., & Prausnitz, J. (2006). *J. Biomed. Mater. Res. A, 77*, 230-241.

Wichterle, O. (1971). *Encyclopedia of Polymer Science and Technology* (Vol. 15). (N. Bikales, Ed.) New York : Interscience.

Williams, G. (1979). *Adv Polym Sci, 33*, 59-92.

Williams, G., & Watts, D. (1970). *Trans. Faraday Soc., 66*, 80.

Williams, G., Watts, D., Dev, S., & North, A. M. (1971). *Trans. Faraday Soc., 67*, 1323.

Wübbenhorst, M., & Van Turnhout, J. (2002). *J. Non-Crystal. Solids, 305*, 40-49.

Xu, H., Kuo, S., Lee, J., & Chang, F. (2002). *Macromolecules, 35*, 8788-8793.

Yamauchi, A. (2001). *Gels Handbook, Vol.1 The Fundamentals*. Academic Press.

Yanez, F., Concheiro, A., & Alvarez-Lorenzo, C. (2008). *Eur. J. Pharm. Biopharm., 69*, 1094-1110.

Zallen, R. (2004). *The Physics of Amorphous Solids.* New York: Wiley.

Zhang, S., Painter, P. C., & Runt, J. (2004). *Macromolecules, 37*, 2636–42.